Field-Deployable Microfluidics for Species Identification in Conservation

Hallie Ray Holmes

A dissertation
submitted in partial fulfillment of the
requirements for the degree of

Doctor of Philosophy

University of Washington
2018

Reading Committee:
Karl F. Böhringer, Chair
Barry Lutz
Samuel K. Wasser

Program Authorized to Offer Degree:
Bioengineering

University of Washington

Abstract

Field-Deployable Microfluidics for Species Identification in Conservation

Hallie Ray Holmes

Chair of the Supervisory Committee:
Professor Karl F. Böhringer
Department of Electrical Engineering, Department of Bioengineering

This work explores the development of anisotropic ratchet conveyors (ARCs), a type of microfluidic system that can transport small liquid quantities in the form of droplets. ARCs derive their function from a passive, microfabricated surface pattern and applied orthogonal vibrations. A fundamental solid mechanics model is developed to describe how droplets convert a vertical vibration to horizontal droplet transport. Results demonstrate the droplet system can be modelled as a damped-harmonic-oscillator and elucidate the effect of vibration and substrate parameters on droplet behavior. An investigation of how the interface between the substrate and droplet edges affects droplet transport demonstrates that the substrate can influence resonance behavior of the droplet. These results also demonstrate that transport velocity is the result of a summation of discrete step size probabilities, as edge movement is quantized by the rung intervals. This understanding led to the development of new ARC devices that can enable controlled synchronization, sorting, and transfer of droplets. Finally, the capabilities of this system are focused on the development of a field-deployable platform for species identification. Key problems in conservation that have need for new DNA testing technologies and would substantially benefit from the application of microfluidic systems are discussed. A prototype chipset and driving unit is created that can perform an isothermal nucleic acid amplification test by delivering reagents with the ARC system. This initial foray of the ARC microfluidic system into species identification for conservation demonstrates a promising potential for this system and introduces an impactful application setting for microfluidics research that has been previously unexplored.

TABLE OF CONTENTS

LIST OF FIGURES

LIST OF TABLES

ACKNOWLEDGEMENTS

This work was supported by the National Science Foundation (ECCS-1308025), the National Fish and Wildlife Foundation, Schmidt Marine Technology Partners, and a National Defense Science and Engineering Graduate Fellowship. Fabrication of ARCs was performed at the Washington Nanofabrication Facility, an NNCI site supported in part by the NSF (1542101, 1337840 and 0335765), the Washington Research Foundation, the M. J. Murdock Charitable Trust, Altatech, ClassOne Technology, GCE Market, Google and SPTS. I would also like to thank the engineers at the Washington Nanofabrication Facility - Michal Khbeis, Duane Irish, Darick Baker, Mark Morgan, and David Nguyen, for their patience and guidance in my microfabrication processes, Conservation X Labs for their support in providing essential equipment, materials, reagents, and guidance for 3D printed prototypes and DNA amplification tests, and Timothy A. Holmes for the fabrication of custom high-speed camera mounts.

DEDICATION

My thesis is dedicated to all of the mentors I have been so fortunate to have throughout my life and career. Beginning with my parents, Timothy and Sandra Holmes encouraged my curiosity from the start and taught me a plethora of practical skills that I have relied on throughout my life. In high school I learned important lessons from my teachers, Robert Peters – who first taught me to think like scientist and gave me the confidence to begin my career in engineering, and Alan Boydston - who taught me that intelligence is wasted if not accompanied with hard work and perseverance. When I entered my undergraduate studies, Rupak Rajachar took a chance on me as a young freshman, welcoming me into his lab and teaching me core bench skills, as well as the mindset to design experiments, evaluate data, and how to navigate life with a tasteful eccentricity. This experience was bolstered by Keat Ghee Ong, who fostered my interest in electrical engineering and encouraged me to expand my skillset because the future will be multidisciplinary. Throughout my graduate studies, my thinking was simultaneously broadened and focused by my committee members – Albert Folch, Barry Lutz, Indroneil Ganguly, and Samuel Wasser. My mentors at Conservation X Labs, Alex Dehgan and Paul Bunje provided me an entirely distinct perspective, teaching me the importance of stepping back from the microscope to look at the big picture and how to communicate my science story. David Baisch propelled me to success faster than I could have possibly imagined, providing me invaluable knowledge and training in molecular biology, conservation, and the practical translation of these skills to real world problems. Finally, upon beginning my PhD, I chose to study under my advisor, Karl Böhringer, because he is not only an accomplished scientist and engineer, but he is the kind of person I want to be like throughout my life and career. The lessons I've learned from Karl, spanning from MEMS and microfabrication to European history and global politics, are too numerous to detail. Karl has provided me countless examples of how to handle difficult situations with integrity and accountability, confirming my initial motivation for seeking his mentorship with our every interaction. Thank you, Karl, for an incredible graduate school experience.

Chapter 1. A BRIEF HISTORY OF MICROFLUIDICS

Microfluidics is broadly defined as the control and manipulation of fluids with a feature size or volume at the micro scale. The first microfabricated fluidic devices appeared in the form of ink-jet printing nozzles, produced at IBM,[1,2] and gas chromatograph sensors at Stanford University [3–5] in the late 1970's (Figure 1.1). The success of these initial devices was enabled by advances in microfabrication techniques spurred by integrated circuit and microelectromechanical systems (MEMS) research.[6]

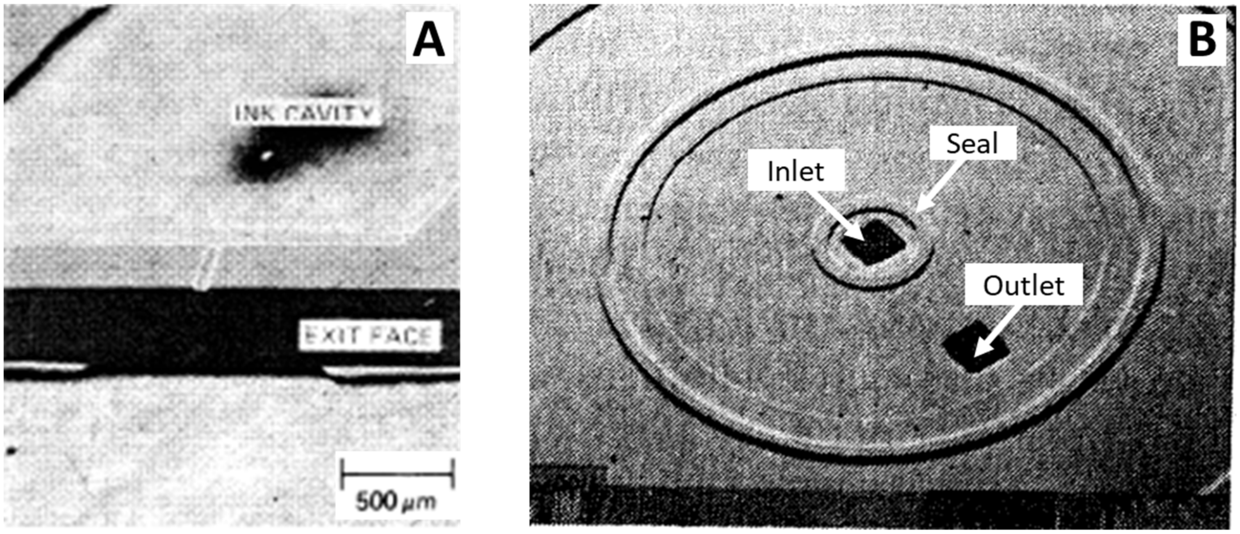

Figure 1.1: Original microfluidic devices. Microfabricated ink-jet prinking nozzles (A) developed at IBM (© 1982 IEEE)[7] and silicon membranes (B) for gas chromatograph sensors (© 1979 IEEE)[3] were the first microfabricated devices used for handling fluids at the microscale.

Following these initial accomplishments, researchers began developing microfluidic valves[8–10] and pumps[11–14] to serve as check valves and flow regulation systems (Figure 1.2). As these endeavors led to improved methods and capabilities for fabricating microchannels in silicon and glass substrates, microfluidics began to see increased use in basic scientific research, and the development of systems with integrated sensors to measure flow[15–18] and perform chemical analyses[19–21] soon followed.

The advent of soft-lithographic fabrication techniques[22] provided for microfluidic devices that were less-expensive, flexible, and stackable.[23–25] These properties enabled the development of three-dimensional microfluidic networks[26,27] and microfluidic devices with material properties more suitable for interfacing with biologic systems.[24,25] This new generation of soft microfluidic devices propelled the field towards many applications in medicine and biology, resulting in rapid growth and interest in microfluidics as researchers envisioned “lab-on-a-chip” or “micro-total analysis systems” that could perform high-throughput analyses of chemical and biologic systems.[24,28]

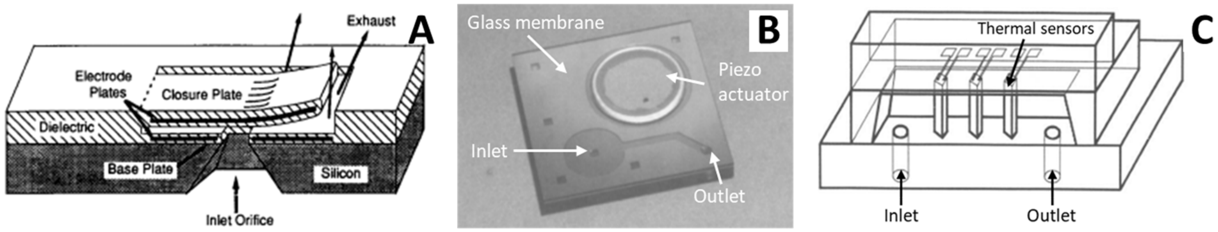

Figure 1.2: Early microfluidic devices. Microfabricated valves (© 1990 IEEE)[9] (A), micropumps (adapted from Reference 12, Copyright (1994), with permission from Elsevier)[12] (B), and flow sensors (© 1991 IEEE)[16] (C) greatly expanded the capabilities and applications of microfluidics.

Despite many innovations, few of these microfluidic devices met commercial success. A major barrier to the commercial development of these monolithic microfluidic systems is packaging, which is estimated to account for as much as 80% of final device cost and severely impedes scalable manufacturing.[24] The development of paper microfluidic devices[29,30] provided an ultra-low cost microfluidic platform to perform automated tests and analysis. Paper microfluidics have rapidly developed over the last decade, gathering much excitement for their potential to serve as point-of-care or point-of-contact (POC) diagnostic tests in low-resources areas.[31–33] However, paper-based microfluidic devices are restricted by poor transport efficiency of target molecules and low measurement sensitivity.[31]

Another problem faced by monolithic continuous flow and paper microfluidic systems is undesired interaction between flows and the system, such as Taylor dispersion and cross-contamination between flows, and solute-surface interactions between the flows and channels.[34–36] Segmented flow or droplet microfluidic systems generate micro- or nano-scale droplets by applying a shear flow of a second immiscible fluid (typically water droplets in oil).[37–39] These segmented flow systems provided consistent, isolated samples with significantly reduced volume and reactant quantities compared to continuous flow systems,[34–36] and led to applications requiring high-throughput enzymatic and cell assays[40–42] and combinatorial chemistry.[43–45] However, droplets in segmented flow systems cannot be individually addressed. The advent of digital microfluidic systems provided a platform that can transport and manipulate individual, compartmentalized droplets without microchannels or encapsulating fluids. However, digital microfluidic systems operate with larger droplet volumes and at lower transport rates than segmented flow systems.[46]

Ink-jet printing nozzles are still the most widely used and commercially successful microfluidic devices. However, the field of microfluidic has experienced tremendous growth and covers a wide variety of applications, exhibiting great potential for widespread commercial use in many scenarios. As of today, four main categories compose the field of microfluidics: continuous flow, segmented flow, paper, and digital[47] (Table 1.1). Each system provides a unique set of advantages and shortcomings, which necessitates the decision for implementing a specific microfluidic system to be determined by the use-case scenario in which it is applied. This thesis will focus on digital microfluidics and the development of a specific system called anisotropic ratchet conveyors to serve as a DNA barcode identification tool for wildlife and timber products.

Table 1.1: Comparison of microfluidic systems

System Type	**Advantages**	**Disadvantages**
Continuous Flow[48*] 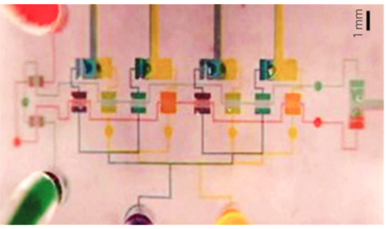	High-throughput Good sensitivity Highly controlled flow	Difficult packaging Poor scalability Complex set-up
Paper[49†] 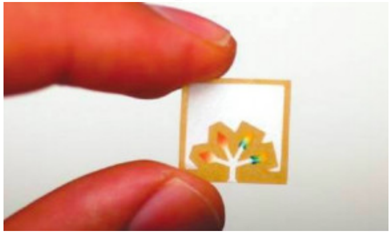	Passive transport Ultra-low cost Simple to use	Difficult flow control Poor sensitivity Low transport efficiency
Segmented Flow[50‡] 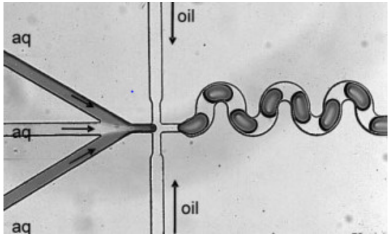	Compartmentalization Minimal volume High-throughput	Packaging/scalability Oil separation No individual control
Digital[51§] 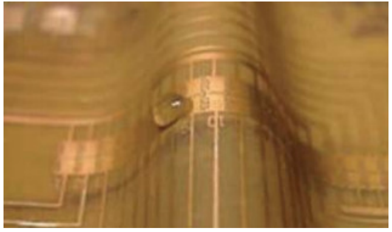	Individual addressability Compartmentalization No oil needed	Larger droplet volume Lower throughput Limited liquid properties

---

[*] Adapted by permission from Springer Nature: Nature Physics Reference 48, Copyright 2010.
[†] Adapted from Reference 49. Copyright (2010) American Chemical Society.
[‡] Adapted from Reference 50 with permission of the Royal Society of Chemistry.
[§] Adapted from Reference 51 with permission of the Royal Society of Chemistry.

Chapter 2. DIGITAL MICROFLUIDIC SYSTEMS

The following sub-sections are adapted from:

Transporting Droplets through Surface Anisotropy[47]*

Hal R. Holmes[1] and Karl F. Böhringer,[1,2] Microsystems & Nanoengineering **1**, (2015)

[1]Department of Bioengineering, and [2]Department of Electrical Engineering, University of Washington, Seattle, WA 98195, USA

2.1 INTRODUCTION

Each droplet on a digital microfluidic system can be thought of as a unit or "bit" of information, and digital microfluidic systems can manipulate droplets independently. This is a significant advantage over segmented flow systems that control droplets in series through the flow of an immiscible liquid in microchannels.[35,46] Digital microfluidic systems discussed here continuously transport droplets through surface anisotropy. This anisotropy can be actively created (e.g., an applied voltage or shining a light source) or passive (e.g., chemical gradients or surface texture). These anisotropies manipulate droplets either by modulating the surface tension or by asymmetrically guiding the contact line ("footprint") of the droplet.

2.2 SURFACE TENSION DRIVEN DIGITAL MICROFLUIDICS

"Surface tension driven" was first used by Lee et al.[52] in 2002 to describe digital microfluidic devices that transport liquid droplets by creating surface tension gradients within the droplet. These gradients induce flow patterns that move the droplet along a substrate. Digital microfluidic systems

---

have employed this principle through the application of electrical or thermal energy, and the use of chemical gradient surfaces.

2.2.1 *Electrowetting*

Electrowetting on dielectric (EWOD) was the first digital microfluidic platform and is one of the most developed methods of manipulating droplets.[46,53] EWOD controls droplets through voltages applied at electrodes just below the substrate surface (Figure 2.1A). The applied voltage creates a charge at the interface between the droplet and the electrode. This charge causes a local reduction in surface tension (also referred to as interfacial energy) at the solid-liquid interface (γ_{SL}), which reduces the contact angle in this region.[52,54] The surface tension is unchanged where no voltage is applied and the contact angle is larger in this region. The effect of voltage on surface tension is described in Lippmann's equation (Eq. 2.1),[54] where ε and d are the permittivity and thickness of the insulator between the electrodes and the droplet, respectively, and V is the applied voltage.

$$\gamma_{SL}(V) = \gamma_{SL}(0) - \frac{\varepsilon}{2d}V^2 \qquad (2.1)$$

This local change in solid-liquid surface tension induces flow in the direction of lower surface tension, effectively wetting the surface where the voltage is applied. This wetting effect is described through a combination of Lippmann's and Young's Equations (Eq. 2.2),[52–54] where θ_0 is the contact angle with no applied voltage, c is the capacitance per unit area of the electrode, and γLG is the surface tension at the liquid-gas interface.

$$\cos\theta = \cos\theta_0 + \frac{1}{2\gamma_{LG}}cV^2 \qquad (2.2)$$

This equation shows that the contact angle (θ) will decrease with applied voltage (V). This makes the electrode surface more hydrophilic and "pulls" the droplet onto the surface over the electrode.[52–54]

EWOD devices are traditionally fabricated by patterning metal electrodes (typically gold or chromium) on a glass or quartz wafer, and coating the electrodes with a hydrophobic, dielectric material, such as Teflon.[52–54] A second wafer, typically etched or coated with a dielectric, is often placed on top to enclose the droplet.[52–54]

Optoelectrowetting (OEW) devices function through the same principles of EWOD, but the voltage is applied by focusing light on a photoconductive material beneath the droplet. OEW devices were first fabricated by patterning a layer of indium-tin-oxide (ITO) on a transparent glass slide, and connecting ITO electrodes to biasing lines with strips of amorphous silicon (a-Si:H).[55] This layer is separated from the glass by a thin layer of silicon dioxide, and coated with Teflon, a hydrophobic dielectric material. A voltage is initially applied to the biasing lines and illumination of the connecting a-Si:H strip triggers the electrowetting effect at the ITO electrode.[55]

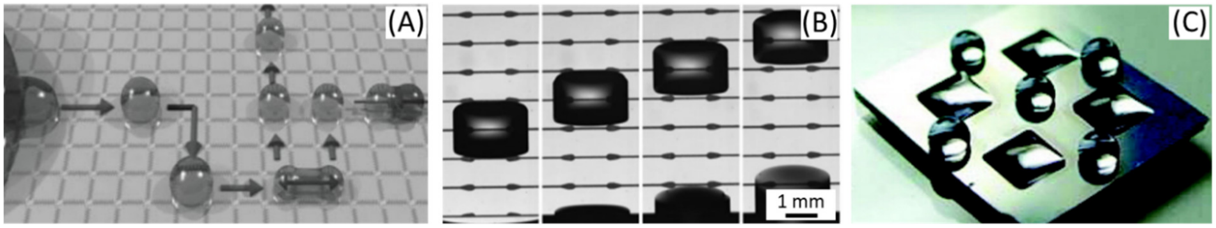

Figure 2.1: Surface tension driven digital microfluidic systems. Droplet transport is accomplished by creating anisotropies in surface tension on EWOD (© 2009 John Wiley and Sons)[46] (A), microheater arrays (© 2003 IEEE)[56] (B), and photoreversible chemical gradient surfaces (adapted with permission from Reference 57, Copyright (2006) American Chemical Society)[57] (C).

2.2.2 *Microheater Arrays*

Microheater arrays transport droplets through thermocapillary forces (Figure 2.1B). As surface tension is a function of temperature, applying a thermal gradient to a droplet will create a surface tension gradient within the droplet, and subsequently a Marangoni flow.[58,59] The Marangoni flow opposes the viscous or "restoring" force caused by the surface acting on the droplet, resulting in a net velocity (*V*). This relationship is described by Eq. 2.3;[58,59]

$$V = V^{*}h_0[\underbrace{\frac{1}{\gamma_{LG}}\frac{dS}{dT}}_{Viscous\ Force} + \underbrace{\frac{3}{2}\frac{1}{\gamma_{LG}}\frac{d\gamma_{LG}}{dT}}_{Marangoni\ Effect}]\frac{dT}{dx} \quad (2.3)$$

where V^* is the characteristic velocity (liquid-gas surface tension, γ_{LG}, divided by viscosity), h0 is the height of the center of mass of the droplet, *T* is the prescribed temperature, and S, the spreading coefficient, is the relationship between solid-gas, γ_{SG} solid-liquid, γ_{SL}, and liquid-gas surface tension ($S = \gamma_{SG} - (\gamma_{SL} + \gamma_{LG})$) observed on the substrate surface. Interestingly, the spreading coefficient shows little response to temperature changes when *S* is small ($dS/dT \approx 0$).[58,59] In this case, the Marangoni flow will dominate and the droplet will actually move in the direction of higher surface tension (i.e. towards the cold side) because $d\gamma_{LG}/dT$ will be negative.[58,59] Microheater arrays employ this phenomenon with periodically placed resistive heaters that essentially "push" droplets towards a cooler region when the substrate is heated.[60]

Microheater arrays have been fabricated by patterning resistive heaters composed of titanium or chromium onto a rigid substrate (e.g. glass). Gold is used to form the leads to the heaters, and self-assembled monolayer patterns are used to prevent the droplets from spreading outside the path of resistive heaters.[60]

2.2.3 *Chemical Gradients*

The surface tension at the solid-liquid interface of a droplet is related to the contact angle (Figure 2.1C) through Young's equation (Eq. 2.4).[61]

$$\gamma_{SL} = \gamma_{SG} - \gamma_{LG}\cos\theta \qquad (2.4)$$

The contact angle of a liquid droplet measures wettability, which is determined by the chemical composition of a surface.[61] Due to this relationship, a chemical gradient surface will cause the spreading coefficient ($S = \gamma_{SG} - (\gamma_{SL} + \gamma_{LG})$) to vary spatially.[58] As no Marangoni flow is present in this case, the droplet will move in the direction of lower surface tension (i.e. towards the hydrophilic region).[58] This is similar to the effect described by Eq. 2.3, but Eq. 2.5 more accurately models the velocity of the droplet in this case.[58]

$$V = \frac{h_0}{3\eta \ln(l_{max}/l_{min})} \frac{dS}{dx} \qquad (2.5)$$

The log defines the limits of the flow region, where l_{max} is the macroscopic cutoff and l_{min} is a molecular size, and η is the viscosity of the droplet.[58] The velocity of the droplet is directly proportional to the surface tension gradient (described by the change in the spreading coefficient along the surface, dS/dx), and thus the wettability gradient. The ability to move a droplet with this concept was first used to show a chemical gradient could transport a droplet uphill.[62] However, these gradients were static and could move droplets only a limited distance. Since then, droplets have been moved on wettability gradients created by selective exposure of photosensitive surfaces.[63]

Fabrication of a photosensitive surface for inducing wettability gradients was first reported by coating a glass substrate with macrocycle amphiphile (O-carboxymethylated calix[4]resorcinarine).[63] More recently, photoreversible or “rewritable” photosensitive surfaces have been fabricated through layer-by-layer deposition of a polyelectrolyte (poly[allylamine hydrocholoride]) and SiO_2 nanoparticles on negatively charged silicon wafers,[57] as well as atomic layer deposition of zinc oxide films on glass and quartz wafers.[64] These systems can continuously drive droplet motion by maintaining surface energy gradients through active control of light beams.

2.3 CONTACT LINE DRIVEN DIGITAL MICROFLUIDICS

When vertical vibrations are applied to a droplet resting on a substrate, axisymmetric waves will form along the surface of the droplet.[65] Once of sufficient amplitude, the vibrations will cause the contact line (the perimeter of the droplet in contact with the substrate) to oscillate.[65] Each oscillation cycle is composed of two phases: an expansion phase and a contraction phase. A droplet oscillating on a homogeneous substrate enters the expansion phase when the contact line is at its smallest circumference. The contact line then advances in all directions throughout this phase. During the contraction phase, the contact line starts at its largest circumference and recedes until the next expansion phase begins. Contact line driven digital microfluidics utilize surfaces that introduce an asymmetry to this oscillation cycle. Unlike surface tension driven digital microfluidic, these systems move droplets through an imbalance of pinning forces on the edges of the contact line.

2.3.1 *Anisotropic Ratchet Conveyors*

Anisotropic ratchet conveyors (ARCs) function through two sources of asymmetry: a heterogeneous surface pattern and a difference in pinning forces during de-wetting compared to wetting.[66–68] The ARC surface pattern consists of a path of arcs or curved "rungs" surrounded by a hydrophobic border (Figure 2.2A) and can be texture or chemical based. In texture ARCs, the rungs are patterned mesas surrounded by a trench, and the hydrophobic region is created by an array of pillars.[66,67] This topography induces a superhydrophobic, or Cassie-Baxter state,[69] as air is trapped under the droplet in the trenches between rungs. Whereas, chemical ARCs are composed of alternating hydrophobic and hydrophilic rungs on a flat surface.[68] Applied vertical vibrations cause the contact line of a droplet to oscillate along the path of rungs. The contact line expands relatively equally in both directions, as the wetting process is less sensitive to ARC surfaces.[67,68]

However, during the de-wetting process, when the contact line recedes, the leading edge of the contact line experiences higher pinning forces than the receding edge due to the conforming shape of the rungs.[67] This phenomenon is described by Eq. 2.6,[68] where χ_{lead} and $\chi_{trail}$are the line fraction of the leading and trailing edges, respectively, that pin to the rungs, w is the width of the drop projected orthogonally to the pinning direction, and θ_1 and θ_2 are the equilibrium contact angles of the relatively hydrophilic rungs and relatively hydrophobic region between rungs, respectively.

$$F_{Anisotropy} = (\chi_{lead} - \chi_{trail}) w \gamma_{SL} (\cos\theta_1 - \cos\theta_2) \qquad (2.6)$$

The difference in pinning between the two edges results in a net force especially during the contracting phase of oscillation.[67,68] Eq. 2.6 shows the difference between the forces on the leading edge (F_{lead}) and the trailing edge (F_{trail}) of the droplet; if we instead look at the ratio (F_{lead}/F_{trail}) of these opposing forces, we obtain Eq. 2.7, which shows the four components that account for the anisotropy in ARC systems: the two contact angles θ_1 and θ_2 and the line fractions χ_{lead} and χ_{trail} on each edge of the droplet. The rung pattern causes the line fraction to be larger on the leading edge of the droplet, without which the forces would be equal on both edges of the droplet and no net motion would occur (Figure 2.2B).

$$\frac{F_{trail}}{F_{lead}} = \frac{\chi_{trail}(\cos\theta_1 - \cos\theta_2)}{\chi_{lead}(\cos\theta_1 - \cos\theta_2)} = \frac{\chi_{trail}}{\chi_{lead}} \qquad (2.7)$$

Both texture and chemical ARCs are fabricated with a single mask process. For texture ARCs, silicon or glass wafers are patterned with photoresist and etched with a deep reactive-ion etching system to create the trenches and rungs. The ARCs are then coated with a hydrophobic silane to prevent the droplets from infiltrating the trenches.[66,68] Texture ARCs can also be fabricated out of polydimethylsiloxane (PDMS) by using a silicon or glass wafer etched with the pattern negative as a mold.[70] Chemical ARCs are fabricated using a similar process, but the wafers are first coated with a relatively hydrophilic layer of trimethylsilanol (TMS). The surface pattern is formed with photoresist and by etching exposed regions of TMS with oxygen plasma. The hydrophobic regions are then created with a silane (perfluorooctyltrichlorosilane) or with gold and dodecanethiol.[68]

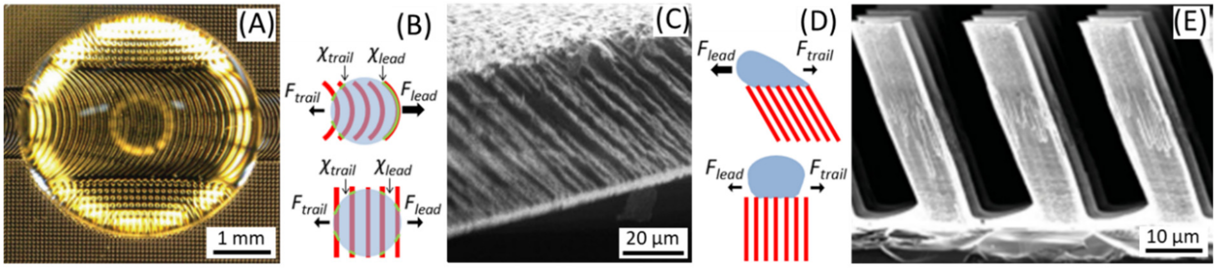

Figure 2.2: Contact line driven digital microfluidic systems. On contact line driven systems transport results from the combination of an oscillating contact line and anisotropic pinning forces between the leading and trailing edges of a droplet. This anisotropy is created by the curvature of periodic structures on anisotropic ratchet conveyors (© 2012 John Wiley and Sons)[67] (A-B) and the geometry of slanted structures on nanostructured Parylene (adapted from Reference 71 with permission from Elsevier)[71] and tilted pillar arrays (© 2014 John Wiley and Sons)[72] (C-E).

2.3.2 *Nanostructured Parylene*

Nanostructured Parylene ratchets are composed of a Parylene film composed in tilted nanorods (Figure 2.2C).[73] Unlike ARCs, the asymmetry of the Parylene ratchets does not come from a surface pattern, but rather the angle of the nanorods. This geometry provides an anisotropic wetting effect on the droplet. The contact angles on the advancing (θ_A) and receding (θ_B) edges of a droplet on these nanofilms exhibit a directional dependence, which results in a net force[73]. The ratio of forces on opposing edges of the droplet is shown in Eq. 2.8.[73]

$$\frac{F_{trail}}{F_{lead}} = \frac{\chi_{trail}}{\chi_{lead}} \frac{\cos\theta_{R,trail} - \cos\theta_{A,trail}}{\cos\theta_{R,lead} - \cos\theta_{A,lead}} = \frac{\cos\theta_{R,trail} - \cos\theta_{A,trail}}{\cos\theta_{R,lead} - \cos\theta_{A,lead}} \text{ with } \frac{\chi_{trail}}{\chi_{lead}} = 1 \qquad (2.8)$$

Droplet transport is induced by vertical vibrations, like in ARCs, which cause the contact line to oscillate.[73] Interestingly, this model is similar to the model for ARC systems shown in Eq. 2.7.

However, the line fraction is the same on both edges of the droplet, and the four components that account for the anisotropy in this system are all contact angles, two on each edge of the droplet. In this case, the net force results from the difference in these contact angles induced by the angle of the nanorods. Hence, removing the tilt of the nanorods results in no net force as the respective contact angles would be the same on each edge of the droplet (Figure 2.2D). The similarity between the models for ARC and nanostructured Parylene systems presents an interesting possibility of combining the key features of each platform. For example, a tilt could be introduced to the rungs in the ARC system, or a nanostructured Parylene device could be fabricated with an ARC surface pattern. Such a combination could potentially provide dramatic improvements to the transport efficiency of these systems.

Nanostructured Parylene ratchets are fabricated using a technique called vapor deposition polymerization (VDP).[71] This deposition process is different from the commonly used physical vapor deposition, as the reactive monomers can only bind to the end of the polymer chain in VDP.[71] This results in high aspect ratio Parylene rods with a nano-scale diameter. To create the angular structure of the Parylene ratchets, the substrate is tipped at an angle with respect to the incident vapor flux[71,73] during the VDP process.

2.3.3 *Tilted Pillar Arrays*

Tilted Pillar Arrays (TPAs) use silicon pillars arranged in an angular nano- or micro-structure to control the contact line pinning of a vibrated droplet (Figure 2.2E).[72] Much like nanostructured Parylene ratchets, the titled pillars create differences between the contact angles on the leading and trailing edges, resulting in a net force that moves the droplet through cycles of contact line oscillation.[72] Interestingly, droplets move with the direction of the tilt on nanostructured pillars, but move against the direction of the tilt on microstructured pillars.[72] This observation provides further intrigue to the possibility of combining titled structures and surface patterns in contact line driven digital microfluidic systems. It would be interesting to understand how the direction of the tilt competes with the surface pattern. For example, if a tilted microstructure is in the same direction as the surface pattern, the net forces from the two anisotropies may cancel out and transport would not be possible. However, if the structures are combined so the net forces are in the same direction, then the transport efficiency may be increased, as described in the previous section.

Fabrication of TPAs begins with a silicon wafer substrate, the pattern for nanostructured TPAs is formed using a metal, thin film de-wetting process,[72,74] whereas the pattern for microstructured TPAs is formed using conventional photolithography. In both cases, the silicon wafer is etched using "glancing-angle" reactive-ion etching (RIE), wherein the substrate is tilted at a 70° angle inside of an RIE chamber.[72,74] Once the tilted pillars have been etched into the substrate, the surface is then functionalized with a silane coating.[72,74]

2.4 FUNCTIONS WITH DROPLETS

In addition to moving the droplets, DMF systems are also capable of performing specific functions on the droplets. Key functions that DMF systems look to achieve are generation, switching, fusion, and fission.

2.4.1 *Generation*

Droplet generation describes the process in which individual droplets of a reproducible size are pulled from a large reservoir. This function allows for a large sample to be divided into many smaller parts, which increases the number of reactions or tests that can be performed with a single sample. DMF systems also require a sample to be divided in small droplets. Without this function a sample has to be distributed into smaller droplets through manual pipetting or with a separate apparatus. Thus far, droplet generation has been reported on with electrowetting (EWOD[75] and OEW[55]) and ARC[70] systems.

EWOD systems generate droplets by first activating a pair of electrodes near the meniscus (edge) of a reservoir (Figure 2.3A). The meniscus is then pulled further from the reservoir by sequentially activating electrode pairs in line with the first pair.[75] The location where the droplet separates from the reservoir determines the size of the generated droplet but is dependent on the initial shape of the meniscus, which is not predictable. However, the shape of the meniscus in the region near the first electrode pair can be stabilized with "side electrodes". The side electrodes are placed on either side of the path formed by the initial electrode pairs. This design has provided for the creation of relatively uniform droplets with a volume of 2 to 3 μL.[75] OEW systems perform this function through similar principles, but with a light beam that activates electrodes adjacent to the reservoir, pulling a droplet on the active OEW region.[55] The sizes of the generated droplets are similar to the spot size of the beam.[55]

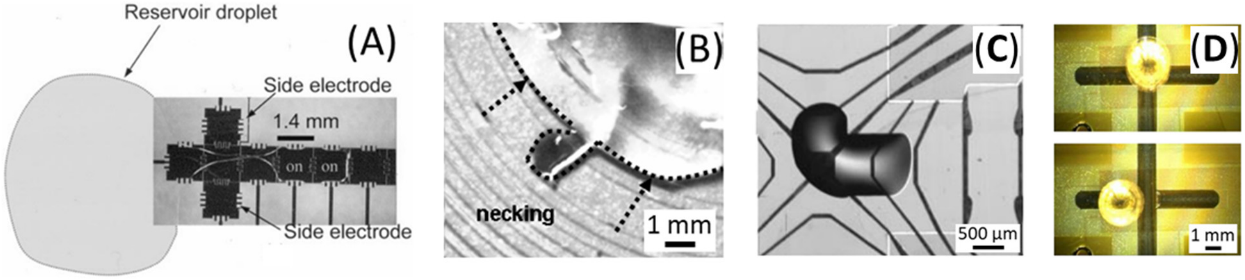

Figure 2.3: Droplet Generation and Switching. (A) EWOD (© 2003 IEEE)[75] and (B) ARC systems (© 2008 IEEE)[70] can generate droplets by pulling liquid from a large reservoir (C) Microheater intersections (adapted from Reference 76, with the permission of AIP Publishing)[76] can also selectively switch droplets (D) EWOD switches (© 2009 IEEE)[77] can be integrated in ARC devices.

Droplet generation for ARCs is possible using a pattern of concentric circles alternating between mesas and trenches.[70] Like smaller droplets, the contact line of this reservoir will oscillate in response to vertical vibrations of sufficient amplitude. As the vibration amplitude is increased over a second threshold, the morphology of the contact line will shift from a relatively perfect circle to a trigonal planar shape.[65,70] The alternating circle pattern distorts or modifies this contact line, which introduces instabilities at the "vertices" of the contact line.[70] As the contact line expands across the surface texture, the vertices become pinned on the mesas. When the contact line retracts, a "pinch-off" occurs as the contact line is sheared over the trench (Figure 2.3B). With this design, the resulting droplet size is dependent on the initial size of the reservoir, and droplets as small as 0.1 μL have been generated.[70]

2.4.2 *Switching*

Switching is the process of selectively moving a droplet from one path to another. This function is essential for sorting droplets and increasing throughput of downstream processes. Switches are relatively simple to implement with DMF systems that move droplets by modulating surface tension, because a surface tension gradient can be created in any direction within the droplet. On an EWOD or OEW device, a droplet will move in the direction of an activated electrode. With an array of individually addressable electrodes, a droplet can be switched by activating an electrode next to the current path of the droplet.[46,55,75] The droplet will be pulled onto this electrode and can be subsequently directed to a new path in any direction. Microheaters are also organized in individually addressable arrays to move droplets, but unlike EWOD electrodes, individual microheaters can only move droplets along a single axis.[76] However, microheater switches have been achieved through the use of specially designed "intersections". These intersections can switch a droplet by turning it 90 degrees onto a new track (Figure 2.3C). The intersection accomplishes this by creating a heated region that pushes the droplet in the direction of the new path while inhibiting movement on the direction of the original path.[76] With photosensitive surfaces, like electrowetting, droplets can be directed in any direction or pattern depending on the location of the light-activated chemical gradient relative to the droplet.[57,64]

Implementing switches on contact line driven systems has been proven to be more of a challenge. ARC systems have been developed that use EWOD electrodes to pull droplets onto a new path of rungs (Figure 2.3D).[77] However, a switch that selectively moves droplets solely through geometric modulation of the contact line has yet to be developed. Interestingly, ARC systems are able to selectively move specific droplet sizes based on the frequency of applied vibrations.[78] This ability is likely present in nanostructured Parylene ratchets and TPAs as well, as the amplitude threshold for contact line oscillation is based on droplet volume.[79] As mentioned previously, the direction of droplet motion is also dependent on the feature size of TPAs. Such phenomena could eventually lead to the realization of a switch that relies only on the geometric control of the contact line.

2.4.3 *Droplet Fusion*

The fusion, or merging, of two droplets is a simple function for DMF systems to perform. With no encapsulating liquid, two droplets will spontaneously merge when they come in contact. Surface tension driven systems can accomplish this by creating surface tension gradients in two droplets that are directed towards each other, which causes the droplets to converge (Figure 2.4A).[75] Droplet fusion can be accomplished on contact line driven systems in a similar fashion by transporting droplets along two converging paths.[67] Fusion can also be performed along a single path with two different sized droplets (Figure 2.4B). This is accomplished by using a vibration frequency that modulates the contact line of only one droplet. This droplet will be transported along the path while the other droplet remains static. When the moving droplet reaches the static droplet, the two will merge, and the resulting droplet can then be transported using a different vibration frequency.[67]

Although droplets can merge spontaneously, this does not guarantee that the resulting droplet will be homogenously mixed. Homogeneity in the resulting droplet will eventually occur through diffusion, but this is a relatively slow process. This process can be hastened on electrowetting devices through a series of “mixing steps” wherein the droplet is moved back and forth between two electrodes or electrode pairs.[80] This mixing step is not necessary on microheater arrays because the thermocapillary convection currents that move the droplet also mix a fused droplet.[76] Similarly, on contact line driven systems, the applied vertical vibrations drive the droplets with a cyclic motion, which also aids in mixing fused droplets.[67]

2.4.4 *Droplet Fission*

Once two droplets have been fused and mixed, it may be desirable to divide the resulting droplet for multiple, subsequent uses. Therefore, the ability to perform droplet fission, or split the droplet into two or more smaller droplets, is very useful for DMF systems. Droplet fission has been accomplished with EWOD, OEW, and microheater systems. With EWOD, droplets can be split by activating electrodes on two opposing edges of the droplet and turning off the electrode beneath the center of the droplet. This pulls the edges of the droplet apart and causes the center of the droplet to neck, pinching apart the droplet (Figure 2.4A).[75] OEW devices perform droplet fission the same way, using two light beams to activate electrodes on opposing droplet edges.[55] Droplet fission on microheater arrays occurs in a similar fashion, but microheaters in the center of the droplet are activated. This induces a diverging Marangoni flow, which thins the center of the droplet[76]. Necking occurs as the droplet center thins, leading to eventual pinch-off and the formation of two new droplets (Figure 2.4C).[76]

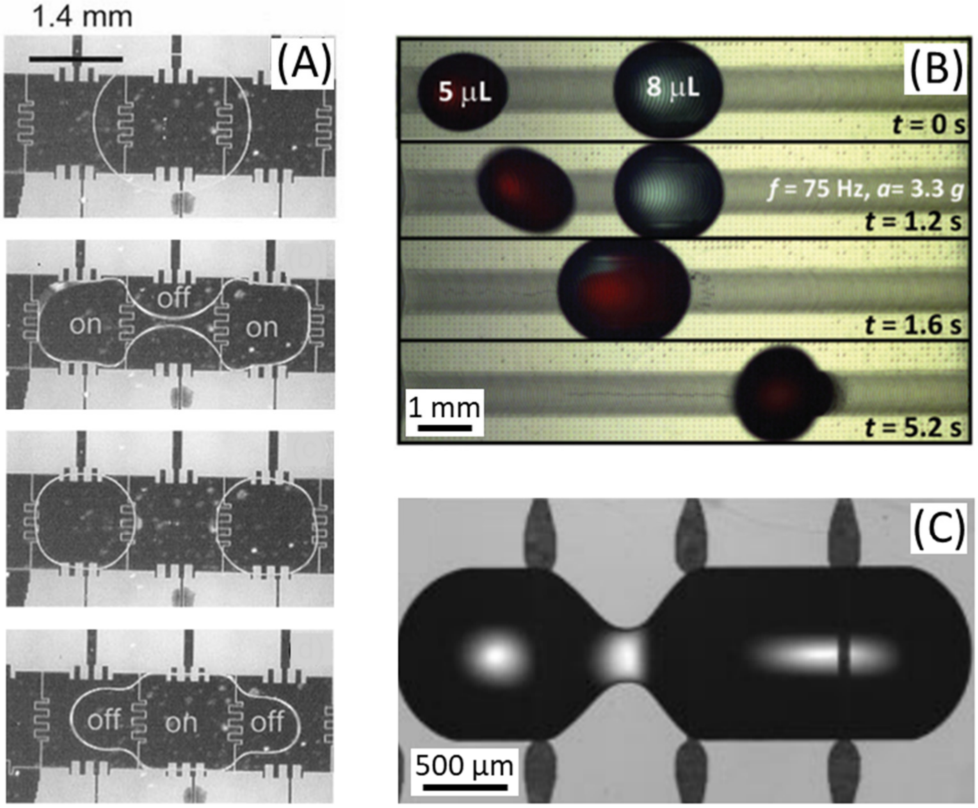

Figure 2.4: Droplet Fission and Fusion. Sequence depicts the fission of one large droplet into two smaller droplets, and the recombination of the two droplets (© 2003 IEEE)[75] (A) Two droplets are merged on an ARC path (B) and the resulting droplet is then transported (© 2012 John Wiley and Sons).[67] Microheater arrays (adapted from Reference 76, with the permission of AIP Publishing)[76] can split droplets by creating thermal gradients (C).

Droplet fission has yet to be achieved with contact line driven systems. Transport with contact line driven systems is possible because the force acting on the leading edge of the droplet is larger than the force acting on the trailing edge. Splitting a droplet requires relatively equal forces acting on two opposing edges. These forces must also be large enough to overcome the surface tension of the droplet and persist long enough for the necking region to reach pinch-off.[81] Electrowetting and microheater systems can maintain such a force for an indefinite amount of time, whereas contact line driven systems can only provide this force during one-half of the contact line oscillation cycle (contracting phase). However, the time required for droplet pinch-off is dependent on the diameter of the necking region.[81] Therefore, contact line driven systems could potentially perform droplet fission if a surface pattern could induce a contact line geometry with a small necked region. Additionally, it may be possible for a surface pattern to create a necking region that induces a resonance with an increasing transient response. Wherein, the diameter of the neck would be reduced during each cycle of oscillation until pinch-off occurs.

2.5 APPLICATIONS OF DMF SYSTEMS

DMF systems can be used for many of the same applications of segmented flow microfluidic systems. Although DMF systems operate with larger droplets and slower throughputs, the ability to selectively control individual droplets makes DMF systems better suited for some applications (e.g. combinatorial chemistry[46]). Furthermore, these DMF systems move droplets through interactions with the substrate surface. While this opens the possibility for issues involving solute-surface interactions, it also provides an opportunity to meet unique applications. For example, droplets can be moved to temperature sensitive regions on a chip or surface to aid in thermal management.[82,83] The movement of droplets along a surface could be used to pick up and remove undesired particulates, serving as a self-cleaning surface,[84] or to transport desirable particulates deposited onto a surface.[85]

EWOD was the first DMF system to be introduced, and therefore has the most well-developed toolbox. As such, EWOD devices have already been investigated for applications such as cell isolation and analysis,[86] bio-assays,[87] and DNA analysis.[88,89] Despite this success, a major criticism of EWOD technology is the complex circuitry that is required to address individual electrodes in an array.[35,46] Driving droplets on microheater arrays and photosensitive chemical gradient surfaces also requires relatively complex circuitry or off-chip control systems. However, a more recent type of OEW system called single-sided continuous optoelectrowetting (SCOEW) uses a continuous layer of photoconductive amorphous silicon instead of a pixilated grid of electrodes to perform electrowetting. This system can also drive droplets with light produced from a liquid crystal display.[90] Additionally, contact line driven systems only require an externally applied vibration to move droplets. Continued development of these more recently conceived systems could potentially lead to a platform that can more efficiently meet many applications. Furthermore, hybrid DMF systems are also possible.[91] Combining features of multiple DMF systems could potentially lead to the realization of a robust platform for micro-total analysis and lab-on-a-chip systems.

Another field of microfluidics, known as paper or paper-based microfluidics, transports liquid through capillary forces (paper wicking) in channels defined by hydrophobic barriers.[31,92] These devices can be made from relatively inexpensive materials and do not require external stimuli to function, properties which have recently gained much attention for applications requiring low-cost analytical platforms (e.g., healthcare diagnostics, environmental monitoring, food quality control, and forensics).[31,92] However, paper microfluidics are limited by poor efficiency, as large portions of a sample are often retained in the channel or lost to evaporation during transport.[31] Many paper microfluidic systems also use a colorimetric based detection method that usually has a high limit of detection.[31] This approach prevents these systems from accurately measuring solutions with low analyte concentrations. The complexity of most surface tension driven DMF systems may become cost- or resource- prohibitive, but SCOEW shows much potential for low-cost diagnostic and analytic systems. The low power requirements and ability to drive droplets with a liquid crystal display make this system a good candidate for portable diagnostic systems. Additionally, contact line driven DMF systems require only a passive surface architecture and a vertical vibration. These surfaces can be made from many different materials, and the required vibrations are within the parameters of commercially available speakers found in cellular phones,[67,72,85] which have become virtually ubiquitous and can be easily transported. DMF systems transport droplets as an entire self-contained entity, which avoids issues of sample retention experienced by paper microfluidic systems. Additionally, this property allows for integration with many detection systems, as the entire droplet can be transported onto a desired detection region. Implementing sensitive detectors with DMF systems could meet applications requiring detection limits outside the capabilities of paper microfluidic devices. These DMF systems could serve as a more efficient platform for low-cost analytical devices or potentially be combined with paper microfluidic detection zones to improve the transport efficiency of this technology.

2.6 CONCLUSION

Digital microfluidic systems provide the capability to transport individually controlled droplets without channels or an encapsulating fluid. Droplets on digital microfluidic systems can be transported by anisotropies acting through surface tension or on the contact line of the droplet on a substrate. The following chapters will focus on the underlying mechanisms of a specific digital microfluidic system – anisotropic ratchet conveyors – and describe the development of a DNA barcode identification tool for conservation from this platform.

Chapter 3. ANISTROPIC RATCHET CONVEYORS: CHARACTERIZATION AND MECHANICS

Anisotropic Ratchet Conveyors (ARCs) were invented in the Böhringer Laboratory at the University of Washington.[93] This technology evolved from investigations of droplet transport on micropatterned textured gradient surfaces by Shastry et al.[94] The initial gradient patterns only provided for droplet transport over a finite distance, but continued development of this system led to periodic gradients[95] that could enable continuous droplet transport (Figure 3.1). Later, Duncombe et al. showed that the gradient was unnecessary and transport was actually enabled by an anisotropy in pinning forces between droplet edges, simplifying the ARC system to a periodic track of curved microstructures that could be formed from textured[96] or chemical[97] patterns.

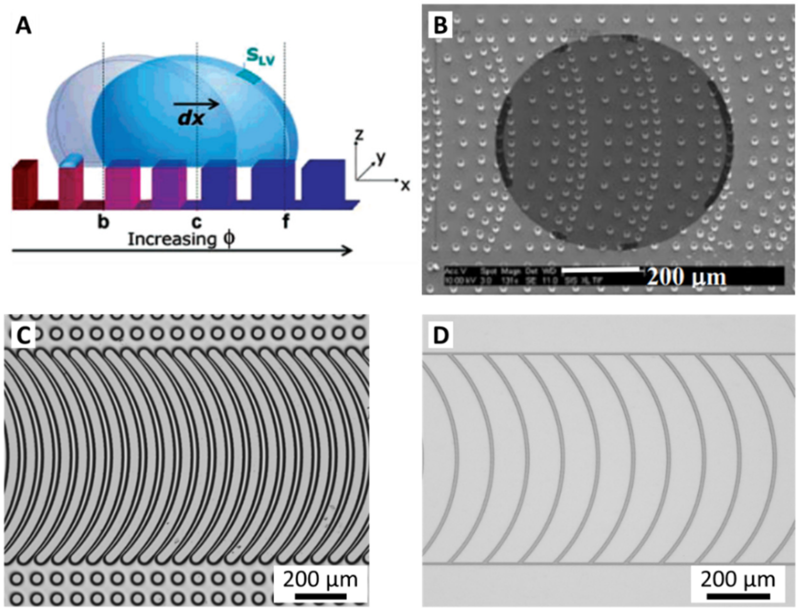

Figure 3.1: Evolution of Anisotropic Ratchet Conveyors. Micropatterned texture gradients (adapted from Reference 94, Copyright (2006) American Chemical Society)[94] (A) lead to periodic gradient patterns (© 2007 IEEE)[95] (B) and eventually periodic texture (C) and chemical (D) ARC patterns that provide continuous droplet transport with applied vibrations.

Droplet transport on ARC devices is the result of two key factors. The first is a difference in pinning forces between leading and trailing edges of the droplet, which is provided for by an asymmetric surface pattern of periodic, curved rungs (Figure 3.2). This pattern is composed of

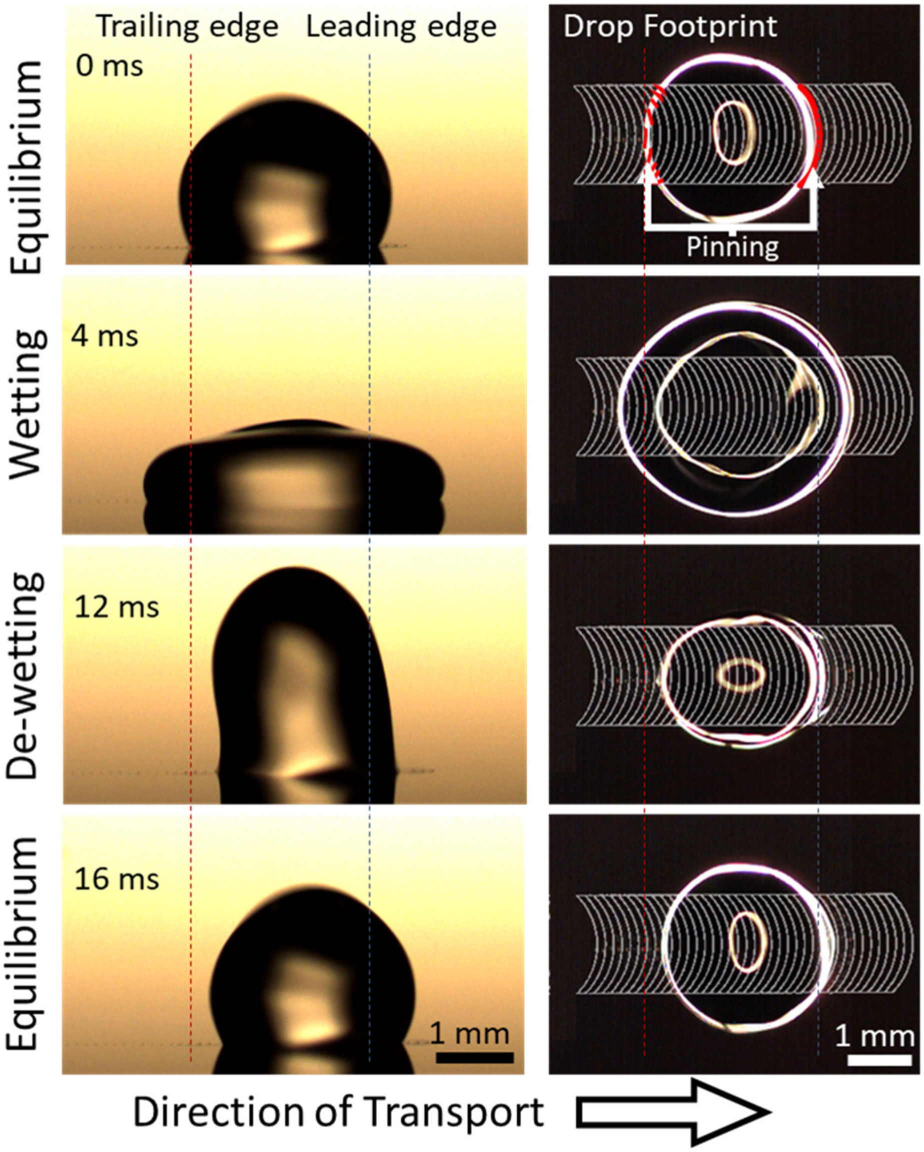

Figure 3.2: Fundamentals of droplet transport on ARCs. The ARC pattern creates a difference in pinning forces between leading and trailing edges, and applied vibrations induce the edges of the droplets to oscillate. This combination of pinning force anisotropy and edge oscillation provides a net force throughout each vibration cycle, propelling the droplet along the ARC pattern.

alternation hydrophilic and hydrophobic regions, where the rungs are hydrophilic and defined by a hydrophobic background. Wherein, pinning is the interaction of the droplet edges with the hydrophilic regions, and can be thought of as a frictional force, as pinning resists the movement of droplet edges. Droplets resting on this pattern will maintain a spherical shape because of their surface tension, allowing only the leading edge to conform to the curvature of the hydrophilic rungs to create this difference in pinning forces.[97]

The second feature of ARC transport is the oscillation of droplet edges, which is typically induced by an applied orthogonal vibration to the substrate. Vibrations cause the droplet edges to expand and contract, cycling the droplet through phases of wetting – droplet edges advancing on the substrate – and de-wetting – droplet edges receding from the substrate (Figure 3.2).[96] Combining this oscillation of droplet edges with a difference in pinning forces between edges produces a net force in the direction of the leading edge throughout one vibration cycle. In other words, the droplets will take a step forward throughout each vibration cycle. Over the course of many vibration cycles, these steps provide for the propulsion or net transport of the droplets along the surface. For droplets on ARC devices, there is a minimum vibration amplitude, called the ARC threshold, required to initiate transport. This amplitude is determined by the geometry and chemical composition of the ARC track, physical properties of the transported droplet, as well as the frequency and waveform of the applied vibration. ARC threshold profiles effectively describe the performance of an ARC device with a specific droplet and are collected across a functional frequency range. At frequencies outside of this range, transport is not possible as droplets will either bounce off the substrate or rupture before transport occurs (Figure 3.3). This functional frequency range is also determined by the same factors listed above that account for the ARC threshold. For vibration amplitudes above the ARC threshold, transport will still occur until the amplitude is so high as to cause the droplet to completely depin (bounce off) of the substrate or rupture. However, these amplitudes are typically quite high within the functional frequency range.

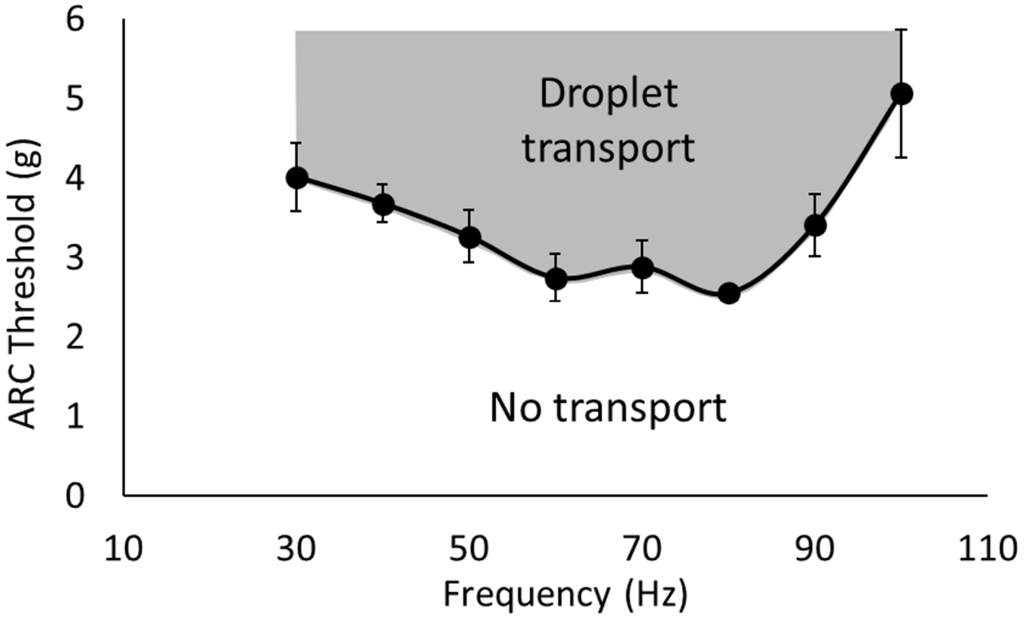

Figure 3.3: Characterization of droplet transport. The performance of ARC devices is evaluated by the minimum vibration amplitude (ARC threshold) required to initiate droplet transport. This threshold is determined by the properties of the droplet, substrate, and parameters of the applied vibration. Transport is also only possible over a specific frequency range determined by similar factors.

Lastly, ARC thresholds are reported in terms of acceleration to account for the energy input in the system (Figure 3.4). Displacement measurements provide useful mechanical information, but do not account for the frequency of the vibration. At higher frequencies, considerably more energy is required to provide the same displacements as a lower frequency. Therefore, the performance of ARC devices is characterized by the minimum amount of energy required to initiate droplet transport.

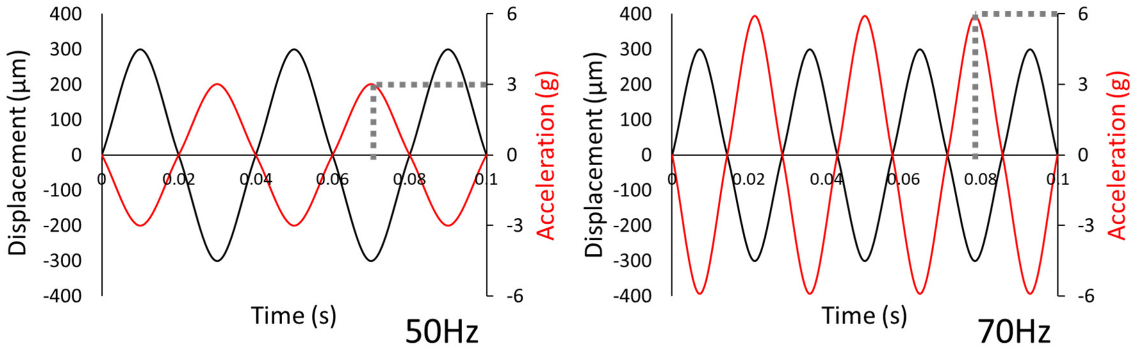

Figure 3.4: Substrate displacement does not account for energy input. Sinusoidal motion of a substrate with the same displacement amplitude (black curves) requires greater acceleration (red curves) at higher frequencies (acceleration amplitude shown by gray dotted lines). For sinusoidal motion, the acceleration amplitude is the product of the displacement amplitude and the square of the frequency, which captures the effect of frequency on the energy input into the system.

Having broadly defined the fundamental functional concepts and characterization principles for ARC devices, we can now take a closer look at the underlying mechanics of ARC systems. In which, the proceeding discussion will describe the basic equations and theory that govern droplet transport on ARC devices and present a simplified mathematical model to simulate this phenomenon.

3.1 Modelling Droplet Transport

The following subsections are adapted from:

Converting Vertical Vibration of Anisotropic Ratchet Conveyors into Horizontal Droplet Motion[98*]

Yan Dong[1], Hal R. Holmes[1], and Karl F. Böhringer[1,2] (*Langmuir,* **33**(40), 10745-10752, 2017)

[1]Department of Bioengineering and [2]Department of Electrical Engineering, University of Washington, Seattle, Washington, 98195, USA

---

[*] Original work of the author adapted with permission from Reference 98. Copyright (2017) American Chemical Society.

The ability to manipulate small droplets in parallel is of great interest because it provides a rapid and economic means to carry out biochemical analysis and disease diagnostics at the microscale.[34,99,100] Two general types of droplet-based microfluidic devices have been developed. One comprises a series of microchannels in a closed system where discrete droplets are generated and manipulated in an immiscible continuous fluid (i.e., two-phase emulsion).[101,102] The other type, on the contrary, is an open system where sessile droplets move in air on a usually hydrophobic surface.[103,104] The latter has many advantages such as precise control of droplet motion and prevention of droplet dilution caused by diffusion or contamination across the two-phase boundary. These open system devices, mainly developed in the past decade, can transport sessile droplets with a surface energy gradient generated by electrowetting,[105–107] superparamagnetism,[108] Leidenfrost effect[109,110] or mechanical vibration.[111–113] To create an energy gradient, surfaces are treated by either chemical deposition[114] that gradually changes the surface material property, or by microstructure design[94,111] that changes the surface morphology. Shastry et al. introduced a texture ratchet with periodic micropillars, creating a repeating pattern of local hydrophobic gradients that can transport droplets with mechanical agitation.[95] Duncombe et al. built on this idea and developed similar ratchets with tracks of periodic curved rungs where droplets can move under a pure vertical vibration.[96] Duncombe et al. also demonstrated that this functionality is not limited to textured ratchets, but is present on flat surfaces with chemically patterned ratchets.[97]

Although the phenomenon of droplet transport on these devices, called anisotropic ratchet conveyors (ARCs), has been characterized empirically, no theoretical work has been done to explain the underlying physics. However, in other similar systems several models have been proposed to describe the mechanism of droplet motion, with the droplet often modeled as a sliding or rolling solid. A few examples are given below. Noblin's model[115] was based on a smooth substrate and demonstrated that the combination of horizontal and vertical vibrations can create a force asymmetry, thus causing a net droplet motion. Malvadkar et al.[116] proposed a model that describes the pin-release mechanism of a ratchet by analyzing the contact angles at a microscopic level. Daniel,[112,117] Buguin,[113] Mettu[118,119] and their co-workers investigated similar systems and described how horizontal vibration can overcome the contact angle hysteresis and cause a net droplet motion. Goohpattader et al. studied drift of a sphere during stochastic rolling on a patterned substrate.[120,121] All these models help to better understand the mechanism of droplet motion on a vibrating surface, but none of them can explain how a pure vertical vibration propels a sessile droplet across a horizontal substrate.

In this chapter, we propose a model that describes how a vibration applied perpendicularly to the ARC pattern induces a lateral droplet motion on horizontal and inclined substrates. We first generalize the condition of droplet motion by non-dimensionalizing the data with different droplet characteristics (i.e., volume, density, viscosity, surface tension), and then introduce a compact model that captures the important features of a moving droplet to describe the mechanism behind droplet motion. The simulation results of this model show good agreement with the experimental data.

3.2 EXPERIMENTAL SETUP AND OBSERVATIONS

The ARCs investigated in this work are patterned with photolithography on an oxidized silicon wafer to create the designated surface features. In this work, the hydrophilic silicon dioxide (SiO_2) rungs are 10 μm wide with a radius curvature of 1000 μm and have a period of 120 μm. A thin coating of fluoro-octyl-trichloro-silane (FOTS, Sigma Aldrich) is then applied by vapor deposition to make the surface regions not covered with photoresist hydrophobic. Stripping the photoresist reveals the transparent, hydrophilic SiO_2 pattern that is chemically defined by the hydrophobic FOTS.

The schematic of the final device is shown in Figure 3.5, where a droplet moves along the track of curved rungs in the longitudinal direction (x-axis). The hydrophobic background keeps the droplet confined to the track. The orthogonal vibrations cause the contact line, or droplet 'footprint', to oscillate as the droplet edges advance and recede in response to the vertical mechanical stimuli (definitions of key terms are listed in Table 3.1).

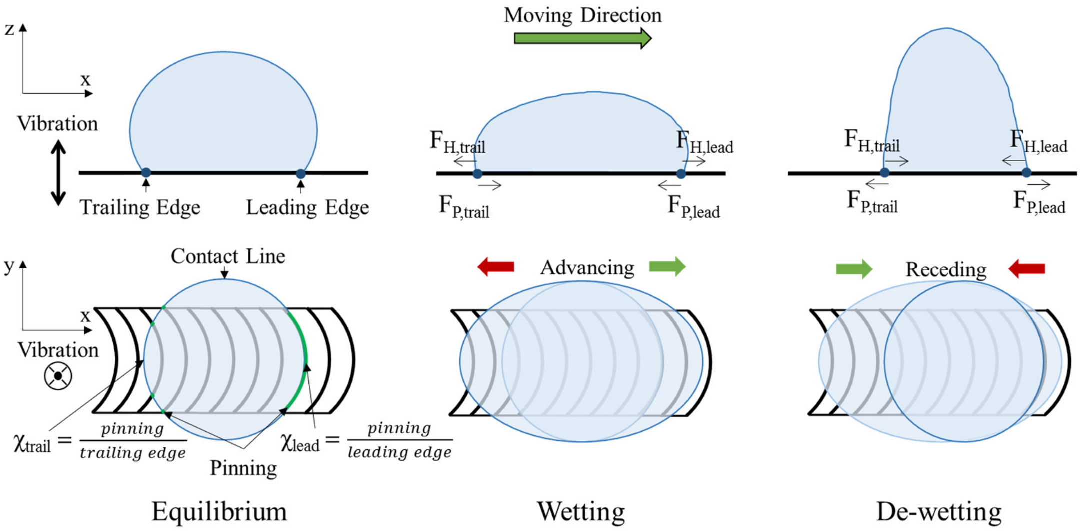

Figure 3.5: Schematic of ARC function. Applied vibrations cause the contact line to oscillate between wetting and de-wetting states (top sequence). The asymmetric surface pattern creates a difference in pining forces between leading and trailing edges. This imbalance of forces results in net transport through each vibration cycle (bottom sequence).

During wetting, the contact line advances to wet additional rungs in each direction. However, as the droplet de-wets, the asymmetric shape of the ARC pattern pins the leading edge more than the trailing edge (Figure 3.5). This phenomenon has been empirically described by Duncombe et al.,[97] and provides a net force in the direction of droplet motion through each vibration cycle. The detailed experimental setup can be found in Duncombe et al.[96]

Table 3.1. Definitions and parameters of droplets on ARC systems

Symbol	**Parameter**	**Definition**
	Contact line	The perimeter of the droplet region contacting the substrate surface (i.e. droplet “footprint”)
	Advancing	Describes an edge that is moving away from the center of the droplet
	Receding	Describes an edge that is moving towards the center of the droplet
	Equilibrium	Resting state of a static droplet
wet	Wetting	Process occurring when the contact line advances, increasing the substrate area contacted by the droplet
dewet	De-wetting	Process occurring when the contact line recedes, decreasing the substrate area contacted by the droplet
lead	Leading edge	The edge of the droplet that faces the direction of movement
trail	Trailing edge	The edge of the droplet that faces the direction opposite of movement
PIN	Pinning	Contact of the droplet with hydrophilic regions on the substrate surface
χ	Line fraction	The fraction of an edge that is pinning to the surface pattern
F_P	Pinning force	Forces acting on the droplet edges due to pinning
F_H	Hydrodynamic force	Forces acting on the droplet edges due to the liquid (e.g. surface tension, flow, molecular interactions, inertia, mass, etc.)

3.3 NON-DIMENSIONALIZATION OF DROPLETS WITH DIFFERENT CHARACTERISTICS

For a droplet vibrated at a certain input frequency, there is a threshold amplitude (ARC threshold) of the substrate acceleration, beyond which the droplet experiences a net lateral motion. If a droplet is vibrated across a range of input frequencies, a minimum ARC threshold appears at a frequency determined by the material properties of the droplet and the substrate. For example, increasing the droplet volume will decrease both the frequency and amplitude of the corresponding minimum ARC threshold. The experimental characterization of droplet motion on ARCs (discussed with more detail in the following subsection) indicates that although the relationship between input frequency and ARC threshold is dependent on the properties of the vibrated droplet, there is a more general relationship between these two entities as the profiles of each curve are all similar.

In order to study this general relationship, angular frequency (ω) and ARC threshold acceleration (a) are non-dimensionalized to factor out the differences in droplet properties. We hypothesize that two non-dimensionalization factors, ω^* and a^*, can be chosen such that the relationship between ω/ω^* and a/a^* is identical across different droplets. For this general relationship to hold, ω^* must be proportional to the resonance frequency of the droplet and a^* must be proportional to the ARC threshold. Even though an exact analytical expression for the resonance frequency and threshold acceleration of an oscillating sessile droplet on an ARC device may be difficult to obtain, these proportionalities allow us to express the scaling of the resonance frequency with respect to basic droplet properties such as volume, density and surface tension. Furthermore, with an input signal $z(t) = Z\sin(\omega t)$, where Z is the amplitude of displacement, we can infer that a^* scales with $Z{\omega^*}^2$.

In this work, the sessile droplet is modeled as a mass-spring-damper system. Viscous effects are measured by the Reynolds number $Re = \sqrt{\rho\gamma R_c}/\mu$, where ρ is droplet density, γ is surface tension, R_c is radius of curvature and μ is viscosity.[122] In this case, all droplets are nearly spherical because 1) all droplet radii $R = \sqrt[3]{3V/4\pi}$ (V is droplet volume) are smaller than the capillary length ($Ca = \sqrt{\gamma/\rho g}$, where g is gravitational acceleration) of the respective liquid, and 2) the surface of the supporting substrate is highly hydrophobic. As a result, the radius of curvature R_c can be approximated by the spherical droplet radius R. By calculation, the minimum Re in this work is 37 for a 50% v/v glycerol droplet. According to Wilkes and Basaran,[123] viscous effects are negligible for sessile droplets with $Re > 20$. Therefore, viscous damping is not considered in our calculation for resonance frequency. This is consistent with other systems in the literature where viscous effects are neglected when studying sessile droplets.[115,124]

When viscous damping is neglected for a forced vibration, the resonance frequency of a droplet equals its natural frequency, which is proportional to $\sqrt{\gamma/m}$ or $\sqrt{\gamma/\rho V}$.[125–127] Therefore, we set the characteristic frequency $\omega^* = \sqrt{\gamma/\rho V}$.[122] During harmonic oscillation, the droplet deformation is proportional to the droplet size and the vibration amplitude of the substrate. Thus, we use the droplet radius R to non-dimensionalize the amplitude of substrate vibration Z. The corresponding characteristic amplitude of acceleration is then set as $a^* = R\omega^{*2}$.

3.3.1 *Non-dimensionalization: results and discussion*

Non-dimensionalized curves for the three water droplets with different volumes coincide very well (Figure 3.6A), and the ARC threshold is similar for each droplet across the entire frequency range. The non-dimensionalized profiles for three 50% v/v glycerol/water droplets (Figure 3.6B) also align well, and, although the 13 μL droplet profile is slightly higher, the standard deviations of ARC thresholds overlap in multiple regions. This result indicates that the behavior for droplets vibrated on ARC devices is consistent across droplets with different volumes.

Figure 3.6C compares droplets of water and 50% glycerol. The non-dimensionalized frequency profile coincides for all of the curves, but the normalized threshold amplitude of all 50% glycerol curves is higher than the profiles for water droplets. However, wettability measurements on native surfaces (SiO_2 and FOTS) showed significant differences in the contact angle between water and glycerol droplets (Figure 3.7). This difference in the surface interaction between water and glycerol would likely affect the ARC threshold and could account for the observed discrepancy in non-dimensionalized amplitudes. Overall, this data suggests that the behavior of vibrated droplets on ARC devices can be modelled as a harmonic oscillator-based system.

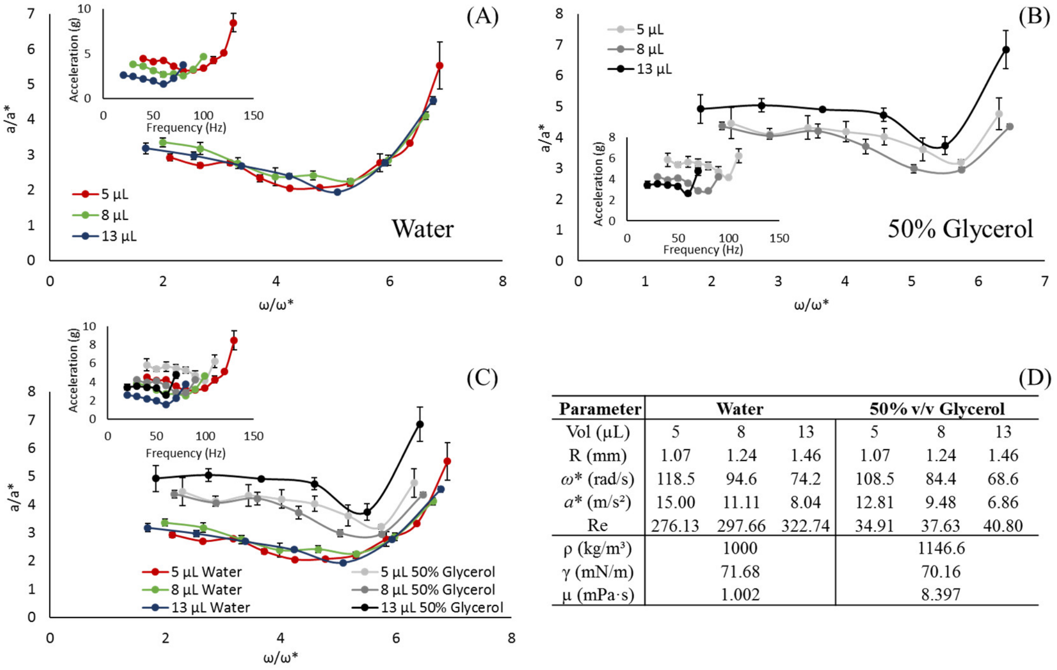

Parameter	Water			50% v/v Glycerol		
Vol (µL)	5	8	13	5	8	13
R (mm)	1.07	1.24	1.46	1.07	1.24	1.46
ω^* (rad/s)	118.5	94.6	74.2	108.5	84.4	68.6
a^* (m/s²)	15.00	11.11	8.04	12.81	9.48	6.86
Re	276.13	297.66	322.74	34.91	37.63	40.80
ρ (kg/m³)		1000			1146.6	
γ (mN/m)		71.68			70.16	
µ (mPa·s)		1.002			8.397	

Figure 3.6: Non-dimensionalization of ARC thresholds. Non-dimensionalized frequency versus amplitude of threshold acceleration for water (A) and 50% glycerol (B) droplets with volumes of 5, 8, and 13 µL. Non-dimensionalized ARC threshold profiles are also compared between water and 50% glycerol (C). Values used for non-dimensionalization are summarized (D). The insets show the raw data from these experiments and error bars represent ± standard deviation.

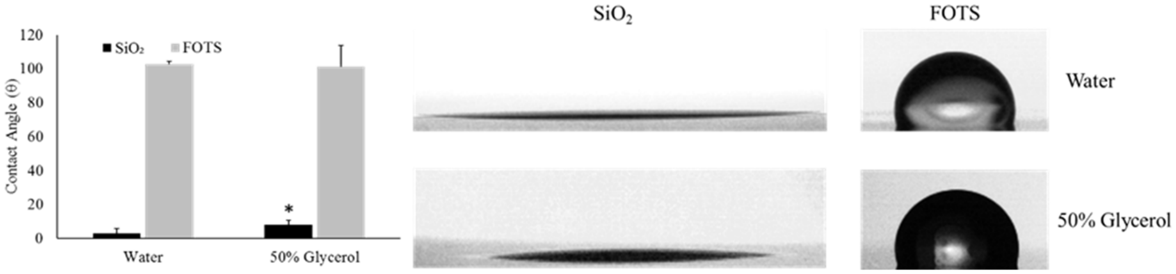

Figure 3.7: Wettability of water and glycerol on ARC surface chemistries. Both water and 50% v/v glycerol wet SiO_2 readily with a very low contact angle and form droplets with a high contact angle on FOTS. However, water has a significantly lower contact angle on the SiO_2 surface, which could account for differences in the behavior of droplets transported on ARC devices. Error bars indicate ± standard deviation; * indicate statistically significant ($p < 0.01$) differences between the contact angles of water and glycerol on specified surface.

3.4 MODELING HORIZONTAL DROP MOTION DRIVEN BY VERTICAL RATCHET VIBRATION

The previous section shows the relationship between dimensionless frequency and ARC threshold, which suggests that the droplet motion on a vibrating ARC device is a general phenomenon that occurs consistently for different physical conditions. However, it is still unclear how vertical vibration translates into horizontal droplet motion. Nevertheless, a few theoretical and experimental studies have made significant advances in understanding the droplet motion under horizontal or combined horizontal-vertical vibrations.[115–121] These studies generally consider the forces acting on the droplet at its center of mass and at its contact line, i.e., along the footprint defined by the solid-liquid-air interface. It is understood that vibrations cause non-equilibrium pinning forces along the contact line. Surface tension couples the center of mass to the contact line. Therefore, during each oscillation cycle, the center of mass proceeds in response to this non-equilibrium force. On ARC devices, the asymmetric forces between the leading and trailing edge of the droplet arise from the directional curved rungs across which the droplet is moving. In order to better describe this phenomenon, we propose a compact model that captures the essential features of this system and that qualitatively explains how a pure vertical vibration can translate into a horizontal droplet motion. Since there is no net droplet motion in the transverse direction, our two-dimensional model will focus on the droplet behavior in the cross-sectional plane centered along the ratchet track.

3.4.1 *Droplets on ARCs as mass-spring-damper systems*

Recall that for non-dimensionalization, viscous damping was neglected while determining the resonance frequency of the droplet; this simplification is adequate when describing the behavior of the droplet before lateral motion occurs. However, damping effects need to be taken into account when the droplet is moving along the track as they cause friction or drag, both inside the droplet and at its interface with the ratchet track. Damping also determines how much energy is coupled into the droplet from the oscillating platform and how quickly it is dissipated. Periodic external forces due to vibration act on the droplet at its leading and trailing edge; in our cross-sectional model, these edges are represented as points *L* and *T*, which are connected to the center of mass *C* and to each other by damped springs. Figure 3.8 illustrates this droplet model as a triangular mass-spring-damper system.

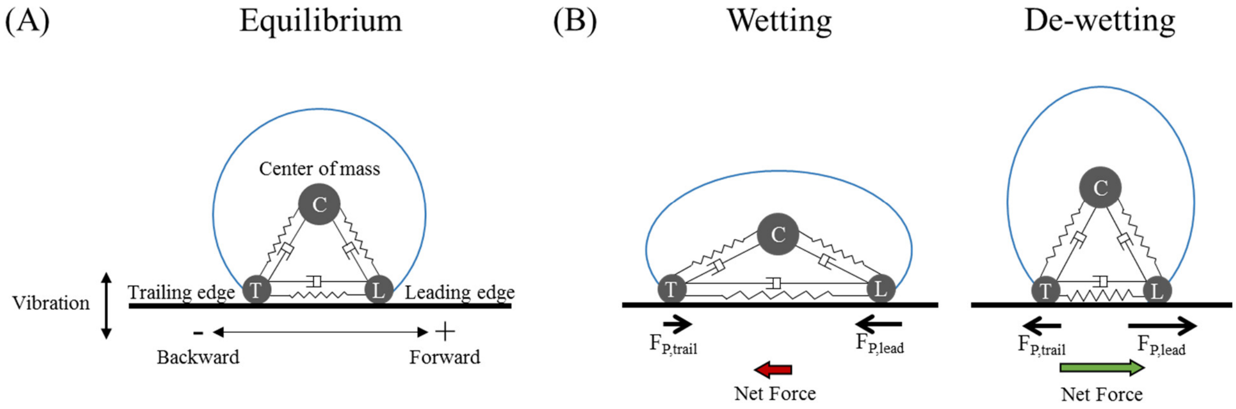

Figure 3.8. Theoretical model of droplets on ARC devices. (A) Sessile droplet in equilibrium modeled with a triangular mass-spring-damper system. (B) The deformation and motion of a droplet during one cycle of vertical vibration. The droplet flattens and experiences a net force in the direction of the trailing edge (left) during wetting and beads up with a larger net force in the direction of the leading edge (right) during de-wetting. The pinning forces are modeled as friction forces at the leading and trailing edges. Note that during wetting, pinning forces act in the positive (forward) direction at the trailing edge, but in the negative (backwards) direction at the leading edge. Whereas, during de-wetting, pinning forces act in the positive direction at the leading edge, but in the negative direction at the trailing edge. Hydrodynamic forces are accounted for through the components in the model (mass, springs and dampers).

The mass at the center m_{C} corresponds to the bulk volume of the droplet, while the two masses at the leading and trailing edges (respectively, m_{L} and m_{T}) correspond to the droplet regions along the contact line. In practice the following conditions are assumed to hold: the edge masses are equal and both smaller than the center mass ($m_T = m_{\mathrm{L}} < m_{\mathrm{C}}$). The springs between T, L and C represent surface tension; we assume $k_{\mathrm{TC}} = k_{\mathrm{LC}} < k_{\mathrm{LT}}$ because pin-release events at the contact line create the effect of a stiffer spring. The lengths of the springs under zero load are equal ($l_{\mathrm{TC}} = l_{\mathrm{LC}} = l_{\mathrm{LT}}$), and that the viscous damping coefficient b is the same for all dampers and given by Stokes' law as $b = 6\pi\mu R$. The sum of these components account of the hydrodynamic forces acting on the droplet edges in this model as shown in Equation 3.1:

$$\begin{aligned} F_{H,lead} &= \gamma \Delta l_{LT} + \gamma \Delta l_{LC} \cos\alpha_{LC} + b\frac{\Delta l_{LT}}{dt} + b\frac{\Delta l_{LC}}{dt}\cos\alpha_{LC} + m_L\frac{\Delta l_{LT}^2}{dt^2} \\ F_{H,trail} &= \gamma \Delta l_{LT} + \gamma \Delta l_{LC} \cos\alpha_{TC} + b\frac{\Delta l_{LT}}{dt} + b\frac{\Delta l_{TC}}{dt}\cos\alpha_{TC} + m_T\frac{\Delta l_{LT}^2}{dt^2} \end{aligned} \tag{3.1}$$

wherein, α_{LC} and α_{TC} are the out-of-plane angles between the leading and trailing edge and the center of mass, respectively. From this equation, we see that the spring and damper between the leading and trailing edges will act on both edges with equal force. We also note from empirical observation that the centroid of the droplet is relatively centered between the leading and trailing edges, suggesting that, generally, $\alpha_{LC} \approx \alpha_{TC}$. Therefore, to simplify this model, we assume that ($F_{H,lead} = F_{H,trail}$), and net lateral droplet motion must be the result of asymmetric pinning forces.

3.4.2 *Force asymmetry along the contact line*

During each vibration cycle, the droplet undergoes advancing (wetting) and receding (de-wetting) motion with time-varying pinning forces acting at the contact line of the droplet (Figure 3.8B). In general, these pinning forces have components in the x, y and z directions. However, since the ARC pattern is symmetric with respect to the central axis of the track (Figure 3.5), the net force in the transverse direction (y-axis) must be zero. Furthermore, as we are primarily interested in the lateral motion of the droplet, let us consider only the horizontal portion (x-component) of the pinning forces. These forces are opposite in direction to the local motion of the contact line and can therefore be interpreted as friction. The equation for these forces comes from the model proposed by Duncombe et al. in 2012[97] and is shown in Equation 3.2.

$$\begin{aligned} F_{p,lead} &= \gamma w \cos\theta_{lead}\,\chi_{lead} \\ F_{p,trail} &= \gamma w \cos\theta_{trail}\,\chi_{trail} \end{aligned} \qquad (3.2)$$

In these equations w is the width of the ARC track and χ is the line fraction of the contact line pinned to the hydrophilic regions of the ARC track (as described in Figure 3.5). θ_{lead} and θ_{lead} are the contact angle of the leading and trailing edge of the droplet, respectively. It should also be noted that these line fractions and contact angles summarize the complex interaction between the droplet and ARC design (i.e. period, curvature, width, geometry, and surface hydrophobicity), and are difficult to predict quantitatively.[97]

To simplify subsequent equations, we aggregate all pinning and hydrodynamic forces at the footprint of the droplet into two combined forces at the leading and trailing edges, F_{lead} and F_{trail}, respectively (Equation 3.3). Hydrodynamic forces are accounted for through the components of the droplet model (masses interconnected with springs and dampers as shown in Equation 3.1). It should also be noted that hydrodynamic forces are balanced at equilibrium and do not provide a source of asymmetry during contact line oscillation ($F_{H,lead} = F_{H,trail}$), so any force imbalance will be the result of the pinning forces acting on the droplet.

$$\begin{aligned} \text{Leading Edge: } F_{P,lead} + F_{H,lead} &= F_{lead} \\ \text{Trailing Edge: } F_{P,trail} + F_{H,trail} &= F_{trail} \end{aligned} \qquad (3.3)$$

The relationship between F_{lead} and F_{trail} is the key to understanding how the ARC device works: if we can show that the sum of F_{lead} and F_{trail}, integrated over one period of oscillation, is non-zero, then we can expect lateral droplet motion.

To complete this argument, we make several observations. First, because of the geometric design of the rungs, the line fraction χ (portion of the contact line pinned by the rung) is larger at the leading edge. In other words, the droplet footprint is conforming to the curvature of the rung along the leading edge while bridging several gaps between rungs along the trailing edge (Figure 3.5). Therefore, $F_{P,lead}$ is always larger in magnitude than $F_{P,trail}$. In general, this results in a net backwards force during the wetting and a net forwards force during de-wetting, as shown in Equation 3.4.

$$\begin{array}{ll} \text{Wetting:} & F_{lead,wet} - F_{trail,wet} < 0 \\ \text{De-wetting:} & F_{lead,dewet} - F_{trail,dewet} > 0 \end{array} \qquad (3.4)$$

However, it remains to be shown that the effect of these forces does not cancel out over a complete cycle of vibration. The second observation was obtained by Shastry and co-workers,[94,96] who noted that the receding contact angles of the two edges differ more than the advancing contact angles. Duncombe et al. confirmed this observation on both textured[96] and chemical[97] ARCs, demonstrating that the contact angles of both the leading and trailing edges are close to the native contact angle of the hydrophobic background (135° and 110° for textured and chemical ARCs, respectively). However, during de-wetting, the contact angle of the leading edge is significantly lower than the contact angle of the trailing edge.[97] These observations indicate that pinning forces acting on the droplet are lower during the wetting phase of contact line oscillation, or in other words wetting is less sensitive to pinning (Figure 3.9). From this insight, we can conclude that the net force acting on the droplet is greater in magnitude during de-wetting than during wetting (Equation 3.5).

$$\left|F_{lead,dewet} - F_{trail,dewet}\right| > \left|F_{lead,wet} - F_{trail,wet}\right| \qquad (3.5)$$

From Equation 3.4 we know the net force is in the negative direction during wetting and in the positive direction during de-wetting. Substituting these signs into Equation 3.5, we see that during transport the magnitude of the net force in the positive direction (de-wetting) is greater than that of the net force in the negative direction (wetting). Therefore, a net force in the direction of droplet transport will result throughout the course of an entire vibration cycle.

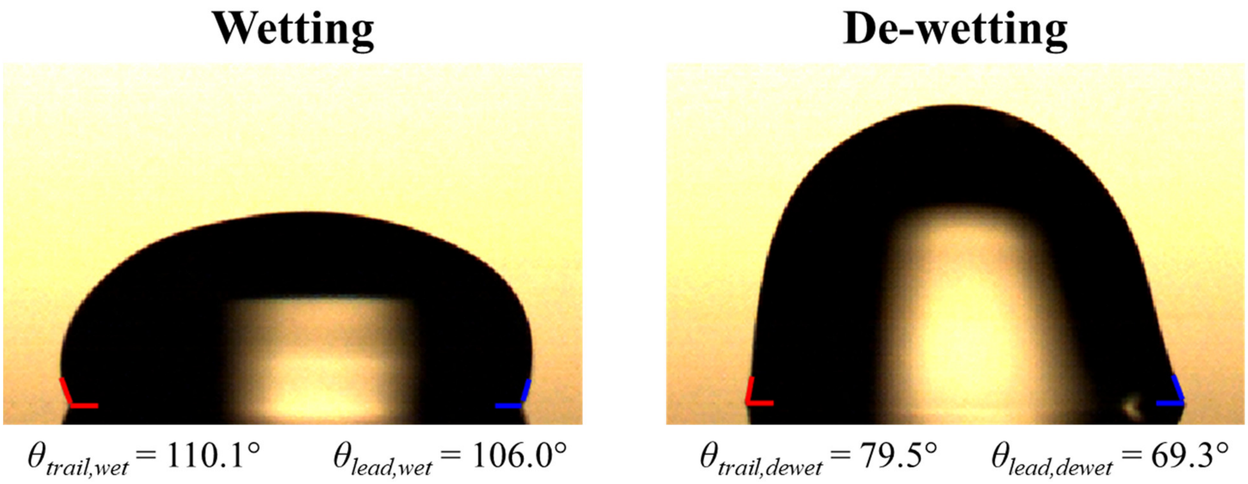

Figure 3.9: Force asymmetry is dependent on the phase of contact line oscillation. The difference in contact angle between the leading and trailing edges is larger during de-wetting than during wetting. This indicates that a larger net force (in the direction of the leading edge) will be present during the de-wetting phase, which provides for net transport of the droplet throughout each vibration cycle.

3.4.3 *Simulation of droplet motion*

We have created a simulation for droplet motion that models the droplet as a two-dimensional triangular mass-spring-damper system with friction forces as described above. As we are studying the droplet motion, the displacement of the three masses in both x and z axes are set to be our independent variables. For each mass in each direction, the total force including inertia, spring force, damping force, normal force and friction needs to be zero. Therefore, a total set of six equations can be set up to solve this problem with six degrees of freedom.

Regarding initial and boundary conditions, we start the simulation in an equilibrium state of the droplet. During simulation, the two edge points *T* and *L* are assumed to always remain in contact with the substrate. Since the substrate vibrates vertically with a sinusoidal signal at frequency ω and amplitude Z, the vertical displacement of the edge masses m_{T} and m_{L} is always $z(t) = Z\sin(\omega t)$. This effectively reduces the system to four degrees of freedom with four unknowns.

In conventional dry friction models, the friction force is the product of friction coefficient, magnitude of normal force and negated unit velocity vector. Such models often cause difficulties in simulations since the time-varying normal force is unknown a priori, resulting in a system that cannot be described by second-order ordinary differential equations. However, in our case viscosity and pinning are the dominant sources of friction, which are both independent of normal force. Viscous forces are linear in mass, velocity and viscosity, while pinning forces are simple step functions that we approximate with smooth sigmoid functions, leading to a system of differential equations that can be simulated numerically with standard techniques.

3.4.4 *Modeling: results and discussion*

Figure 3.10 shows the droplet position in the horizontal plane as a function of time as produced by our model. The three solid curves represent the location of the three masses m_{T}, m_{L} and m_{C}, respectively. The amplitude of oscillation at the trailing edge (red) is always larger than at the leading edge (blue), which corresponds to the smaller friction at the trailing edge. Meanwhile, it can be observed that the leading and trailing edges usually move in opposite directions, but not always, and not always at the same rate; lateral motion is a consequence of this asymmetry. The experimental data adopted from Duncombe's paper[96] is shown in the inset figure. There is good agreement between the model and the experimental data, indicating that our model and all associated parameters provide a reasonable representation of the droplet characteristics and behavior of droplet motion. Furthermore, this model also shows qualitative similarities to the motion of vibrated droplets on chemical gradient surfaces,[128] suggesting this model could also serve as a template for studying vibration driven droplets on many different platforms.

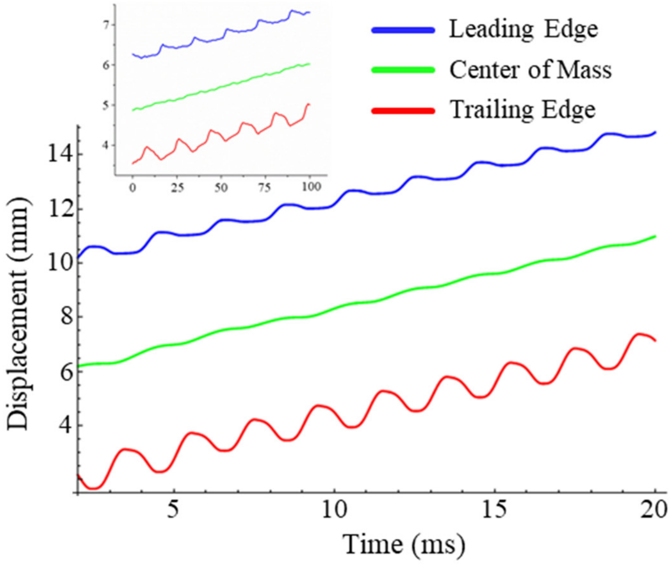

Figure 3.10: Simulation of ARC transport corresponds to experimental data. Lateral displacement of the simulated droplet at its center of mass (green), leading (blue) and trailing (red) edges matches the behavior of a transported droplet (inset).

In this system, there are two conditions that are not essential for our model: horizontal substrate and sinusoidal input signal. With modest adjustment, our model can be adapted to other systems such as inclined surfaces and sawtooth or square wave input. For inclined surfaces with a small tilted angle, an extra resistance force due to gravity will apply. However, the droplet can still move uphill as long as the net uphill force dominates in each oscillation cycle. Yet for each droplet, there is a critical angle beyond which no uphill motion can be observed. For other input signals such as a square wave function, net droplet motion has been observed experimentally on a texture ratchet.[94,95] In our model, the sinusoidal wave function can be easily replaced with a square wave function. For a sinusoidal wave input, unexpected "overtones" of the base oscillation were observed by Fourier analysis,[96] probably because of the stick-slip behavior of the contact line.

With a square wave input, we would expect more such overtones, making the displacement curves more jagged. However, further empirical data will be required to account for more complicated droplet responses, such as higher vibration modes.[129]

3.5 CONCLUSIONS

This section presents a theoretical study of the horizontal droplet motion on a vertically vibrating anisotropic ratchet conveyor device. By non-dimensionalizing the input frequency and threshold amplitude of vibration to initiate droplet motion, we reveal a general relationship between these two input factors across droplets with different volume, density and surface tension. This relationship indicates that the condition to initiate droplet motion on such a device is predictable and reliable. For the droplet motion on an ARC device, a qualitative analysis reveals that the pinning forces at the contact line are the driving force. A compact model is proposed to describe how force asymmetry arising from the vertical vibration results in horizontal droplet motion. This model could be applied to a variety of input signals and surfaces with asymmetric features and may lead to a better understanding of droplet mechanics. Furthermore, this model could also serve as an essential tool for the development and optimization of new devices that can manipulate droplets through interfacial interactions between the contact line and substrate surface.

Chapter 4. TRANSPORT VELOCITY ON ANISOTROPIC RATCHET CONVEYORS

The efficiency of ARC devices is related to the characteristic ARC threshold profiles; however, the velocity of droplets transported on ARC devices is not described by this characterization. Thus, the next task in this work was to understand how the velocity of droplets was related to the ARC threshold, or more specifically to investigate how vibration parameters and the design of ARC transport paths affected the resulting velocity of transported droplets.

The following sections are adapted from:

Transport Velocity of Droplets on Ratchet Conveyors[130*]

Hal R. Holmes[1] and Karl F. Böhringer[1,2] (*Advances in Colloids and Interfaces*, 2017)

[1]Department of Bioengineering, [2]Department of Electrical Engineering, University of Washington, Seattle, WA 98195

4.1 UNDERSTANDING ARC THRESHOLD

In order to better understand the underlying mechanisms of droplet transport, we characterized the behavior of 8 μL water droplets transported on three different ARC tracks with rungs composed of silicon dioxide (SiO_2) pattern and a fluorooctyltrichlorosilane (FOTS) background (Figure 4.1). These tracks are defined by the relationship of the width and period of the hydrophilic rungs (Figure 4.2).

---

[*] Original work of the author © 2017 Elsevier B.V. All rights reserved.

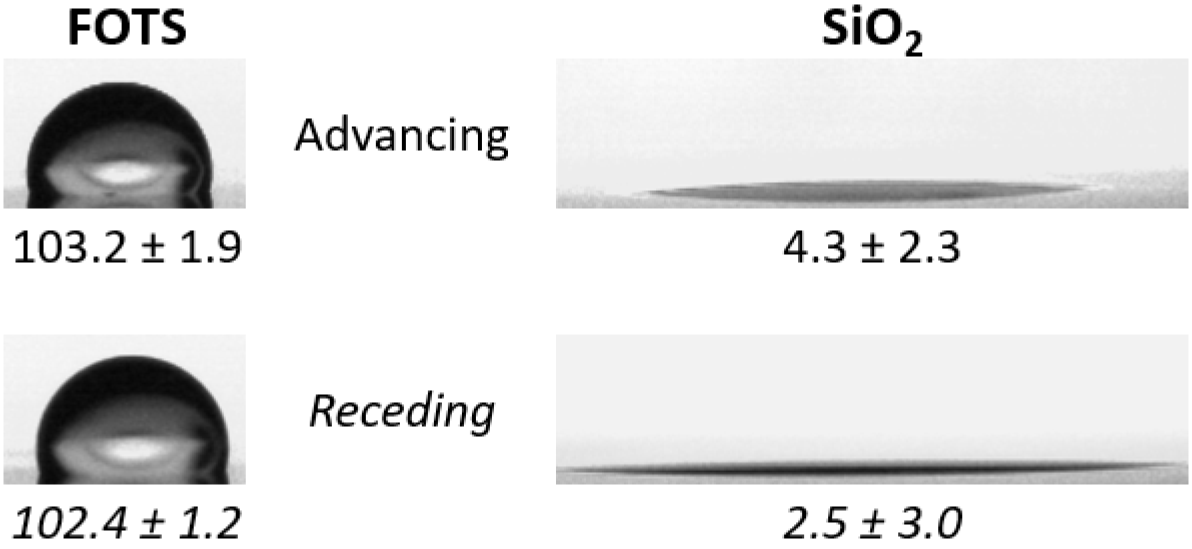

Figure 4.1: Wettability of native surfaces used in ARC tracks. Contact angle measurements verify that FOTS provides a hydrophobic background to define the hydrophilic SiO_2 rungs.

Two different rung periods were used in this work, 120 µm and 60 µm. Additionally, if the hydrophilic rung is thought of as the working region of the track, then a duty cycle can be calculated, where duty cycle is defined as the width of the rung divided by the period or spacing interval between rungs.[131] The two ARC duty cycles used in this work are 8.3% and 16.6%. Additionally, all tracks used in this portion of our work had a rung radius of 1000 µm.

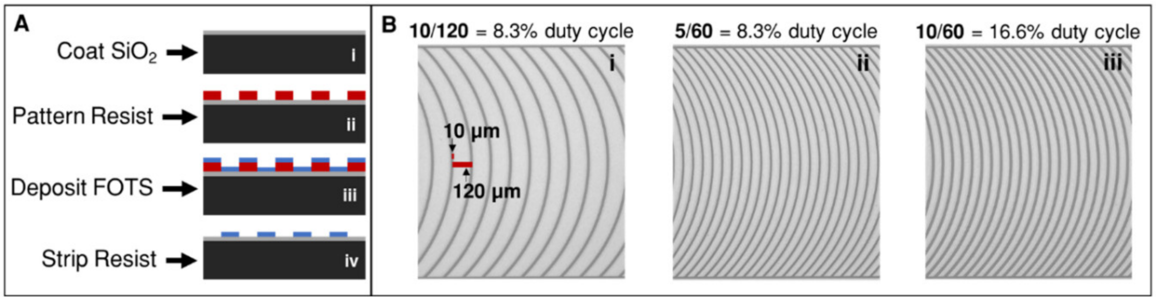

Figure 4.2: ARC fabrication and track design. ARCs are fabricated by patterning photoresist on an SiO_2 surface and coating exposed regions with FOTS through vapor deposition. Stripping resist reveals a flat, optically transparent pattern of hydrophilic SiO_2 rungs defined by the hydrophobic FOTS background (A). ARC track designs consisted of 10 and 5 µm wide rungs and 60 and 120 µm periods, providing combinations with 8.3% and 16.6% duty cycles (B).

ARC devices are characterized by the minimum vibration amplitude (ARC threshold) that is required to initiate droplet transport. These measurements are reported and discussed in terms of acceleration to account for the energy input to the system, but the corresponding substrate displacement (Figure 4.3) is provided for reference. Above the ARC threshold, droplet transport will still occur, but the effect of larger vibration amplitudes on droplet transport has not been previously characterized. The ARC threshold profiles obtained for all three tracks were characteristic of previous ARC threshold measurements,[97,132] and all exhibited a minimum ARC threshold around 80 or 90 Hz (Figure 4.3). If the frequency of minimum ARC threshold occurred at resonance, a local maximum in the wetting area of the droplet would occur at this frequency (wherein wetting area is defined as the maximum area of the droplet during a complete cycle of contact line oscillation, which occurs at the end of the wetting phase). However, the wetting area was actually smallest at the frequency of minimum ARC threshold on all three devices. These observations indicate that the factors determining the minimum ARC threshold are more complex than indicated by previous models,[97] and the specific design of the ARC devices has a larger effect on the droplet response to vibrations than expected.

The 10/120 ARC track was the most efficient, exhibiting the lowest ARC threshold at all frequencies except 90 Hz (Figure 4.4). Wetting area measurements confirmed the expansion of the droplet is also the smallest on the 10/120 track (except 90 Hz). The frequency of minimum ARC threshold also shifts from 80 to 90 Hz, and a local peak in wetting area shifts from 60 Hz to 50 Hz when the period of the tracks is reduced from 120 μm to 60 μm. These measurements indicate that the ARC design significantly influences droplet response to vibrations.

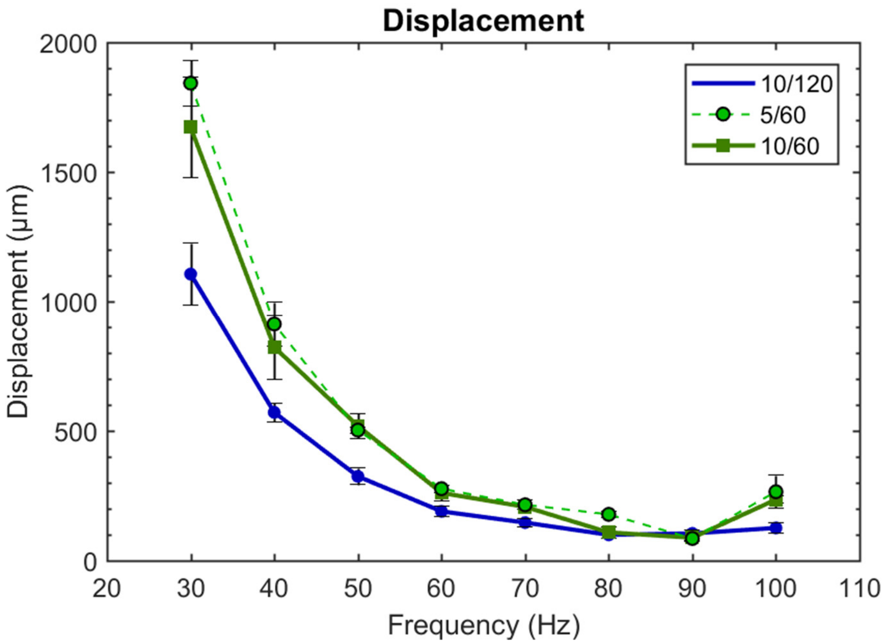

Figure 4.3: Substrate displacement at ARC threshold. ARC threshold is reported in terms of acceleration to account for the energy input into the system. Displacement of the substrate at these vibration amplitudes show a similar trend in the relationship between ARC tracks (10/120 tracks require the smallest displacement to initiate droplet transport), however these values demonstrate that displacements can be quite large at lower frequencies even though the acceleration of the substrate is not very high.

At the point of maximum wetting area (Figure 4.4C), the shape of the droplets is dependent on the vibration frequency and the ARC track. All droplets are oscillating in a mode with only two nodes (i.e. the vibrated droplets are not forming multiple lobes during wetting).[124,133,134] Droplets vibrated on the 5/60 track at 50 Hz may be at the transition to a higher mode, as the contour is not perfectly elliptical, but this irregularity in contour may also be in part due to the anisotropy of the ARC substrate.

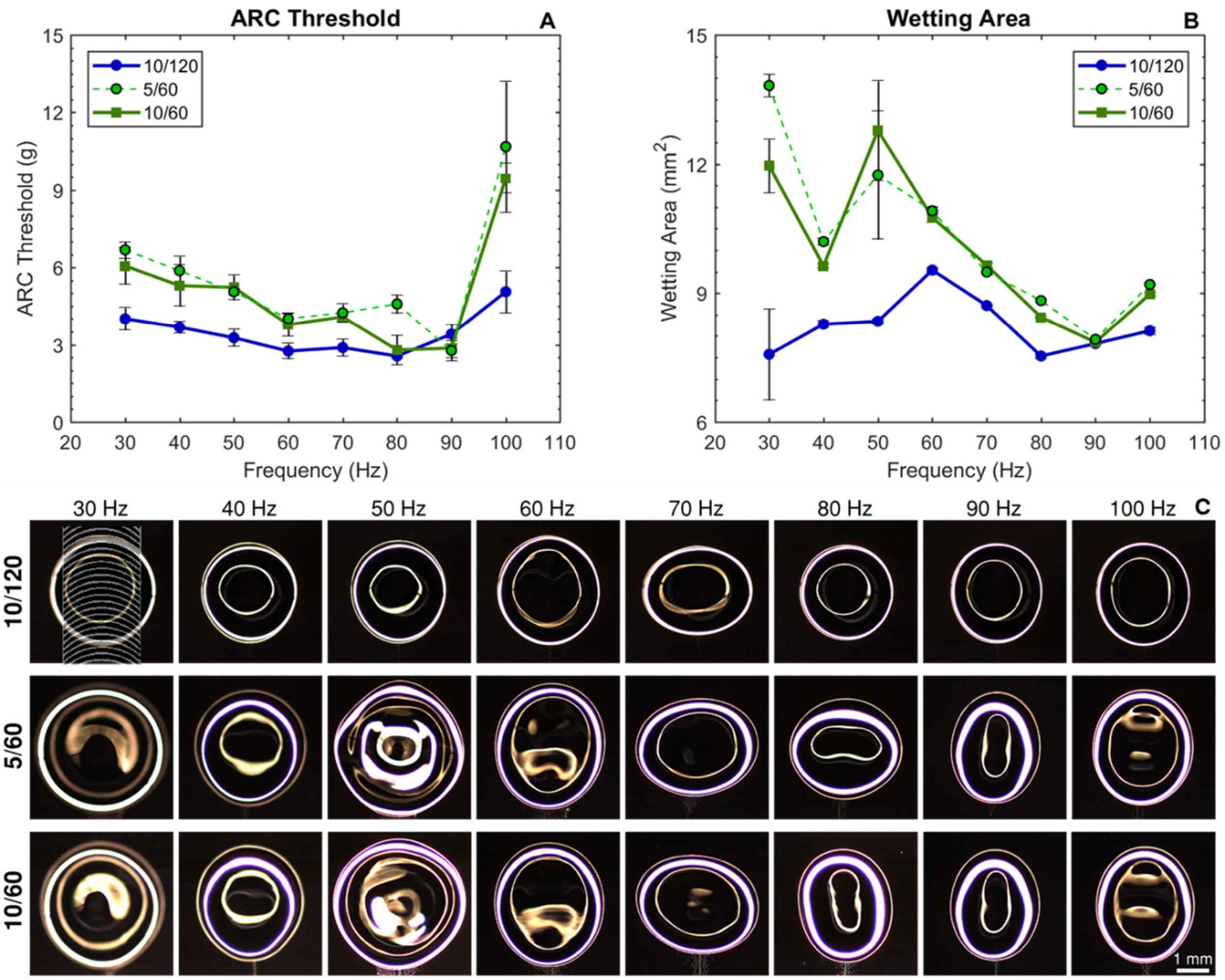

Figure 4.4: Transport efficiency is correlated to the period of ARC tracks. The ARC threshold profiles for the 60 μm period tracks were most similar over most of the functional frequency range, but the ARC track with the larger 120 μm spacing had a lower ARC threshold across this entire range, with the exception of 90 Hz (A). The shift in minimum ARC threshold from 80 to 90 Hz also indicates that the design of the ARC track has some influence over the droplet response to vibrations. A similar trend is observed for the maximum wetting area of the transported droplets (B). The differences in droplet size during maximum wetting are clear when these areas are viewed together (C). The shape of the droplets during this state also provides some explanations for the droplet response to vibrations, particularly note the pronounced expansion of the droplet edges perpendicular to the ARC track (direction of the ARC track is indicated by superimposition in top right panel).

Another important observation is the stark contrast in aspect ratio of droplets on all tracks when vibrated at 70 Hz compared to other frequencies. The length to width aspect ratio (Figure 4.5A) of droplets vibrated at this frequency is substantially lower than all other frequencies. This means that the droplets are expanding much more in the direction perpendicular to the ARC track than at other frequencies. This could explain the slight increase in ARC threshold from 60 to 70 Hz for all tracks. Furthermore, the length to width aspect ratio is smaller at 80 Hz on the 5/60 track than on the 10/60 track, and accordingly the ARC threshold is higher on the 5/60 track than the 10/60 track at this frequency. Therefore, such differences in the aspect ratio as well as the height (Figure 4.5B) of the droplets play an important role in the frequency response of droplets on ARC devices.

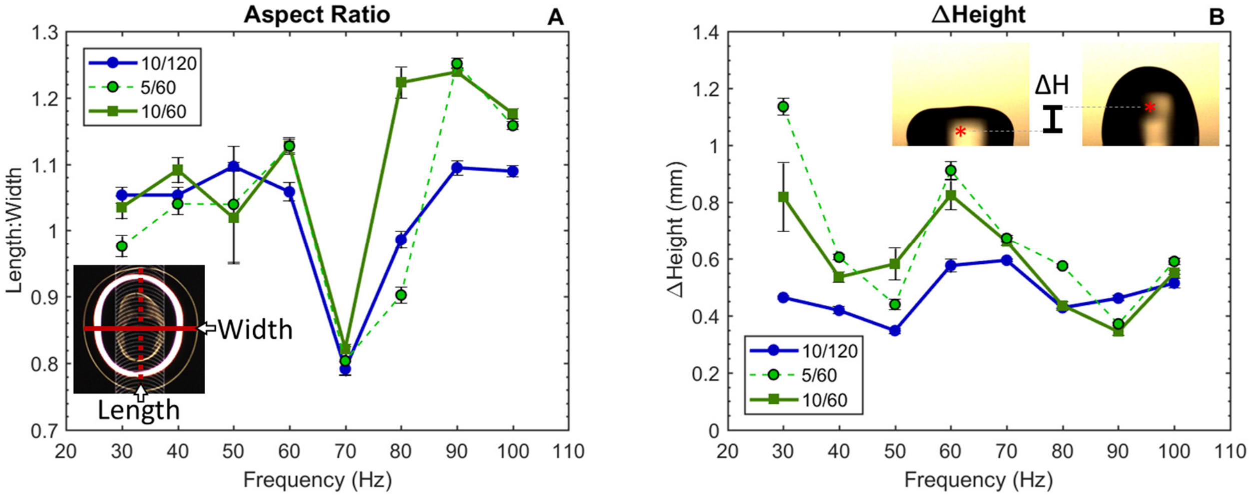

Figure 4.5: Aspect ratio and height of droplets. The aspect ratio (A) is defined as the ratio of the length (parallel to ARC track) to width (perpendicular to the ARC track) of the droplet during maximum wetting (inset - A). The change in height (B) of the droplet is the difference in the vertical position of the droplet centroid between wetting and de-wetting phases (inset - B). The aspect ratio is substantially lower at 70 Hz on all droplet tracks and the profile of the change in height of the droplets is similar to the droplet velocity, except at 70 Hz – which is likely due to the low aspect ratio. The change in height of droplets on 5/60 tracks is also larger than on 10/120 tracks, even though the velocity is similar.

These observations further demonstrate the effect of ARC track design on the droplet response to vibrations. However, it is unclear how the ARC design creates such dramatic differences in the aspect ratio of droplets between different frequencies. Further investigation of this question could lead to additional discoveries or applications for vibrated sessile droplets on micro-patterned surfaces. Together, these measurements show that transport velocity can be controlled through substrate design and applied vibration signal.

4.2 DROPLET VELOCITY AND EDGE MOVEMENT

The motion of droplets transported at the ARC threshold of each track was recorded at 2000 frames/s. Velocity is measured as the net horizontal displacement of the droplet centroid throughout one vibration cycle, divided by the time of the cycle (or multiplied by the vibration frequency). Thus, these measurements describe the net velocity for each step of the transported droplets.

The velocity profiles all exhibit a local maximum at 60 Hz, and the velocity appears to level off as frequency increases (Figure 4.6). The overall velocity profile is also relatively similar for all tracks. Although most notably defined by the local maximum at 60 Hz, all tracks also exhibit a sharp drop in velocity at 70 Hz and slight increase at 80 Hz. This effect is likely due to the low aspect ratio of droplets driven at 70 Hz (as seen in Figure 4.5), wherein the contact line would not expand as much in the direction of the ARC track compared to frequencies with a higher aspect ratio. These results indicate transport velocity is correlated with contact line advance in the direction of the ARC tracks and not the total wetting area of the droplet.

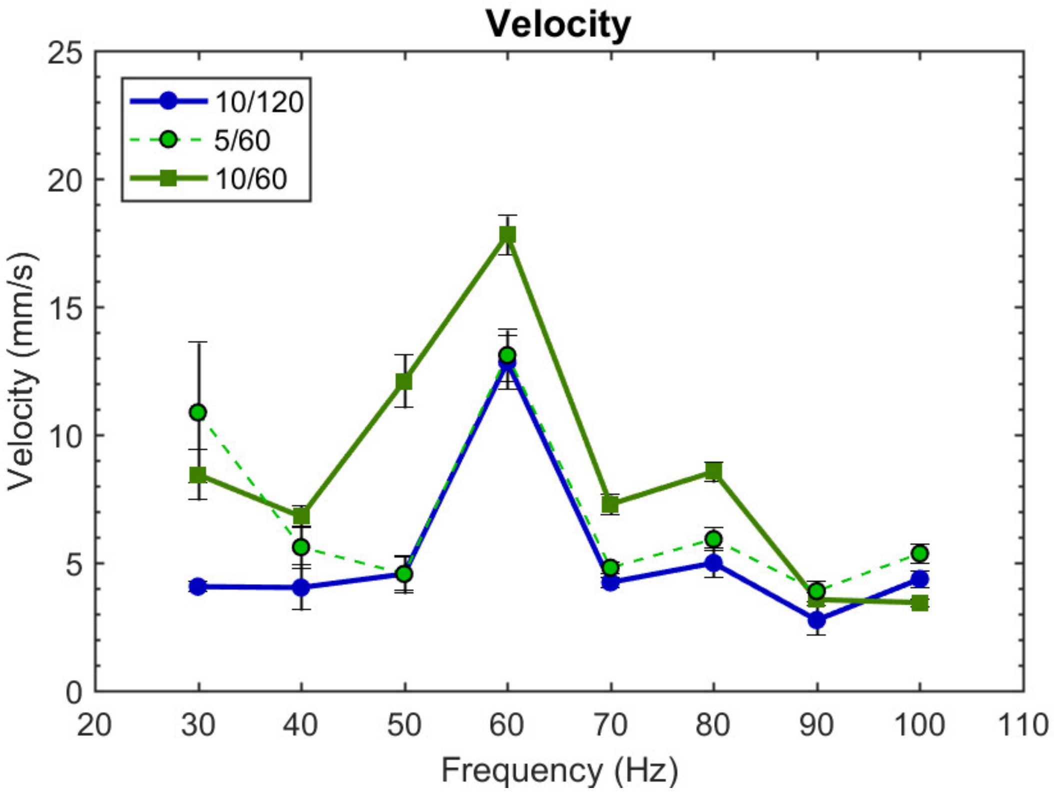

Figure 4.6: Transport velocity is correlated with ARC duty cycle. The transport velocity for the 10/120 and 5/60 tracks that have the same duty cycle (8.3%) exhibits a virtually identical profile for frequencies above 40 Hz. The 10/60 track with the higher duty cycle exhibits a similar profile, but the velocity is shifted up by 3 to 7 mm/s over the range of 50 to 80 Hz. Error bars indicate ± standard error of the mean.

The transport velocity is entirely dependent on the movement of the droplet edges. The two phases of contact line oscillation are wetting, when the edges are advancing or expanding away from the center of the droplet and de-wetting, when the edges are receding or contracting towards the center of the droplet (Figure 4.7A-B). The cross section (side view) of droplets during transport, shows that during wetting the advance of both edges is the same or greater on 60 µm period tracks than 120 µm period tracks, except at 90 Hz (Figure 4.7C-D). This result is consistent with wetting area measurements, especially when considering the aspect ratio.

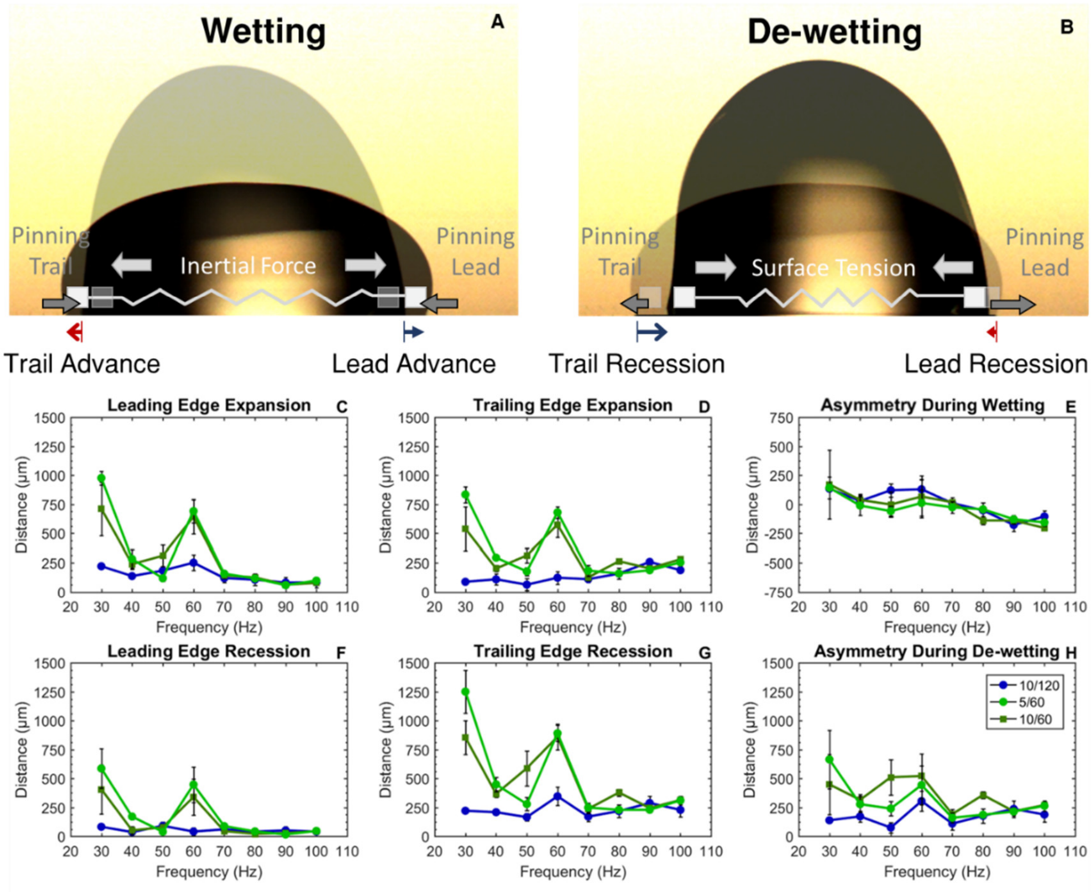

Figure 4.7: ARC threshold and transport velocity profiles are dependent on droplet volume. ARC threshold measurements of 5, 8, and 13 µL show the frequency and amplitude are both inversely correlated with droplet volume (A), while velocity profiles show that only the frequency of maximum velocity is correlated to drop volume, with 8 µL droplets exhibiting the highest velocity (B). Side view images for 5, 8, and 13 µL (C-E) droplets transported at maximum velocity (80, 60, and 50 Hz, respectively) show how wetting (superimposed in front) and de-wetting (background) phases differ by droplet volume. Error bars indicate ± standard error of the mean for velocity measurements.

The asymmetry during wetting (determined by subtracting the trailing edge advance from leading edge advance) describes the net forward progress of the droplet at the end of the wetting phase. These measurements are near zero or slightly positive at low frequencies, but generally decrease with increasing frequency (Figure 4.7E). This trend implies that the centroid of the droplets will move backward during wetting at higher frequencies and this cross-over appears to occur at or near 70 Hz, which may explain the sharp decrease in aspect ratio observed at this frequency. During de-wetting, the leading edge of droplets on the 10/120 track recedes on average less than 120 µm. This measurement implies the leading edge remains pinned or slips by only one rung during most wetting phases at all frequencies (Figure 4.7F). Meanwhile, the trailing edge recedes by an average of at least 240 µm, which is equivalent to two or more rungs (Figure 4.7G), resulting in net forward transport (Figure 4.7H). However, the leading edge recedes by a much greater amount on the 5/60 and 10/60 tracks at 30 and 60 Hz. These frequencies are also where the droplet edges expanded the most during the wetting phase. The surface tension forces (if modelled as a spring[122,125,135]) would therefore be largest at these frequencies during the de-wetting phase. This observation indicates that the surface tension forces acting on the leading edge are greater than the pinning forces of the rungs acting against the recession of this edge. In these cases, net transport occurs because the recession of the trailing edge is still larger than that of the leading edge (i.e. pinning forces acting on the trailing edge are even smaller because of the asymmetric ARC pattern). These effects are clear when looking at asymmetry during the de-wetting phase (determined by subtracting the recession of the leading edge from the recession of the trailing edge). The consistency of edge movement measurements to transport velocity is confirmed by multiplying the net forward progress of droplet edges (the sum of wetting and de-wetting asymmetries) by the vibration frequency, which provides a virtually identical reproduction of the measured centroid velocity profiles (Figure 4.8).

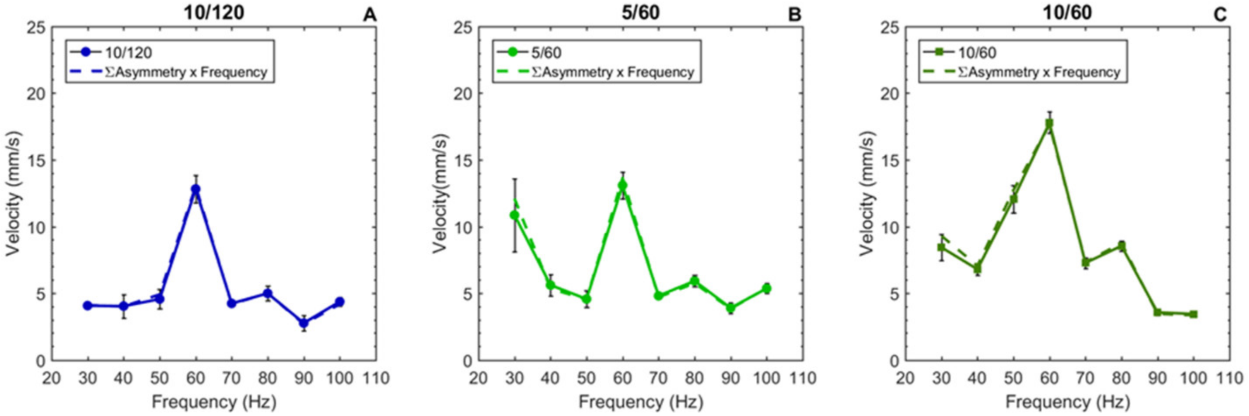

Figure 4.8: Relationship of droplet velocity to edge movement. Asymmetry is the difference between leading and trailing edge movement during each phase of contact line oscillation. Multiplying the sum of asymmetry in both phases by the vibration frequency results in a velocity profile that is nearly identical to the measured centroid velocity for 10/120 (A), 5/60 (B), and 10/60 (C). This verifies that measurements are consistent on all tracks.

4.3 EFFECT OF DROPLET VOLUME

ARC threshold and velocity measurements were repeated for 5 and 13 μL droplets on 10/120 tracks to understand how consistent these findings are across droplet volumes (Figure 4.9). The ARC threshold profiles looked similar for all droplet volumes, but both the ARC threshold and minimum frequency of ARC threshold appear to be inversely correlated with droplet volume (i.e. smaller droplets require higher frequency and amplitude vibrations for transport). These observations are consistent with established models of droplet mechanics.[125,135,122]

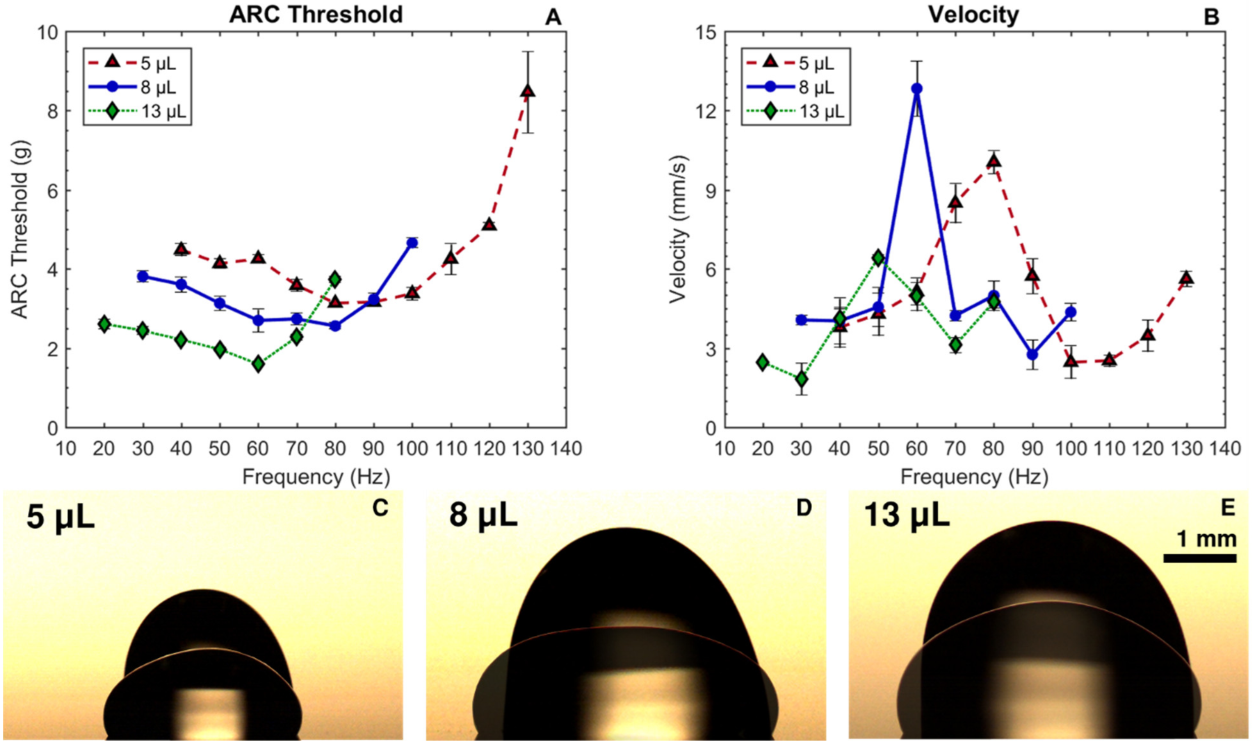

Figure 4.9: ARC threshold and transport velocity profiles are dependent on droplet volume. ARC threshold measurements of 5, 8, and 13 μL show the frequency and amplitude are both inversely correlated with droplet volume (A), while velocity profiles show that only the frequency of maximum velocity is correlated to drop volume, with 8 μL droplets exhibiting the highest velocity (B). Side view images for 5, 8, and 13 μL (C-E) droplets transported at maximum velocity (80, 60, and 50 Hz, respectively) show how wetting (superimposed in front) and de-wetting (background) phases differ by droplet volume. Error bars indicate ± standard error of the mean for velocity measurements.

The velocity profiles were also similar, with all droplets exhibiting a characteristic local maximum at a frequency slightly below the frequency of minimum ARC threshold. These measurements verify that our findings and observations of droplet transport on ARC devices are consistent. However, the frequency of the maximum velocity is correlated to the droplet volume but the actual maximum velocity is not. This effect is likely due to the combination of surface tension forces and size of the droplet footprint. The 13 μL droplet has the largest footprint and therefore could take the largest step throughout each vibration cycle. However, the surface tension forces are less dominant (compared to gravity and inertial forces) in this droplet.[122,129] While this reduces the likelihood of the leading edge slipping, the relatively weaker surface tension forces also result in less recession of the trailing edge. On the other end, the 5 μL droplet experiences the largest surface tension forces but has the smallest footprint. Even though the trailing edge recedes by the largest distance proportional to the droplet size (thus the relatively high velocities observed for the 5 μL droplets), the smaller droplet footprint limits the maximum step size of the droplet. This implies that there is an optimum droplet volume for the fastest transport on ARC devices. Furthermore, the variations in transport velocity observed for 8 μL droplets on different ARC tracks also demonstrate the design of the ARC track can provide some level of control over transport velocity. These considerations present much potential for tailoring the ARC design and selecting droplet volumes to meet the demands of specific applications.

4.4 VELOCITY AND VIBRATION AMPLITUDE

Finally, we characterized the effect of vibration amplitude on the resulting transport velocity by recording the movement of 8 μL droplets driven by vibrations 0.5 g below, 0.5 g above, 1.0 g above, and at the ARC threshold on 10/120 ARC tracks. The transport velocity was correlated to, albeit with a non-linear relationship, to the vibration amplitude (Figure 4.10). Qualitatively, we observed that increasing vibration amplitude results in droplets that are flatter and more spread out during wetting and taller during de-wetting.

At vibrations below the ARC threshold (-0.5 g) no average net velocity occurred, but the droplet edges were oscillating, particularly at higher frequencies. This observation indicates the ARC threshold does not necessarily occur at the transition from a pinned to a mobile contact line.[124,133,134] Increasing the vibration amplitude to 0.5 g above the ARC threshold caused the velocity to increase at some frequencies, but remain unchanged at other frequencies (or even slightly decrease at 50 Hz). Increasing the amplitude further to 1.0 g above the threshold amplitude results in a more pronounced increase in transport velocity at all frequencies except 100 Hz. Furthermore, the vibration amplitudes at +1.0 g are relatively close to the ARC threshold profile of the 10/60 track, and the velocity of droplets on the 10/120 track at this amplitude are slightly higher than that of droplets on the 10/60 track (Figure 4.11) at most frequencies. This indicates the increased velocity at the ARC threshold of the 10/60 track (Figure 4.5) is a result of the higher vibration amplitude and increased advance of the droplet edges. Additionally, we have observed velocities over 2 cm/s on ARC tracks, which is 2 to 3 times faster than velocities observed on electrowetting systems,[136,137] and we hypothesize that similar velocities could be obtained with other contact line driven DMF systems.

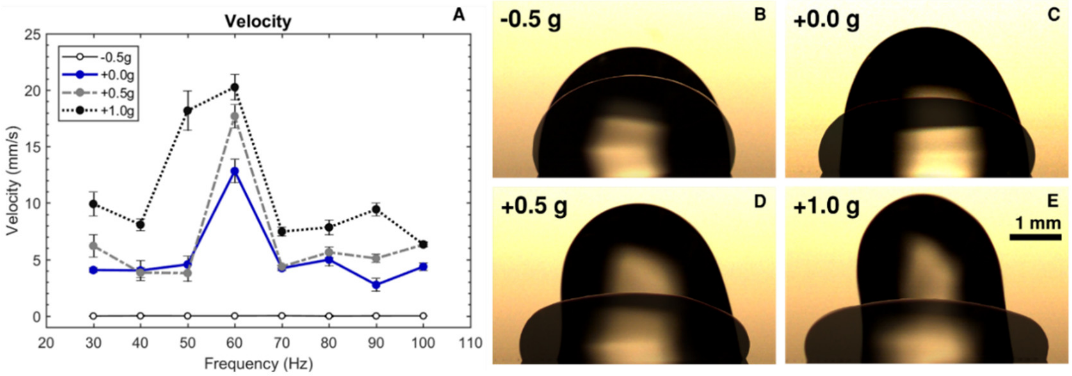

Figure 4.10: Transport velocity is correlated to vibration amplitude. Velocity measurements (A) of 8 µL droplets driven by vibrations at -0.5, +0.0, +0.5, and +1.0 g (B-E), with respect to the ARC threshold, show velocity increases with increasing vibration amplitude. Side images of droplets at maximum velocity (60 Hz) increasing vibration amplitude increases the advance of the droplet edges along the ARC track during wetting (front) and increases edge recession and droplet height during de-wetting (back) phases. Error bars indicate ± standard error of the mean.

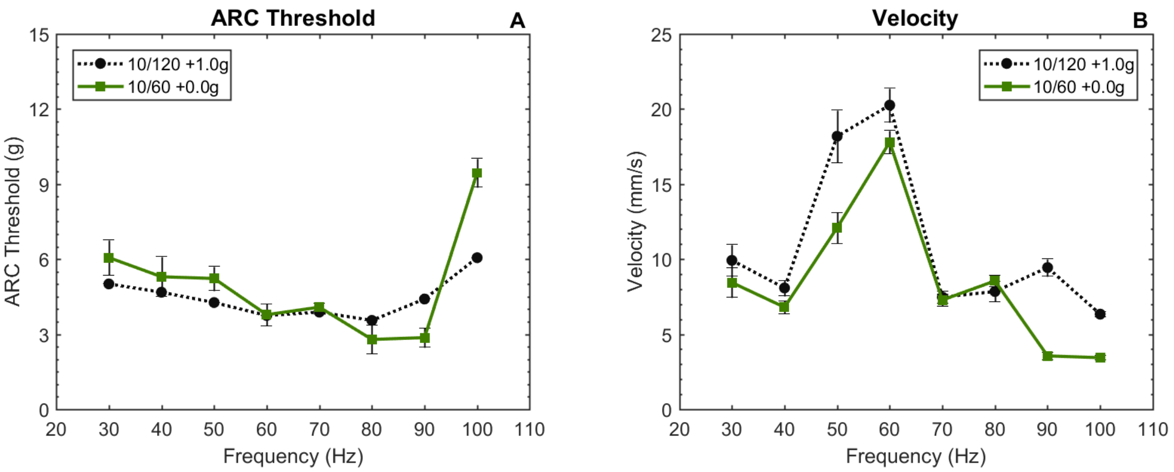

Figure 4.11: Increased velocity of 10/60 track is due to higher vibration amplitude. When the vibration amplitude applied to 10/120 tracks is similar of that applied to 10/60 tracks (A) the transport velocities are similar in magnitude. This indicates the increased velocity of droplets driven on 10/60 tracks at the ARC threshold is due to the increased vibration amplitude. However, at many frequencies the velocity is higher on 10/120 tracks even though the vibration amplitude is slightly lower. This observation provides further evidence that the larger hydrophobic spacing interval on 10/120 tracks may increase the stability of droplet edges, particularly the leading edge, on the hydrophilic rungs.

Looking at the edge movement of droplets at different vibration amplitudes, the edges, particularly the leading edge, jumped from rung to rung rather than moving with a smooth continuous motion. Plotting the distances of edge step shows that the edge movement forms clusters around 120 µm intervals (Figure 4.12). These clusters are more pronounced on the leading edge, which conforms to the ARC rungs, but also show up on the trailing edge (Figure 4.12). Additionally, it should be noted that measuring the micrometer scale edge movement of millimeter sized droplets pushed the resolution limits of our camera (i.e. a single pixel accounted for 10 – 15 µm in length), which likely contributed to a larger distribution of these measurement values. Overall, these observations indicate the movement of the droplet edges is in effect quantized or restricted to discrete step distances that are an integer multiple of the rung period.

Furthermore, these clusters and edge quantization provide us some additional information about the droplet response to vibration amplitude. In cases where increasing amplitude did not result in an increase of transport velocity, we do not observe a change in the clusters for either edge between the two amplitude groups. For example, at 50 Hz no increase in transport velocity was observed between +0.0 and +0.5 g groups, and the net change for both edges exhibits clusters around 0 and 120 µm (0 and 1 rung, respectively). However, at +1.0 g we see clusters appear at 240, 360, and 480 µm (2, 3, and 4 rungs, respectively) for both edges (Figure 4.12), indicating the droplet takes larger steps each cycle (which is reflected by an increase in the measured transport velocity). This change in edge movement suggests that the +1.0 g vibrations increased the surface tension force sufficiently to induce the trailing edge to slip (recede) from additional rungs without increasing slip at the leading edge. On the other hand, the velocity increased only slightly at 60 Hz when increasing the velocity from +0.5 to 1.0 g. In this case, we observe clusters for both leading and trailing edges (Figure 4.12) at a larger number of rungs, indicating the surface tension force is large enough to induce slip of the leading edge. This implies a terminal velocity exists for droplets on ARC tracks, in which further increases in vibration amplitude will no longer increase the asymmetry between leading and trailing edge recession. Overall, these measurements show that droplet transport on ARC devices is a result of a complicated balance between the surface tension forces within the droplet and the pinning forces from the substrate.

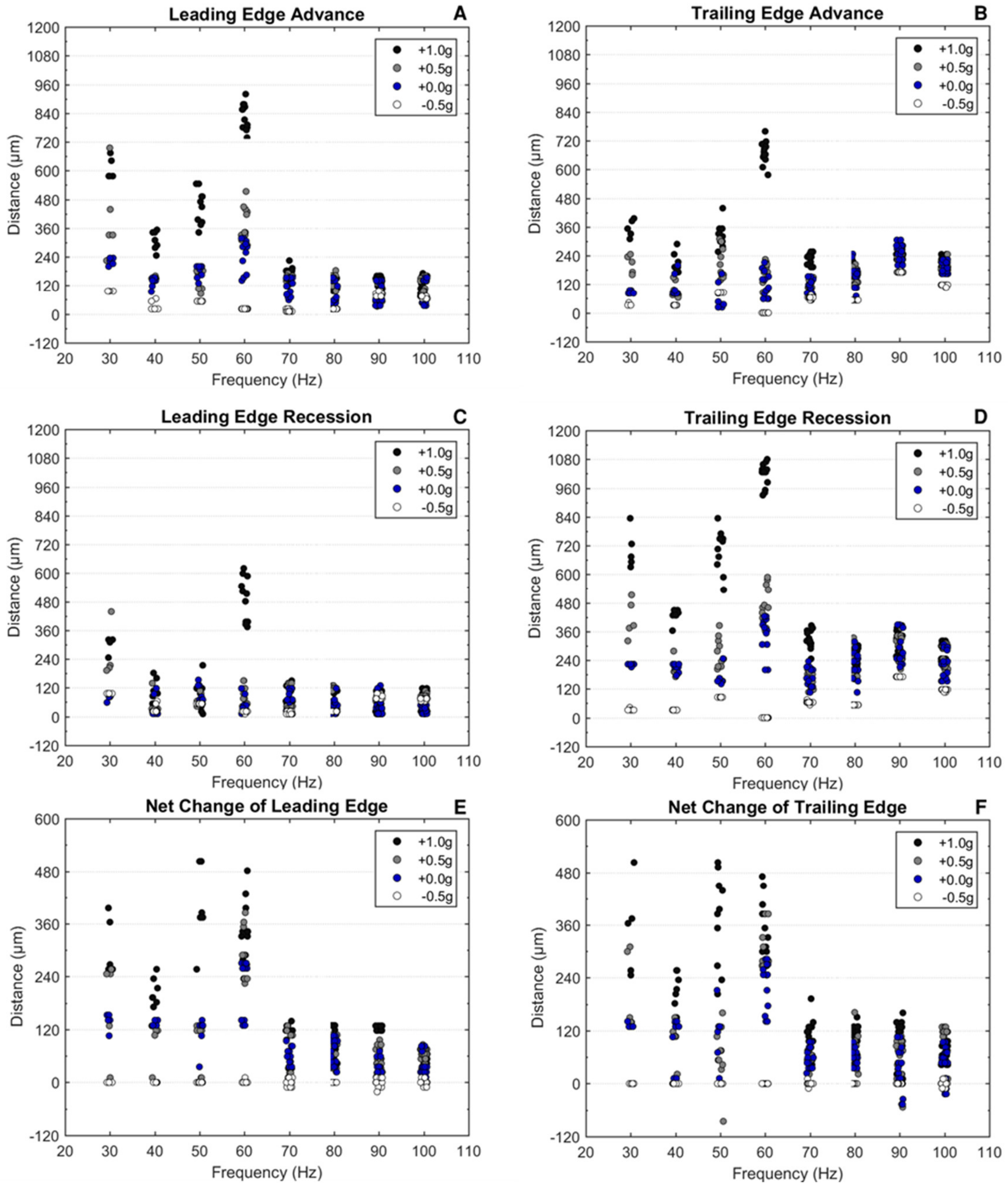

Figure 4.12: Edge movement is quantized to rung period. The edge advancement (A-B) during wetting and recession (C-D) during de-wetting forms clusters at intervals equivalent to rung period on both leading and trailing edges. The clusters are more apparent in measurements of the net change in leading (E) and trailing (F) edges throughout an entire vibration cycle. These clusters shift in response to vibration amplitude, with higher amplitudes resulting in clusters appearing around larger multiples of rung periods.

4.5 DISCUSSION AND CONCLUSION

The anisotropic ratchet conveyor platform is a contact line driven digital microfluidic system that transports liquid droplets through the interaction of droplet edges with a microfabricated surface pattern and applied orthogonal vibrations. In this work we show how the design of this surface pattern influences the droplet response to vibrations and affects the resulting transport velocity of the droplets.

Transport efficiency (ARC threshold) is correlated to the period of the rungs, while transport velocity is influenced by the duty cycle of the ARC track. Previous models of ARC transport[97] would predict transport behavior to be entirely dependent on duty cycle, as the fraction of the contact line pinned to the hydrophilic regions at the trailing edge (Figure 4.2) is determined by the duty cycle (e.g. the percent of the trailing edge pinned to hydrophilic regions is the same on 10/120 and 5/60 tracks, but this percentage is higher on the 10/60 tracks). However, these models do not account for the geometry of the rungs. The thinner (5 µm) width of the 5/60 track likely accounts for the increased recession of the leading edge (Figure 4.8) even though the pinning ratio is the same as the 10/120 track. Thus, the leading edge of the 10/120 track is more stable (less recession) during de-wetting and provides for transport at lower vibration amplitudes.

Increasing the vibration amplitude provides for higher transport velocities by increasing the advance of the leading and trailing edges. A larger distance between leading and trailing edges results in higher surface tension forces acting on the droplet edges (assuming surface tension acts like a spring[122,125,135] – Figure 4.8A-B). Pinning on the hydrophilic rungs resists recession of the droplet edges, acting in a similar fashion to friction. This pinning force is larger on the leading edge, and more able to resist edge recession when the surface tension forces are increased. The lower pinning forces at the trailing edge allow increased recession, and a larger step throughout each vibration cycle. This relationship between pinning and surface tension forces accounts for the initiation of droplet transport and higher transport velocities in response to increasing vibration amplitude. However, this relationship between transport velocity and vibration amplitude is non-linear due to the interplay of many factors – substrate pattern, droplet volume, and vibration frequency that have been detailed in this work, as well as additional factors that have yet to be characterized.

Despite the underlying complexity of this system, several clear patterns are still apparent. First, transport efficiency is determined by the minimum wetting area required to initiate transport. This trend is observed from transport on different tracks and across the frequency profile of each track. Transport initiates when the distance between leading and trailing edges (surface tension force) during wetting is large enough to induce a net force during de-wetting (e.g. de-pin the trailing edge without de-pinning the leading edge). Therefore, to optimize transport efficiency, the substrate pattern must 1) maximize length to width aspect ratio during wetting, and 2) minimize leading edge recession during de-wetting. Second, increasing wetting (specifically the distance between the leading and trailing edges) increases transport velocity. Higher surface tension forces increase the recession of the leading edge, resulting in larger steps throughout each vibration cycle. This trend is observed from the frequency profiles of each track, droplet volume, and effects of increasing vibration amplitude. Higher surface tension forces increase the net force propelling the droplet, until these forces are high enough to de-pin the leading edge. Thus, maximum velocity is determined by the highest obtainable difference in pinning forces between the leading and trailing edges. Lastly, velocity is an average of quantized steps throughout many vibration cycles. The size of the step is an integral multiple of the rung period, as the edges of the droplets move discretely between the hydrophilic rungs. However, the step size is not always the same because the dynamics between pinning and droplet forces can change with each vibration cycle. These variations are due to effects such as the droplet shape, edge position, momentum, and a thin liquid film on the track from previous vibration cycles.

Overall, these results show the complex droplet and interfacial mechanics that provide for droplet transport on ARC devices result in consistent and predictable trends that can be utilized to enable practical microfluidic devices. However, these results also raise new questions about the mechanisms through which surface patterns can influence the droplet response to vibrations and what other behaviors can be elicited with designed surface patterns.

Chapter 5. DROPLET FUNCTIONS ON ANISOTROPIC RATCHET CONVEYORS

Having gained a clearer understanding of the dynamics of droplet transport on anisotropic ratchet conveyors (ARCs), the next portion of this work looked to explore how well the combination of the passive surface pattern and vibration parameters could control droplet behavior and perform particular tasks, or functions, with selective droplet responses.

The following sections are adapted from:

Enabling Droplet Functionality on Anisotropic Ratchet Conveyors[138*]

Hal R. Holmes[1], Ana E. Gomez[1], and Karl F. Böhringer[1,2] (*Micromachines*, **8**(12), 2017)

[1]Department of Bioengineering, [2]Department of Electrical Engineering, University of Washington, Seattle, WA 98195

While ARCs do not offer the robust programmability available to electrowetting-on-dielectric (EWOD) or dielectrophoresis (DEP) based DMF systems,[139–141] this platform provides the ability to handle liquid droplets with a passive surface pattern and a globally applied sinusoidal vibration (e.g. a speaker). This configuration allows for droplets to be driven with a single signal source, which substantially simplifies the circuitry and programming required to operate an ARC system. Like EWOD and DEP systems, the ability of ARCs to handle liquid in the form of discrete droplets can reduce required sample volumes and reagent quantities compared to continuous flow devices.

Droplets also provide a form of ‘compartmentalization’, wherein the contents of each droplet are individually isolated, preventing undesirable interactions between samples or reagents.[139]

The simple microelectromechanical systems (MEMS) based fabrication process allows for high-throughput manufacturing of ARC devices, which could provide for inexpensive ARC chips with integrated MEMS components or electronic sensors. Such a system could fill the niche for diagnostic or analytic applications that require more process control or measurement accuracy than paper-based or passive microfluidic systems.[31,142] The simplicity of this system makes it a good candidate for field-ready or point-of-contact (where the sample is first encountered in the field) tests, potentially enabling a point-of-contact platform with improved clinical utility,[143–145] or for molecular (nucleic acid) assays that are less expensive and more easily deployable.[146–148] Furthermore, ARCs could also provide a useful research tool, such as in applications for automating protein[149] or nucleic acid[150] purification.

However, before any applications for an automated ARC platform can be realized, the functional toolbox available to ARC systems must be expanded. Thus, we have developed three new modules for the ARC system: 1) ARC gates that can selectively pause droplet transport, 2) ARC switches that can select the direction of droplet transport between two paths, and 3) ARC delivery junctions that can controllably deliver droplets on a convergent path. In electrowetting systems, these functions are innately enabled by the position of electrodes, with respect to the droplets, being activated.[139,151,152] On ARC systems, functionality is dictated by the design of the passive surface pattern. Therefore, each droplet function on ARC systems must be enabled with a specific design strategically placed on chip. The following sections will demonstrate how the design of the surface pattern on these ARC modules pairs with the applied vibrations to enable essential functions for automated liquid handling processes on ARC systems.

5.1 EFFECTS OF DUTY CYCLE

The ARC threshold of the SiO_2-FOTS tracks was first determined over a range from 60 to 100 Hz for 10 µL droplets (Figure 5.1). We observed that the ARC threshold profiles, although not identical, were relatively similar on tracks with both 8.3% and 16.6% duty cycles.

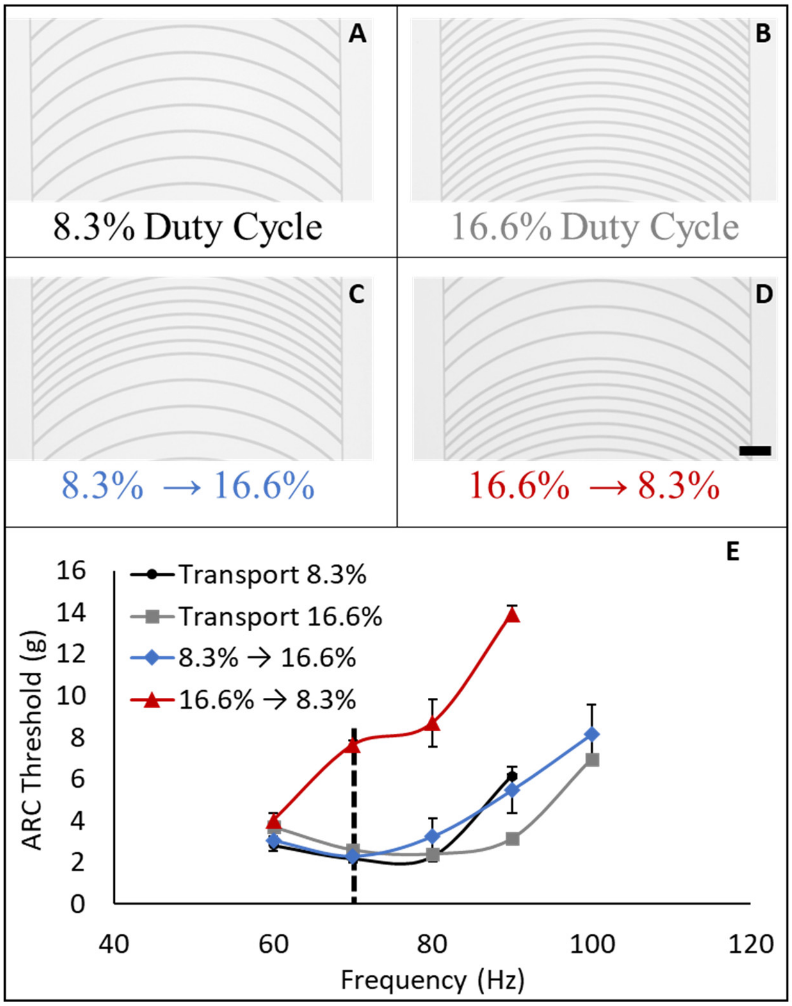

Figure 5.1: Rung duty cycle modulates ARC threshold. The ARC threshold for vibration induced transport of 10 µL diH_2O droplets was measured on ARC tracks with 8.3% (A) and 16.6% (B) duty cycles, and transitions from 8.3% to 16.6% (C) and 16.6% to 8.3% (D). Only the transition from 16.6% to 8.3% required a higher ARC threshold at frequencies above 60 Hz (E). The dotted black line indicates 70 Hz used in subsequent experiments. Scale bar = 200 µm.

Additionally, the transition from 8.3% to 16.6% duty cycle also demonstrated an overlapping ARC threshold profile. However, the ARC threshold for the transition from 16.6% to 8.3% duty cycle exhibited a unique profile with significantly higher vibration thresholds above 60 Hz. We hypothesized that the observed increase in ARC threshold is due to the combination of increased pinning on the higher duty cycle region (trailing edge – facing the direction opposite of transport) and increased slip (de-wetting) on the lower duty cycle region (leading edge – facing the direction of transport).

To investigate this hypothesis, we recorded the motion of droplets on the 16.6% to 8.3% transition region when driven by vibrations above (8.5 g) and below (4 g) the ARC threshold for this transition at 70 Hz (Figure 5.2). The slip, or the de-wetting distance from maximum to minimum wetting in the first half of the cycle, and spread, the wetting distance from minimum to maximum wetting in the second half of the cycle, of both the leading and trailing edges were measured from these recordings. These measurements indicated that the distance of edge spread during wetting was essentially the same as the distance of edge slip during de-wetting, for both edges, with 4 g vibrations. However, with the larger 8.5 g vibrations, the overall slip of the leading edge was less than its spread, and the slip was greater than the spread of the trailing edge. The average of these differences provides for a net transport of the droplet (Figure 5.2). It is important to note that the average transport (90.8 μm) is less than the distance between the 120 μm spaced rungs on the leading edge but greater than the 60 μm period of the ARCs on the trailing edge. The large standard deviation (41.7 μm) also indicates the droplet does not take the same size step each cycle. For example, the leading edge may advance by one large step (rung) some cycles and zero steps in others, while the trailing edge has a higher probability of advancing by a smaller step each cycle (this effect can be seen in the edge tracking curves - Figure 5.3). However, these step sizes and probabilities ultimately average out and provide for net transport over many vibration cycles.

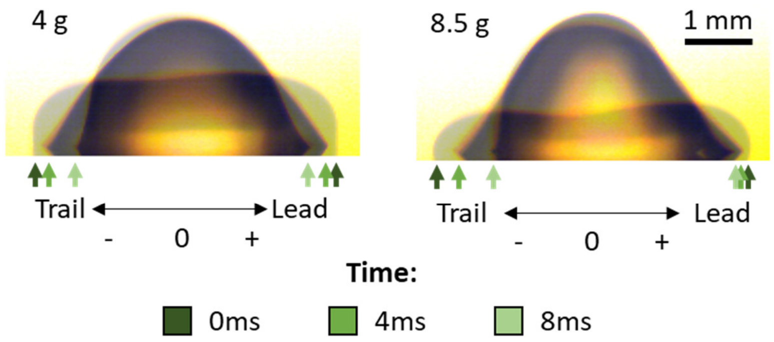

Acceleration Amplitude (g)	**4 g**	**8.5 g**
Leading Edge Spread (µm)	373.6±2.5	305.5±36.9
Leading Edge Slip (µm)	-371.9±4.3	-197.3±35.9
Trailing Edge Spread (µm)	-628.6±7.4	-768.2±27.5
Trailing Edge Slip (µm)	621.6±2.5	841.6±8.9
Net Transport (µm)	**-2.6±6.6**	**90.8±41.7**

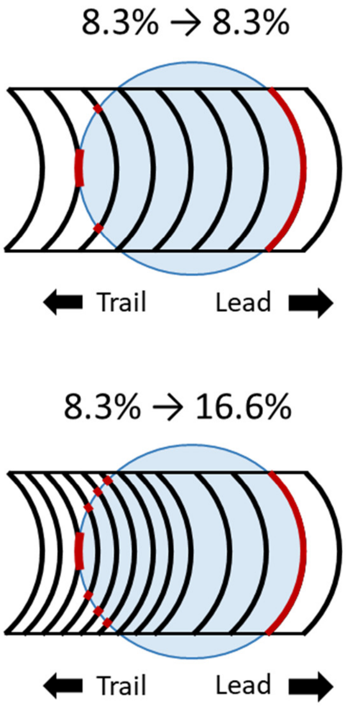

Figure 5.2: Increased trailing edge mobility reduces slip at leading edge. De-wetting sequence (figure overlay) demonstrates the difference in droplet response when vibrated on a 16.6% to 8.3% duty cycle transition at 4 and 8.5 g. Graphics illustrate differences in pinning at the trailing edge between transport on 8.3% tracks and the 16.6% to 8.3% transition. Measurements of droplet edges (table) indicate slip (de-wetting) and spread (wetting) is the same for both edges at 4 g. Raising the vibration amplitude to 8.5 g increased the spread of the trailing edge, but actually reduced the spread of the leading edge. However, this resulted in a lower slip at the leading edge and higher slip at the trailing edge (compared to spread), which provided for droplet transport.

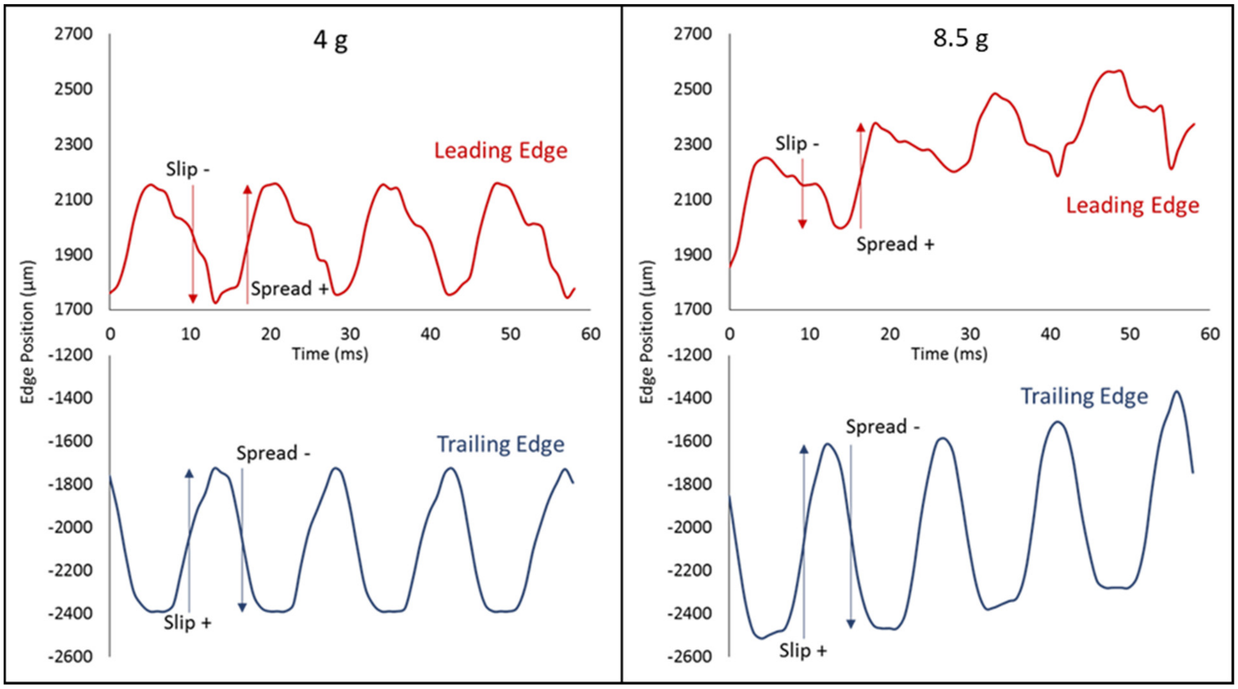

Figure 5.3: Increased vibration amplitude induces droplet transport by increasing mobility of trailing edge. Real-time positions of droplet edges (with respect to the droplet center at 0 ms) at 4 g and 8.5 g demonstrate how these observed differences in slip and spread translate to net transport at 8.5 g. Note that at the leading edge, spread is in the positive direction (direction of net transport) and slip is in the negative direction, conversely, at the trailing edge, spread is in the negative direction while slip is in the positive direction. Additionally, slip is defined as the distance from maximum to minimum wetting, while spread is the distance from minimum wetting to maximum wetting in the next half of the cycle.

We also observed that the total motion of the trailing edge was greater than the leading edge under both vibration conditions. Due to the curvature of the droplet and asymmetry of the ARC design, the pinning on the trailing edge is less than the leading edge during both wetting and de-wetting cycles. Therefore, this anisotropy accounts for the difference in displacement distances between edges. Unexpectedly, the spread (wetting) of the leading edge is actually reduced when the vibration amplitude is increased to 8.5 g. This observance initially seemed paradoxical, as net transport occurs at 8.5 g but not at 4 g. However, the maximum droplet footprint is larger at 8.5 g, as the total displacement of the trailing edge is increased to a larger extent by the higher amplitude vibrations.

The increase of the droplet footprint size in response to a larger vibration amplitude is also consistent with established theory in vibrated sessile droplets.[134,122,124] This observation likely results from the difference in pinning forces acting on the leading and trailing edges, as the increased energy in the larger vibrations is more easily dissipated through movement of the trailing edge (less pinning). This asymmetry indicates that the leading and trailing edges are mechanically linked by internal droplet forces (e.g. surface tension). The subsequent reduction in the slip of the leading edge suggests that the increased mobility of the trailing edge results in a reduction of pinning forces acting against the trailing edge during de-wetting. This change in forces would then be translated to the leading edge, reducing slip as observed in the data.

5.2 ARC Gates

The effects of duty cycle transitions were then employed to enable “ARC gates”, which can selectively pause droplet transport based on the signal of the applied vibrations. Droplet gates were developed by nesting a region with a higher (16.6%) duty cycle within a track composed of a lower (8.3%) duty cycle. Droplets driven by vibrations below the ARC threshold for the gate will pass through the transition from low to high duty cycle but will pause on the transition from 16.6% to 8.3% duty cycle. When the vibration signal is increased above the ARC threshold for the gate, droplet transport will resume (Figure 5.4). Additionally, if a droplet is driven with a vibration above the ARC threshold for the gate before entering the gate, then it will pass through without stopping.

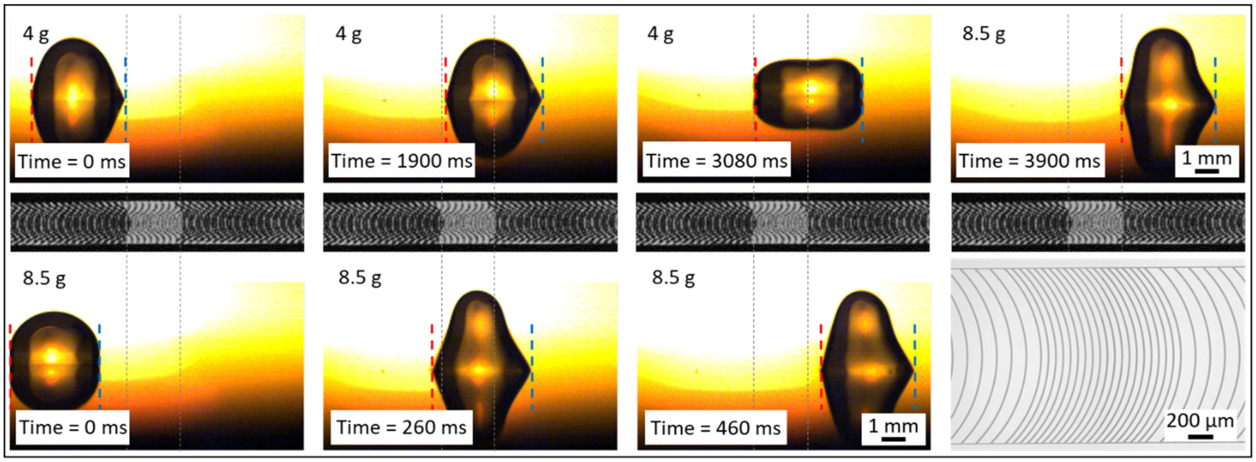

Figure 5.4: Droplet gate selectively passes droplets. Droplets (10 µL) driven with a 70 Hz vibration of 4 g stopped at the gate (design - bottom right) until a vibration of 8.5 g was applied (top sequence). Droplets driven with a vibration of 8.5 g moved through the gate without stopping (bottom sequence). Center panels and gray dotted lines depict the track and gate with respect to the droplets. Blue and red dotted lines depict the leading and trailing edges of the droplets, respectively.

Stopping droplets on an ARC chip was previously achievable by turning off the vibration signal. However, this would stop all droplets being transported on a chip, and selective movement of droplets was only possible if the droplets had different physical properties (i.e. volume).[132] ARC gates provide the ability to pause a single droplet without affecting the transport of other droplets on chip, allowing for a variety of additional functions. For example, Figure 5.5 demonstrates how droplets with unique transport paths can be synchronized with ARC gates. On this chip, three droplets, each on a unique ARC path, are transported by vibrations below the ARC threshold for the gate. The transport of each droplet will be paused once it reaches the gate. This allows for droplets on longer paths, such as the droplet on the left, or droplets that are performing processes elsewhere on chip to continue their transport. Once all three droplets have lined up on the gates, the vibration amplitude is increased, resuming the transport of all droplets in a tight distribution.

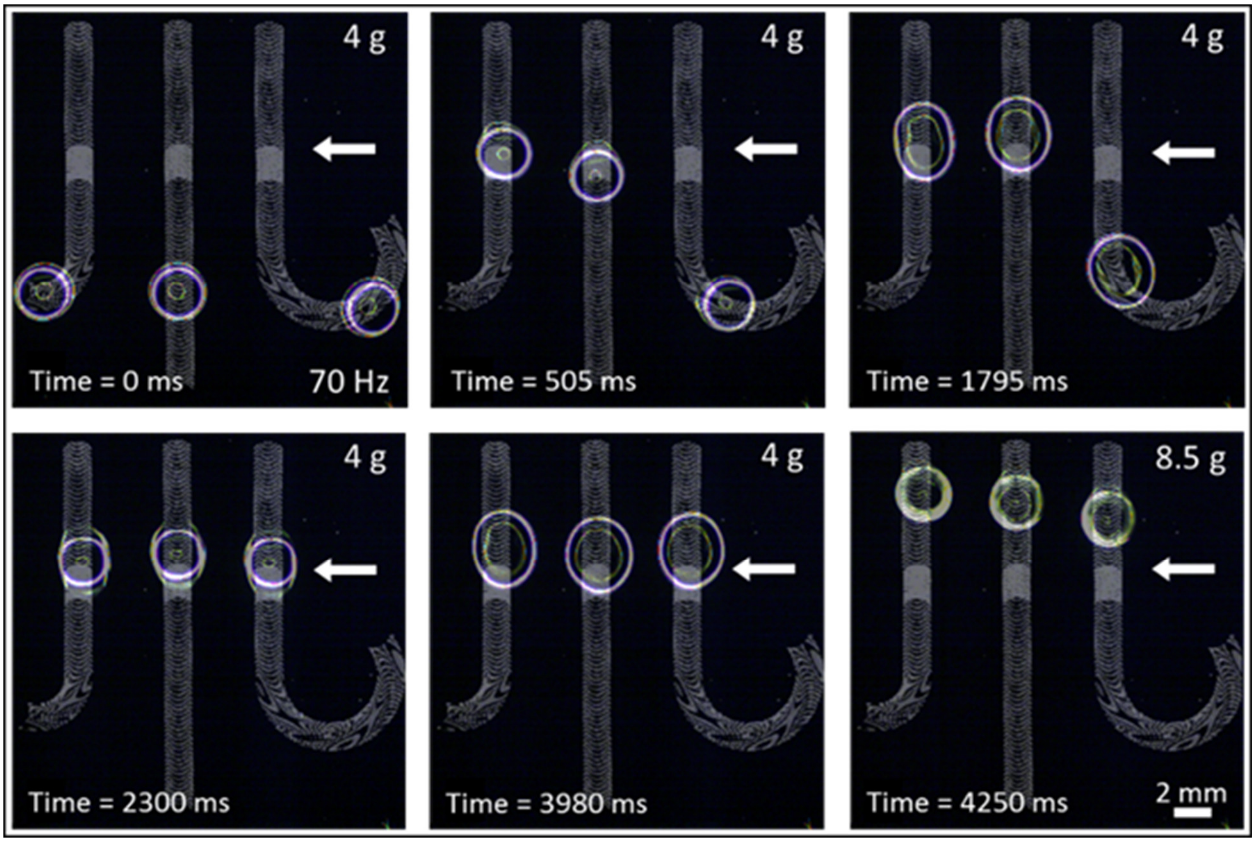

Figure 5.5: Droplet synchronization with ARC gates. Droplets transported on unique ARC paths with vibrations below the threshold of the ARC gate will pause at the transition from 16.6% to 8.3% duty cycle (indicated by the white arrow). Droplets will remain indefinitely at this position in the ARC gate, which allows droplets on all transport paths to line up (ARC patterns are superimposed in gray). Increasing the vibration signal above the gate threshold continues droplet transport in a tight distribution.

In addition to synchronization, these devices can also be applied on an ARC system to hold droplets over a detection region or sensor, controllably mix droplets in the same transport path, and control the timing of a droplet on chip. For example, two droplets can be controllably mixed on ARC gates (Figure 5.6). Without ARC gates, mixing two droplets with the same volume (or physical properties) would not be possible as the droplets would be propelled along the track with the same velocity and the distance between them would never be closed. With ARC gates, the first droplet is paused at the duty cycle transition, allowing the following droplet to advance on and merge with the first droplet. The subsequent droplet can also be held in place as required (i.e. until sufficient mixing has occurred).

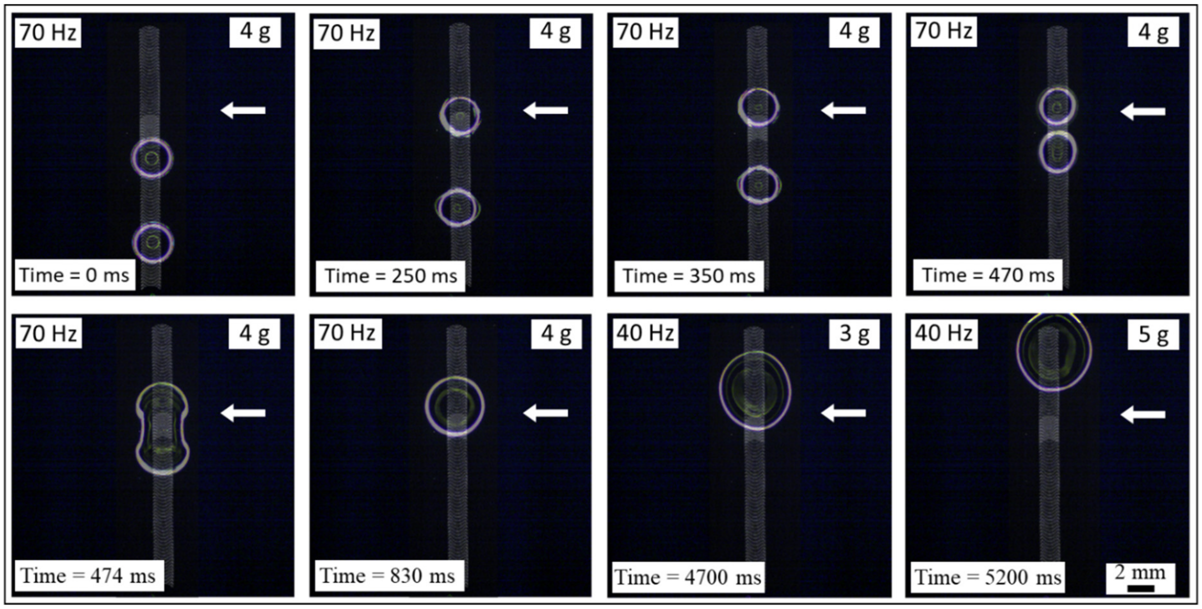

Figure 5.6: Droplet gates can mix droplets of the same volume. Two droplets (10 μL) are transported on an ARC track with a droplet gate. Both droplets are transported, maintaining their initial separation, until the first droplet comes to the droplet gate. The gate holds this droplet in place until the second droplet comes in contact. The droplets spontaneously merge, forming a larger droplet. The larger droplet is then held in place by the droplet gate until sufficient vibration amplitude is applied (5 g). Note that the larger droplet has a lower natural frequency, which requires a lower vibration frequency for transport (40 Hz). The track design is depicted by the overlay (gray) and the white arrows indicate where the transition from the 16.6% to 8.3% duty cycle occurs.

5.3 ARC SWITCHES

A transition in duty cycle changes the balance of pinning forces along one dimension of the droplet (between the leading and trailing edges). To understand how this balance of forces responds to changes in two dimensions, we added a second perpendicular track next to a main track. In this case pinning forces are acting on the leading and trailing edges of the droplet like a normal ARC device, but when the droplet reaches the perpendicular track, pinning forces will also act on one ‘side’ of the droplet. We found this simple combination provides an intersection, or ‘switch’, that can dictate the direction of droplet transport based on the applied vibration signal (Figure 5.7). Previously, switches on ARC devices had been realized through pairing with electrowetting,[77] but the devices presented here are the first to provide the capability of controlling droplet directionality with no active surface components. The threshold profile for ARC switches was determined as previously discussed. However, data presented here describes two thresholds – 1) the vibration required for a droplet to be transported through the intersection on the main track (straight) and 2) the vibration required for the droplet to turn onto the perpendicular track (turn). Expectedly, turning is more efficient when the duty cycle of the perpendicular track is higher than that of the main track (Figure 5.8). The directional thresholds indicate that the increased pinning of the 16.6% perpendicular track induced droplets to turn at the intersection with considerably lower amplitudes than switches with an 8.3% perpendicular track. Interestingly, droplets transported on switches with the 16.6% perpendicular track only turned when vibrations of 60 and 70 Hz were applied. On these switches, turning was also possible with 50 and 80 Hz vibrations, but, for all frequencies other than 60 or 70 Hz, droplets on switches with an 8.3% perpendicular track would rupture or bounce off the substrate before turning. It should also be noted that vibration parameters exist where droplets can both go straight or turn with some probability (e.g. within the standard deviation of the turn threshold). Therefore, it is more accurate to describe these parameters as “having a high probability” of driving the droplet straight through or turning at the intersection.

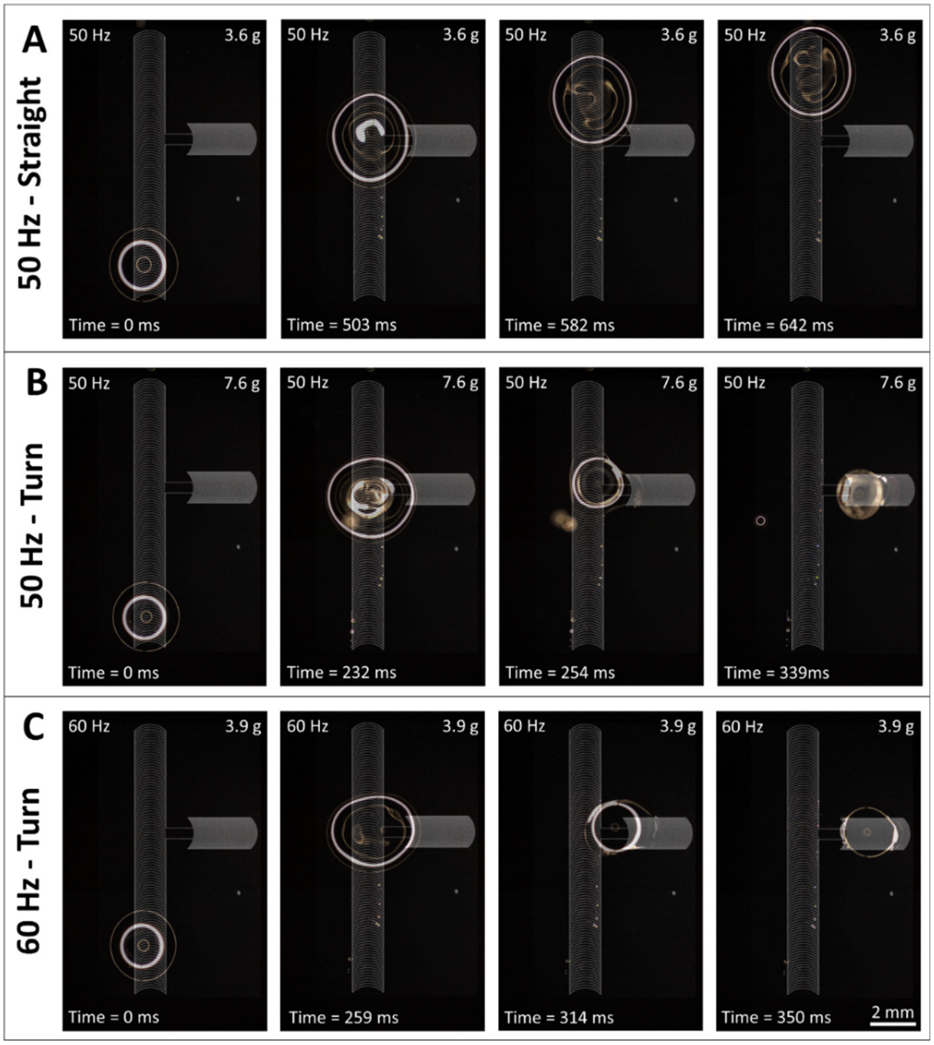

Figure 5.7: ARC switches can select direction of droplet transport. Image sequence shows droplets transported on an ARC switch having a main track of an 8.3% duty cycle with a perpendicular track of a 16.6% duty cycle. Droplets transported at 50 Hz and 3.6 g (A) contact the perpendicular track but move straight through the intersection. Raising the amplitude to 7.6 g (B) reduces the aspect ratio, causing the droplet to turn at the intersection. Vibrations of 60 Hz and 3.9 g (C) also provide sufficient wetting and aspect ratio to turn the droplets at the intersection.

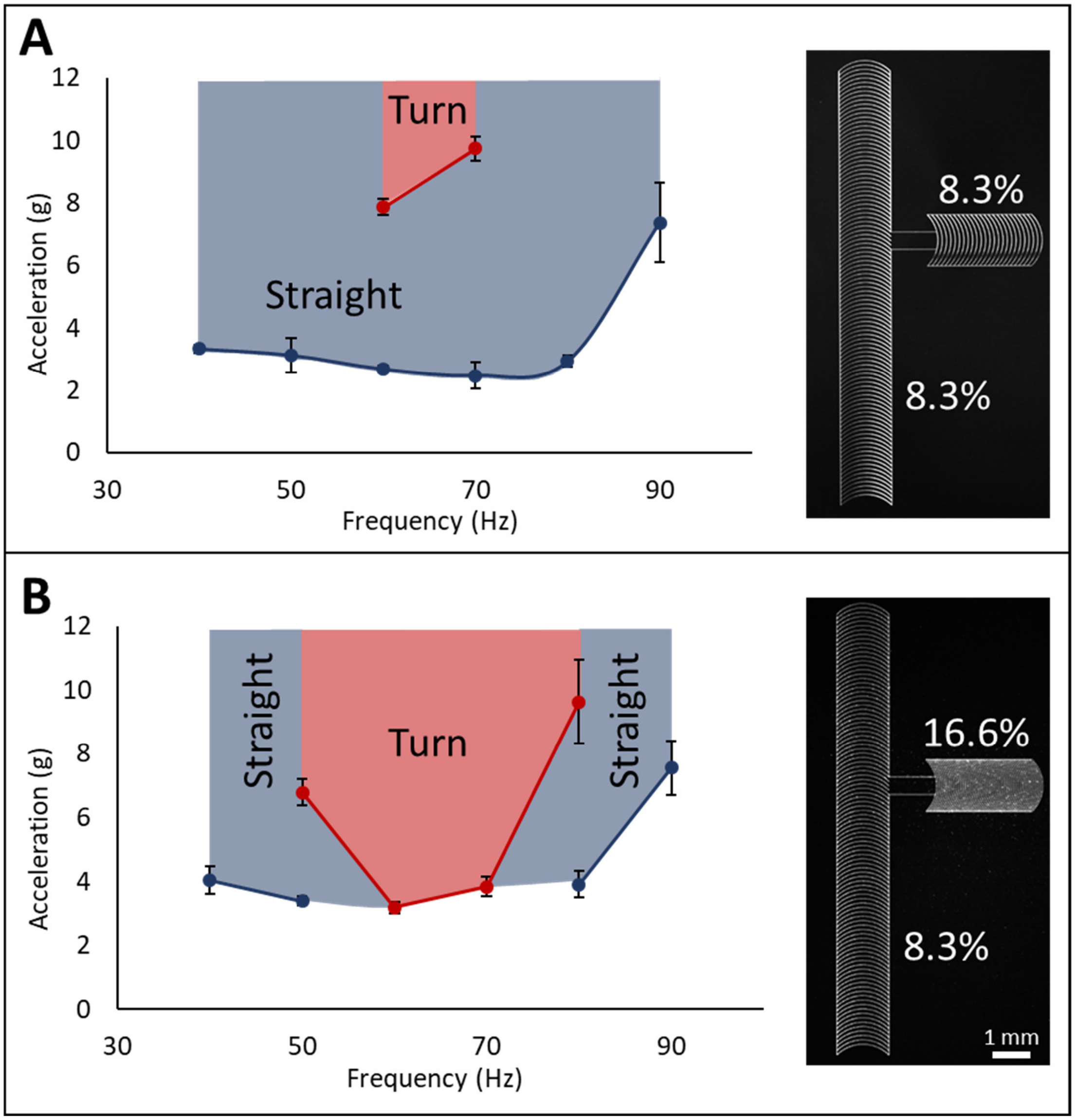

Figure 5.8: Perpendicular intersection enables ARC switch. The ARC thresholds for transporting droplets straight through or turning at the intersection were measured for switches having main and perpendicular tracks with 8.3% duty cycle (A) and a main track of 8.3% with a perpendicular track of 16.6% duty cycle (B). The increased pinning of the higher duty cycle perpendicular track enabled droplets to turn at much lower vibration amplitudes. Light blue regions correspond to vibration parameters that drive the droplet straight through the intersection, while red regions correspond to parameters that turn the droplet at the intersection.

Data gathered from videos of droplets on the switches (shown in supplementary information) also indicate that two conditions must be met for turning to occur. The first condition is that the droplet edges must expand enough to contact the perpendicular track (Figure 5.9). Although this condition is somewhat trivial, it suggests that these switches could innately sort droplets based on volume, as small droplets would be unable to sufficiently expand to contact the perpendicular track. However, the droplet width was large enough to reach the perpendicular tracks when the droplet went straight at 50 Hz. This observation indicates that another condition must be satisfied in order for droplet switching to occur. We also observed that raising the vibration amplitude increased the width of the droplet more than the length. The length-to-width aspect ratio (Figure 5.9B) demonstrates this trend, as this ratio is reduced with increasing vibration amplitude. Through these measurements, we see that a threshold aspect ratio appears to be present for turning to occur, as droplets transported with 50 Hz vibrations require an aspect ratio below 1.05 to turn. Although the spread and slip of each edge was not analyzed here, the observed changes in aspect ratio with increasing vibration amplitude are similar to the results of increasing vibration amplitude on the ARC gate, discussed previously. Meaning that the energy of increased vibration amplitude is distributed through the droplet where pinning is lowest (least resistance on the edges next to the ARC track). Furthermore, the shape of the droplets was always circular or elliptical and the formation of additional nodes was not observed. This indicates that a change in vibration mode[135,126] is not responsible for the droplet response.

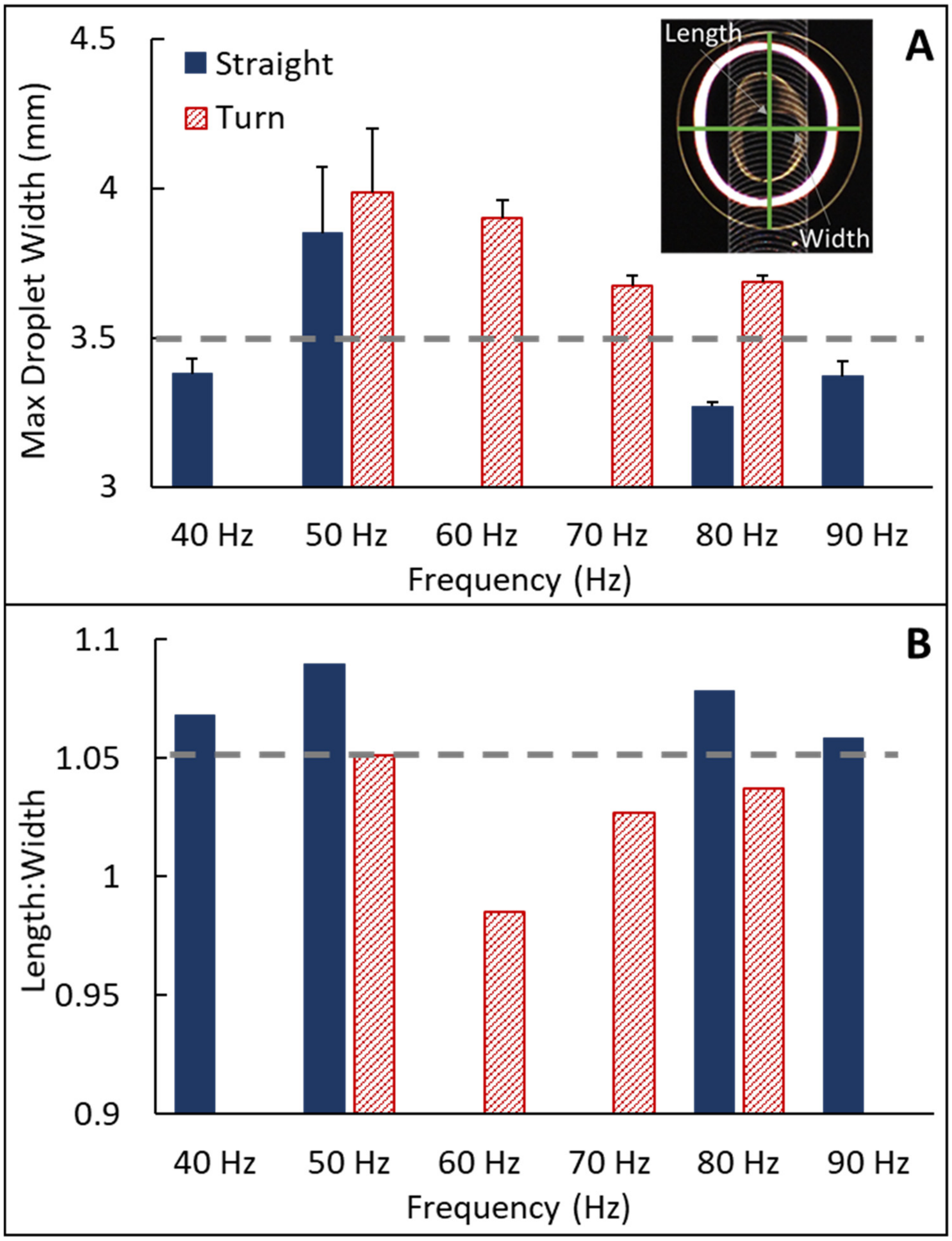

Figure 5.9: Turning droplets depends on droplet width and aspect ratio. The length and width (insert) of droplets during maximum wetting were measured for switches with a 16.6% duty cycle perpendicular track. These data indicate that two conditions must be met for a droplet to turn: the width of the droplet during wetting must be large enough to contact the perpendicular track (this distance is indicated by the dotted grey line - A), and the aspect ratio (B) must be sufficient for pinning forces on the right edge of the droplet to dominate.

This balance of forces is dependent on the ARC design (e.g. duty cycle and spacing) and the parameters of the applied vibrations. Future ARC designs will provide for a larger variety of switch profiles that could present a programmable platform with a high level of droplet multiplicity. The relationship between vibration frequency and the resulting aspect ratio of the transported droplet is not yet well understood but is an observation unique to our ARC platform. Future characterization of this phenomenon could further expand the capabilities of our ARC platform and could improve our understanding of fundamental droplet mechanics.

5.4 DELIVERY JUNCTIONS

Passing droplets from one track to another is an important capability that is necessary for mixing droplets processed on alternate paths or derived from very different sources. However, this function is non-trivial with ARC systems because simply merging two paths can create a local concentration of pinning forces (hydrophilic regions) that can impede transport through these regions (i.e. droplets get stuck). In order to provide this functionality to our ARC system, droplet junctions were developed that can deliver a droplet to an adjacent track without compromising transport of droplets on either track. This was accomplished by connecting the two tracks with hydrophilic guides. The spacing of these guides was adjusted to provide for delivery of a droplet from the terminating track without compromising the transport of droplets along the main track (i.e. if the guides are too close together droplets will get stuck at the junction, but if they are too far apart the droplet on the terminating track cannot be delivered to the main track). We hypothesize that the hydrophilic guides promote delivery from the terminated track by wicking or pulling the droplet edge towards the main track. When paired with the correct vibration signal, pinning forces on the main trail will overtake the droplet from the terminating track. Due to these interactions of droplets from different directions, two thresholds also exist for the delivery junctions: 1) Pass – the vibration amplitude required for the droplet to travel on the main track and pass the hydrophilic guides without getting stuck, and 2) Deliver – the vibration amplitude required to transfer a droplet from the terminating track onto the main track (Figure 5.10). Interestingly, the relationship of the pass and deliver thresholds appears quite similar to that for ARC gates.

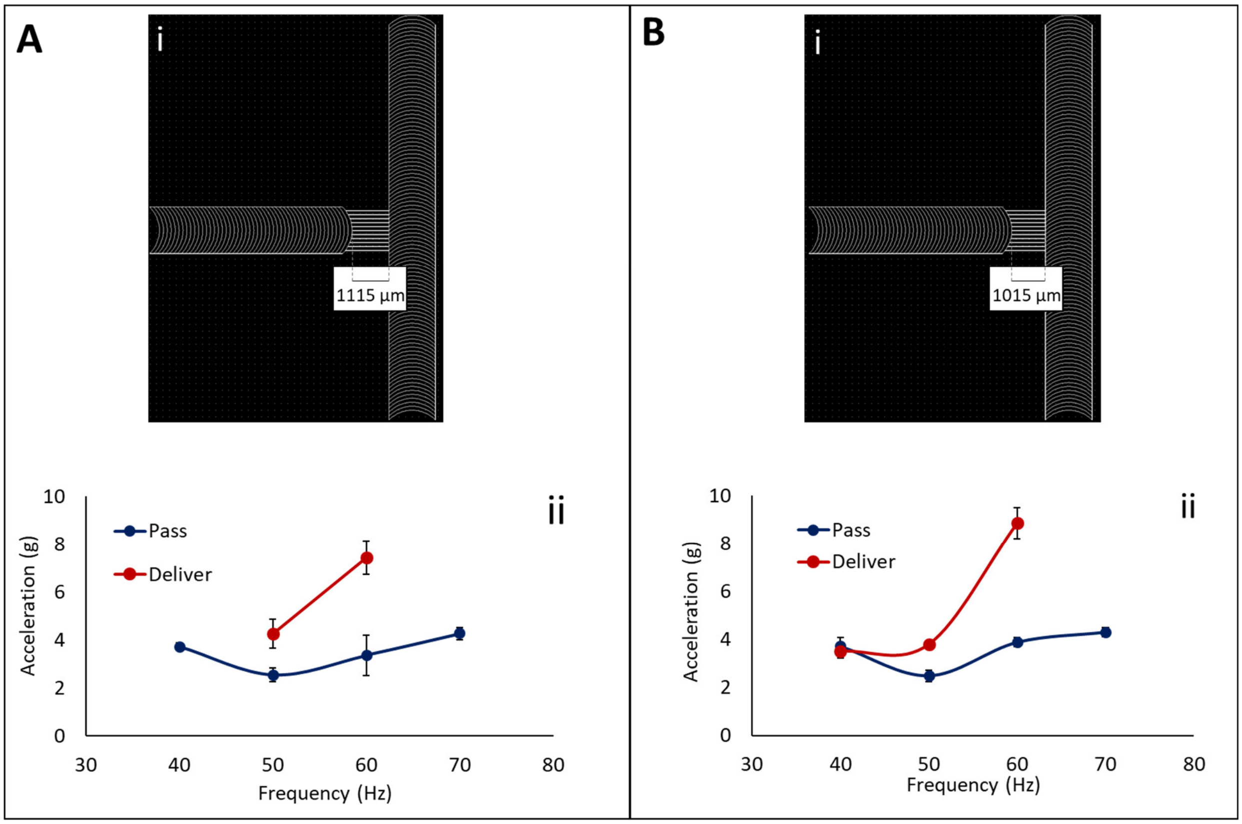

Figure 5.10: Delivery junctions can transfer droplets between tracks without impeding transport. Pass and delivery thresholds for delivery junctions with (A) 1115 an (B) 1015 µm separation between the terminating track and the main track. Thin hydrophilic guides (Ai and Bi) provide connectivity between the terminating track and main track without impeding transport of droplets on the main track. ARC thresholds (Aii and Bii) to pass a droplet on the main track by this junction and deliver a droplet across this junction were characterized for 10 µL droplets.

Additionally, we discovered that these thresholds also provide distinct droplet behaviors when two droplets meet at this junction. Under vibration parameters that meet the conditions for passing the junction but not delivery, a droplet will be held at the junction while the droplet on the main track passes by. The droplets will remain separate, even though they appear to nearly touch, and the droplet at the junction can be later delivered with appropriate vibration signal (Figure 5.11A). However, if vibration parameters for delivery are applied, the droplets will merge at the junction, and the merged droplet will be subsequently delivered to the main track (Figure 5.11B). Thus, this seemingly simple configuration presents a large variety of possible functions that can be performed through strategic selection of vibration parameters.

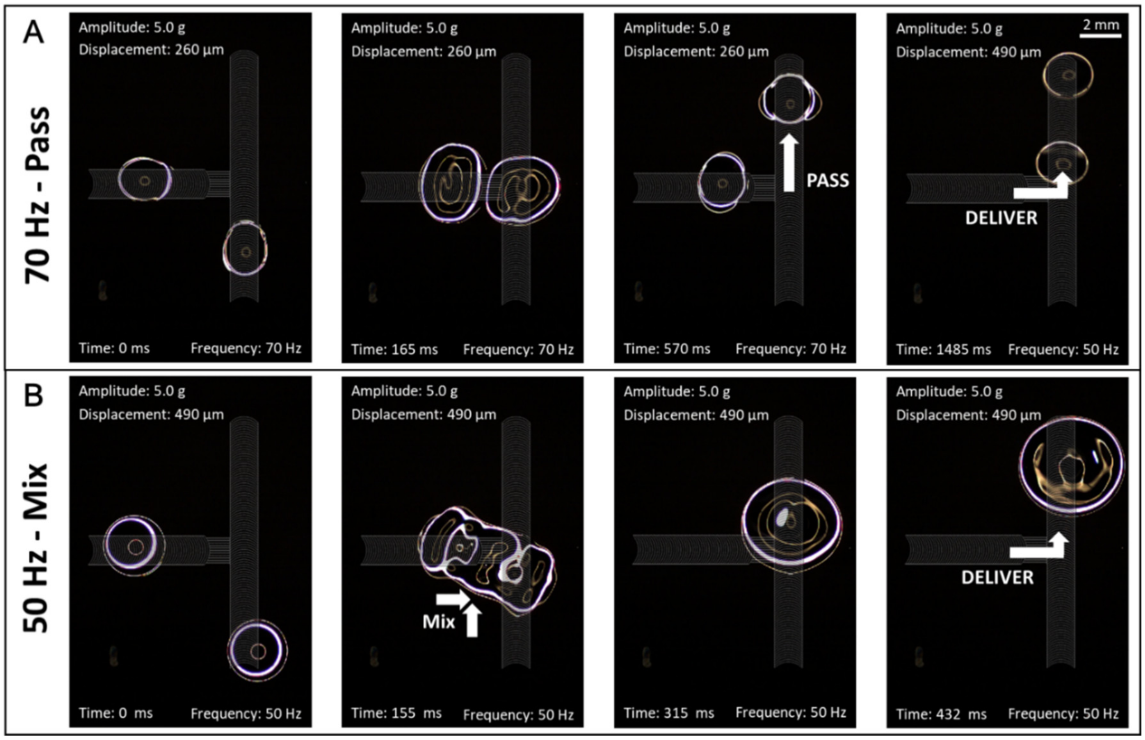

Figure 5.11: Delivery junctions can transfer, gate, and mix droplets. Droplets on a terminated track can be delivered to a main track with a delivery junction. At this intersection droplets can be (A) merged or (B) passed depending on the applied vibration signal. Most importantly, delivery junctions accomplish this functionality without impeding transport of droplets on the main track.

5.5 CONCLUSION

We demonstrate new expansions to the ARC functional toolbox with the development of ARC gates, switches, and delivery junctions. All three modules derive their utility by changing the balance of pinning forces between edges of a transported droplet, either in one or two dimensions. ARC gates can controllably pause droplet transport through an increase in pinning forces at the trailing edge of a droplet, ARC switches provide control over droplet direction at an intersection by applying pinning forces at a side edge of the droplet, and ARC delivery junctions use hydrophilic guides to transfer droplets between tracks without impeding transport. In short, this system combines a simple hardware platform with a sequence of sine wave signals. Expanding on this work, future ARC devices could perform complex protocols that require conditional processing steps, or sequential regimens.

Chapter 6. APPLICATIONS IN CONSERVATION

The work and devices presented thus far have broadened our understanding of droplet mechanics and improved the potential of controlling droplets with ARCs, but the real-world utility of this system has yet to be tested. Using a passive surface to control droplets, the ARC system does not have the level of programmability available to EWOD and would be best suited to a tailored application or regimen, similar to a paper microfluidic device. However, the ARC system is innately more complicated and would not be truly competitive against paper microfluidic devices for ultra-low-cost systems, such as in global health diagnostics. Therefore, in their present state, ARCs would be most suitable for a niche of applications that require better sensitivity or more adaptability than paper microfluidic systems can provide but does not require the level of re-programmability or addressability that is more advantageous to EWOD systems. Such a niche was found in conservation, and a collaboration was formed with Conservation X Labs, a non-profit conservation technology organization. The goal of this collaboration was to create a platform that could perform a rapid DNA test on a sample, in the field, with as few steps as possible, by a nonscientist.

6.1 PRESSING PROBLEMS IN CONSERVATION

Working with collaborators at Conservation X Labs, we identified three critical problems threatening the survival of sensitive species, which require new tools in order to reverse accelerating trends of human-induced extinction. The common fiber between all three applications is a crucial need for a field-deployable method that can rapidly provide a species-level validation or identification to a user with a limited scientific or technical background.

6.1.1 *Critical Problem 1: Wildlife and Timber Trafficking*

Transnational environmental crime is exponentially accelerating the rate of human induced extinction. The illegal wildlife and timber trade market, incited by increasing wealth in emerging economies, now measures in the billions of dollars and threatens the survival of iconic species. Demand for timber and wildlife products has rapidly increased, and has attracted transnational criminal networks who have modernized the illegal wildlife trade, making wildlife trafficking the fourth largest illicit economy in the world.[153] The market for trafficked wildlife has become grossly profitable, with certain wildlife products exceeding the value of gold, platinum, or diamonds in end markets. Such trafficking also undermines the national security of countries, weakens the force of laws, hinders economic development, and promotes massive corruption at all levels of government. The exact cost of illegal logging and trade has been difficult to measure because there are few reliable statistics. In 2012, the United Nations Environment Programme (UNEP) and the International Criminal Police Organization (Interpol) estimated that annual losses globally from illegal logging are from US $30 to $100 billion,[154] an amount equal to 10 to 30 percent of the total global wood trade. The loss of timber can create a cascade of extinctions in other endangered species, such as the Amur leopard and Siberian tiger.[154]

6.1.2 *Critical Problem 2: Seafood Fraud*

Overfishing, particularly illegal, unreported and unregulated fishing, as well as trafficking in marine products from threatened species has become an accelerating driver of species extinction. These activities are disrupting natural communities and depleting innumerable species - some to the brink of extinction. In a fishing industry that is inherently decentralized and global, the act of understanding seafood's origins becomes much more critical. There is evidence that such fraud is widespread and much greater than previously imagined. Oceana, an international non-profit ocean conservation and advocacy organization, conducted a meta-analysis of 67 peer-reviewed studies performed in 20 U.S. states and Washington D.C., and found seafood species substitution averaging 22% but reaching 100% for some products.[155] Oceana also conducted one of the largest seafood fraud investigations in the world to date, collecting more than 1,200 seafood samples from 674 retail outlets in 21 states and found one-third (33 percent) of the 1,215 samples analyzed nationwide were mislabeled, according to U.S. Food and Drug Administration (FDA) guidelines.[156] Another study found that 20-32% of wild-caught imported seafood in the U.S. comes from illegal, unreported and unregulated (IUU) fisheries.[157] Further, there is evidence traffickers are "laundering" (labelling an illicit good as a legal product to bypass enforcement officials) endangered or vulnerable species as more sustainable choices, including sturgeon caviar sold as legal caviar, and bluefin tuna, blue shark, thresher shark, and skate substituted for legal products. Even products with eco-labels are not immune to fraud – some Marine Stewardship Council certified Chilean seabass was mislabeled as sustainable sourced, but was actually derived from other uncertified fisheries.[158]

6.1.3 *Critical Problem 3: Invasive Species Monitoring and Control*

Invasive species, defined here as a nonindigenous species that is widespread and has adverse effects on colonized habitat,[159] can have disastrous impact on invaded ecosystems and the survival of native species. Invasive species are estimated to be the leading cause of extinction for birds and second leading cause of extinction for North American fish.[160] It is estimated that over 50,000 invasive species have been introduced to the United States throughout its history.[161] In addition to threatening native ecosystems and habitats, invasive species are also responsible for an estimated $120 billion per year in the US in damage control costs.[161] While considerable measures have been implemented to combat the introduction and spread of invasive species, successful eradication of an invasive is a Sisyphean battle. Eradication programs must often cover huge areas and sterilize or neutralize virtually every invasive individual capable of breeding without having an adverse effect on sensitive native species in the same area.[162] This effort is incredibly costly, requires careful organization and eradication has really only be truly successful on isolated populations.[162,163] Furthermore, following an eradication, measures must also be taken to insure that the invasive is not reintroduced.[162] Therefore, the most successful strategy for dealing with invasive species is early detection – prevent the nonindigenous species from being introduced or identify and address the problem before the invasion becomes widespread.[162,164,165]

6.2 CURRENT APPROACHES

Identification and screening of illegal timber and wildlife products and seafood are traditionally reliant on visual taxonomic identification.[154] However, this requires highly trained personnel that can distinguish key features of closely related species. For timber, even microscopic analysis by experts can only reliably provide genus level identification.[166] Additionally, many marine and wildlife species are also processed into products (i.e. filets, powders, ground meat, or oils) that further complicate visual identification.

Alternative approaches involve chemical analysis through mass spectrometry,[167–173] near-infrared spectroscopy (NIRS),[174–179] and detection dogs.[180] Mass spectrometry analysis has been proven to be capable of differentiating timber at the species level,[168,173] but there is great variation between individuals of the same species and results can be substantially affected by variables such as climate or nutritional availability.[181] NIRS presents a simple, inexpensive option for screening and is already commonly used for determining material properties of wood,[174,179] but this system also requires a large chemical reference database to be collected. Detector dogs have demonstrated 90% accuracy for distinguishing between two different species, but the dogs require extensive training to reach this point, and it is still unclear how many different types of species even a highly trained dog can distinguish.[180]

Similarly, detection and monitoring of invasive species is typically performed through traditional field studies relying on identification and sampling from visual or auditory encounters.[182] To expand the reach of these techniques, conservationists often recruit citizen scientists, or local individuals that are interested in protecting their natural resources and ecosystems but do not necessarily have technical training. Increased information from citizen scientists can help add to data systems tracking the expanse of invasive species, but the quality of this information has been shown to be only reliable to the genus level.[183]

6.3 DNA BARCODING – THE BARCODE OF LIFE

Traditionally, we define a species as a group of individuals that are reproductively compatible,[184] and historically, species groups were classified taxonomically (i.e. by their physical and behavioral traits, or phenotype),[185] as the field of taxonomy long predates our knowledge of DNA and genetics. However, we now know that a ‘species’ is fundamentally a genetic concept. In 2003, Paul Hebert and his team at Guelph University proposed a method of molecular taxonomy using genetic ‘barcodes’.[186] In this sense, DNA barcodes refer to genetic sequences that are unique to a species, but vary relative little, or are conserved, between individuals within a species group. Therefore, successful species barcodes depend on a divergence gap, or a separation between intra- and interspecies variation within the target sequence (due to similar temporal rates of mutation).[187] Herbert and his group identified the mitochondrial gene, cytochrome oxygenase 1 subunit I (COI) as the best candidate for a universal species barcode for animals (metazoans).[186] The cytochrome oxygenase complex, composed of both mitochondrial subunits (including COI) and nuclear subunits, is responsible for the final step in cellular respiration.[188] As a result, the mitochondrial and nuclear genes must all be compatible or a developmental failure (i.e. hybrid breakdown) will occur. Furthermore, new alleles in nuclear genes are introduced with every generation through sexual reproduction, whereas mitochondria divide asexually and mitochondrial genes typically change much faster than nuclear genes.[188] Therefore, successful divergence, or speciation, within a population is dependent on the adaptation of these mitochondrial and nuclear genes to each other.[188] In other words, COI is regarded as a good barcode or indicator of a species because its divergence rate is similar to speciation rates in metazoans[186], but it is also theorized that the divergence of COI is a driver for speciation within a population.[188] However, while COI is a capable marker for many species, it is not necessarily the best choice for all species. For some species groups, divergences in COI are in regions that are difficult to amplify or sequence and others, such as with Anthozoa or Porifera,[187] divergence rates are too slow to provide sufficient intra- and interspecies differences for reliable identification. For these reasons, alternative mitochondrial genes such D-Loop[189] and cytochrome b[190] are also commonly used genetic targets for DNA barcoding (Figure 6.1).

Similarly, mitochondrial sequences are highly conserved in plants, making them very poor species indicators. However, the survival of plants is not as closely linked to mitochondria as with metazoans but is dependent on a different plasmid – the chloroplast. As such, chloroplast genes serve as a better species barcode for plants, but divergence rates are still slower in chloroplast DNA compared to its mitochondrial counterpart and a single gene has yet to be identified that can provide definitive species identification with the level of near universality as COI.[191–193] Therefore, a combination of barcode genes will likely be necessary to account for all plants, but a few singular chloroplast barcodes can provide reliable species identification within defined use cases. The most common barcode for plants is the chloroplastic maturase K (matk) gene, which can distinguish a large variety of species but is often difficult to amplify and sequence. Therefore, the chloroplastic ribulose 1, 5 bisphosphate carboxylase/oxygenase (rbcL) gene is also commonly used for many plants even though it is more conserved between species.[191–194]

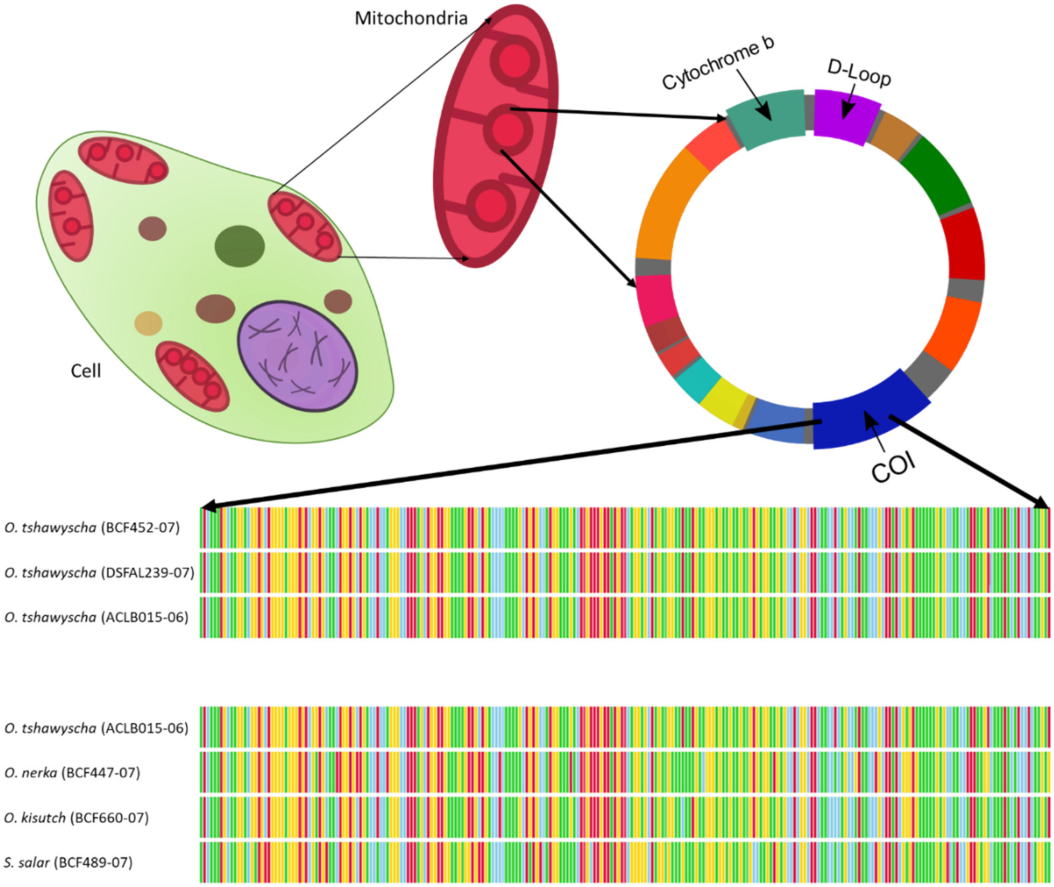

Figure 6.1: Plasmid DNA provides species specific genetic targets. Cytochrome-b, D-Loop, and COI genes in the mitochondria are commonly used barcodes for species identification. A 250-base pair region of COI is identical between individuals of chinook salmon (*Oncorhynchus tshawyscha*) but exhibits a large number of mutations when compared to sockeye salmon (*Oncorhynchus nerka*), coho salmon (*Oncorhynchus kisutch*), and Atlantic salmon (*Salmo salar*).

The work by Paul Hebert and his team lead to the creation of the Consortium for the Barcode of Life (CBOL), hosted by the Smithsonian Institution in an effort led by David Schindel and Scott

Miller. CBOL oversees standards for DNA barcode and the data from these efforts. Barcodes accepted by CBOL are hosted by the Barcode of Life Data Systems (BOLD) at the University of Guelph and available for the international public.[195,196] Following the development of this database, researchers have been successfully using DNA barcoding – the technique of comparing the barcode of an unknown specimen to the barcode references in BOLD, as a species identification tool.[197–202]

The efficacy of using the COI gene to verify marine species has already been demonstrated with a 98% identification success rate,[197] and can provide regional as well as species level identification in some cases.[202] Similar approaches have also been applied to identify timber samples with matK and rbcL.[199,200] However, all of these molecular identification techniques are performed in laboratories with specialized equipment and highly trained staff.[203,204] This approach requires samples to be collected and sent to a laboratory for analysis, during which time any illicit products will have continued along their distribution pathway and will be incredibly difficult to retrieve and connect back to the traffickers.

6.4 VISION: BARCODE IDENTIFICATION TOOL

The time delay for laboratory testing, combined with the limited number of facilities capable of maintaining chain of evidence and providing court admissible evidence, substantially limits the impact that DNA barcoding can bring to conservation efforts. In order for the potential of DNA barcoding in conservation and enforcement to be fully realized, this technique needs to be applied at the first point of interception, preventing illicit or fraudulent products from ever reaching the market. However, translating a technique performed by highly trained personnel in a fully equipped laboratory to a user with a limited technical background in the field presents many challenges. Furthermore, due to the relatively small commercial market that comprises conservationists and wildlife enforcement, this tool must also be scalable to additional markets and applications for such an approach to be sustainable. Therefore, a tool is needed that can provide a clear result, with the highest-ease of use, as rapidly as possible. As a result, this tool will not provide the fidelity of an expertly performed laboratory test but rather enables implementation with a broad user base to maximize the impact of this approach, which can serve as a powerful triage tool for detecting high priority samples.

Based on these requirements, it is unrealistic, if not naïve, to think that a single device could serve as a universal DNA test system for all sample types and all user bases. As such, it is necessary to create a modular platform with an architecture that can accommodate individually modifiable or replaceable components. The key components of the envisioned DNA Barcode Identification Tool (DNA BIT) platform (Figure 6.2) will be a portable driving unit and a disposable cartridge. The driving unit will be composed of a user interface, control hardware (e.g. a microcontroller or microprocessor board with embedded software), and on-board sensors (e.g. GPS, temperature, humidity, carbon dioxide, and pressure) for environmental variables of concern to the sample test or use case. The disposable cartridge will initially be composed of the on-chip sample handling and amplification components described in the proceeding chapter. However, this architecture provides for an extremely adaptable system. While the chemistries for species targets can be exchanged like existing field-ready DNA test systems that use tubes or paper[205], the cartridge format allows for facile integration of future developments in MEMS, micro- and nanosensors, and microfluidic technologies to address additional use cases. Finally, this architecture and approachability to a broad user base allows this platform to serve not only as a screening tool but also as powerful sampling tool – incorporating and organizing metadata from on-board sensors and user input with tests results to create an extensive database.

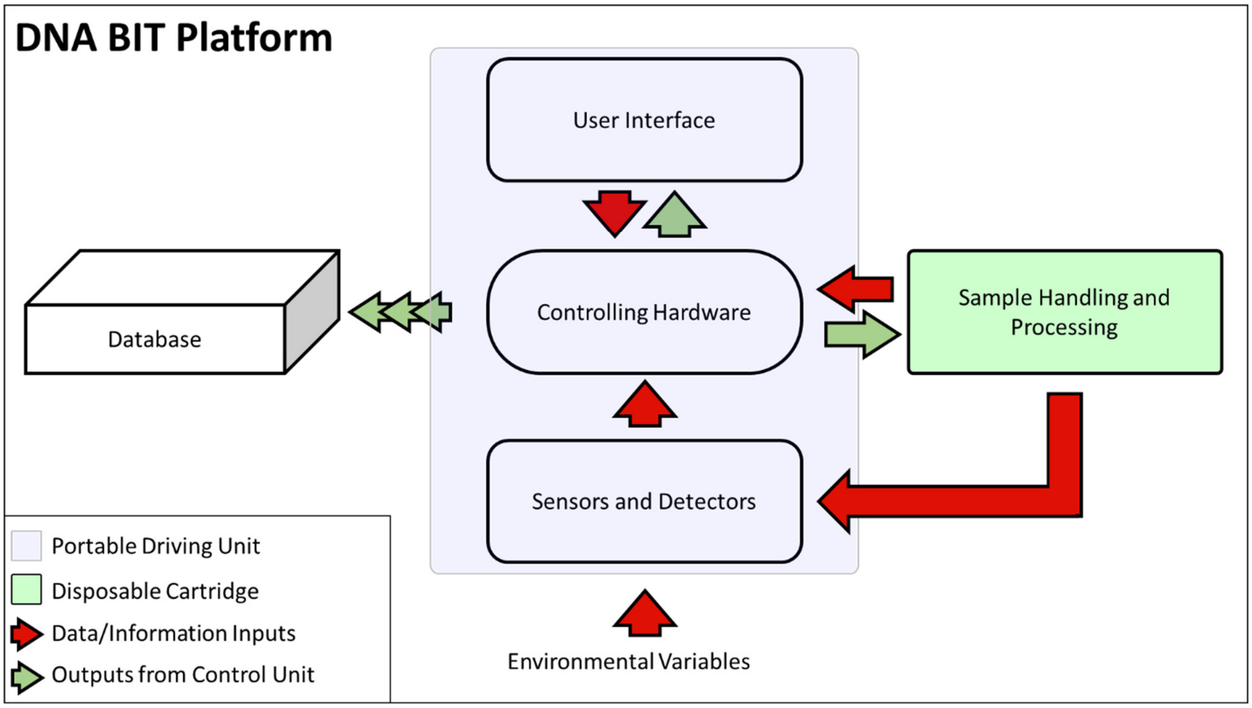

Figure 6.2: DNA BIT architecture. The primary physical components of the DNA BIT are a portable driving unit and a disposable cartridge. The cartridge will handle applied samples and perform the desired tests while the driving unit will control the devices housed in the cartridge, collect data from additional sensors and interface with the users. This format allows metadata from the user and additional sensors to be paired with the result of the test for upload to an organized database.

Chapter 7. DEVELOPMENT OF THE DNA BARCODE IDENTIFICATION TOOL

The goal of this work is to develop a new technology that allows for barcode sequences of timber, wildlife, marine products and environmental samples to be verified upon first contact with law enforcement, customs, or conservation officials. To accomplish this, advances in global health research[205] will be leveraged to enable a point of contact (POC) DNA barcode identification tool (BIT). This device is intended to be a screening tool for conservation. Therefore, the tool does not need to have medical-grade accuracy but must be simple and automated to fit into the process flow of a law enforcement or customs official.

7.1 AMPLIFICATION TECHNIQUE

Currently, DNA barcoding approaches accomplish species identification by processing and amplifying a sample in the laboratory with traditional polymerase chain reaction (PCR) techniques. The amplicons produced from these reactions are then sequenced or measured for fragment length.[206,207] The sequencing reads or fragment analyses are then compared to reference samples to provide a definitive species identification. However, in the field, a definitive species identification is rarely necessary. Rather, users are often more interested in validating the presence of a target species or distinguishing a species from a small number of alternatives. For example, in seafood inspection the user is interested in confirming that the product is consistent with its label rather than determining exactly what species the product came from. Similarly, in invasive species monitoring, a user is more interested in determining if the target species was present or not rather than profiling the entire biodiversity of the sample. Therefore, a qualitative result for target species is sufficient for this application.

This approach allows for the implementation of isothermal amplification. Compared to PCR, which amplifies DNA through a thermocycling process, isothermal amplification amplifies target DNA by maintaining a single temperature throughout the reaction process (Figure 7.1).[208] The thermocycling process in PCR consists of denaturing, annealing, and extension phases. Wherein, the double stranded DNA is first denatured or separated – allowing molecular probes (primers) to access target sequences, the molecular probes then hybridize as the DNA strands anneal back together, and finally a polymerase enzyme extends the 3' end of the molecular probes. The number of target sequences is essentially doubled through each of these thermocycles,[209] exponentially amplifying a target sequence into many identical copies (amplicons). In isothermal amplification, target sequences, or in some cases the molecular probes, are continuously being replicated throughout the entire reaction process. In most cases, isothermal amplification reactions result in a large DNA product, rather than many identical amplicons. Furthermore, because isothermal amplification is continuous and not staged in cycles, the formation of a detectable DNA product occurs much more rapidly compared to traditional thermocyclic PCR.[210] The large DNA products formed during isothermal amplification often allow for detection methods that target the by-products of the reaction, such as hydrogen (pH)[211] or pyrophosphate.[212] These alternative detection approaches, which can be performed with minimal equipment or with the naked eye, have made isothermal amplification methods very popular for use in low resource settings and in point-of-care diagnostics.[146,147] Similarly, the simplicity of a single temperature step, rather than requiring a control system to enable thermocycling, has made isothermal amplification a popular choice for integration in microfluidic systems.[210]

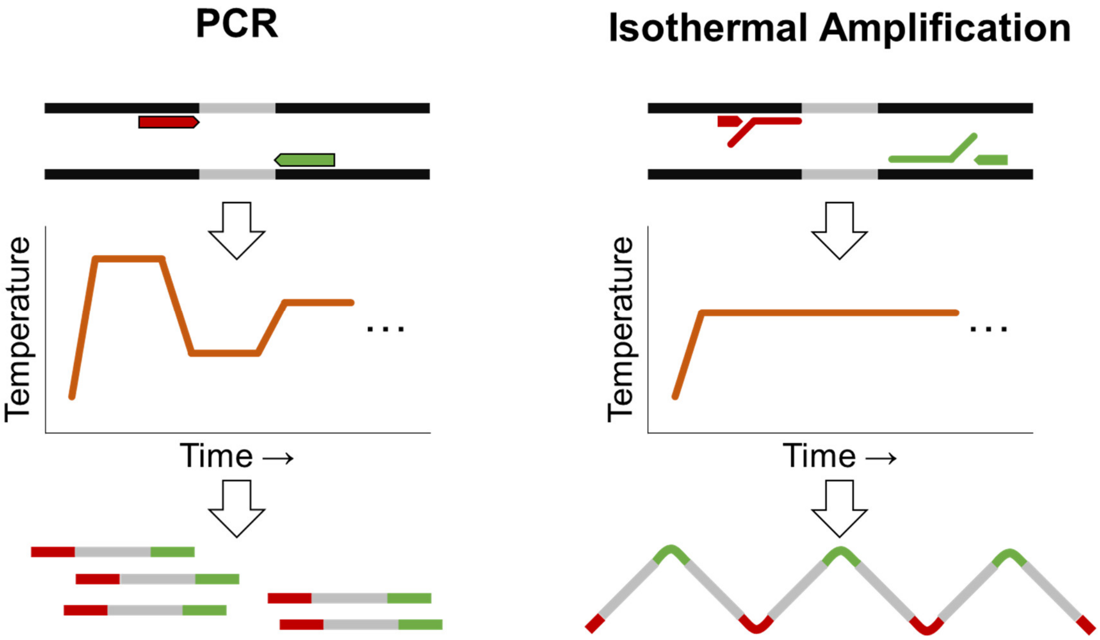

Figure 7.1: Comparison of thermocyclic PCR to isothermal amplification. PCR amplifies DNA through a series of discrete steps, resulting in a large number of identical amplicons. Whereas in isothermal amplification, DNA is being replicated continuously, typically this process produces large DNA products of various length.

While isothermal amplification is distinct from PCR, this method of nucleic acid amplification has been achieved with a variety of different techniques that all have their advantages and disadvantages. This work focuses on the development of molecular probes for an isothermal amplification technique called loop-mediated isothermal amplification (LAMP).

LAMP was chosen as a model amplification technique for this tool because LAMP has one of the fastest reaction times of isothermal amplification techniques, producing detectable product in as little as 15 minutes,[213] LAMP does not require additional enzymes or proteins for the probes to reach their target or require a single stranded target, and LAMP produces copies of the target and regions between the target sequences.[210] LAMP amplification is achieved through the use of four to six primers (Table 7.1) and typically uses a version a *Bacillus stearothermophilus* (*Bst*) polymerase, or similar polymerase with strand displacement that has an optimal efficiency between

60 and 65 °C.[210] The forward inner primer (FIP) and backward inner primer (BIP) are composed of three regions. Regions F2 and B2, on the 3' end of these primers, bind to the sense and anti-sense strands of target DNA, respectively, at complementary sites (F2c and B2c). The regions on the 5' end, F1c and B1c, self-bind to F1 and B1 regions, respectively, once the 3' end of the FIP and BIP is extended, forming a loop structure.[214] The loop region between F2/B2 and F1c/B1c regions is typically composed of a poly-T region or a non-specific sequence. This region provides room for the loop to form, improving the favorability of the F1c/B1c to F1/B1 self-binding. Without this spacing region, the self-binding event would create a lot of strain on loop, ultimately slowing or preventing the reaction.[214] The second primer pair are the F3 and B3 primers, which are much like standard PCR primers. These primers bind to F3c and B3c regions that are behind (in the 5' direction) of the F2c and B2c regions, respectively. Extension of these primers from the 3' end will displace FIP and BIP from their target regions.[214] The final primer pair is optional, but can increase the reaction rate of LAMP for more rapid detection. This primer, LF and LB, binds to the loop region in BIP and FIP primers.[215]

Table 7.1 LAMP Primers and Functions

Forward		Reverse		Function
FIP	F2	BIP	B2	Land on target
	loop		loop	Reduce strain on loop
	F1c		F1c	Self-bind to form loop
	F3		B3	Land on target – displace FIP/BIP
	LF		LB	Land on loop - accelerate amplification

Although there are no cycles in LAMP, as binding and extension will be occurring continuously, the amplification reaction is divided into stages. In the first stage, the F2 region of the FIP primer will bind to the F2c target and the polymerase will extend the 3' end across the F1c, B1, B2 regions and onward along the sense target (Figure 7.2A – note that this step is also happening with the BIP primer on the antisense target).[214] When the F3 primer lands on the F3c region, the polymerase will extend the 3' end, displacing the FIP primer and its extension. This displacement exposes the F1, B1c, and B2c regions, which are identical copies of the corresponding regions on the anti-sense target (Figure 7.2B). This allows the F1c region of the FIP primer to self-bind to the exposed F1 region, creating a loop. The BIP primer is also able to land on the exposed B2c region as well as the B3 primer on the exposed B3c region.[214] Extension of the BIP primer, followed by extension of the B3 primer to displace the BIP, results in a dumbbell structure with two loops (Figure 7.2C). However, one loop on this dumbbell is the complement to the FIP primer and has a 3' end that can be extended, creating a hairpin structure with exposed F2c in the loop (Figure 7.2D). Binding and extension of another FIP primer to this site displaces a strand of this hair pin, allowing the region complementary to the BIP form a loop, terminated with a 3' end (Figure 7.2E). Extension of this end creates two products, one of which will enter a stage wherein binding of FIP or BIP primers will continue displacing and extending these hairpins, creating many cauliflower shaped products of increasingly larger length.[214] The other product is another hairpin structure that after two cycles of binding and extension by the BIP/FIP primers, will create a product that is identical to that in Figure 7.2D.

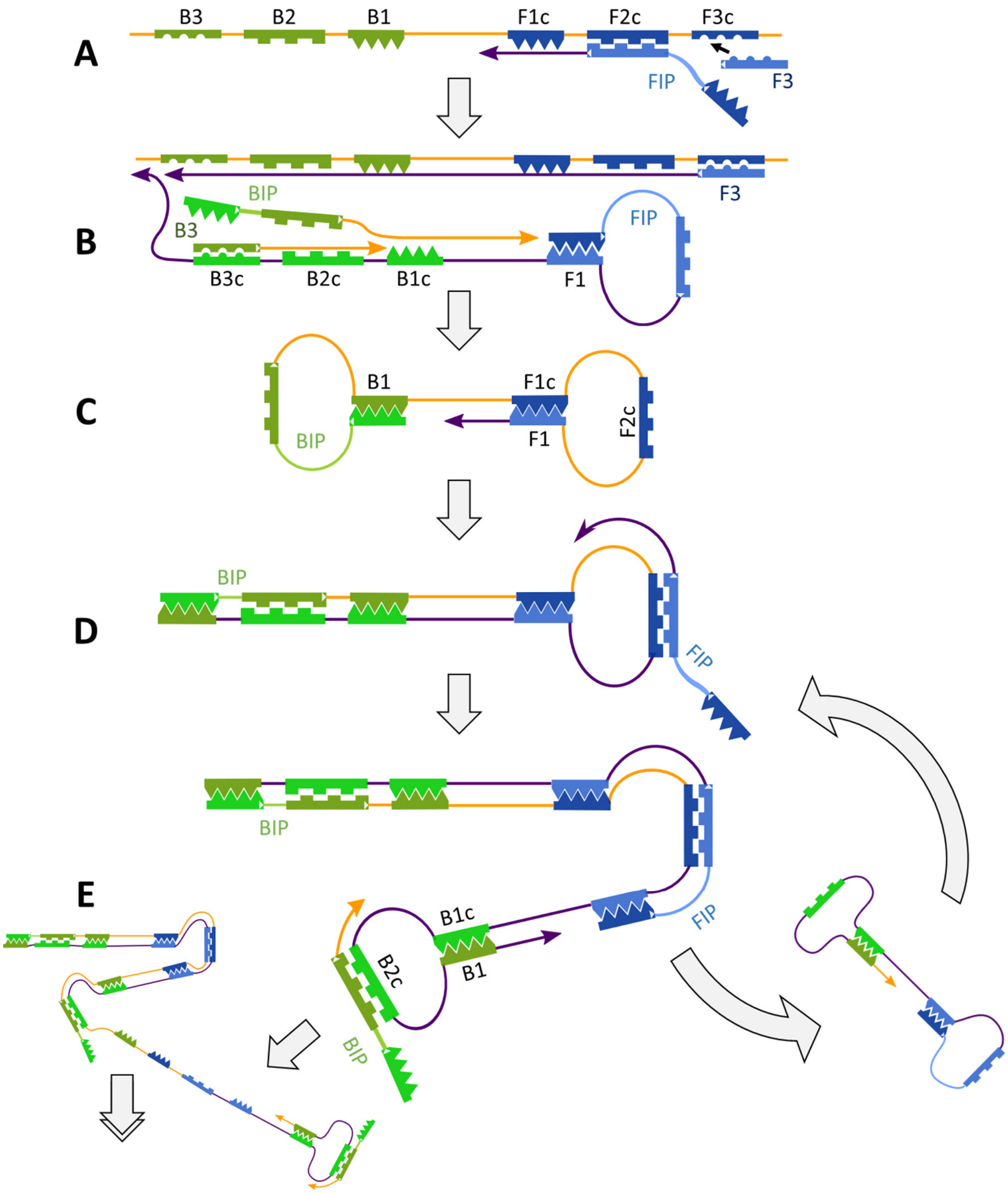

Figure 7.2: Schematic of loop-mediated isothermal amplification (LAMP). Extension of FIP creates a copy of target sense (A), which is displaced by extension of primer F3 (B). Extension of BIP and displacement by primer B3 on the displaced copy releases an oligomer that forms a dumbbell (C). Extension of the F1 end of this dumbbell creates a hairpin with an exposed F2c region (D). Extension and displacement by FIP creates an additional loop (E). This process continues, forming increasingly larger products and small products that repeat this cycle.

In this amplification process, there are six distinct regions (F1, F2, F3, B1, B2, and B3) that must be present in a sample target in order for amplification to occur, compared to the two regions that are necessary for amplification in PCR.[214] However, the *bst* polymerase exhibits a lower fidelity than the *Taq* polymerase typically used for PCR.[210] This results in increased likelihood of errors in the amplified products.

For the purposes of qualitative species test, the specificity must come from the primers and no sequencing is necessary. As the user will likely want a result as fast as possible, the advantages of LAMP outweigh the disadvantages, and this amplification method is a very promising approach for species identification in conservation. Furthermore, LAMP reactions have been shown to be more robust than traditional PCR under certain conditions,[216] and LAMP tests have already been developed for point-of-care diagnostics, demonstrating their ability to perform outside the laboratory in field conditions.[217–219] These additional characteristics are particularly attractive for the sample types and conditions likely to be encountered in the field.

7.2 SAMPLE TYPES AND TARGETS

The first step of any DNA test is to extract DNA from the sample. While many standardized DNA extraction methods have been developed, almost all of them require some form of specialized laboratory equipment to provide amplifiable DNA.[220] The challenges of getting amplifiable DNA can also come in the form of entrapment, inhibition, or a combination of both. For many samples the target DNA is enclosed within the cell, contained within a cell membrane or cell wall. For some samples this physical barrier can be extremely difficult to disrupt, particularly without damaging the target DNA. This problem makes the collection of amplifiable DNA from samples with low template or potentially degraded template, like timber, especially challenging.[221–224] Inhibitors slow or prevent an amplification reaction and originate from the sample itself or from the chemicals and equipment used during the DNA extraction process.[225] For example, many timber and soil samples contain phenolic or polyphenolic compounds that are known inhibitors[223,226], and compounds like ethanol, isopropanol, sodium hydroxide commonly used for DNA extractions have also demonstrated inhibitory effects.[227] Overcoming inhibition is a difficult challenge because inhibitors come in many forms and act through a wide variety of mechanisms. Inhibitors can bind, degrade or denature the DNA polymerase, or alter the ion composition of the solution.[228] These effects often reduce the amplification efficiency of the reaction and can be identified by noting the amplification rates of a real-time PCR reaction.[229,230] Inhibitors also bind or degrade template DNA,[228] which causes the copy number to appear lower than what is actually present or push the number of amplifiable targets below the detection limit for the reaction.[229,230] With these considerations in mind, it becomes obvious that an extreme range of heterogeneity will exist among all the possible types of samples that will be encountered in the field. Therefore, it is important to understand the level of difficulty that extracting amplifiable DNA from a potential sample will incur, particularly when developing a device meant to perform this amplification in the field. For simplification, sample types have been classified as DNA-Ready, DNA-Confined, and DNA-Locked (Figure 7.3). DNA-Ready describes the easiest use case that can be encountered wherein the DNA is already exposed and few inhibitors are present in the sample. This type of sample is most similar to a DNA extract that would be obtained after a laboratory extraction process. Samples collected for environmental DNA (eDNA) analysis,[231–233] or from carefully collected swabs[234] can also provide target DNA that does not require further sample preparation. DNA-Confined samples refer to a majority of samples that are likely to be encountered. This classification describes samples of whole cells that contain DNA within intact membranes or thin cell walls. Therefore, the DNA must be liberated through a cellular lysis process. Samples in this group will also likely contain a variety of inhibitors that require some processing but can be separated or purified with known techniques.[228] DNA-Locked is the classification of samples that is the most difficult to acquire DNA from. For samples in this group, DNA is bound or entrapped in thick cell walls, dense tissue, or surrounded by a plethora of inhibitors. DNA is very difficult to extract from dense tissue (pulverization, such as with ivory samples,[235] is often used as a pre-treatment for DNA extraction). Inhibitors from samples in this group are also extremely challenging to deactivate or separate. As such, for some samples that would fall in this group, like timber from tropical hardwoods,[223] there are still no laboratory techniques that can provide amplifiable DNA.

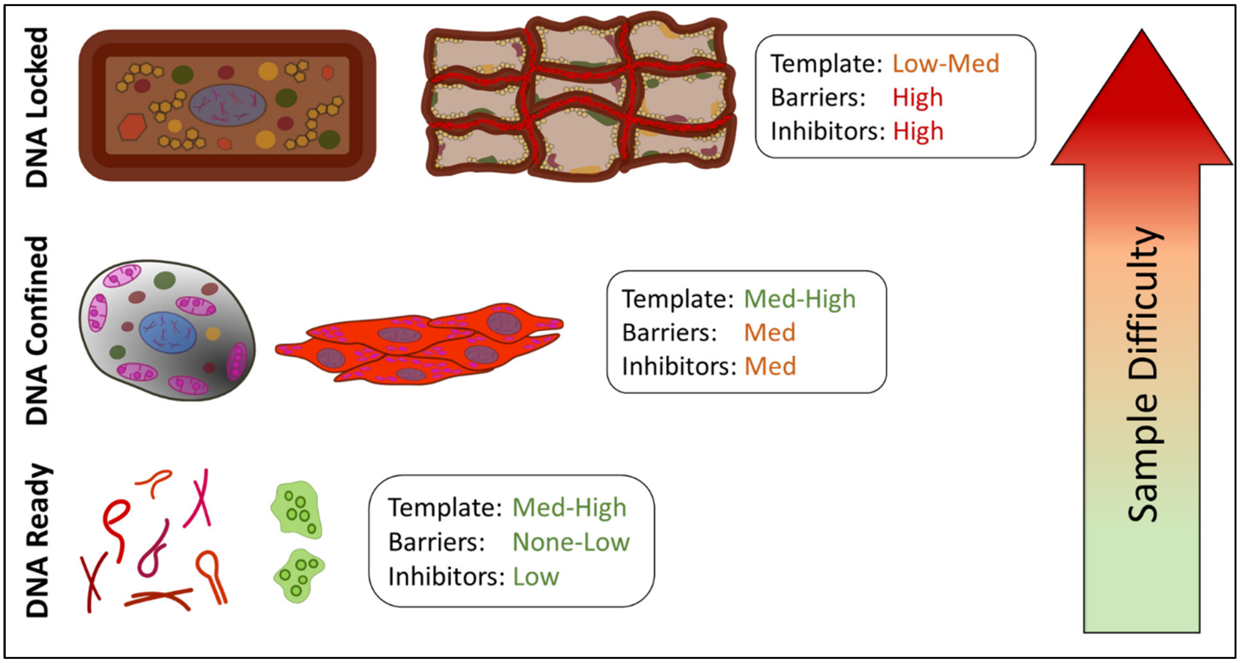

Figure 7.3: Classification of sample types. Sample types that are commonly encountered by conservationists and enforcement officials were broken into DNA-Ready, DNA-Confined, and DNA-Locked groups based on the difficulty of acquiring amplifiable DNA from a sample.

Looking at the sample types from this viewpoint, it was determined that DNA-Locked samples still required a fair amount of basic science research to identify more accessible methods of providing for DNA extraction. Therefore, this work looks to develop a system that can enable a test for DNA-Confined samples by applying established methods of DNA extraction and purification to an on-chip platform. As such, successful amplification on this platform can also be applied to DNA-Ready sample types.

7.3 INITIAL PROTOTYPE

The first step in the development of this tool was to design the chip that would be used to perform the test. The initial design employed two ARC tracks connected by a delivery junction. One ARC track would terminate at a hydrophilic zone on top of a microheater. The second ARC track would be separated from the microheater by a delivery junction. With this configuration, a sample droplet would be placed on the track connected to the microheater and a buffer droplet would be placed on the track connected to the delivery junction. The sample droplet would contain a sample with target DNA that could be extracted and purified with thermal lysis and the buffer droplet would contain the polymerases and other temperature sensitive reagents necessary for LAMP. Therefore, the regimen of an automated test would be 1) Transport sample to heater, 2) Lyse sample at 95 °C, 3) Reduce temperature to 65 °C, 4) Deliver buffer with reagents to sample, initiating LAMP (Figure 7.4).

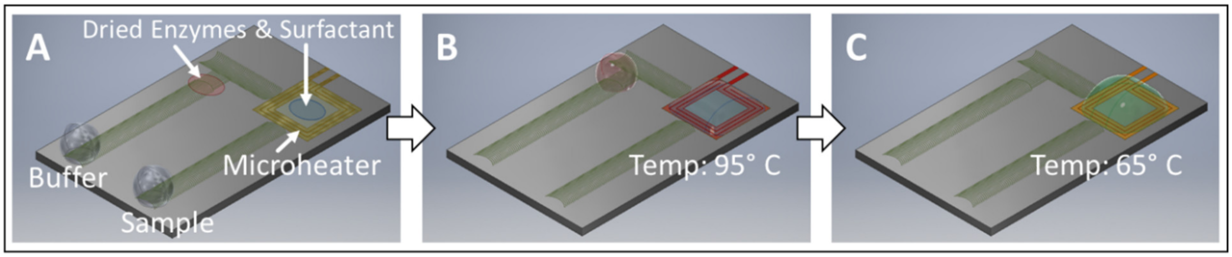

Figure 7.4: DNA BIT chip prototype schematic. (A) The ARC chip is composed of the ARC pattern (green), microheaters, and dehydrated reaction components. (B) One droplet transports the sample to the microheater for lysis. Another droplet reconstitutes thermally sensitive reagents (e.g. enzymes and molecular probes) at the delivery junction. (C) After lysis, the second droplet is transported across the junction to deliver reagents for isothermal reaction.

The chip fabrication is performed on glass wafers, providing for a transparent window to facilitate optical detection. Additionally, glass is a superior thermal insulator to silicon, which will better isolate high-temperature regions spatially when the microheaters are operated. Specifics on the fabrication of these chips is provided in Appendix A. In a field-ready version of this chip, surfactants, lysis enzymes, and components that are not temperature sensitive will be lyophilized over the microheater while polymerases and other reagents that will be degraded or denatured by the thermal lysis will be lyophilized over the delivery junction.

7.3.1 *Portable Driving Unit*

A field-deployable system must be taken out of the laboratory. While all previous characterizations and demonstrations of ARC transport was performed on a large linear electric motor in the laboratory, it was necessary to demonstrate that the droplet can be driven with a portable system. A driving unit was developed based on a DC solenoid that was controlled with an Arduino Uno (Figure 7.5). The voltage supplied by the Arduino signal is not sufficient to actuate the solenoid on its own, so an N-channel metal-oxide-semiconductor field-effect transistor (MOSFET) is used as a precision switch to connect the power supply directly to the solenoid. The signal from the Arduino is thus applied to the gate of the MOSFET, metering power to the solenoid in pulses of the desired frequency. With this configuration, the waveform delivered to the solenoid is in the shape of a square wave. However, the spring in the solenoid acts like a low-pass filter, smoothing the wave and delivering a sinusoidal waveform (characterizations of these waveforms are shown in Appendix E). A housing unit for the electronics and solenoid and a cradle to hold the chip was 3D printed (Figure 7.5B). ARC chips inserted into the cradle can be operated with the Arduino controlled solenoid (Figure 7.5C).

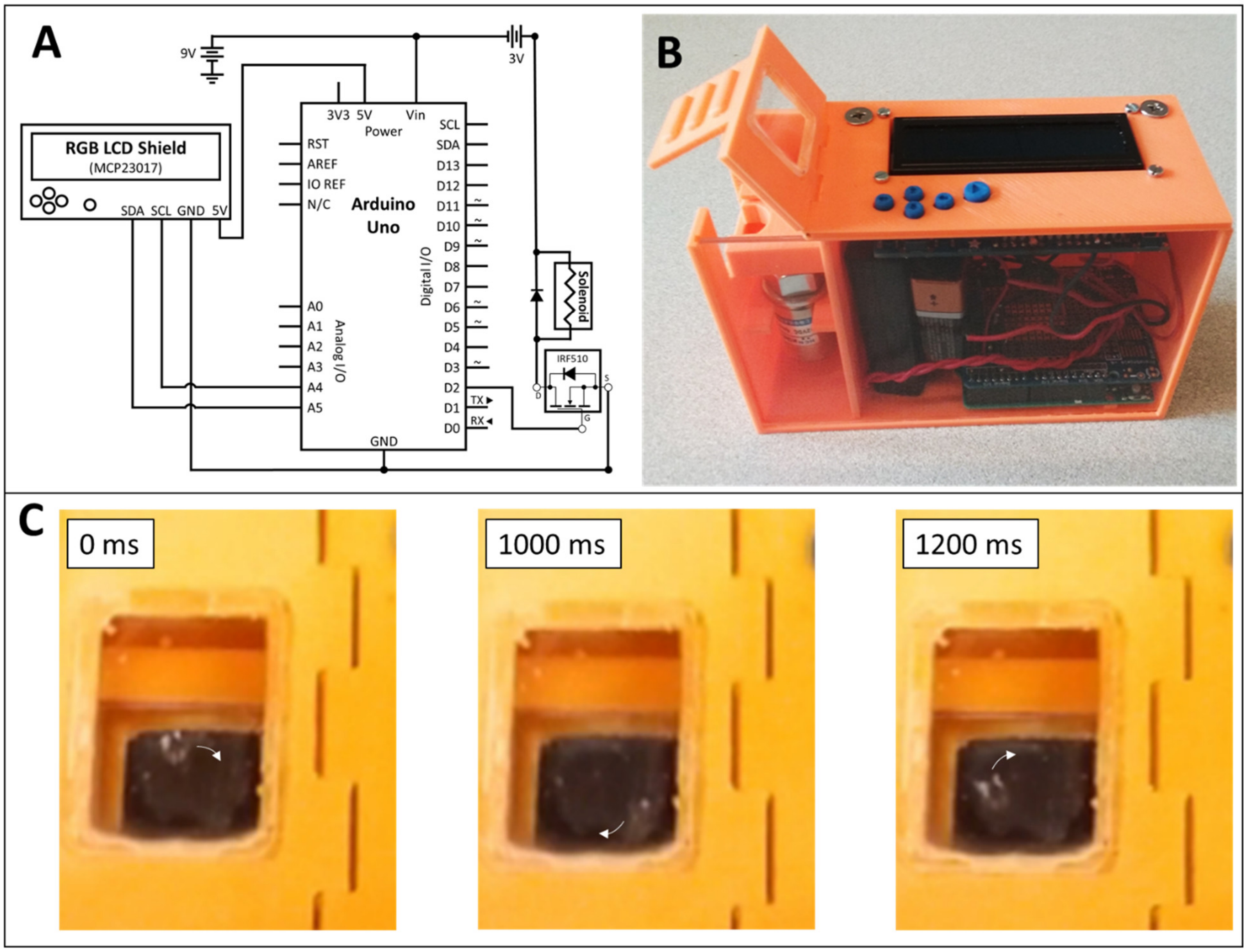

Figure 7.5: Portable driving unit. Circuit schematic shows the configuration used to drive the solenoid with an Arduino Uno. The requirement of only a single pin to operate the ARC device allows for future integration of many more components on this platform (A). A 3D printed casing houses the electronics, supports the solenoids, and provides a cradle to connect ARC chips to the solenoid piston (B). Droplets are driven on a circular ARC pattern with the portable driving unit at 50 Hz (C).

7.3.2 *Microheater optimization*

Microheaters are composed of molybdenum with a thickness of approximately 350 nm. Multiple designs of the microheater were examined to optimize the efficiency of the system. In this case, a balance between power consumption and voltage must be carefully considered. Reducing the amount of material reduces power consumption, but also increases the resistance of the microheater. When resistance is increased, a higher voltage is required to conduct sufficient current through the device to hit target temperatures. At a certain point, the required voltage will be too high for a portable device to be practical.

Designs evaluated here consisted of thick (250 µm width) and thin (25 µm width) leads that formed the microheater through a single (short) or triple (long) winding (Figure 7.6). The short thick microheater exhibited the lowest resistance and required the lowest voltage to hit the temperature targets. Conversely, the long thin heater exhibited the highest resistance and required the highest voltage to hit the target temperature. If the microheater was the only component of this system, it would be expected that the short thin microheater would be the most power efficient, as it would be the smallest amount of the resistive heating material that is required to be heated. Consequently, the long thick heater, with the largest mass of molybdenum, would be expected to be the least efficient. However, in this case the microheater must also heat up the entire region of glass about which the droplet will be present. The mass of this glass will remain constant, regardless of the microheater design, and the glass will also be cooling to the outside environment. As such, it was discovered that both thin heaters and the thick long heater all exhibit similar power efficiencies for heating the system to the lysis temperature of 95 °C and the LAMP reaction temperature of 65 °C. However, the short thick heater had a slightly higher power consumption than the other three, particularly at the higher 95 °C temperature target. Interestingly, the heater that was expected to be the least efficient exhibited the same efficiency as the heater expected to be the most efficient. This effect is likely due to the surface area of the heater offsetting the cooling rate of the glass chip.

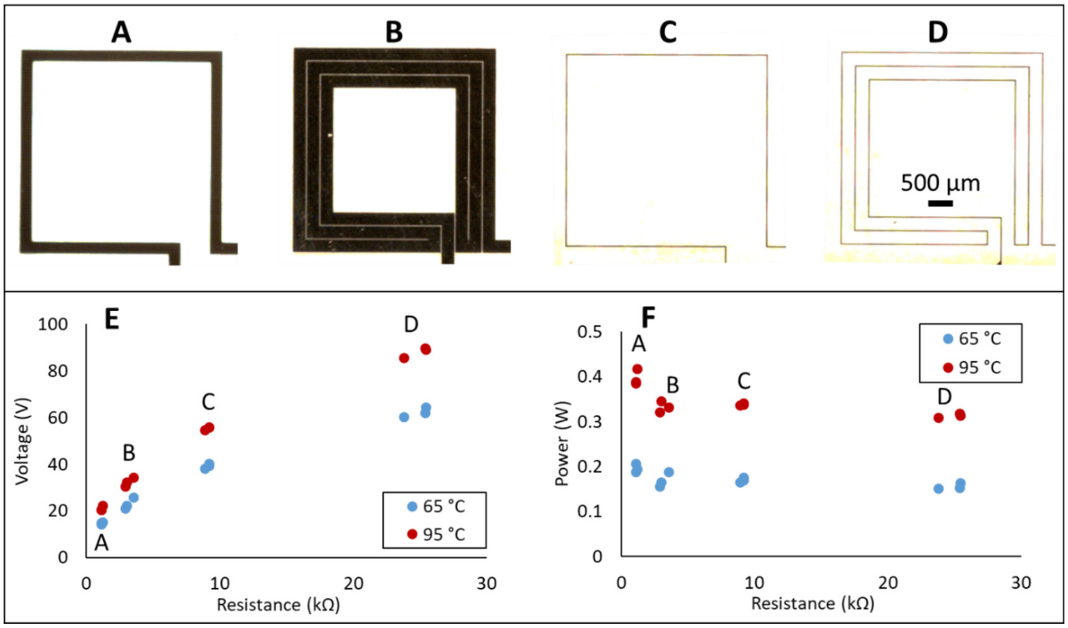

Figure 7.6: Microheater design and performance. Thin-film (350 nm) molybdenum microheaters with a width of the 250 µm (A, B) and 25 µm (C, D) tested for voltage (E) and power consumption (F) required for heating glass substrates to 65 and 95 °C. While voltage was a function of resistance, power consumption was similar for all heaters except the short thick heater.

Although the thin heaters would be more efficient on their own, a similar amount of energy must be delivered to them in order to maintain the temperature of glass regions not covered by the heater traces. Continued optimization could further improve the efficiency of the heaters, the performance of the long thick heater was suitable for the goals of this work and decided on as the model heater for use in subsequent experiments.

Thermal images of the long thick microheater at target temperatures show that the glass substrate also provides sufficient insulation to isolate the higher temperature region around the heater (Figure 7.7). Localizing the temperature increases the efficiency of the system, but, more importantly, insures that temperature sensitive enzymes lyophilized on the droplet junction will not be exposed to higher temperatures during sample lysis.

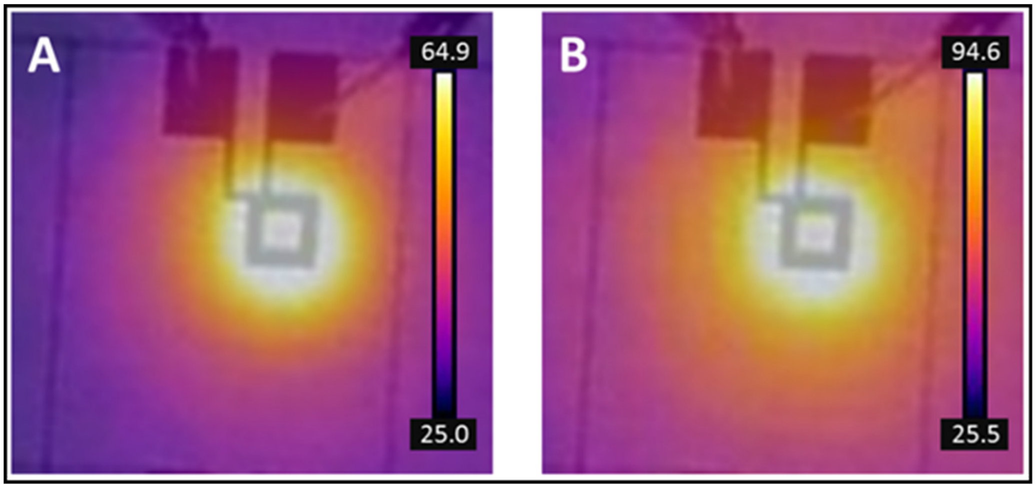

Figure 7.7: Microheaters in glass produce isolated thermal gradient. Heating to (A) 65°C and (B) 95°C provides a temperature gradient with high-temperature regions isolated around the microheater. Microheater image is superimposed on thermal image.

Power consumption measurements also indicate a routine isothermal test (5-minute lysis and 20-minute amplification) will consume 0.30 Wh. This is on the order of the power consumed by a cell phone screen on low brightness and will allow for an average of 30 tests to be conducted with a commercial 9V battery on a single charge.

7.3.3 *Chip Performance*

The chip design shown in Figure 7.4 was fabricated with an integrated microheater with the glass substrate. This chipset demonstrated that the device performed as predicted – the ARC tracks could transport water droplets and the delivery junction properly gated and delivered droplets to the microheater (Figure 7.8). The microheaters also exhibited the same performance as characterized in Figure 7.6 and Figure 7.7. While these measurements demonstrated that the chip met key performance goals, it was yet to be shown that this system could ultimately provide for isothermal amplification.

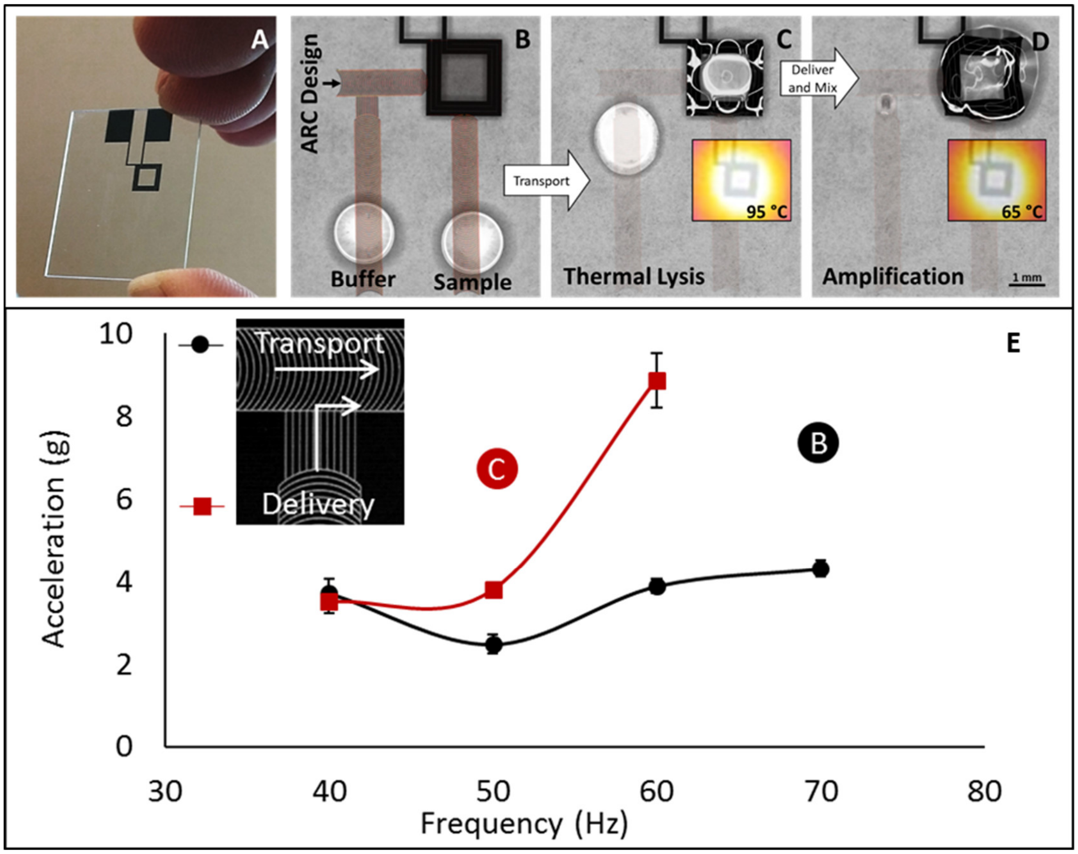

Figure 7.8: Delivery junctions enable process regimen. Two droplets are (A) transported towards the microheater, but one is (B) held at the junction until the (C) vibration signal is changed to deliver the droplet across the junction and merge with the droplet on the microheater. Junction characterization (D) shows transport and delivery thresholds for 10 µL droplets. The dots indicate the vibration parameters applied when images B and C were acquired. Design overlay depicts superimposed image of photoresist. Error bars indicate ± standard deviation.

7.4 DROPLET HEATING

The fundamental driver for isothermal amplification is a stable temperature within the functional range of the polymerase (about 60 to 68°C for *bst* and LAMP). Therefore, the thermal profile of the droplet must be within this range, preferable with a narrow tolerance, when heated by the microheaters. While measuring the two-dimensional temperature profile on a chip is manageable with a thermal imaging camera, determining the three-dimensional temperature profile of a heated droplet empirically is much more challenging. Therefore, a finite element model was created to predict the temperature uniformity of droplets heated on chip. The effects of convection were applied to this model by determining the heat transfer coefficient at the air water interface. This coefficient was derived from the Nusselt number of a droplet in an air.[236,237]

$$Nu = 2.0 + 0.6Pr^{1/3}Re^{1/2} = \frac{HD}{k} \qquad (7.1)$$

In Equation 7.1, Pr is the Prandtl number (the product of specific heat capacity and dynamic viscosity divided by the thermal conductivity of the fluid - $C_p\mu/k$) and Re is the Reynold's number (the product of the velocity and contact length divided by the kinematic viscosity of air - VD/v). H is the heat transfer coefficient and D is the diameter of the droplet and k is the thermal conductivity of air (0.02 W/m·K).[238] In our case, with droplets heated on a static surface, the velocity of air moving across the droplet is assumed to be zero or near zero, and the component with the Reynold's number drops out. This leaves us with a very simple equation to determine the heat transfer coefficient of a static droplet in ambient air. However, this coefficient is dependent on the size of the droplet (Table 7.2).

Table 7.2: Heat transfer coefficients of droplets

Droplet Volume (µL)	***H* (W/m²·K)**
5	18.85
10	14.96
25	11.03

This model demonstrates that the small droplets reach the target temperature within about 30 seconds, but larger droplets take about a minute to equilibrate. Small droplets also show a more uniform temperature profile, with the entire volume of 5 and 10 µL droplets within 3 degrees of the target temperature, while less than 50% of the larger 25 µL droplet is within 5 degrees of target temperature (Figure 7.9). However, this model does not account for the effects of Marangoni flows[239] or contact angle hysteresis[240] that occur in response to droplet heating and it is still unclear what fraction of a droplet must be at the target temperature to enable amplification.

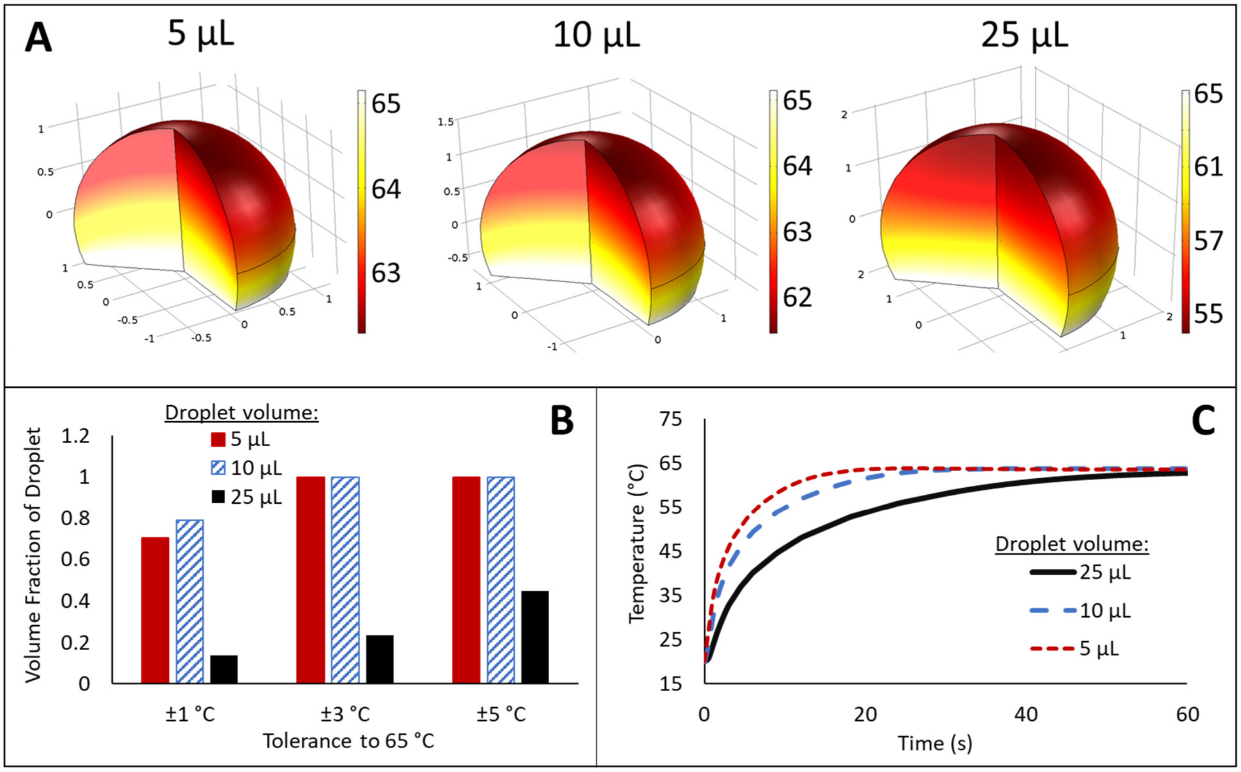

Figure 7.9: Temperature profile is less uniform for larger droplets. Finite element models for temperature profiles of 5, 10, and 25 µL droplets (A) show that smaller droplets exhibit a tight temperature tolerance when heated, but only a small volume fraction of larger droplets stays within the target temperature range (B). Smaller droplets also reach equilibrium more rapidly when heated (C).

Furthermore, these models do not account for evaporation, which is a critical concern for heating droplets in this open configuration. Anecdotal evidence of droplets at room temperature suggested that this evaporation rate was slow enough that sufficient volume would be maintained long enough for a 15 to 20 minute reaction. While quantitative measurements of this evaporation rate confirmed this observation for droplets at room temperature, they also showed that evaporation rates for heated droplets are far too high for a reaction to occur on this time frame (Figure 7.10).

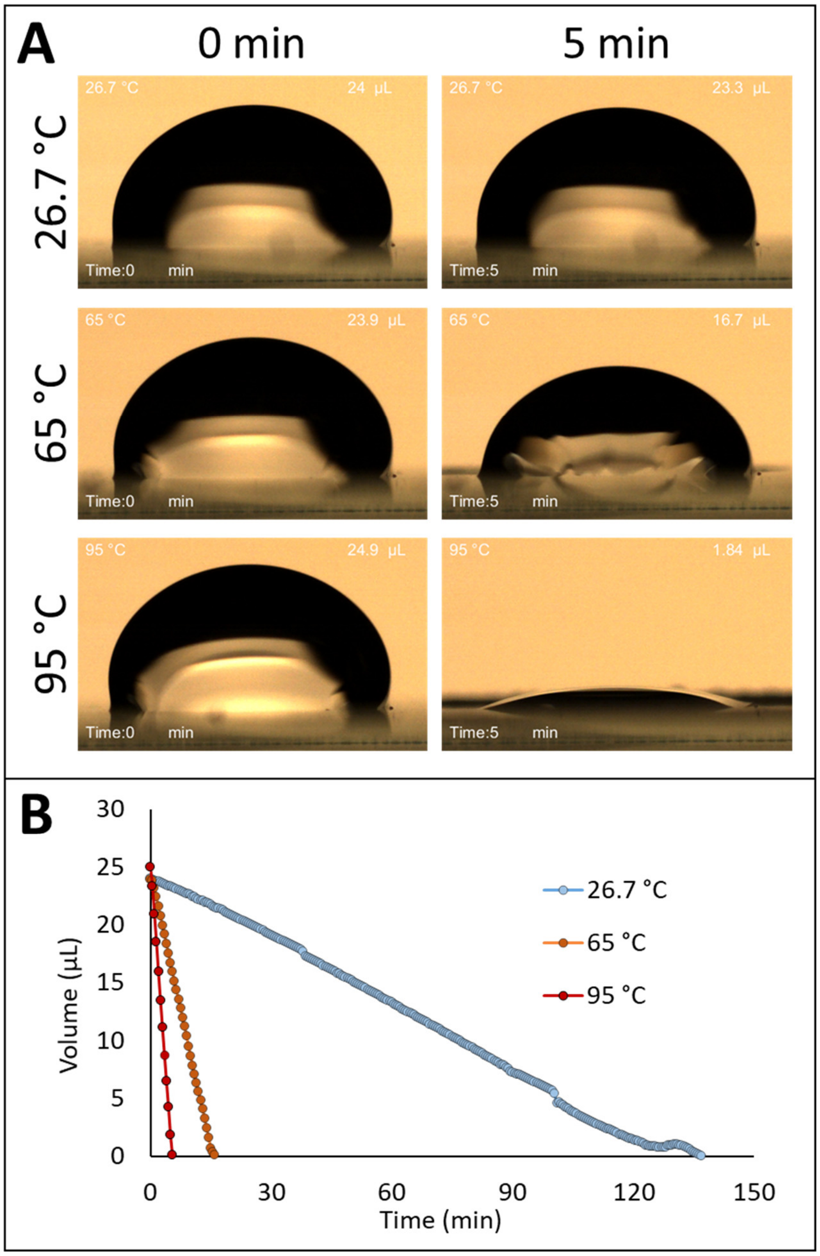

Figure 7.10: Evaporation rates of heated droplets. Time-lapse frames demonstrate how heating at 65 and 95 °C affects droplet volume compared to room temperature (A). While the volume of droplets at room temperature persists for almost two hours, droplets heated to 65 or 95 °C are completely evaporated within 15 minutes.

7.5 TOP-PLATE CHARACTERIZATION

Droplet heating measurements demonstrated that additional measures must be taken to sufficiently reduce evaporation rates to enable an isothermal amplification. However, the addition of a top enclosure to slow evaporation rates will likely contact the top of transported droplets. In order to understand how this confinement affected ARC transport, a 3-D printed fixture was constructed to hold two chips with a known separation.

The ARC threshold required to initiate transport was characterized as described in Chapter 3 and the transport of droplets in the set-up was also recorded. The configurations used in this test consisted of the ARC pattern on bottom and hydrophobic coating on top (ARC-FOTS) and the ARC pattern on both top and bottom (ARC-ARC). Separations of 2 and 2.5 mm were also used for both of these configurations with 8, 13, and 18 µL droplets (Figure 7.10). Measurements of 8 µL were only recorded with the 2 mm plate separation because 8 µL droplets did not contact the top plate when separated by 2.5 mm. Qualitatively, droplets transported in this configuration appear more 'pillar' like, with leading and trailing edges on both plates and a liquid node oscillating back and forth between the two plates. ARC threshold measurements demonstrate that droplets transported in the two-plate system require a larger vibration amplitude for transport at low frequencies, but at the upper end of the functional frequency range of the open plate system, a cross over occurs and the two-plate system becomes more efficient (Figure 7.10).

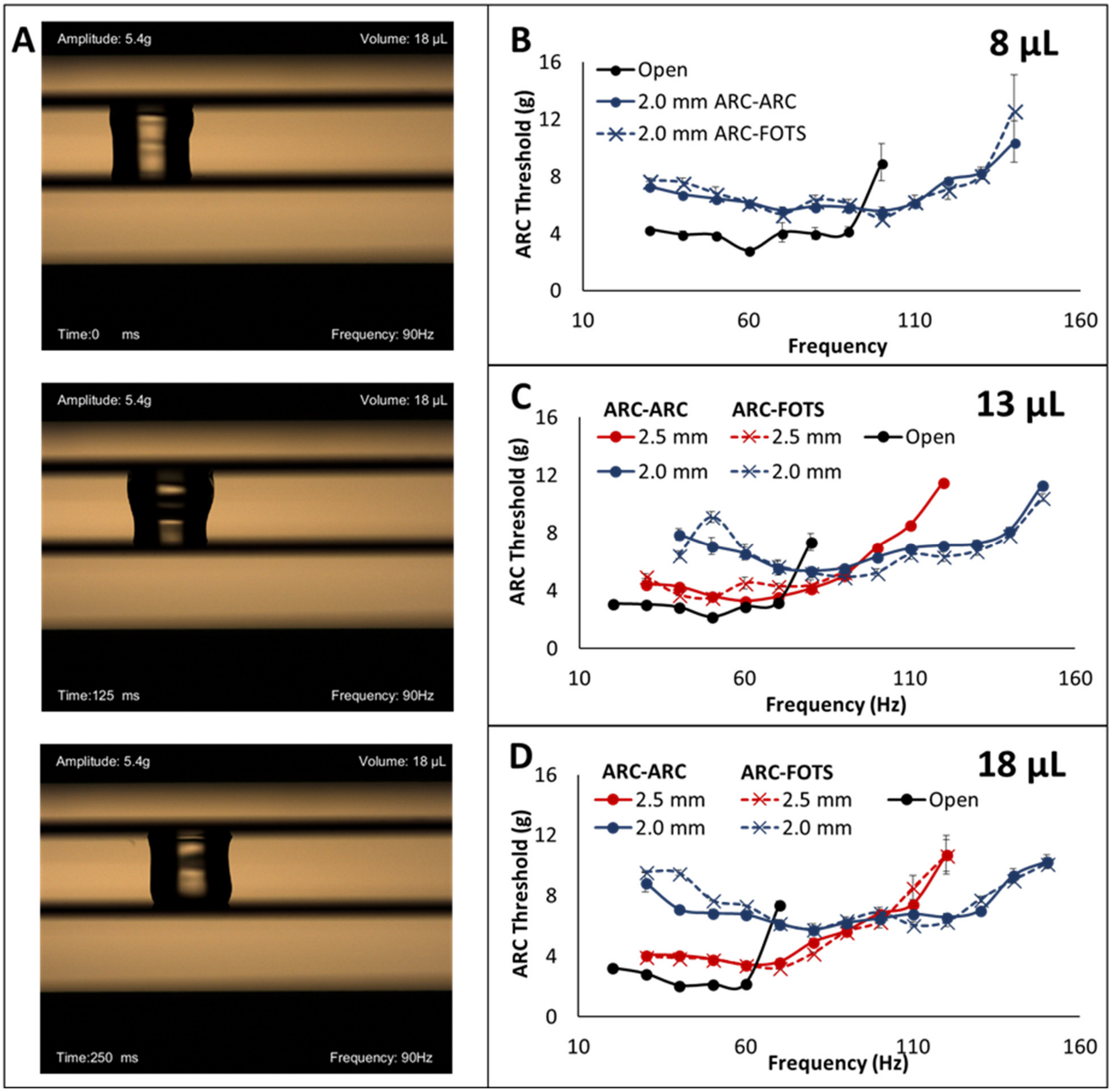

Figure 7.10: ARC threshold is dependent on separation distance with a two-plate system. Droplets transported between two plates (A) exhibit a higher ARC threshold at low frequencies, but lower ARC threshold at higher frequencies, as well as a larger functional frequency range (B-D). This trend also repeats as the separation distance between plates is reduced. These observations are consistent for both ARC-ARC and ARC-FOTS configurations and all droplet volumes.

The functional frequency range for the two-plate system is also much broader than that of the open system. As the separation distance is reduced, a similar trend occurs – the ARC threshold is higher at low frequencies but crosses over near the end of the functional frequency range of the two-plate system with a larger separation. While droplets appeared more stable with the ARC-ARC configuration (de-pinning from the top plate was observed during some vibration cycles with the ARC-FOTS system), no quantitative difference in performance was observed.

Interestingly, transport on the top plate system also appears to be independent of droplet volume (Figure 7.11). Plotting these measurements on the same axes shows aligned ARC threshold profiles extremely similar to the results of non-dimensionalization described in Chapter 3.

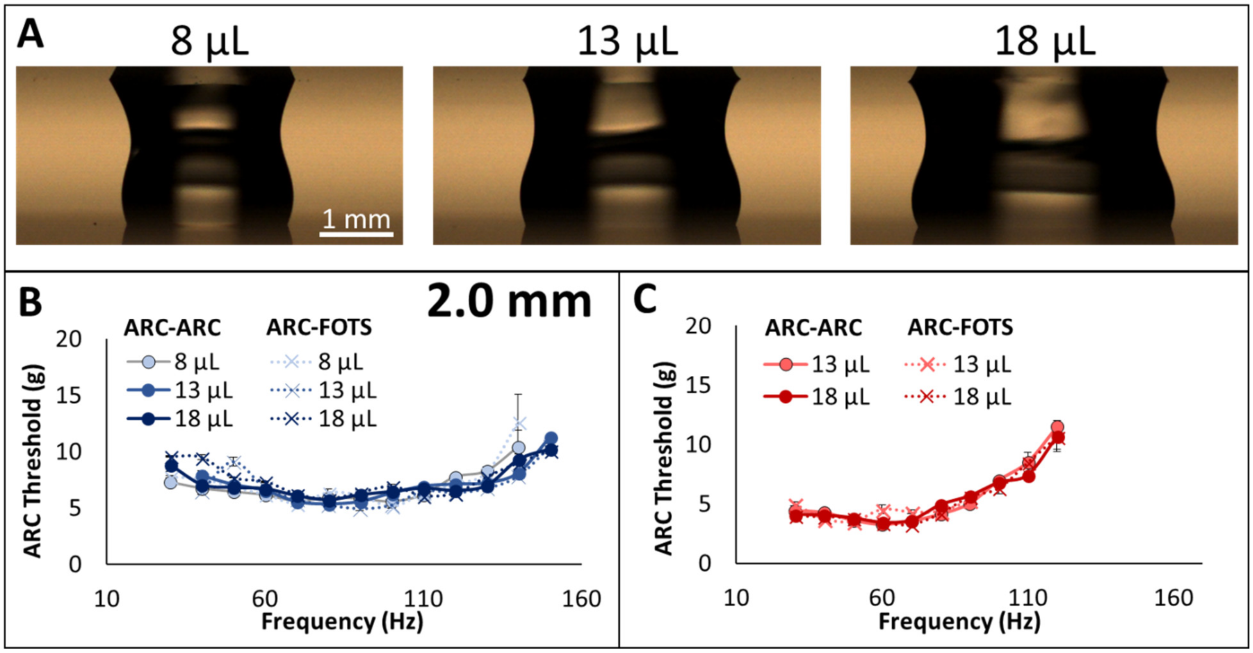

Figure 7.11: ARC threshold is independent of droplet volume in two-plate system. ARC threshold values are similar for droplets of different volume (A) transported in 2.0 mm (B) and 2.5 mm (C) tracks.

This data suggests that the two-plate system normalizes the length scale of the droplets. In other words, while the distance between leading and trailing edges will increase proportionally to droplet volume, the distance that the liquid node must travel is constant (e.g. regardless of the droplet volume, the distance between plates remains the same). However, there are limits on this normalization effect, and measuring a broader range of droplet volumes would likely show a bandpass (or 'volume-pass') effect where droplets too small to contact the top-plate or too large to sufficiently respond to the ARC track will not be transported, but all volumes in between will exhibit a similar ARC threshold profile. Practically, this attribute could be extremely beneficial for a user-friendly device, as it would allow a very large tolerance for the application of droplets by a user that does not have access to precision pipetting equipment.

Lastly, the velocity of droplets transported under these configurations was also determined. Interestingly, these measurements suggest that velocity on the two-plate system is correlated to the vibration frequency (Figure 7.12), rather than being a result of droplet resonance as suggested in Chapter 3.

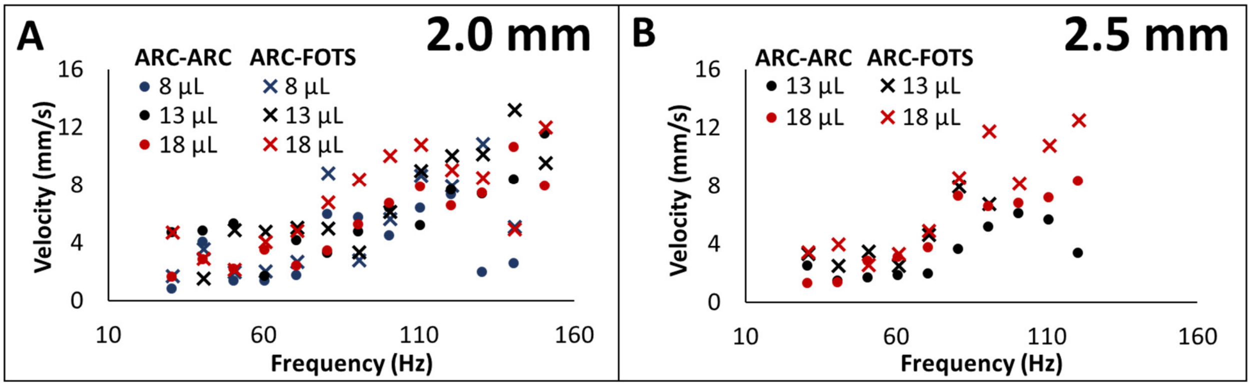

Figure 7.12: Transport velocity is correlated with vibration frequency on a two-plate system. Transport velocity trends upward with increasing frequency on two-plate systems with 2.0 (A) and 2.5 mm (B) separations. The local maxima that occur for some frequencies suggest that resonance effects are also at play in these systems as well.

This result is likely due to the tethering of the droplet to both top and bottom plates. The movement of droplet edges is almost perfectly out of sync, so the leading edge on one plate cannot advance too far ahead of the other in any particular vibration cycle. Thus, the droplet appears to consistently advance by one rung on each plate throughout each vibration cycle. Therefore, increasing frequency results in the droplets taking regular steps of the same distance more quickly. However, these plots also show local maxima occur in velocity for some frequencies, indicating that resonance effects still play a notable role, albeit comparatively diminished, in two-plate systems as well.

7.6 REAGENT DELIVERY

Having demonstrated that the ARCs and microheaters can be successfully integrated and that transport in a confined two-plate system is controllable and predictable, the next step was to determine how well ARCs could transport real reagents for an isothermal reaction. A mix containing all the ions, polymerases, and dNTPs required for a LAMP reaction was actuated on an ARC pattern. Immediately it was observed that the reagent droplet spread out across a larger area than a water droplet, indicating reduced surface tension (Figure 7.13).

Comparing the response of a water droplet to a droplet containing these reagents, we see that the edges of the reagent droplet exhibit very minimal edge displacement throughout vibration cycles. This droplet response effectively prohibited droplet transport in this configuration. However, the droplets still seemed affected by the ARC pattern, and it was discovered that transport can be achieved by added a slight inclination to the substrate (Figure 7.14). It should also be noted that this inclination was too small to independently initiate slip or movement of the droplet on these substrates and the droplet would not follow a defined path without the ARC pattern, which indicates ARC transport of the reagent droplets is due to the combination of vibrations and substrate inclination, rather than either of these features on their own.

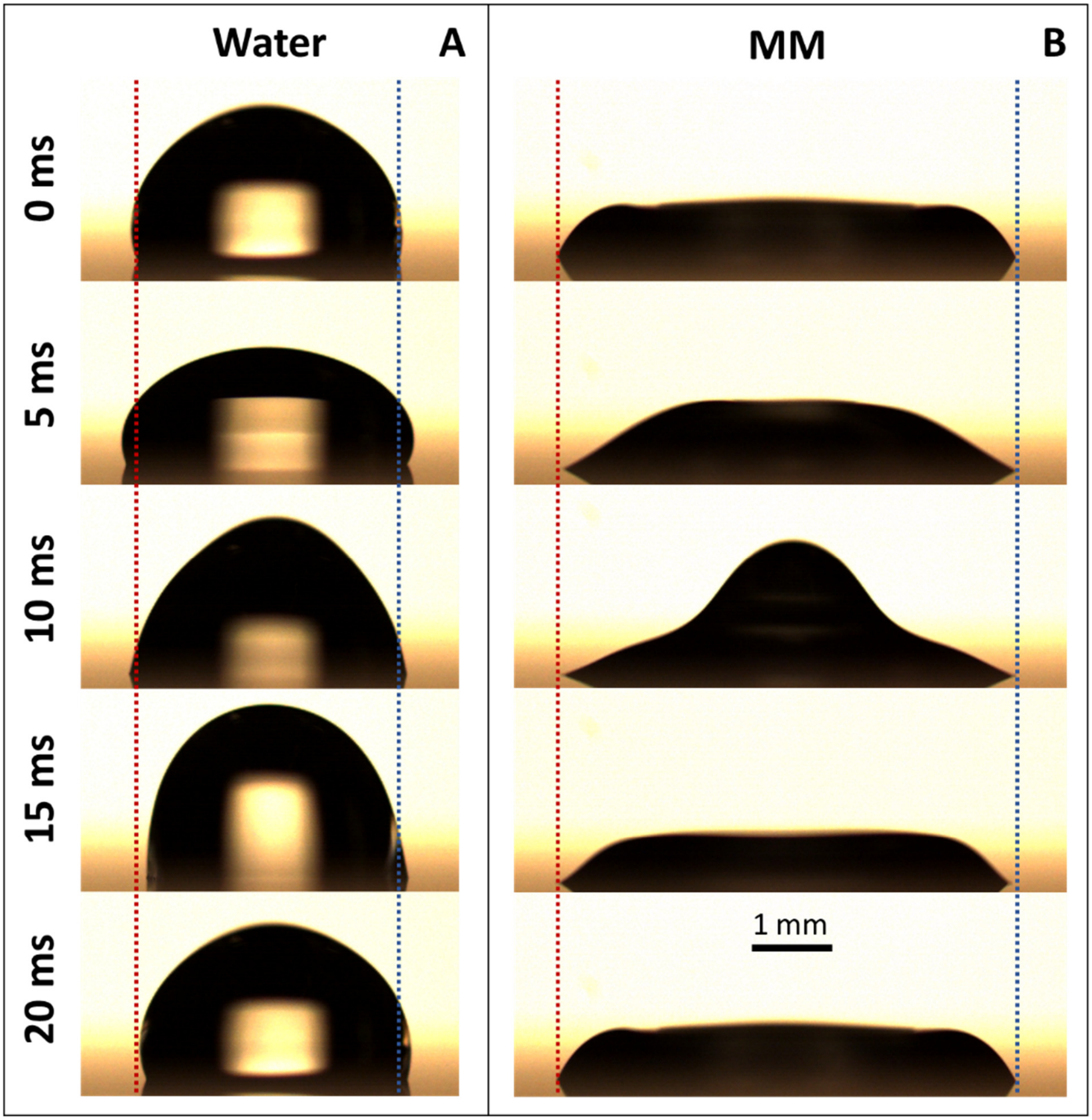

Figure 7.13: Droplet edges of master mix exhibit extremely small oscillation in response to vibrations. Edges of a water droplet (A) oscillate and exhibit pronounced differences in contact angle between wetting and de-wetting phases. Isothermal reagents (B) have substantially reduced surface tension and do not exhibit nearly as large of an edge oscillation as water droplets.

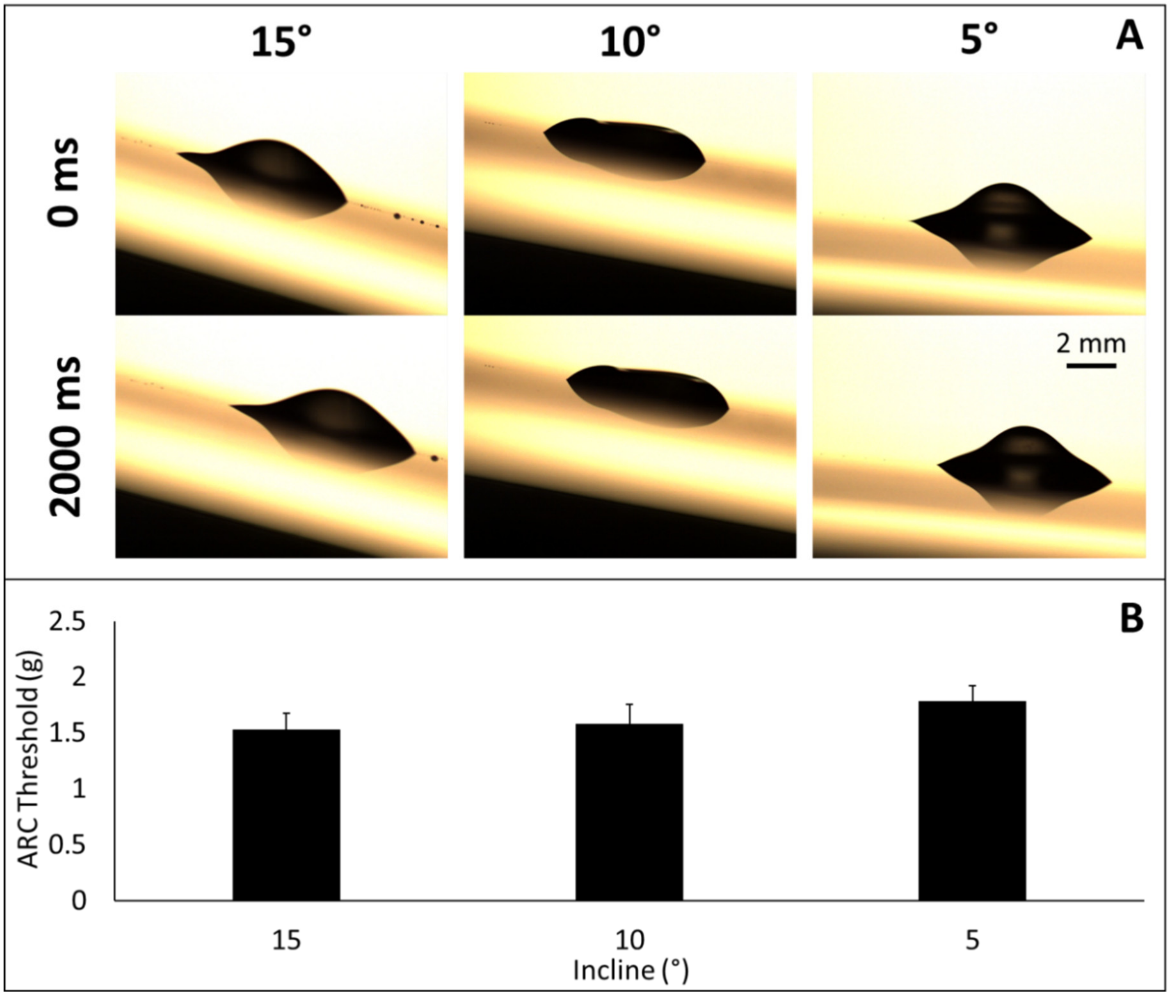

Figure 7.14: Substrate inclination provides for vibration-controlled transport of master mix. Tilting the substrate in the direction of desired transport by 5, 10 and 15° enables controlled transport of isothermal master mix (A). The ARC threshold is lower as the incline is increased (B) and the transport velocity is observable higher with increasing incline.

7.7 IMPROVED ARC ISOTHERMAL PROTOTYPE

Informed by the results of the previous sections, a cartridge style format was developed to enclose the droplets with a top-plate and silicone elastomer (polymethyldisiloxane – PDMS) gasket. While this enclosure slowed evaporation to some extent, condensation became a major issue, and large amounts of liquid were condensing on the edges of gasket. To account for all these findings, the chipset was redesigned. A heater was added to the top-plate and the design of the heater was extended to outline a larger region. This design warmed regions of the chip outside the droplet to reduce condensation during amplification but did not reach temperatures high enough to risk damaging temperature sensitive reagents (shown in Appendix E). The ARC pattern was adjusted to minimize open air space in the chamber. With this design, the sample droplet will be deposited directly to the heater while the reagent droplet will be deposited on the ARC track (Figure 7.15). Following high-temperature lysis of the sample, the reagent droplet will be transported to the sample and heater to initiate amplification. In an effort to further reduce condensation, the gasket is designed to surround the microheater, reducing surface area when contacting the sample and reagent droplet. Fabrication of this prototype demonstrated that the reagent droplet could be successfully transported to the sample. It was also observed that, while some evaporation still occurred, liquid volumes persisted for up to 30 minutes.

Samples containing copies of a synthetic barcode template were used to test the ability of this system to drive an isothermal amplification with LAMP primers (detailed methods can be found in Appendix A). Amplification at 65 °C was driven by the microheaters after the delivery of reagents to sample. The volume of this mixture was collected after 20 minutes and measured with a qPCR. These measurements indicated that the ARC chip successfully amplified the sample target with a similar efficiency as a qPCR for samples containing as little as about 6000 initial copies (Figure 7.16). However, a larger variability between samples was observed for the ARC chip. This variability could be the result of the evaporation causing non-uniform changes in concentration throughout the amplification process, the mixing step of delivering reagents (e.g. some reagents sticking to the ARC track), the extra pipetting step required to transfer the amplified product to the qPCR for measurement, or a combination of these factors.

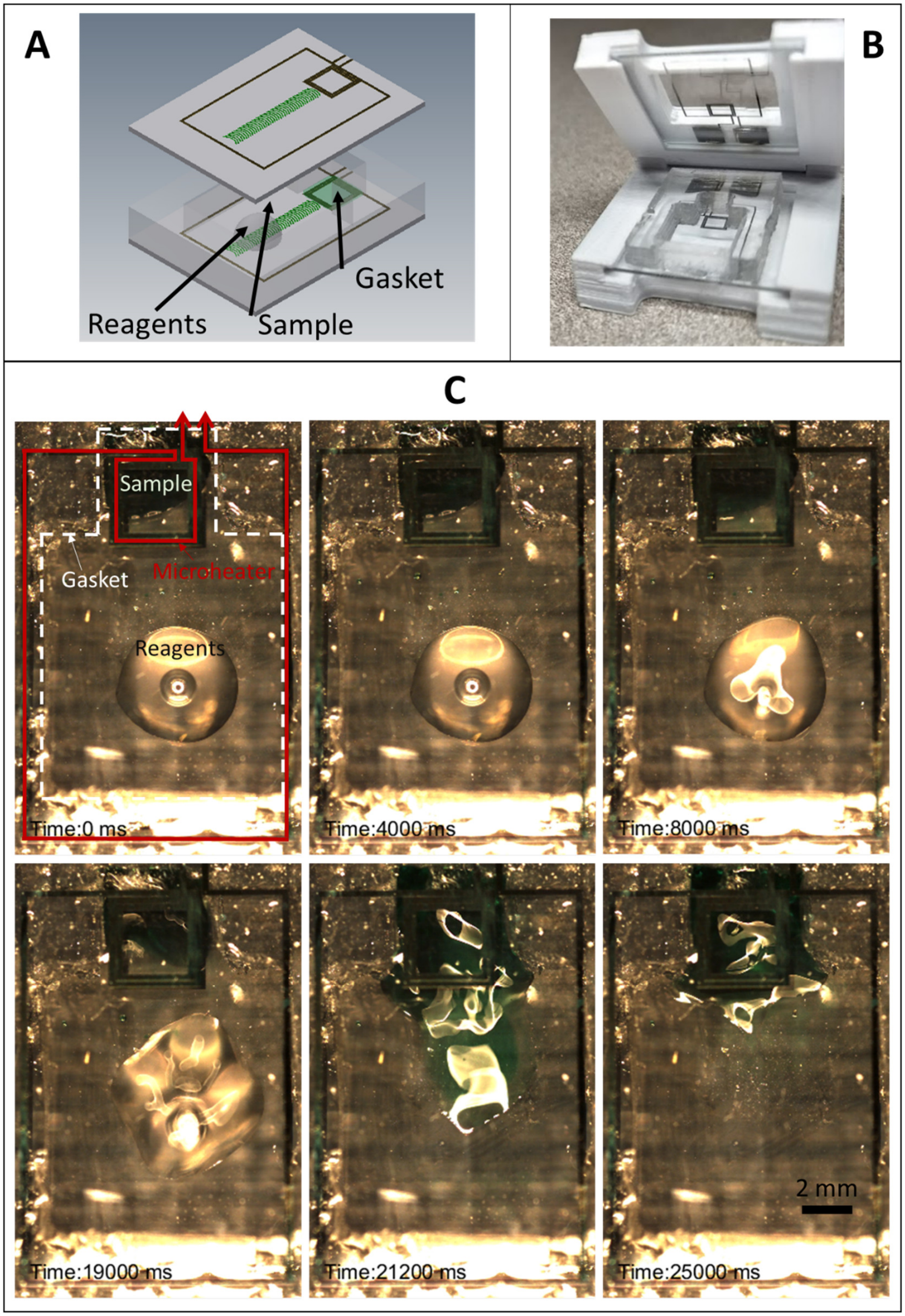

Figure 7.15: Improved isothermal ARC prototype enables LAMP amplification. The enclosed ARC system (A) is contained within a cartridge (B) to deliver reagents to a sample via an ARC track (C).

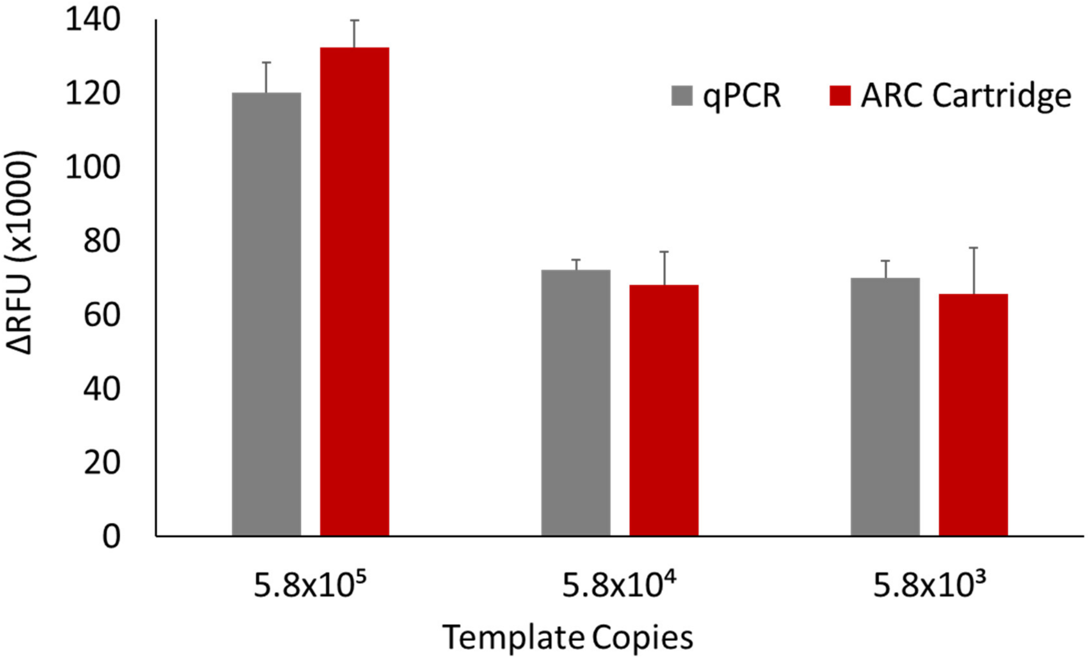

Figure 7.16: ARC cartridge enables comparable amplification of template targets. Droplets with isothermal reagents were delivered to sample droplets containing synthetic barcode templates. Amplification was successful for template concentrations down to 5.8x10^3 copies.

Overall, these results indicate that the envisioned ARC device can deliver reagents and drive an isothermal amplification reaction. However, the difficulty encountered in transporting reagent droplets with vibrations and reducing evaporation rates indicate that this approach will be difficult to adapt to different sample types and applications. These challenges will be a significant barrier for commercialization, so continued development will be required to improve the capabilities of this system to serve as an automated sample preparation tool.

7.8 CONCLUSION

Vibration driven droplets on anisotropic ratchet conveyors were explored as a means of automating an isothermal amplification test for species identification. The efforts of this work have produced droplet transport on a portable device, microheater integrated ARCs, and a two-plate configuration for droplet transport. These developments enabled an ARC chipset that could deliver reagents and perform an isothermal amplification on a target template. While these results demonstrate that ARCs are a promising method of automating DNA tests, continued development must be invested in this platform before it will be ready for commercial translation – particularly, the ability to handle liquids with lower surface tension must be improved.

Chapter 8. CONCLUSIONS AND FUTURE WORK

"How much can I learn from a drop of water?"

This seemingly simple question, fraught with unexpected challenges, was the underlying motivation for this work. Droplet transport on anisotropic ratchet conveyors (ARCs) is enabled by two simple features – an asymmetric surface pattern and a sinusoidal vibration. However, the underlying mechanics of this system present an intricate web of opposing forces, material properties, and interfacial interactions that are layered with complexity.

Starting with a fundamental solid mechanics model, this work aimed to elucidate these variables and enable a system that can leverage the unique properties of water droplets. The behavior of droplets driven on an ARC device was captured with established models of damped-harmonic oscillators. However, it was unclear how the forces acting at the edges of the droplet could be determined or predicted without empirical observation. The modulation of substrate parameters was then applied to better understand how these interfacial forces affected droplet transport. This investigation provided fascinating new insights into how the substrate affected the droplet response to vibration – having a substantial influence on both the frequency response and transport velocity of droplets. Continued analysis demonstrated that the transport velocity on these systems is determined by a complex summation of step sizes with various probability. Further, this step size is not a continuous value, but is quantized by the interaction of the rungs with the droplet edges.

These efforts provided new insights into how substrate design could be used to modulate the behavior of transported droplets. This understanding was first applied to create a droplet gate, which could selectively pause the motion of a transported droplet. This gate was enabled by a transition in the duty cycle, or the periodic spacing, of the rungs. This transition increased the pinning forces acting on the trailing edge of the droplet, requiring a higher amplitude or lower frequency vibration signal to pass the droplet. Exploiting a similar imbalance of forces, droplet switches were created that could select the direction of droplet transport at an intersection with a predictable combination of signal parameters. Delivery junctions, the final addition to the droplet functions toolbox for ARC devices in this work, were developed by spacing a terminating track with wicking guides that carefully balanced pinning forces to transition a droplet between tracks without leaving it stuck on the junction.

Upon expanding the capabilities of this platform, the question "How much can I learn from a droplet?" transitioned into "How much can I do with droplets?" However, like many technologies developed in an academic setting, this platform was becoming a solution without a problem. Fortunately, an opportunity to investigate the capability of this system to serve as a platform for DNA testing in conservation arose. Three key challenges in conservation that exhibited a strong demand for a field-deployable DNA test device were identified: 1) illegal timber trafficking, 2) seafood fraud and trafficking, and 3) invasive species monitoring. The problems faced by these challenges were examined and it was determined that substantial knowledge gaps currently prevent DNA from being readily extracted from timber samples. As such, the focus of development was directed towards samples that required implementation of manageable DNA extraction and purification techniques, particularly seafood. Loop-mediated isothermal amplification (LAMP) was chosen as the detection method for species identification and a design to enable this test on an ARC device was envisioned. Microheaters were integrated within ARC devices and initial characterizations were performed. Rapid evaporation lead to the development of a two-plate ARC system that could encapsulate droplets within a humidified chamber. Ultimately, these efforts lead to an ARC system that could deliver reagents to a sample droplet and perform an isothermal amplification (Figure 8.1). While this system demonstrates great potential for automated sample processing and DNA testing continued development will be required before it will be ready for commercialization.

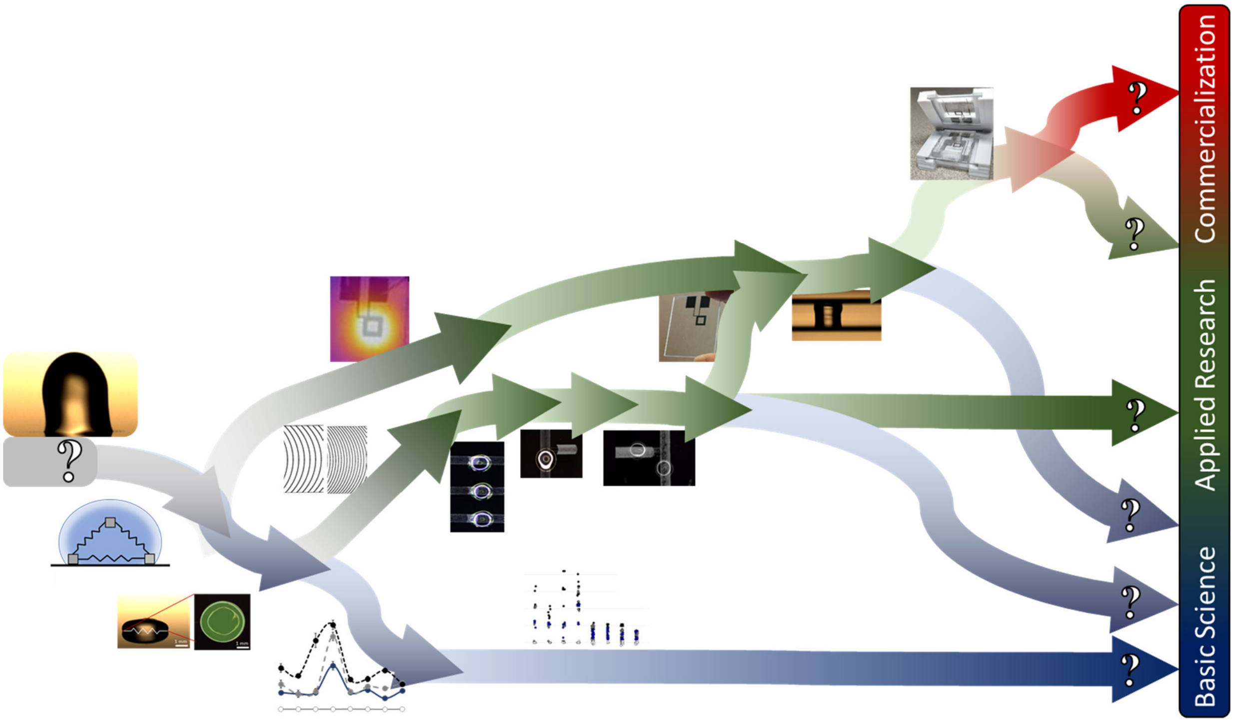

Figure 8.1: Path of developments and discoveries with anisotropic ratchet conveyors.

8.1 FUTURE WORK

Throughout the course of this project, many developments created new questions and ideas for investigation. Typically, answering a basic science question provided an understanding that could be applied to enable new functionality. However, the development of new functionalities could also present unforeseen intricacies or pose new questions. Finally, as the project neared a commercial prototype, weaknesses in the current system informed new avenues of applied research that could provide essential advancements.

8.1.1 *Transitions of droplet edges*

Analyses of edge motion and their effect on transport velocity demonstrated that droplet edges on ARCs do not exhibit a continuous motion but move in jumps from rung to rung. In this process, edges appear to move quickly across a hydrophobic space but more slowly across the hydrophilic rung, even during wetting phases. However, this behavior is not consistent with traditional models of canthotaxis,[118,119,129] although it appears to occur consistently on ARC tracks and a similar phenomenon was observed with ARC switches. A thorough investigation of the movement of droplet edges on patterned surfaces, particularly with different surface chemistry combinations, could provide novel insights into the behavior of droplet edges at the transition of hydrophilic and hydrophobic interfaces.

8.1.2 *Selective Merging*

While developing the delivery junctions, it was observed that at certain frequencies and amplitudes, droplets would pass each other, although they would merge at the same location when different vibration parameters were applied. Characterizing the parameters that enable or prohibit droplet merging, particularly if paired with high-speed video analyses, could provide novel discoveries about droplet behaviors. Delivery junctions could serve as tool to study this phenomenon and enable new discovery.

8.1.3 *Two-plate modelling*

The ability of the two-plate system to normalize the ARC threshold of droplets with different volumes presents an interesting phenomenon that could provide new insights through the development of a mathematical model. Continued investigation of this configuration may also elucidate aspects of interfacial interactions that could enable a predictive model for droplet transport on ARCs.

8.1.4 *Droplet splitting*

Controlled droplet splitting was not accomplished throughout the course of this project. Barriers to splitting droplets on ARC devices include 1) the high surface tension of pure water droplets and 2) the cyclic nature of applied vibrations. In other digital microfluidic systems, droplet transport was performed with droplets containing additives or some surfactant. The water droplets in this work exhibit a surface tension that is much greater than these solutions. Revisiting designs for splitting droplets with a lower surface tension fluid could provide some initial success. In order for a droplet to be split a force has to be applied over a sufficient duration to induce necking and eventual pinch-off of the droplets. With vibrations, this force can only persist over one half of a vibration cycle, as the changing direction of the substrate will remove this force on the droplet. The use of the two-plate configuration may provide a means to circumvent this issue and enable droplet fission.

8.1.5 *Reducing droplet volume and feature scaling*

The two biggest barriers preventing the ARC system from commercialization for nucleic acid testing are the relatively large volume used by current systems and the sensitivity to liquid properties. The volumes used in this work were derived from typical work volumes for laboratory based isothermal amplification, which are also on a scale that is convenient for a human to work with (i.e. dropper or pipettor). However, the required area of these droplets, particularly during the wetting phase of transport, resulted in a large area of open space on chip. To perform a single reaction on chip, this open space is not a major concern, but a practical amplification test for species identification will require at least three integrated controls, and experimental redundancies are also preferred. Subsequently expanding the chipset to address multiple species will therefore require increasing amounts of area on-chip.

A critical challenge encountered through the application of ARC toward a DNA amplification test was the effect of added isothermal reagents on the surface tension of the droplets, and it is likely that any other applications of ARC for handling organic compounds will also face this challenge. The reduction in surface tension caused by these reagents had a substantial effect on the droplet response to vibrations, but the fluid still responded to the ARC pattern. While very low surface tension fluids that do not form droplets will likely remain unmanageable, handling droplets with reduced surface tension may also be improved by reducing volume of the droplets.

Analysis of droplet velocity and step size in Chapter 4 showed that the smallest 5 μL droplets investigated in that work took the largest step proportional to the footprint of the droplet. This is likely due to the reduced mass of the droplet (e.g. surface tension forces are able to dominate over the forces due to gravity). In the work shown in Chapter 7 with droplets containing isothermal reagents, the droplets took very small steps compared to the footprint of the droplet and had a low probability of taking a step with each vibration cycle. Reducing droplet volume could have a similar effect of increasing the proportional step size and probability, but as the surface tension is lower, volumes much smaller than 5 μL will likely have to be used for this effect to be realized. Testing this hypothesis will not be as simple as applying a smaller volume to a device, as the feature size of the ARC rungs will likely be too large to transport droplets of this size. The rung radius will be too large to create the necessary difference in pinning forces between the edges of a smaller droplet, and the distance between rungs may be too much for the edge of the droplet cross over during wetting. Optimizing the rung radius will require some iteration but will not likely require a change in fabrication procedure. However, reducing the spacing between droplets will require a proportional reduction in the width of the rung to maintain the duty cycle of the track, as duty cycle is a key parameter for the performance of a track. This reduction may result in a rung width that is below the capabilities of the conventional photolithography techniques used to fabricate the ARC devices in this work. Furthermore, the use of the top-plate configuration in addition to these scaling efforts may further improve the ability of the system to handle droplets with lower surface tension, as contact with the liquid to the upper plate also reduces the forces due to gravity acting on the droplet. Although, it should be noted that the separation between plates must also scale to the size of the droplets. Overall, working towards a system that can handle much smaller droplet volumes will improve both the multiplicative capacity and the ability to handle droplets containing a wider variety of reagents. Therefore, reducing the volume of droplets and correspondingly scaling key feature sizes should be a focal point for future work.

APPENDIX A: MATERIALS AND METHODS

A.1 FABRICATION OF ARCS

All anisotropic ratchet conveyor (ARC) devices used in this work are fabricated at the Washington Nanofabrication Facility (WNF) on campus. The substrates used for all ARC devices are 100 mm wafers with an approximate thickness of 550 μm and are composed of either <100> p-type single crystal silicon or soda lime glass wafers. Computer automated design (CAD) software (Layout Editor) was used to create masks used to pattern all ARC devices and microheaters.

A.1.1 Silicon Dioxide ARCs

Fabrication of silicon dioxide (SiO_2) ARCs begins by cleaning the wafer with oxygen plasma (Glow Research). This removes any dust or organic contaminates and ensures hydroxyl groups are present at the surface. The wafer is coated with a negative resist, with a thickness of approximately 1.1 μm. The negative resist (NR9-1000PY) is exposed (315-400 nm) with a contact aligner (AB-M) or mask writer (Heidelberg) prior to development in a solution of 3:1 AD10 to deionized water. Proceeding development, wafers are cleaned briefly with oxygen plasma to remove any residual undeveloped photoresist, but not long enough to affect the developed pattern (Figure A.1). A coating of hydrophobic silane (fluorooctyltrichlorosilane – FOTS) is applied to the wafers via vapor deposition. Stripping the resist reveals a transparent pattern of SiO_2 ARCs defined by the hydrophobic FOTS background. Finally, the wafer is baked on a hot plate (150 °C for 15 minutes) to anneal the FOTS, creating covalent siloxane bonds, to improve long-term stability. A process flow table for SiO_2 ARCs is also included in Appendix B.

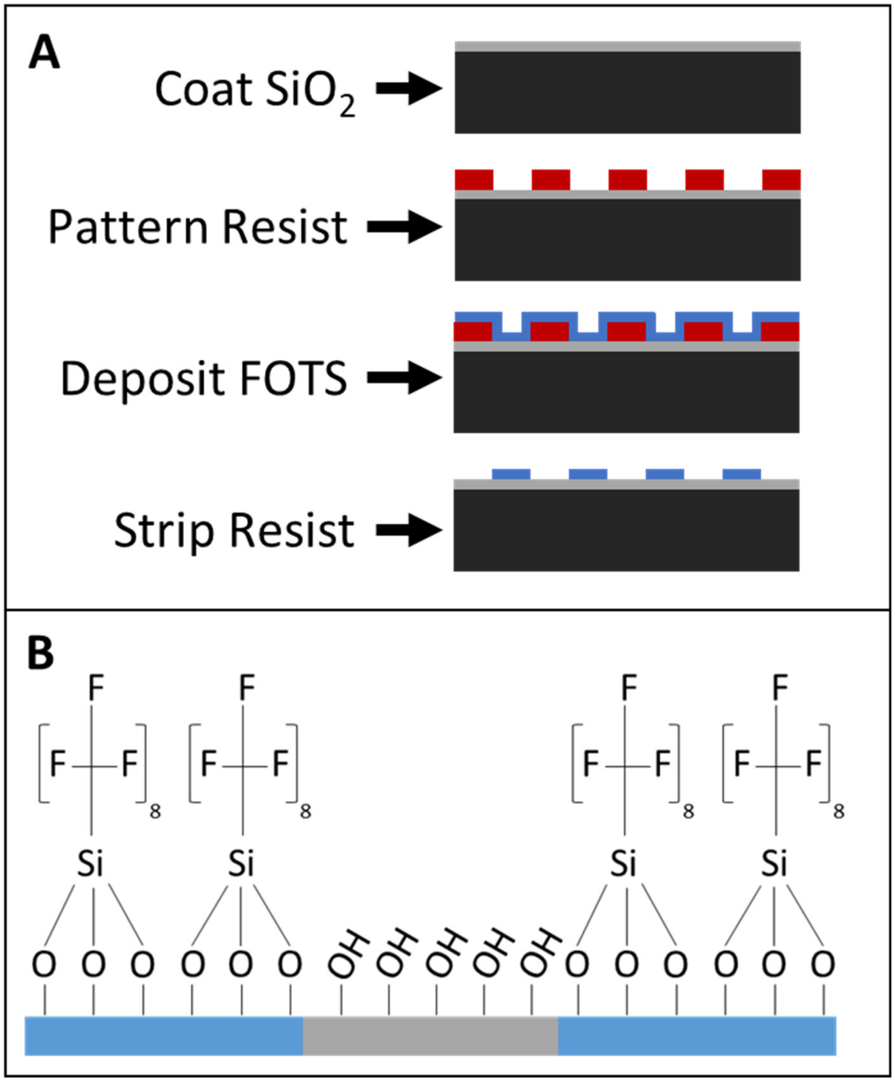

Figure A.1: Fabrication process of SiO_2 ARCs. SiO_2 ARCs are fabricated through a single mask process by patterning SiO_2 with photoresist, depositing silane, and stripping the resist (A). Proceeding resist stripping, a hydrophilic pattern of SiO_2 is defined by the hydrophobic FOTS (B).

A.1.2 Textured ARCs

Initial tests and some additional characterizations shown in Appendix D were performed using textured ARCs. Fabrication of textured ARCs began in a similar fashion as SiO_2 ARCs on silicon wafers, but a positive resist (AZ1512) was used with a 1:4 ratio of AZ340 developer to deionized water to create the pattern. The ARC pattern was etched into the silicon using the Bosch process with a deep reactive ion etcher (SPTS). Following the etching process, residual plasma was stripped with oxygen plasma (Glow Research), and the entire wafer was coated with FOTS to prevent infiltration of liquid into the textured regions (Figure A.2). The process flow for textured ARCs is also provided in Appendix B.

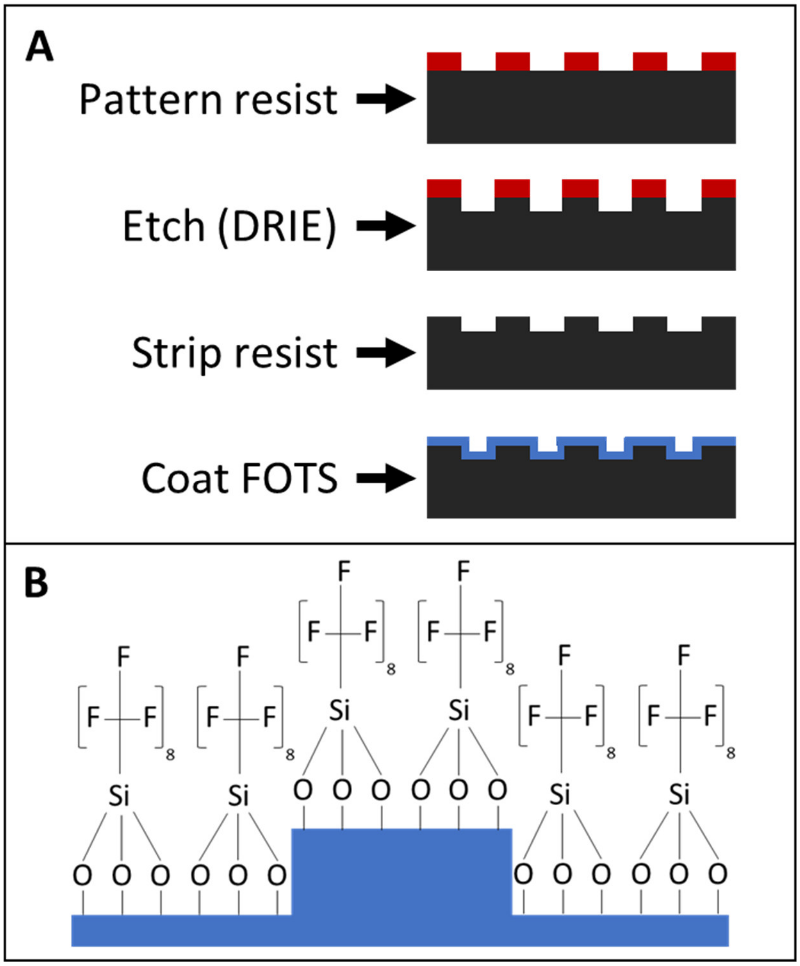

Figure A.2: Fabrication process of textured ARCs. Textured ARCs are fabricated through a single mask process by patterning a silicon substrate with photoresist, etching into the exposed silicon, and coating the entire substrate with silane after the resist has been removed (A). While the entire surface is hydrophobic, air trapped under a droplet in the texture creates a superhydrophobic region that contrasts the hydrophobic pattern (B).

A.2 ARC CHARACTERIZATION AND TEST SETUP

ARC devices are operated in the laboratory with Brüel & Kjær electromagnetic motor. The motor is driven by a functional generator (Agilent) and pre-amplifier (Brüel & Kjær). The vibration amplitude is measured with a laser doppler vibrometer (Polytec OFV) and an oscilloscope (Figure A.3).

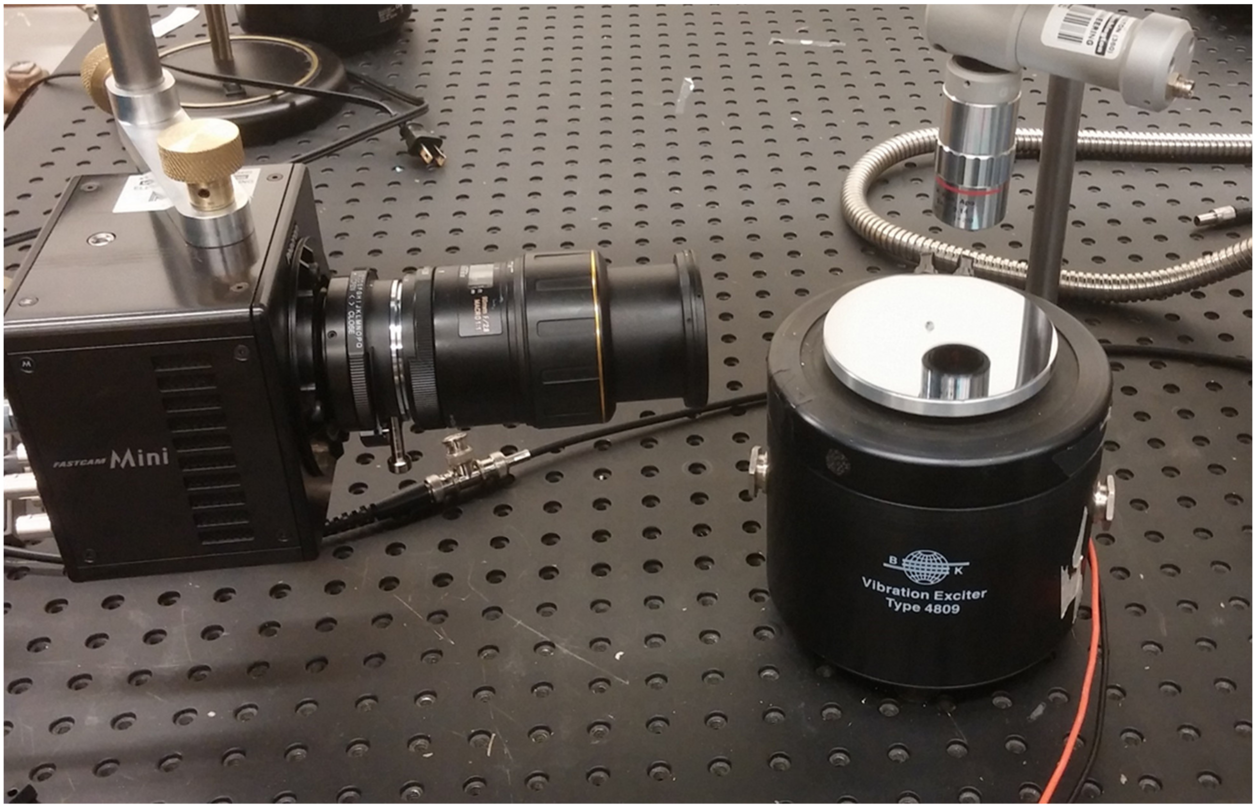

Figure A.3: Experimental set up. Droplets on ARC substrates are driven with an electromagnetic motor. The vibration amplitude is measured with a laser-doppler vibrometer and droplet motion is recorded with a high-speed camera.

High speed recordings are captured from the side with a highspeed camera (Photron UX50) and rectangular fiber optic backlight illuminated by a halogen light source (Dolan-Jenner). The shape of this back light is the cause of the distorted bright rectangles in the center of droplet images. To capture top-down images, the high-speed camera lens is centered in a fiber optic ring light. This lighting configuration is the cause of the illuminated edges and bright circle in the center of top down images of droplets exhibited in this work.

ARC thresholds are determined by setting the function generator to specific frequency and slowly raising the amplitude of the vibration until droplet transport is initiated. Recordings for droplet velocity are performed by setting the frequency and amplitude to a specific target, confirmed with the doppler vibrometer and capturing videos of droplet transport at these vibration parameters.

A.3 ANALYSIS OF DROPLETS

Measurements of the droplet velocity and edge motion were made with MATLAB software using custom image processing algorithms. More specifically, the droplet images are converted to binary using Otsu's threshold holding technique (Figure A.4). In binary, the perimeter of the droplet is the interface between black (0) and white (1) pictures and can then be extracted using simple logical operators in MATLAB. Any reflection of the droplet due to the substrate is removed by clipping any portion of this boundary that falls below the substrate baseline.

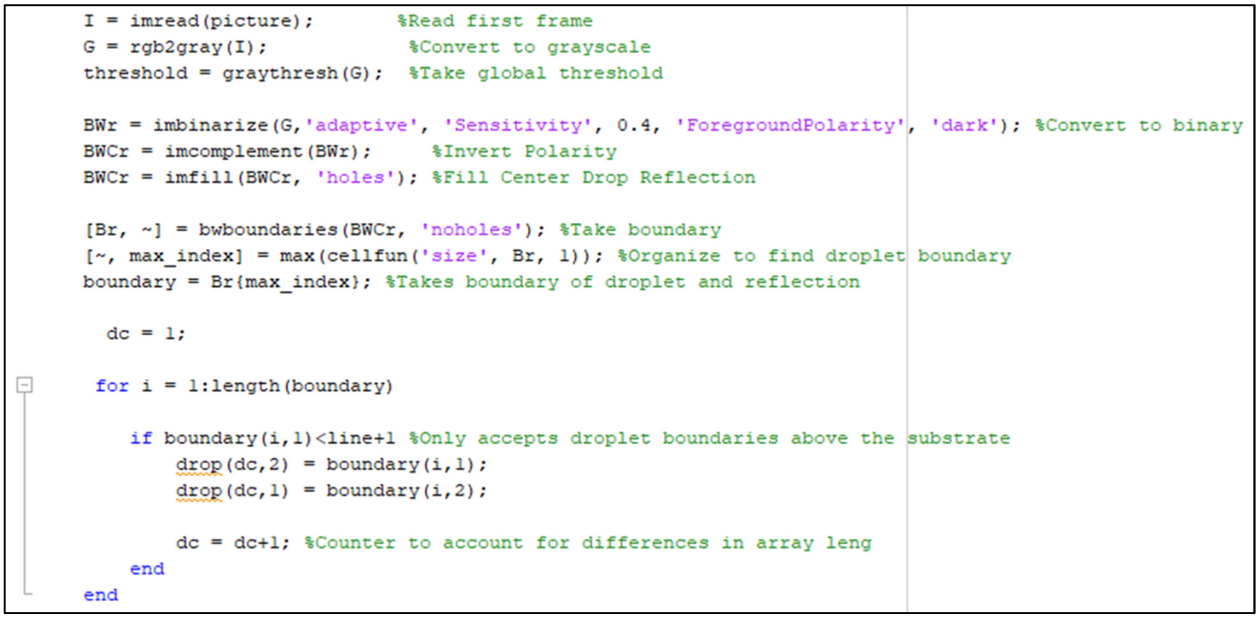

```
I = imread(picture);        %Read first frame
G = rgb2gray(I);             %Convert to grayscale
threshold = graythresh(G);  %Take global threshold

BWr = imbinarize(G,'adaptive', 'Sensitivity', 0.4, 'ForegroundPolarity', 'dark'); %Convert to binary
BWCr = imcomplement(BWr);      %Invert Polarity
BWCr = imfill(BWCr, 'holes'); %Fill Center Drop Reflection

[Br, ~] = bwboundaries(BWCr, 'noholes'); %Take boundary
[~, max_index] = max(cellfun('size', Br, 1)); %Organize to find droplet boundary
boundary = Br{max_index}; %Takes boundary of droplet and reflection

  dc = 1;

 for i = 1:length(boundary)

    if boundary(i,1)<line+1 %Only accepts droplet boundaries above the substrate
        drop(dc,2) = boundary(i,1);
        drop(dc,1) = boundary(i,2);

        dc = dc+1; %Counter to account for differences in array leng
    end
end
```

Figure A.4: MATLAB code to outline perimeter of droplet

The centroid of the droplet was determined by first finding the centroid for a horizontal (x-component) or vertical (y-component) slice of the droplet. The sum of these centroid locations was weighted by area of the corresponding slice and normalized to the total area of the droplet to reveal the geometric centroid of the droplet (Equation A.1). Assuming the droplet is homogenous, this location should also be the center of mass. The MATLAB code used to determine the x-component of the centroid is also shown in Figure A.5.

$$Centroid_x = \frac{\sum(\frac{x_{max,i} - x_{min,i}}{2} A_i)}{\sum A_i}; \; Centroid_y = \frac{\sum(\frac{y_{max,i} - y_{min,i}}{2} A_i)}{\sum A_i} \quad (A.2)$$

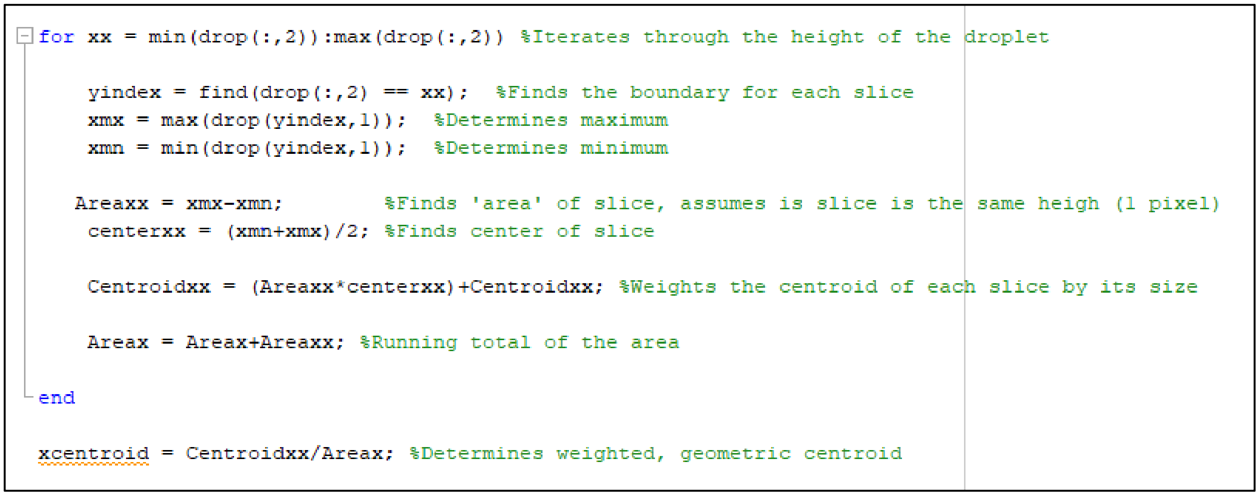

```
for xx = min(drop(:,2)):max(drop(:,2)) %Iterates through the height of the droplet

    yindex = find(drop(:,2) == xx);  %Finds the boundary for each slice
    xmx = max(drop(yindex,1));  %Determines maximum
    xmn = min(drop(yindex,1));  %Determines minimum

   Areaxx = xmx-xmn;        %Finds 'area' of slice, assumes is slice is the same heigh (1 pixel)
    centerxx = (xmn+xmx)/2; %Finds center of slice

    Centroidxx = (Areaxx*centerxx)+Centroidxx; %Weights the centroid of each slice by its size

    Areax = Areax+Areaxx; %Running total of the area

end

xcentroid = Centroidxx/Areax; %Determines weighted, geometric centroid
```

Figure A.5: MATLAB code to determine geometric centroid of a droplet

Finally, leading and trailing edges were identified as the maximum and minimum x-values that correspond to the baseline, or interface between the droplet and the substrate (Figure A.6).

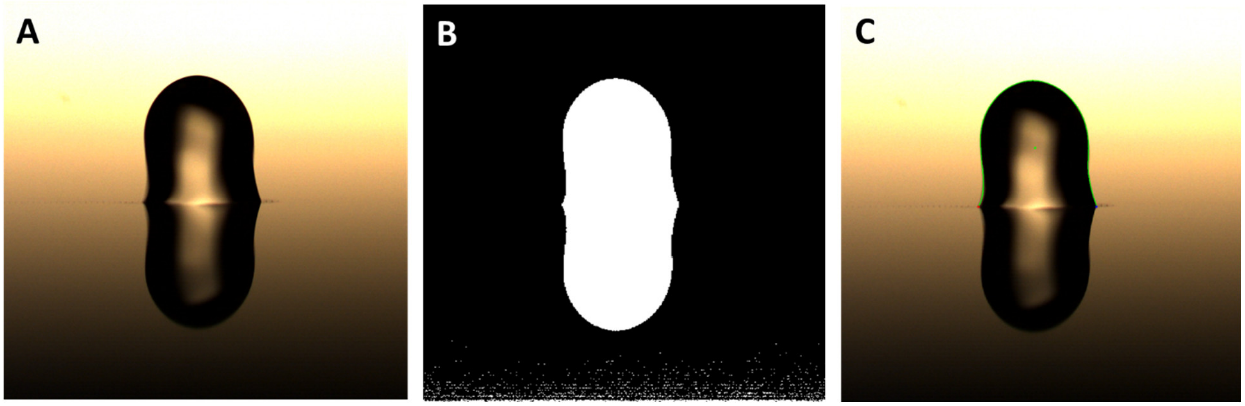

Figure A.6: Droplet analysis process. A still frame of a droplet in motion (A) is analyzed by converting the image to binary and extracting the boundary of the droplet (B). Reflection is clipped, and the droplet outline is used to determine the centroid, leading, and trailing edges of the droplet (C).

The volume of static droplets (e.g. for evaporation rates) was calculated by slicing the two-dimensional cross section of the droplet into stacks 1 pixel high, in a similar fashion as when determining the centroid. This calculation assumes each stack is circular and approximates the volume of the droplet as a stack of thin cylinders as described in Equation A.2. The program (Figure A.7) converts the pixel count of the radius of this stack into a real measurement using a calibration factor that is determined by measuring a known feature size *a priori*. This calibration value is also used to generate real values for the edge movement velocity of droplets.

$$Volume_{drop} = \sum_{k=1}^{n} 2\pi \left(\frac{x_{max,k} - x_{min,k}}{2}\right)^2 \quad (\mathrm{A.3})$$

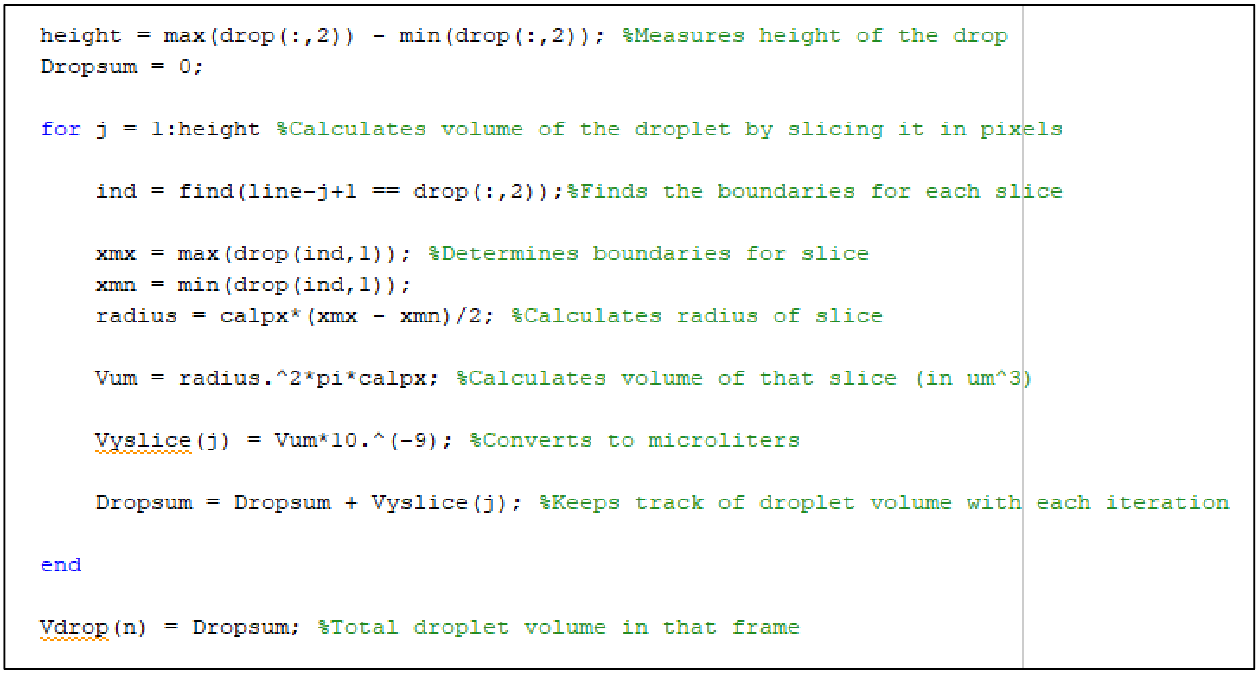

```
height = max(drop(:,2)) - min(drop(:,2)); %Measures height of the drop
Dropsum = 0;

for j = 1:height %Calculates volume of the droplet by slicing it in pixels

    ind = find(line-j+1 == drop(:,2));%Finds the boundaries for each slice

    xmx = max(drop(ind,1)); %Determines boundaries for slice
    xmn = min(drop(ind,1));
    radius = calpx*(xmx - xmn)/2; %Calculates radius of slice

    Vum = radius.^2*pi*calpx; %Calculates volume of that slice (in um^3)

    Vyslice(j) = Vum*10.^(-9); %Converts to microliters

    Dropsum = Dropsum + Vyslice(j); %Keeps track of droplet volume with each iteration

end

Vdrop(n) = Dropsum; %Total droplet volume in that frame
```

Figure A.7: MATLAB code for calculating droplet volumes.

A.4 FABRICATION OF DNA BIT

The DNA BIT is composed of two primary components – the portable driving unit and the disposable chipset. The chipset is comprised of both DNA-ready and ARC-integrated versions.

A.4.1 Fabrication of Chipset

Isothermal chips are fabricated from glass wafers to provide a transparent viewing window and reduced thermal conductivity compared to silicon (Figure A.8). Soda-lime glass wafers are first coated with approximately 350nm of Molybdenum through an evaporation process. The Molybdenum is patterned with a positive (AZ1512) photoresist, exposed as discussed above, and developed with a solution of 1:4 AZ340 to deionized water. Exposed molybdenum is removed by a highly anisotropic etch back process using an inductively couple plasma tool with fluorine gases (Oxford). Remaining photoresist is stripped using wet chemistry (EKC) as removal with oxygen creates adhesion issues to molybdenum in subsequent steps. The thickness of the Molybdenum thin-film is confirmed at this step using a profilometer (Tecron Alphastep-200). The wafer is then capped with a 1 μm layer of silicon dioxide using a plasma enhanced chemical vapor deposition process (PECVD). Contact pads are released by patterning the oxide cap with photoresist and etching the exposed oxide above the contact pads with buffered oxide etchant (BOE) for 6 min. The wafers are then diced into 2 cm x 2.5 cm chips with a 150 μm thick diamond saw blade (Disco).

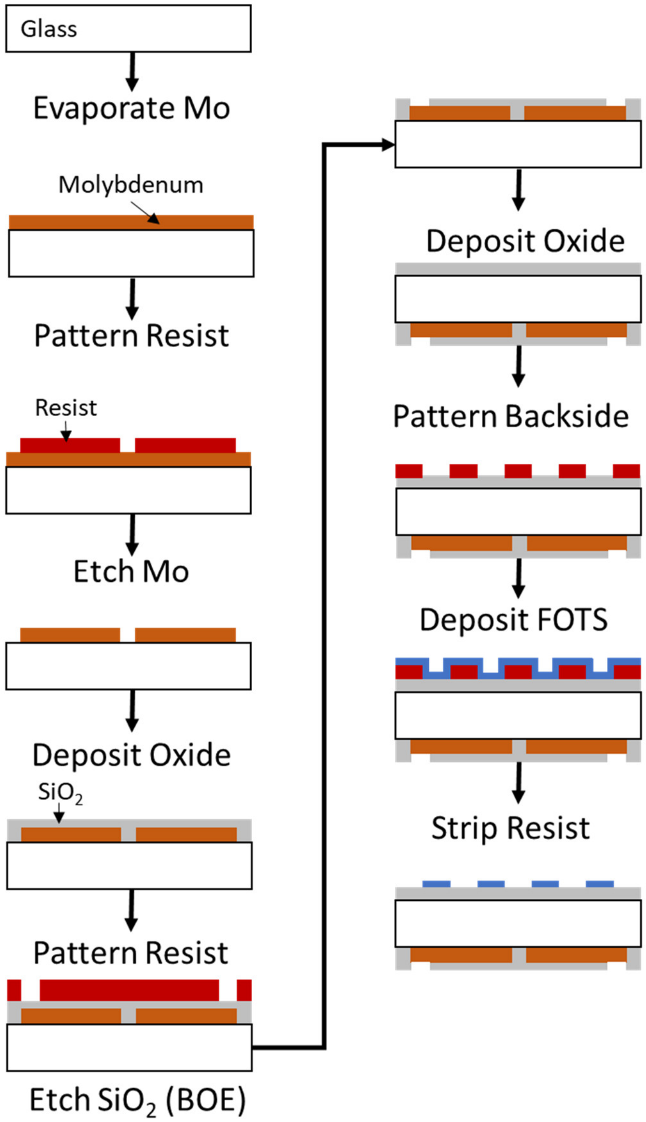

Figure A.8: Fabrication process of isothermal chip prototypes.

For ARC integration, the process is the same as the DNA-ready chipset up until the dicing step. Prior to dicing, the backside of the wafer is coated with 300 nm of silicon oxide using PECVD and the ARCs are applied to this SiO_2 surface using the process detailed in A.1.1. However, the chips are diced before the FOTS is applied.

A.4.2 Fabrication of Driving Unit and Cartridge Packages

The casing for the portable driven unit is developed using Inventor (Autodesk) software and converted to gcode for fabrication with 3D printed PLA+ (Lulzbot) using Cura software. The 3D printed parts were assembled with traditional hardware fasteners and adhesives. The circuitry is centered around an Arduino Uno and connected via printed circuit boards using traditional soldering techniques.

The chipsets are packaged in a 3D printed cartridge that contains spring connectors that interface with the exposed contact pads in the micro heater pattern. Silicone elastomer (PDMS) gaskets are fabricated from 3D printed molds. The gaskets are functionalized with atmospheric plasma and physically bonded to the chips prior to insertion into the 3D printed cartridges

A.5 ON-CHIP AMPLIFICATION

LAMP amplifications performed on the isothermal ARC and DNA-ready chipsets used DNA template and LAMP primers that were measured and verified using a traditional benchtop qPCR prior to translation to the on-chip platform.

A.5.1 Extraction and acquisition of DNA template

In this work, two DNA template targets were used. The first is a synthetic 1600 base pair oligomer that was created with a random number generator in MATLAB. The sequences of this oligomer were compared to all known sequences in NCBI BLAST and any sections of the sequence that matched were re-randomized until an entirely unique sequence, compared to known sequences in the database accessible to BLAST (on 5/30/2017), was created (Table A.1). This oligomer was then acquired from TWIST Biosciences. The lyophilized oligomer was reconstituted in diH$_2$O to and aliquoted into working stocks of 5.8x10^5, 5.8x10^3, and 5.8x10^1 copies/μL.

Table A.1: Synthetic Barcode Sequence

5’−GAAGGAGGGGTGTAGATATAGGGTGTCTACAAATTGGCTTTCGTTCGTGCCATCATAAATGTACAACGGGCAGTAGCGATCGAATGTCAAGAC
GTAGCCTTCCGAAATATGACTGAAATCCAAGGACTGTACCCATGAGTTAAGTTTTCTGTAAGGCCCGCGTACGAGCTGGAACCCTCCCTGCGATA
GATGGAAATCGACTGTGCGCTTGCTTGCTATATGGGTGCGAGTGTCAGTAGTCAGGACCCCGCGAACTTAATCCCGTGGCAATTCGAGGTCCGGA
CAGGTCGCGCCGGGCTGACAATTAACGTACGGATCACCAAATCTTAGGGACTATCCACCGTTTACTCGGGTGCCCACTAATAGCCGCAGACTCGT
ATTGTCATATTAGGCTGGTTGACGACTCCTGAATCTGTCCTAATTCGGATCGCGTCGCCATATGCCGGTGGCCAGACCCAGTAAAACCACCATGAA
TCGAATACAAACGATGGAAACGAGAAGTTTGTACTACAGACCTAGCTCCGCTCCCAGGATTTGTCGCTTGCCACACATCGTTGCTGACAGGATCT
AGAGTGATGCTTAGACTCCGTCGGGCCTATAACACCATCGACGCCGTTCCGAGATACTTGACGGGACGTCGCGAAAATGTAAGCATTTGCGCGGC
AACTGTCCATTCACAATCCCACTACAAAAGACTTGCTCCAAAACACATAGGTCATCCACTGGGCGGTCCAGCGCGAGCTTACTCGTAAGTGACAG
ATGGGCAGGCGCAAGTGAGCATAAGCGATGTAGGTTGAATACCCCTTACTAGAACCCAACCTTTTACCGCAGGAGTGGTCCCGTACGCAACTAGC
ATTGGACGGGGAATTGCACGGCGGAACGCCCGTTTATGTGGCTACCTAAAGCAGAAGAATATACAGATCTCGGGTCGACTGCGGATTCCTCGATA
GCTGGAATCCACCACTGGTAAAGGCTAGACTAGTACCCCTAGGTATGGGGACATGGCCTACGGTGTCTTTGGAGATATAATTAGTTACAGACTCA
GCGGGTGTACATTCCAGTATTCACGCGATAACTTAATTTGTCCGTGTTCCACAACTACCCTCTGAGTGAAAAATAAAGGGCTTGGAAAAACATCG
ACCGAAAGCGTGAGTGTAAGCTAACACTCTGCCCGCCGAAGACCCTGCTTGCGTCCAGAAGAACGGCCCCTTTATGTGAGCACGCCATTACTTCT
TCGGCCTACACCCGGTTATCAATCGTCCGGGTCACTAGGGCACCCGGTTCATACGCTCGCGGACATAGGGCTCTAAAGGAGTGTTATGAAAAGGC
TGTGCGCATGGGCTGATGTTATCGATCGAGGTTGCATTCGGATAGCAGGACGAGGTTCCTTGCCTGCCCTAAACCCCGGAAGAACTCAACCAGAG
GGCCAAGTAAACTTTGTCTGGAGTATGCCTGGGTTTTGGTGCATACCTTCGACGCCATCGTGCTCAATAGCTAAAGTTGATGTGTATGAGCATGTC
GGGAGTAACTTTTTGACTCTAATCACCGGTTCAATTCTCACTCACGACCAGGATCTAGCTACCTCAAAAGTAGGCGCCCG−3’

The second DNA template used in this work was from *Oncorhynchus tshawytscha* (chinook salmon). Samples for *O. tshawytscha* were acquired from a whole fish at a local supermarket and species identification was verified through traditional taxonomy (i.e. scale count and spotting pattern). DNA from *O. tshawytscha* was extracted using the standard QIAGEN Blood and Tissue Kit protocol. Specifically, samples of about 25 mg pieces were incubated at 56 °C in 180 μL of lysis buffer and 20 μL of Proteinase K, vortexed every 60 seconds, until the tissue was completely broken down and the lysate appeared turbid. Next, 200 μL if lysis buffer and 200 μL of 200 proof ethanol were added to the lysate and vortexed. This mixture was transferred to a spin column (which contains a cellulose filter that binds DNA) and a collection tube for centrifugation at 8000 rpm for 1 minute. The spin column was transferred to a new collection tube and 500 μL of wash buffer was added and centrifuged at 8000 rpm for 1 minute. The spin column was again transferred to a new collection tube and 500 μL of a wash buffer containing ethanol (to remove salts) was added prior to centrifugation at 14000 rpm for 1 minute. The spin column was then transferred to a 1.5 mL centrifuge tube. DNA was eluted by adding 200 µL of diH$_2$O to the spin column membrane and incubating at room temperature for 5 min to maximize the yield of DNA. The DNA was collected into the tube via centrifugation at 8000 rpm for 1 minute. This centrifugation was repeated to improve collection yield of DNA from the spin column. The extracted DNA in the centrifuge tube was then stored at -20 °C until use. The DNA content of the extract used in this work was determined to be 4.85 ng/ml using a Qubit dsDNA high sensitivity assay kit.

A.5.2 Primer validation

LAMP primers were designed to amplify the synthetic barcode and the COI region of the *O. tshawytscha* template. These primers are shown in Table A.2.

Table A.2: LAMP primers of for synthetic barcode and *O. tshawytscha template*

Primer	Synthetic Barcode	*O. tshawytscha*
FIP	5’−AGATCCTGTCAGCAACGATGTG GAAACGAGAAGTTTGTACTAC−3’	5’−CCGATGGCTATCATAGCTCAGATT TTATCGTTGCATACTACTCCG−3’
BIP	5’−AGTGATGCTTAGACTCCGTC GGTCCCGTCAAGTATCTCG−3’	5’−TCGTATGAGCCCACCATATGTTTTT AGATGTAAAGTAGGCACGAG−3’
F3	5’−TGTCCTAATTCGGATCGC−3’	5’−TTCTTATCCTCCCAGGCT−3’
B3	5’−GGATTGTGAATGGACAGTTG−3’	5’−TAGCGATAATCATGGTGGC−3’
LF	5’−GCAAGCGACAAATCCTGGG−3’	5’−TCCCATGTACCCAAATGGTTCT−3’
BF	5’−TATAACACCATCGACGCCGTT−3’	5’−ACTGTCGGAATAGACGTTGACA−3’

LAMP amplification with these primers was confirmed on a qPCR (CHAI) using a primer mix consisting of 40 µM FIP/BIP, 5 µM F3/B3, and 10 µM LF/BF. The final 25 µL reaction volume used for these validations and all subsequent tests contained 15 µL of isothermal master mix (Ansera Analytics – ISO-001nd), 6.75 µL diH$_2$O, 1.25 µL CHAI green dye, 1 µL of the primer mix, and 1 μL of the target DNA template. This reaction verifies that the primer designs enable successful LAMP amplification of target template (Figure A.9).

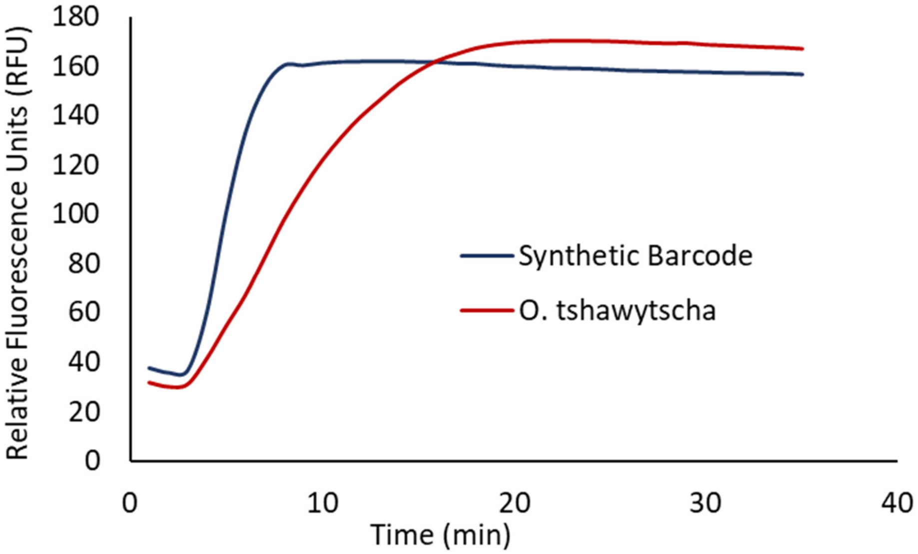

Figure A.9: LAMP primers amplify template target. The fluorescence curves from a qPCR demonstrate that the primers can provide rapid isothermal amplification of synthetic barcode and *O. tshawytscha* template.

A.5.3 Isothermal chip set up and amplification

To prepare the chipsets for isothermal amplification, an array of voltage dividers was created with potentiostats. By connecting a potentiostat in series with a microheater, a voltage divider was formed so the voltage distributed across the microheater, and thus the temperature, could be tuned by the potentiostat (Figure A.10A). The temperature of the both the bottom and top chips were measured independently with a microbolometer (FLIR C2 thermal imaging camera) and tuned to be within ±0.5 °C of the target temperature. It was noted with this particular instrument that the spot measurement setting was the most accurate for determining chip temperature and could differ from the maximum temperature displayed on the range gradient by as much as 10 °C (Figure A.10B). Using this method, it was also determined that the temperature gradient with the extended microheater on the ARC isothermal chips would not damage temperature sensitive reagents when heated to a high temperature for thermal lysis (Figure A.11).

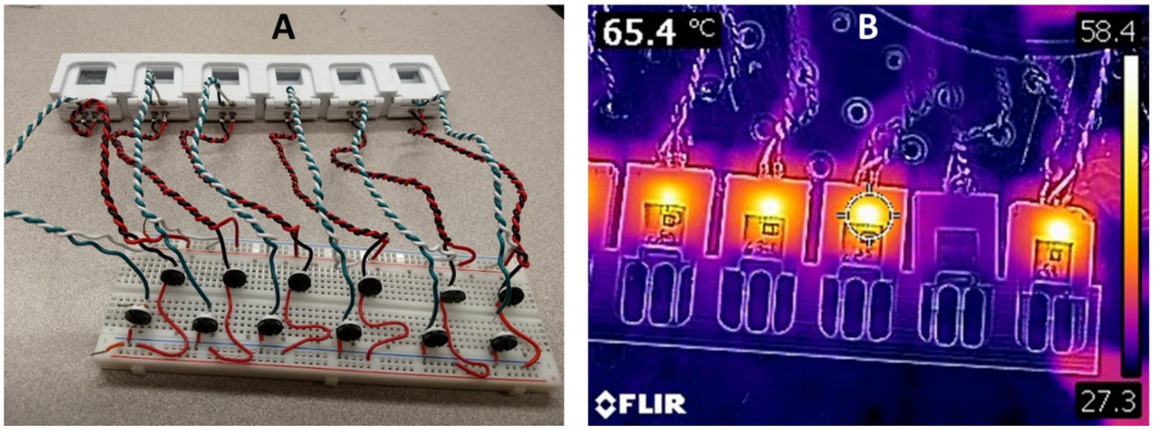

Figure A.10: Multiplex set-up for performing isothermal amplification on chip. Six two-plate cartridge systems were connected in series with a variable resistor (A), creating a rheostat to control the temperature of the heater on-chip (B).

Once the temperature of the chipsets had been tuned, the cartridge was transferred to the electromagnetic motor on a 15° inclined wedge to drive droplet transport. Sample droplets containing template DNA, diH_2O, and non-thermal sensitive reagents - CHAI green dye and primers (a total volume of 10 μL) were placed on the microheater and a droplet containing the thermally sensitive master mix (15 μL) was placed on the ARC track. The master mix was delivered to the sample with vibrations of 60 Hz at 3.2g, and the microheaters were then turned on to initiate isothermal amplification. After 20 minutes, the volume of this solution was collected and transferred into a tube for fluorescent measurement on the benchtop qPCR. Negative controls consisted of unheated solutions containing all reagents with the same concentration and volumes used for on-chip amplification. These controls verify that the intensity of observed fluorescence is not due to initial concentration of target template.

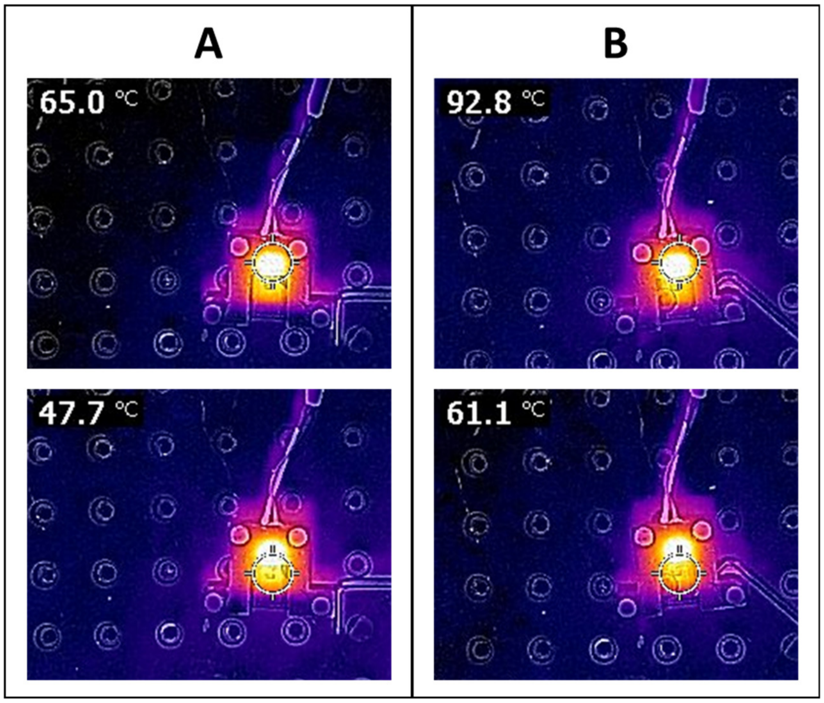

Figure A.11: Improved isothermal ARC prototype creates a temperature gradient. The extended on the improved isothermal ARC chip warms the region outside of the droplet to reduce concentration but does not increase the temperature of this region above a level that is harmful to LAMP reagents (A-B).

For trials on the DNA-ready chipset, all reagents were added to the well in a single solution prior to turning on the heater. Turbidimetric reactions with the DNA-ready chipset were performed by replacing the master mix with a version (Ansera Analytics – ISO-001t) that would form a white precipitate upon a successful reaction. This reaction was monitored with a timelapse on the highspeed camera. It was determined that the turbidimetric reaction took up to 60 minutes to produce a precipitate that could be definitively distinguished.

APPENDIX B: PROCESS FLOWS

Process Flow: SiO_2 ARCs

Sequence	Step	Equipment	Parameters
1	CLEAN	Barrel Etch	125 W, 5 min
2	COAT	SPIN 1/2	NR9-1000PY, spread: 500 rpm, 3 s, 500 / s^2, spin: 3000 rpm, 30 s, 1000 / s^2
3	SOFT BAKE	SPIN 1/2	150 C, 1 min
4	EXPOSE	ABM Aligner	37 s
5	POST EXPOSURE BAKE	SPIN 1/2	100 C, 1 min
6	DEVELOP	BATH5-Develop	3:1 AD10:H2O for 50 s
7	CLEAN	Barrel Etch	125 W, 1 min
8	VAPOR COAT	Desiccator	2 - 3 drops FOTS, >3 hours at vacuum
9	STRIP	Crystalizing Dish	Acetone, until resist is cleared, 15 - 20 seconds
10	BAKE	Hot plate	150 °C for 15 min

Process Flow: Fabrication of Texture ARCs

Sequence	Step	Equipment	Parameters
1	CLEAN	Barrel Etch	125 W, 5 min
2	COAT	SPIN 1/2	AZ1512, spread step: 500 rpm, 3 s, 500 / s^2, spin step: 3000 rpm, 45 s, 1000 / s^2
3	SOFT BAKE	SPIN 1/2	110 C, 1 min

4	EXPOSE	ABM Aligner	3.4 s
6	DEVELOP	BATH5-Develop	1:4 AZ340:H2O for 50 s
7	ETCH	SPTS-DRIE	Hal_27um - 72 cycles of Si etch with Bosch
8	CLEAN	Barrel Etch	125 W, 7 min
9	VAPOR COAT	Desiccator	2 - 3 drops FOTS, >3 hours at vacuum

Process Flow: Isothermal Chips

Sequence	Step	Equipment	Parameters
1	CLEAN	Barrel Etch	125 W, 5 min
2	DEPOSIT OXIDE	PECVD1	Opt - SiOx HDR for 300nm
3	DEPOSIT Mo	EVAP1	Moly Recipe 1
4	COAT	SPIN	AZ1512, spread: 500 rpm, 3 s, 200 / s^2, spin: 2000 rpm, 30 s, 500 / s^2
5	EXPOSE	ABM Aligner	3.5 seconds
6	DEVELOP	BATH5-Develop	4:1 DI:AZ340 for 50 s
7	ETCH	ICP-F	RJB Etch 6 SF6=25sccm C4F8 = 25sccm Pr=15mT Pwr-1200/30W Vdc~94V
8	STRIP	EKC	2 min
9	OXIDE CAP	PECVD2	Opt - SiOx HDR for 1um

11	CLEAN	Barrel Etch	125W, 5 min
12	COAT	SPIN 1/2	NR9-1000PY, spread: 500 rpm, 3 s, 500 / s^2, spin: 3000 rpm, 30 s, 1000 / s^2
13	SOFT BAKE	SPIN 1/2	150 C, 1 min
14	EXPOSE	ABM Aligner	37 seconds
15	POST EXPOSURE BAKE	SPIN 1/2	100 °C, 1 min
16	DEVELOP	BATH5-Develop	3:1 AD10:H2O for 50 s
17	DICE	Disco Saw	Diamond blade, 15,000 rpm, 1-2 cm/s, >550 µm blade exposure
18	CLEAN	Barrel Etch	125 W, 1 min
19	VAPOR COAT	Desiccator	2 - 3 drops FOTS, >3 hours at vacuum
20	STRIP	Crystalizing Dish	Acetone, until resist is cleared, 15 - 20 seconds
21	BAKE	Hot plate	150 °C for 15 min

APPENDIX C: DESIGN FILES

CAD models used to create masks for ARC devices were generated in Layout Editor. The fabrication of textured ARCs required the AZ1512 positive resist in order to withstand the Bosch etching process that defined the features of the device. Positive resists are broken down under UV excitation and exposed regions of the resist will be removed upon development. As mask writers work in binary (i.e. the laser is on or off over a particular region), designs for ARC with a positive resist has to be inverted to provide the designed design. This is accomplished by surrounding the desired pattern with a box or other shape and performing a Boolean subtract in Layout Editor (Figure C.1).

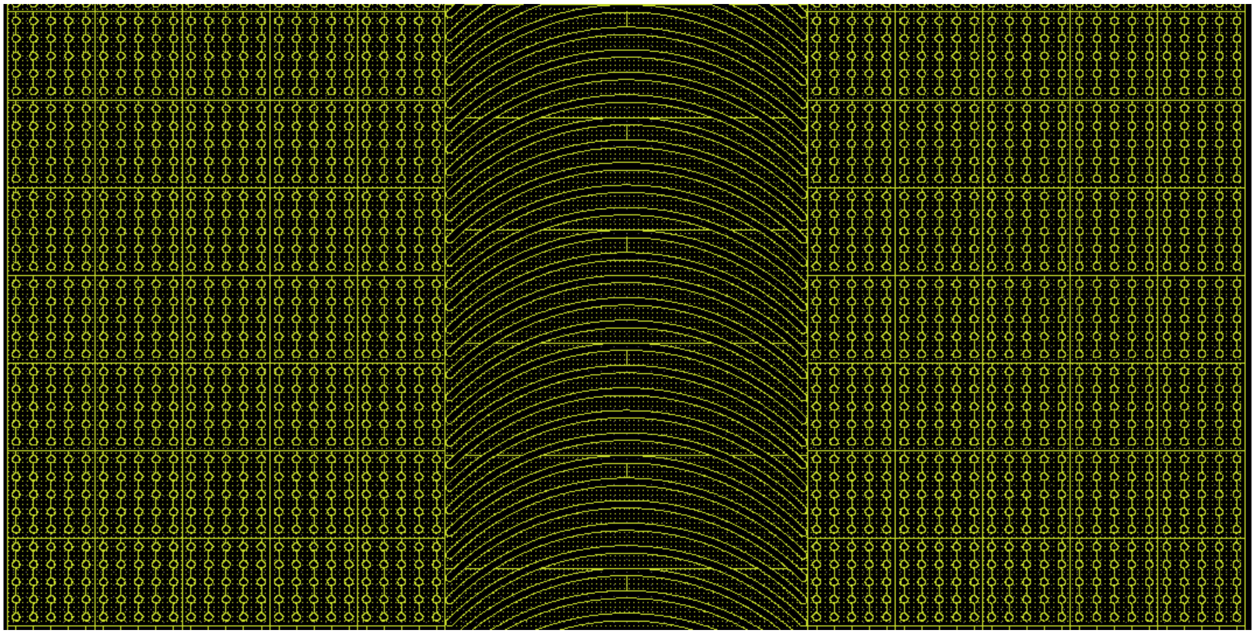

Figure C.1: CAD Model for textured ARCs. Textured ARCs fabricated from a positive resist must use an inverted polarity CAD model to provide the desired pattern.

SiO_2 ARCs use a negative NR9 resist that provides good adhesion to silicon oxide surfaces without an adhesion promotor. With negative resist, UV excitation initiates a polymerization process that is completed after a post exposure bake. Thus, exposed regions of a negative resist will be present on the substrate after development and designs for SiO_2 tracks in this work were not required to inverted prior to mask writing (Figure C.2).

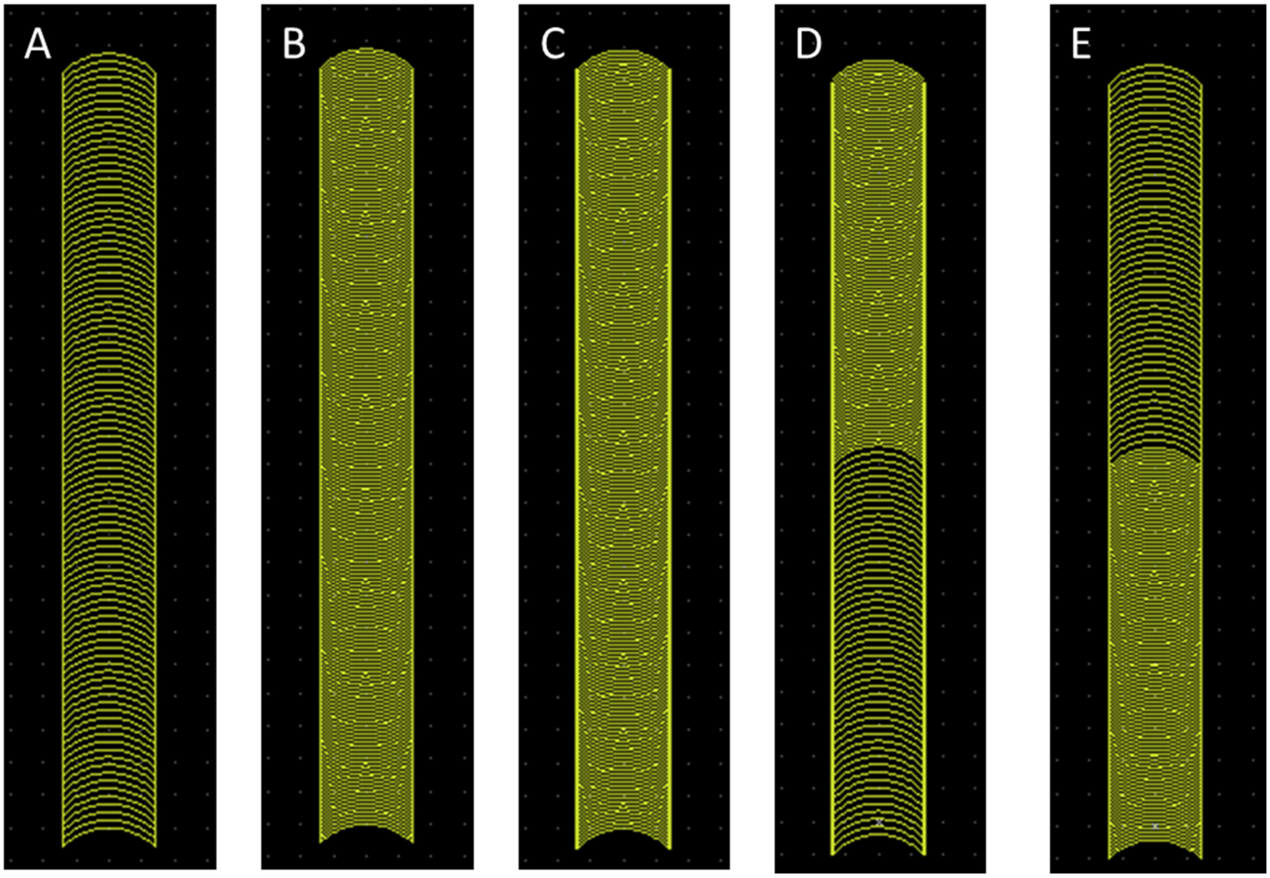

Figure C.2: CAD Models of SiO_2 ARCs. SiO_2 ARCs are fabricated with negative resistant designs for 10/120 (A), 10/60 (B), and 5/60 (C) ARCs characterized in Chapter 4 and transitions from a 8.3% to 16.6% (D) and 16.6% to 8.3% (E) duty cycle characterized in Chapter 5 are shown here.

The use of negative resist facilitated design of more complicated ARC devices to perform droplet functions (Figure C.2). Performing Boolean operations in design cells with this level of complexity is extremely difficult in Layout Editor, so an additional software package (such as Beamer) is required to reproduce these designs in a positive resist format.

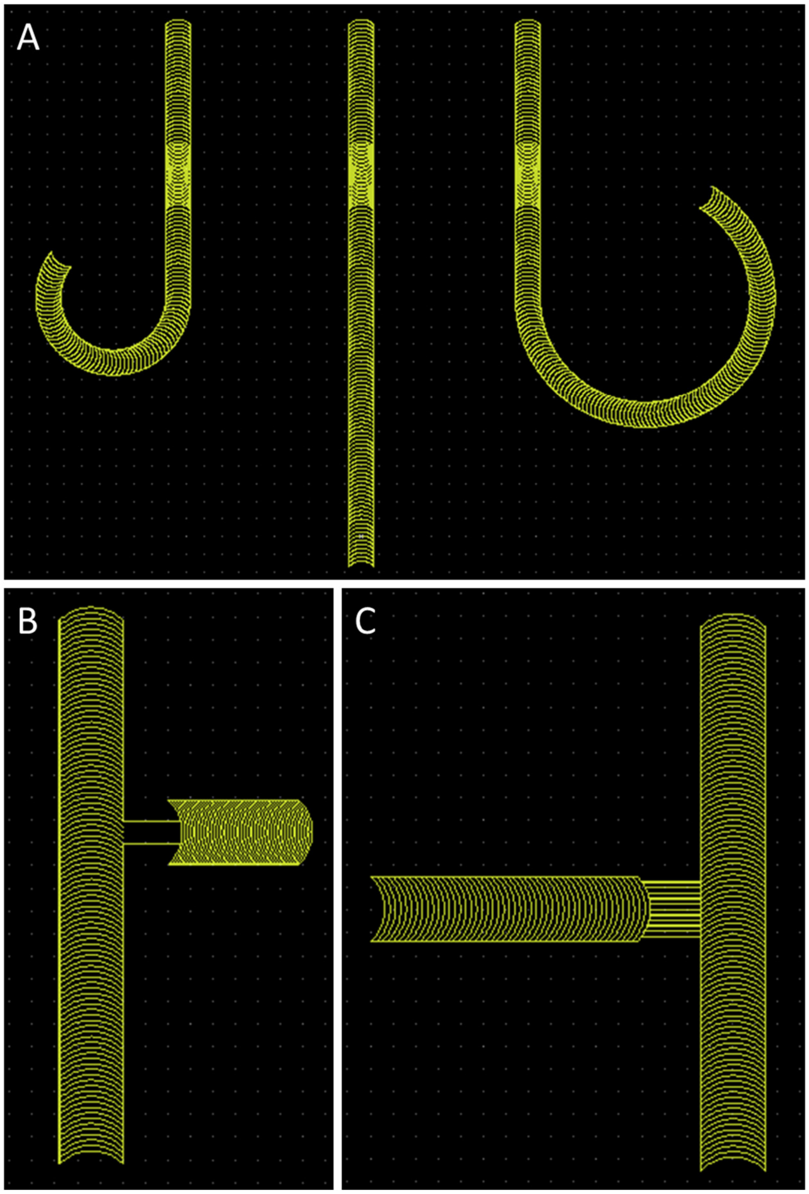

Figure C.3: CAD Models of Droplet Devices. The synchronizer (A), 8.3% to 16.6% switch (B), and deliver junction (C) characterized in Chapter 5 are shown here.

Fabrication of an integrated heater requires two masks (Figure C.4), a negative resist for the ARC system and a positive resist that can with stand the plasma etching process used to define the heaters. These patterns are easily adaptable, enabling rapid design improvements (Figure C.5).

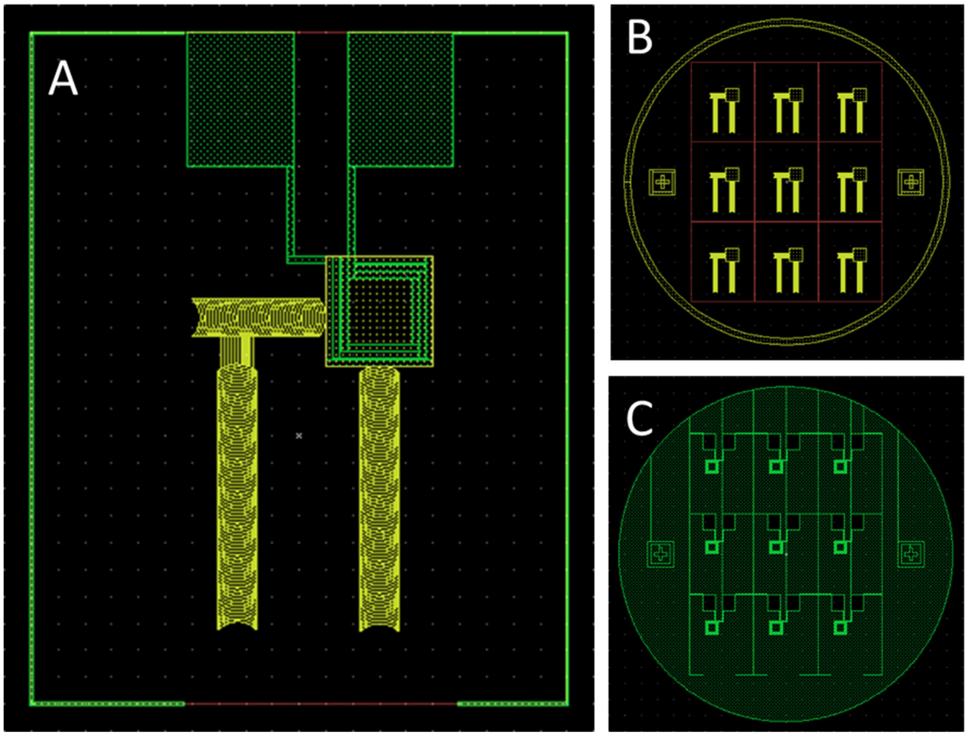

Figure C.4: Two mask CAD Designs for initial isothermal prototype. Cells for the heater integrated device with an ARC delivery junction (A) are also shown at the mask level (B and C).

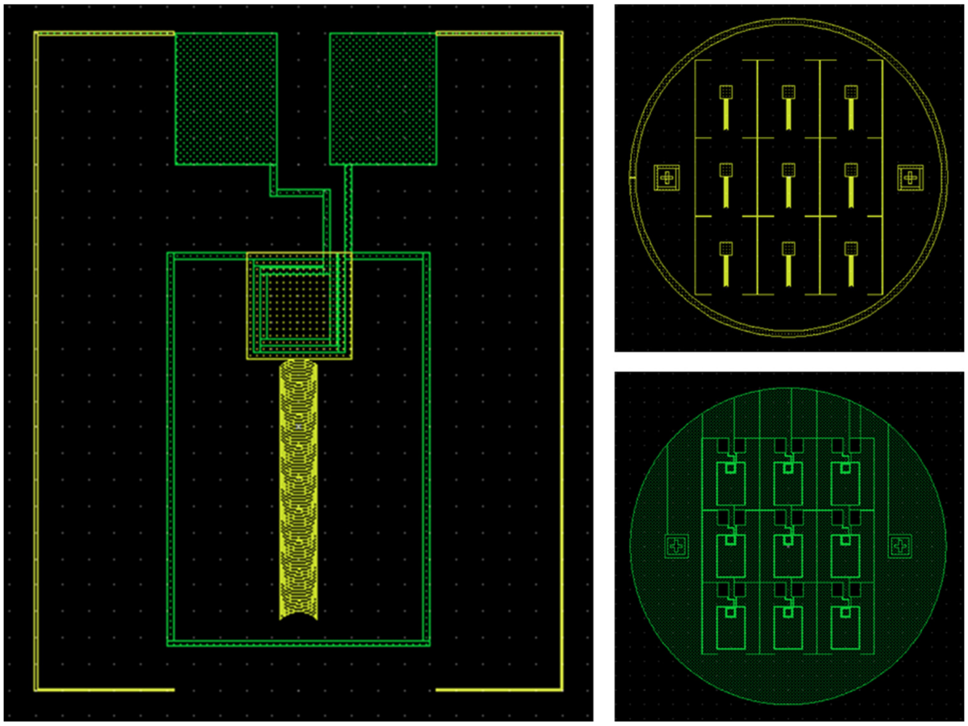

Figure C.5: Two mask CAD Designs for improved isothermal prototype. Cells for the heater integrated device with an ARC delivery junction (A) are also shown at the mask level (B and C).

The DNA-ready chipset does not use an integrated ARC device, and only requires a single positive resist mask. Note that the Boolean subtraction in Layout Editor can be applied to an array of cells to readily provide a complete wafer design (Figure C.6).

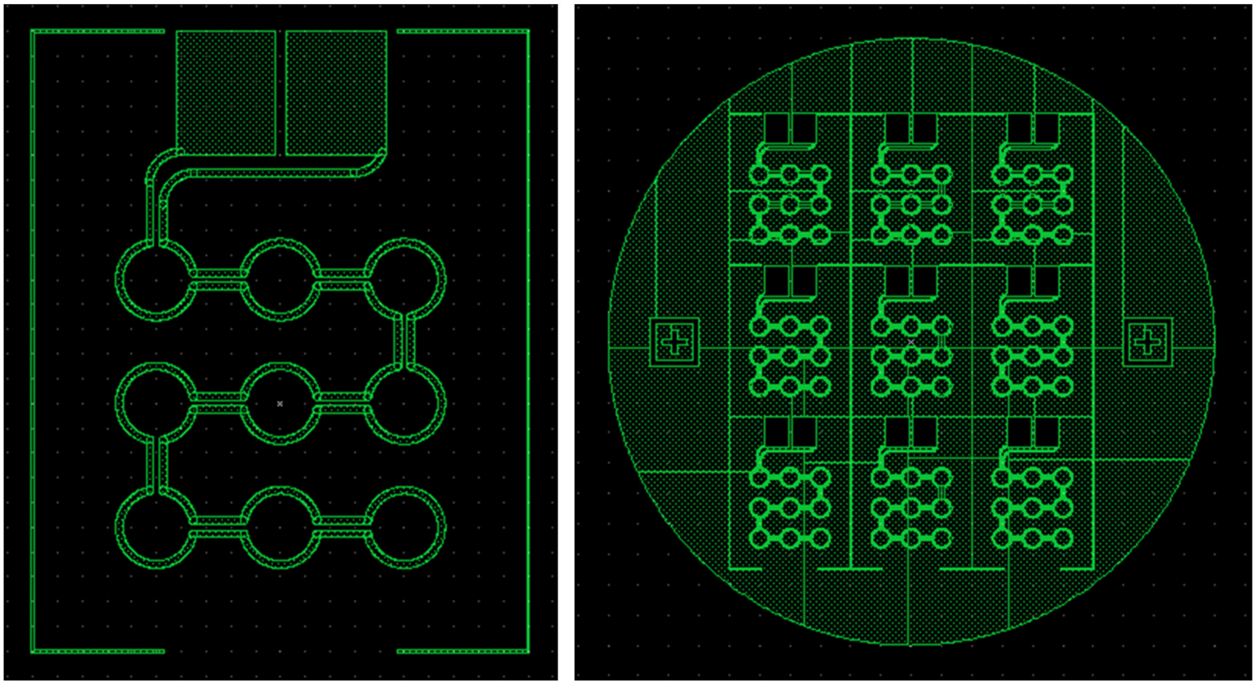

Figure C.6: Nine-well DNA-ready chip design. The single mask design for the nine-well chipset shown in Appendix E is demonstrated here.

APPENDIX D: ADDITIONAL ARC CHARACTERIZATION

Preliminary ARC measurements investigated the effect of rung radius on the ARC threshold and frequency profile of SiO_2 (Figure D.1) and textured (Figure D.2) ARCs. On SiO_2 ARCs it was observed that droplets exhibit a similar response profile for all rung radii, but the ARC threshold was significantly higher for 500 µm radius rungs. This observation is possibly due to the similarity of droplet radius (≈1250 µm) to the 1000 and 1500 µm rungs.

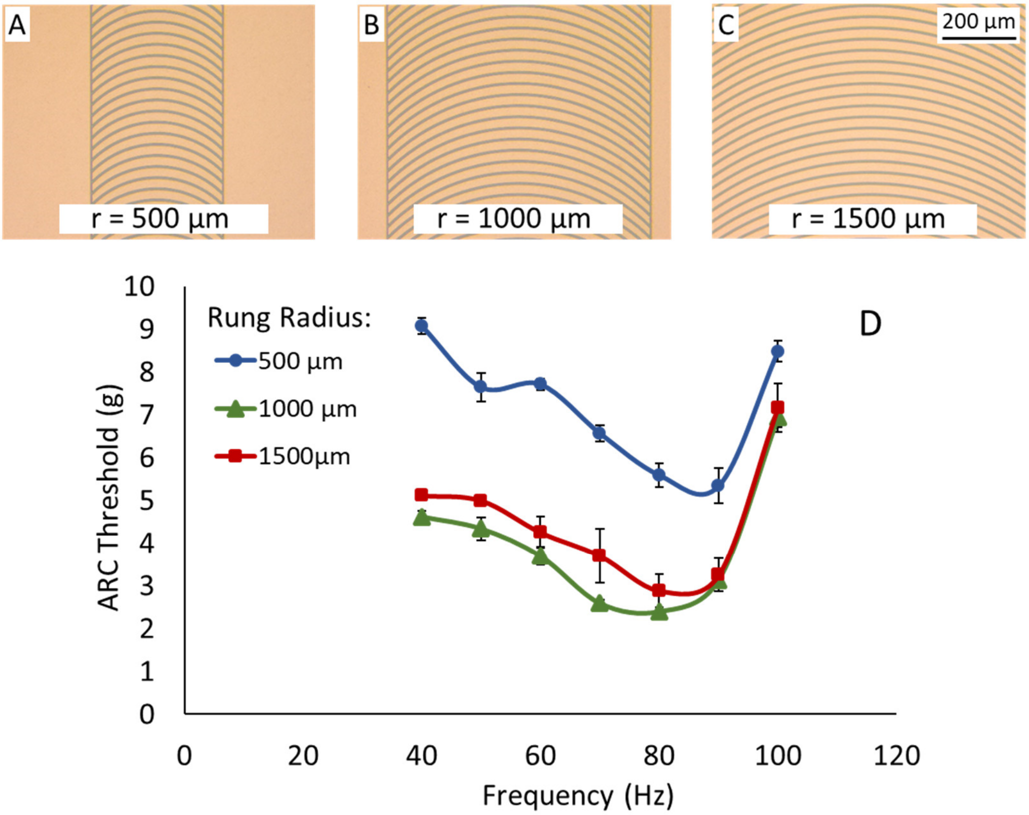

Figure D.1: Rung radius of SiO_2 ARCs influences acceleration amplitude. Water droplets (10 µL; n=3) were transported on silicon oxide ARCs (duty cycle = 16.6%) with a radius of 500 (A), 1000 (B), and 1500 µm (C). The acceleration amplitude was substantially lower on the 1000 and 1500 µm rungs compared to the 500 µm rungs and slightly lower on the 1000 µm rungs compared to the 1500 µm rungs (D). Error bars indicate ± standard deviation.

However, on textured ARCs, the radius of the rung did not appear to influence ARC threshold, but rather shifted the resonant frequency of the droplet when the radius was increased to 1500 μm.

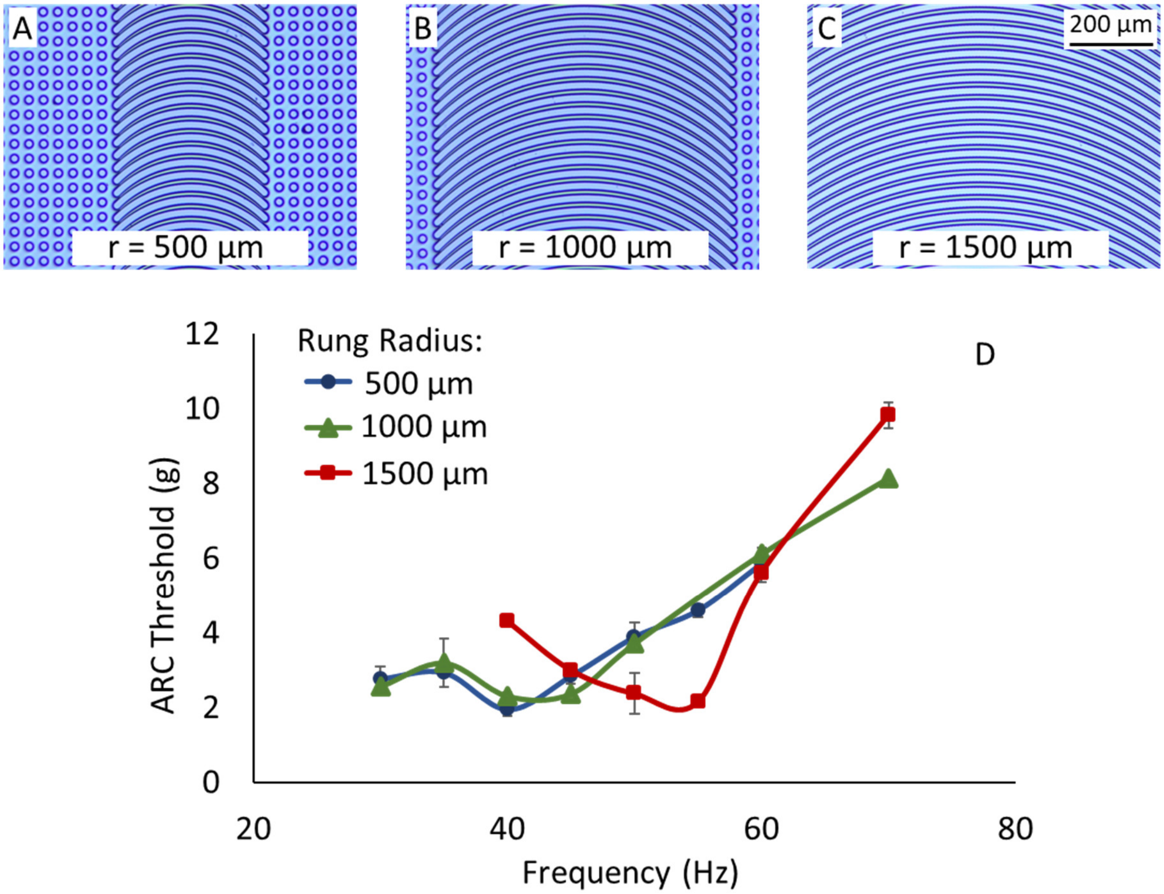

Figure D.2: Resonant frequency is dependent on textured surface feature parameters. Water droplets (10 μL; n=3) were transported on textured rungs (duty cycle = 50%) with a radius of 500 (A), 1000 (B), and 1500 μm (C). A minimal shift was observed between 500 and 1000 μm rung groups, and the dramatic shift between the 1500 μm group and all other groups (D) indicates that textured surface features influence the resonant frequency of a transported droplet. Error bars indicate ± standard deviation.

These results suggest that the textured ARCs force a stronger conformity of the leading edge to the rung, providing similar differences in pinning forces between leading and trailing edges across all rung radii but also influencing the droplet response and resonant frequency of the system.

Non-dimensionalization of droplet volumes on 1000 µm textured ARCs was also investigated as discussed in Chapter 3. However, it was observed that resonant frequency of 5 µL droplet deviated from the other droplets. Based on the observations of textured ARCs effect on resonant frequency, it was determined that textured ARCs would not be a good platform to begin a model for droplet transport on ARC devices with.

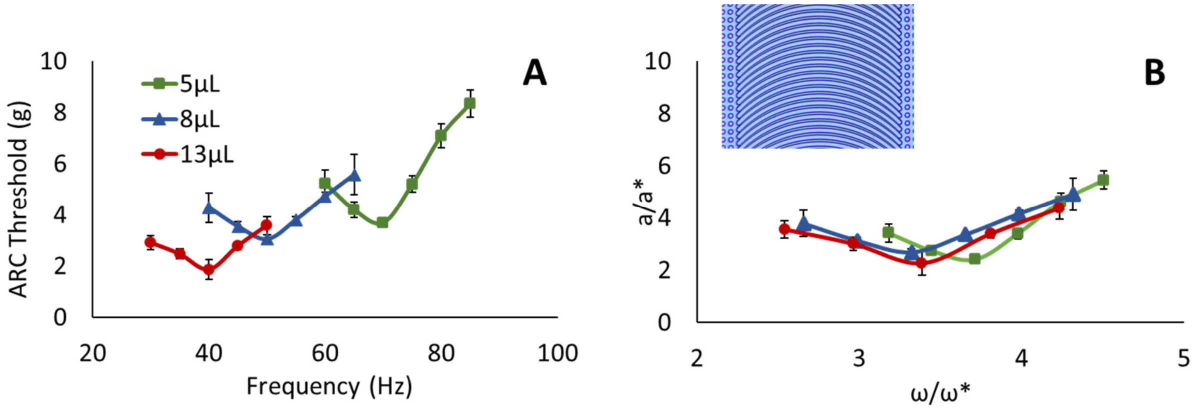

Figure D.3: Non-dimensionalization of texture ARCs. Droplet response profiles for 5, 8, and 13 µL droplets on textured ARCs (A) were non-dimensionalized. While the ARC threshold showed good conformity, the frequency of the 5 µL droplet was shifted (B). This trend was similar to that observed with changing rung radii, indicating that texture ARCs have a considerable influence on the droplet response to vibration frequency. Error bars indicate ±standard deviation.

Recordings of droplet edges 0.5 g below, 0.5 g above, 1 g above, and at the ARC threshold were compiled into a single plot (Figure D.4). This comparison demonstrates that droplet edge movement is still occurring below the ARC threshold but that no progress is being made. At the ARC threshold, the droplet is transported but does not advance every step, and as the vibration amplitude is increased the droplet advances more consistently. This analysis shows that as vibration amplitude is increased, the probability of the droplet taking a step forward (leading edge does not slip) during each vibration cycle is also increased, which results in faster droplet transport.

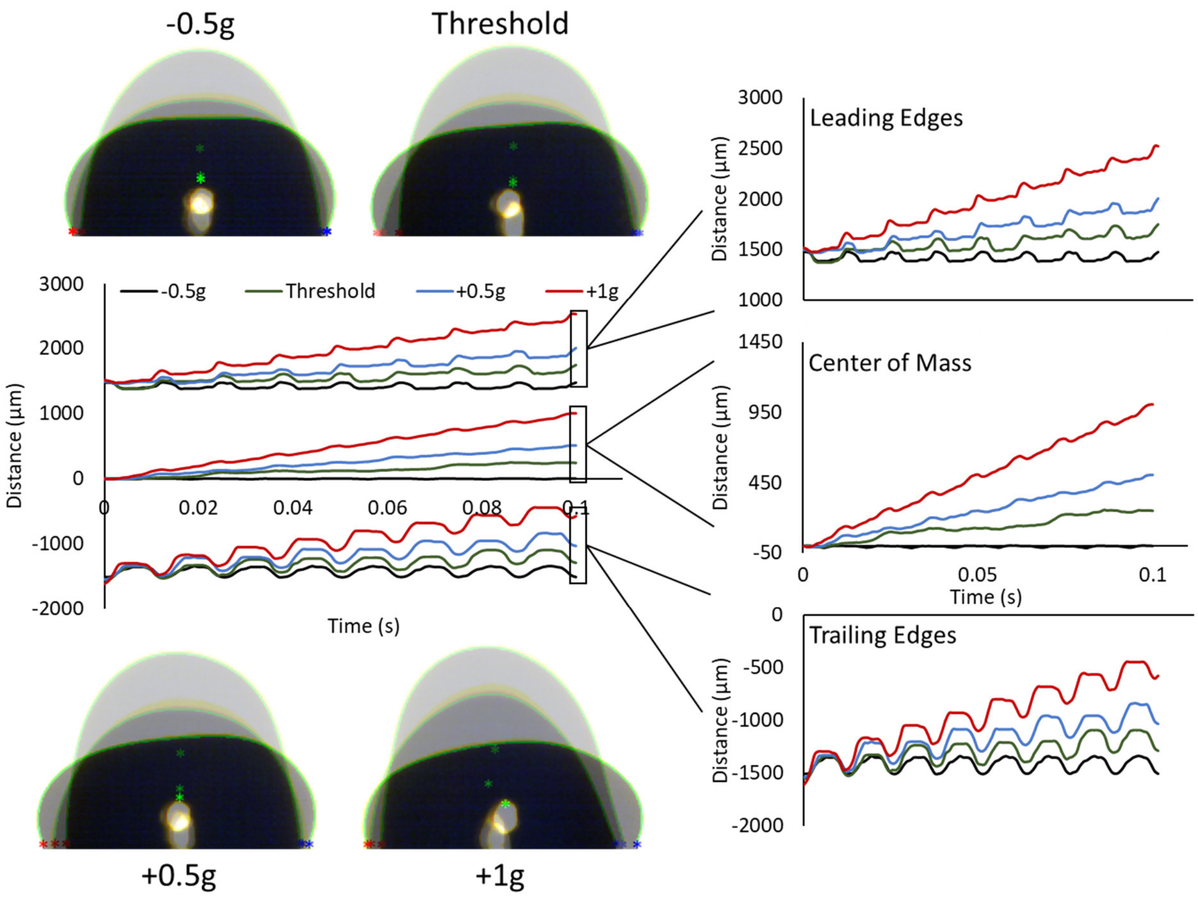

Figure D.4: Effect of vibration amplitude on edge movement. Droplets (10 µL) driven at 80 Hz with vibrations 0.5 g below, 0.5 g above, 1 g above, and at the ARC threshold were recorded and edge movement was analyzed.

The position of droplet centroids recorded in this analysis were also plotted with respect to time (Figure D.5). The cycling patterns of the centroids mimic the edge movement, as the centroid continuously circles below the ARC threshold, advances on some steps but repeats on itself at the ARC threshold and exhibits a more stable pattern of advancing as vibration amplitude is increased. Interestingly, the movement of the droplet centroid appears unstable or noisy at or below the ARC threshold but appears to stabilize as vibration amplitude is increased. This observation suggests that circular, internal flows will be created in the droplet during ARC transport, which could aid in mixing or the formation of nanoparticles.

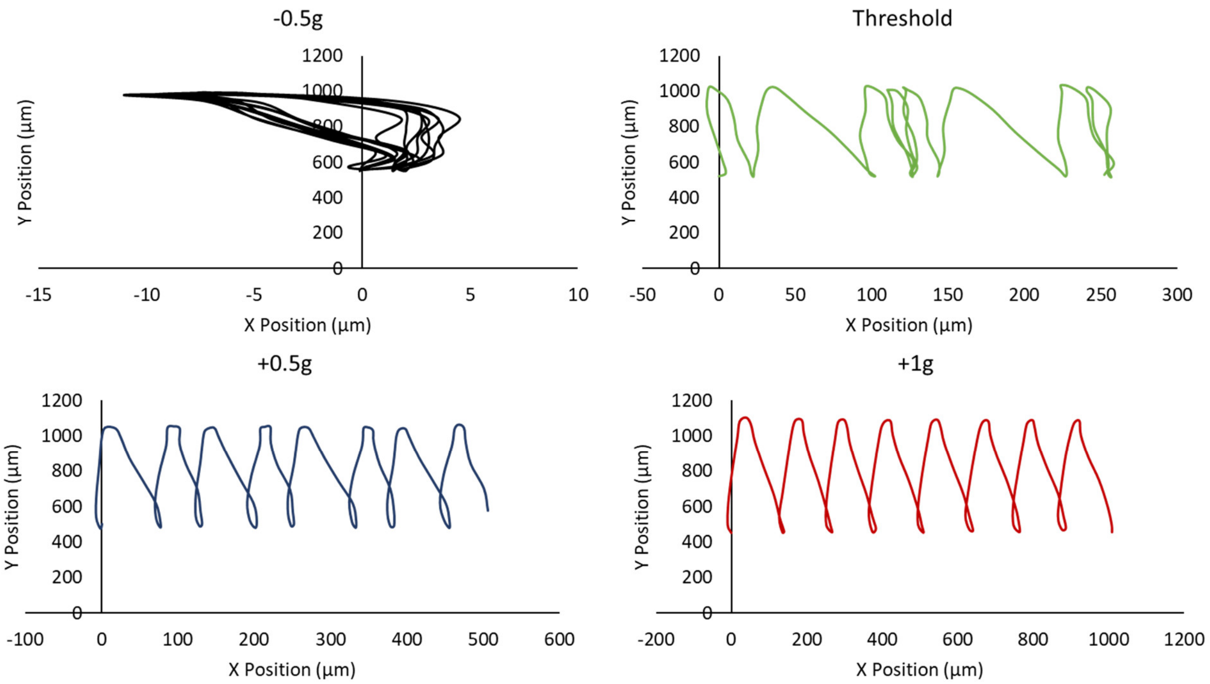

Figure D.5: Droplet centroid cycles during transport. The vertical and horizontal positions of the droplet during transport (80 Hz), show that while the centroid is moving up down, as expected, it is also moving back and forth, creating little circles during transport.

The effect of increasing vibration amplitude on 10/60 and 5/60 tracks was also investigated (Figure D.6). Interestingly, the transport velocity was highest on 10/60 tracks at the ARC threshold but raising vibration amplitude increased the transport velocity only slightly, whereas the transport velocity on the 5/60 track exhibited a large increase when the vibration amplitude was raised to +0.5 g but did not increase further when vibration amplitude was raised to +1.0 g.

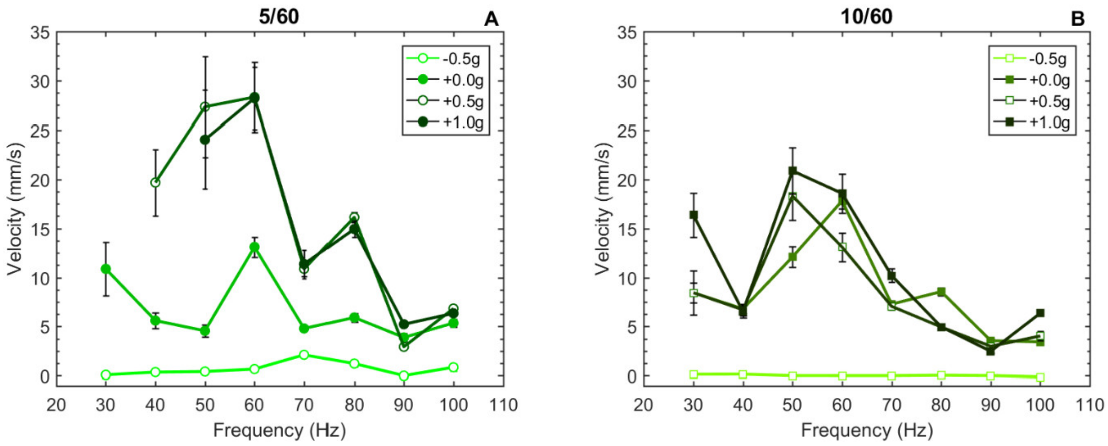

Figure D.6: Maximum transport velocity depends on ARC design and frequency. Increasing vibration amplitude on 5/60 (A) and 10/60 (B) tracks shows that the transport velocity reaches a limit, beyond which further increases in vibration amplitude at that frequency will not increase or may even decrease the transport velocity.

The height of the droplet was also compared to the movement of the substrate. These measurements indicate that the droplet slightly lags the substrate, which may provide some explanation for the cycling effect of the droplet centroids during transport.

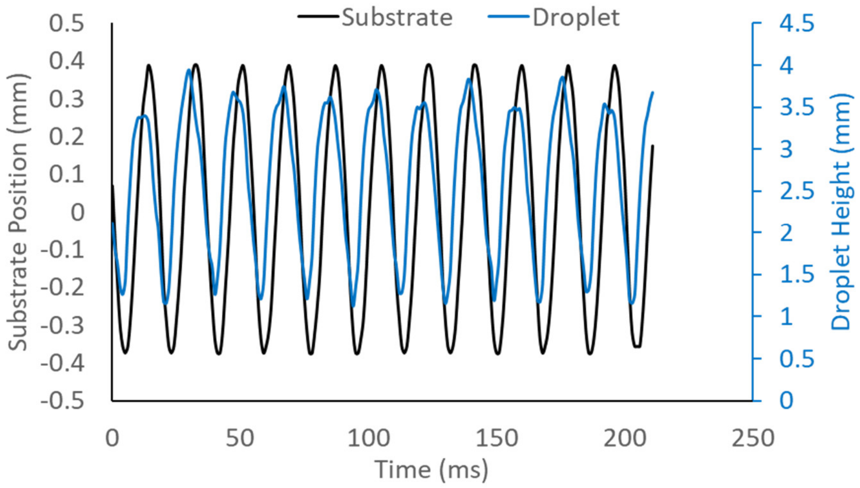

Figure D.7: Phase delay. The sinusoidal height of the droplet lags slightly from the sinusoidal position of the vibrated substrate.

APPENDIX E: ADDITIONAL DNA BIT DEVELOPMENTS AND CHARACTERIZATIONS

Measurements of the substrate actuation created by the electromagnetic motor used for laboratory experiments and the solenoid used in the portable system demonstrate that the solenoid can produce a sinusoid pattern that is slight sawtooth in shape (Figure E.1). The ability of the ARC devices to enable droplet transport with this waveform demonstrates the robustness of the design of this surface pattern.

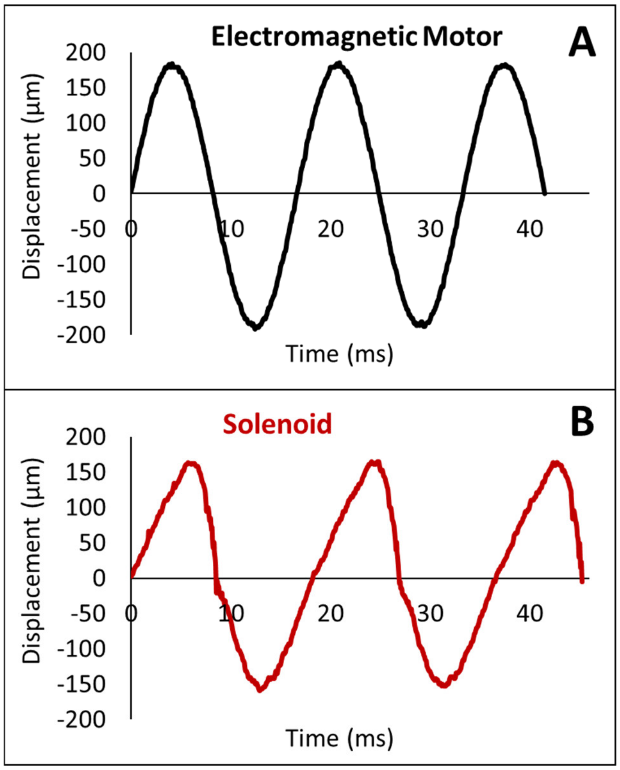

Figure E.1: Solenoid provides sufficient sinusoidal vibration. The sinusoidal motion of from a high-end electromagnetic motor (A) used for laboratory testing is roughly approximated with an inexpensive DC solenoid (B) operated by an Arduino Uno. The slightly sawtooth waveform of the solenoid could be further improved by adding an additional spring to the solenoid and chip holder.

A CMOS camera (Arducam OV2640) was programmed to capture images of droplets on the microheaters. The sensitivity of the color channels was investigated by varying the pH of droplets containing a pH indicator (Figure E.2). This effort demonstrates that a simple camera system can serve as a detector for changes in droplet properties. Future work looks to create a fluorescent detection system this configuration.

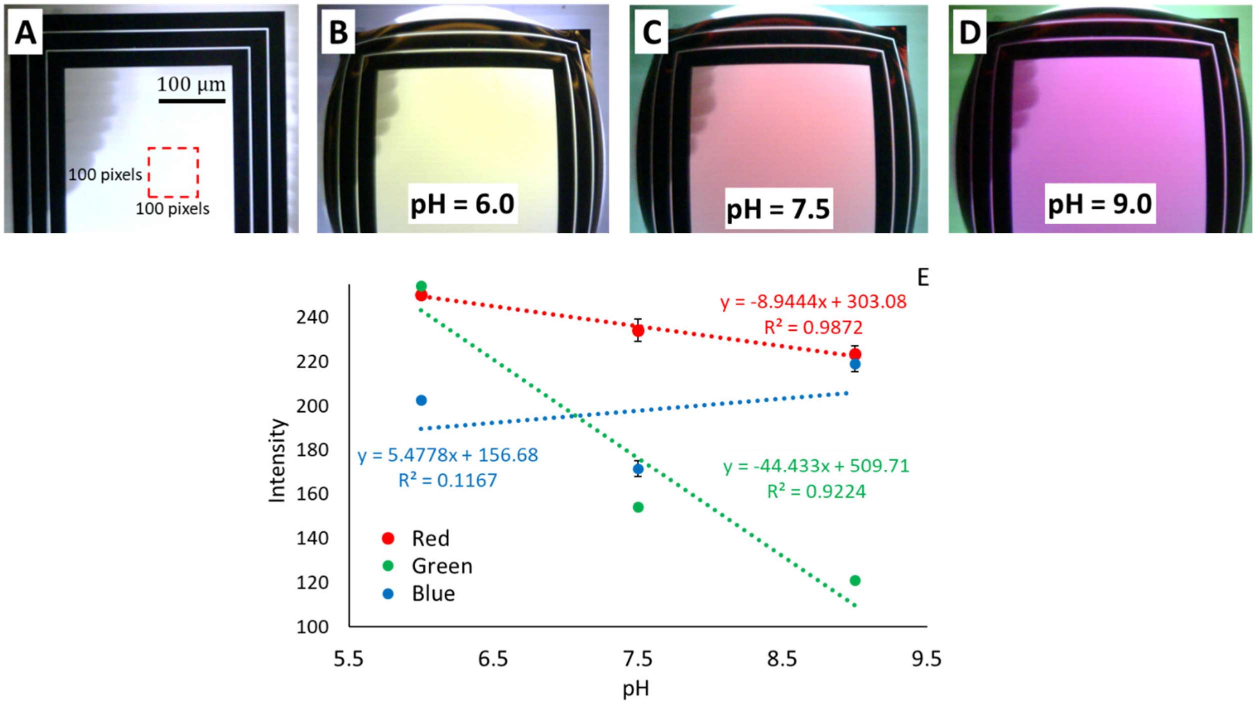

Figure E.2: Arduino driven camera shows good sensitivity to pH changes in phenol red. Images of droplets on microheaters were captured and analyzed in a 100 by 100 pixel region (A) for pH 6.0 (B), 7.5 (C), and 9.0 (D). The green channel exhibited to greatest sensitivity to pH change in phenol red ~44 units of intensity per pH value (E). Based on the standard deviation (n = 3 samples per group), this sensitivity corresponds to a detection limit of ±0.1 pH. Error bars indicate ± standard deviation.

Although further work will be required before the ARC isothermal chip will be ready for commercialization for use with DNA-confined samples. The ability to perform amplification on chip presents a substantial utility for applications in conservation that require analysis of DNA-ready samples. Therefore, this system was also adapted to a simplified chipset to drive isothermal amplification. On this chipset, a microheater is surrounded by a PDMS gasket to form a confined well. This encapsulation effectively prevented evaporation for 60 minute amplification reactions (Figure E.3).

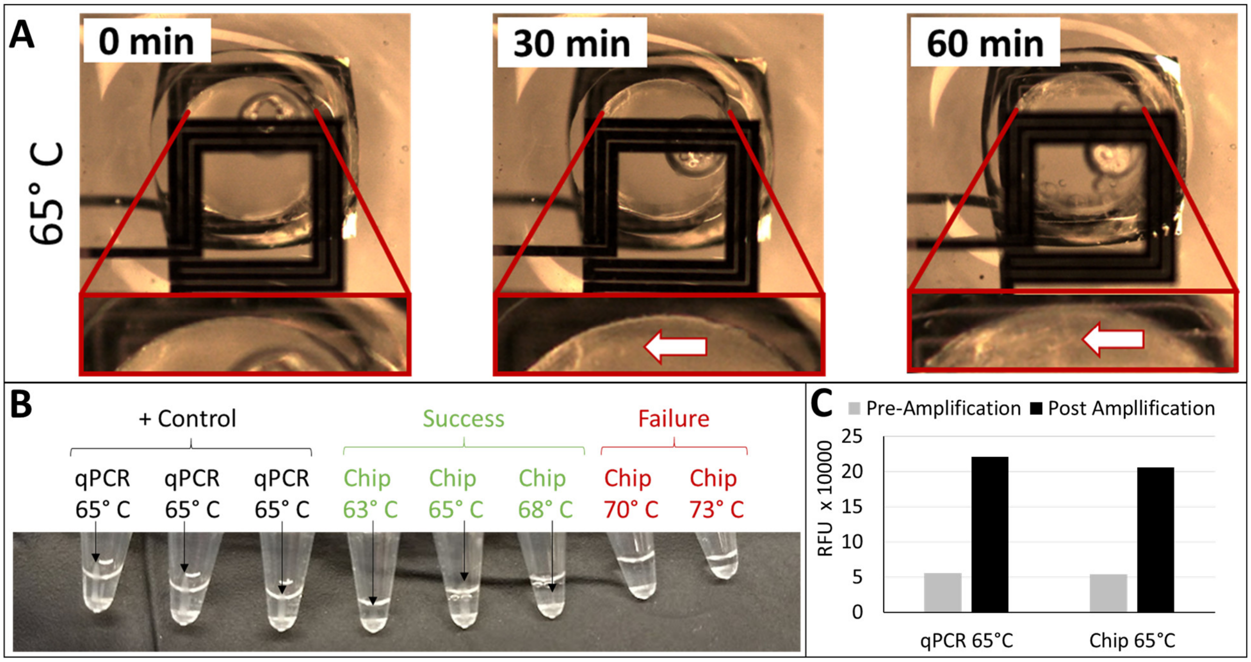

Figure E.3: DNA-ready wells enable isothermal amplification. A turbidimetric reagent set can be monitored through the course of an isothermal amplification with a camera (A). DNA-ready wells can be easily tuned to characterize the effect of different amplification temperatures on the reaction success (B). Amplification in DNA-ready wells is comparable to the results of amplification in a qPCR (C).

The DNA-ready chipset was expanded to define nine-wells with a meandering microheater and complementary gasket. The nine-well chipset is contained within the same cartridge system as the isothermal ARC chip, which will facilitate integration of future chipsets and developments. A user-friendly driving system was developed with feedback from personal interviews with officers at the Washington Department of Fish and Wildlife. This unit interfaces with the user through a simple LCD screen and button panel. A sliding platform that accommodates the cartridge and chipset that positions the cartridge under a CMOS camera housed in the driving unit (Figure E.4). A card-edge connector links the microheaters to the driving circuitry.

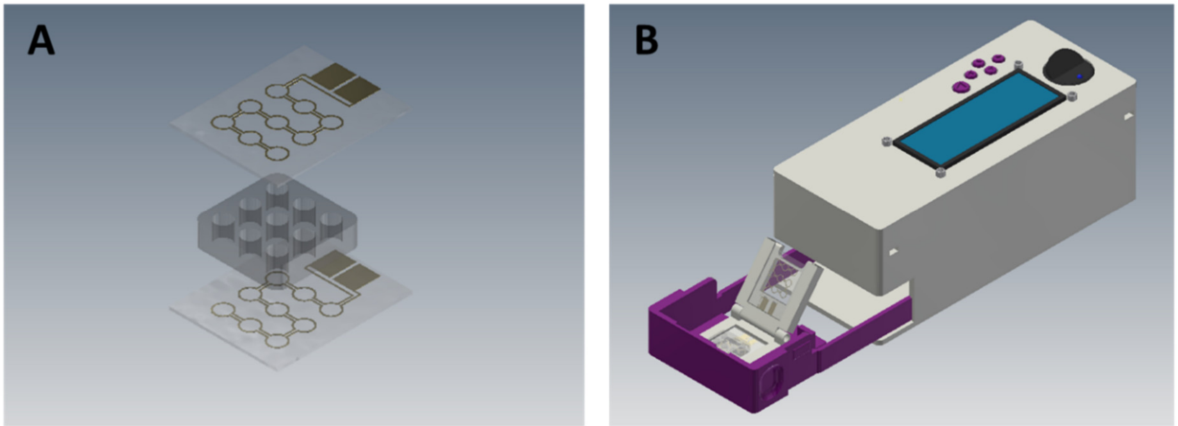

Figure E.4: Design of DNA-Ready amplification system. A nine-well DNA-ready chipset allows for multiple assays to be simultaneously performed (A) and can be driven with a handled control unit (B).

A custom voltage amplifier was designed to control the temperature of the droplets (Figure E.5). In this circuit, an inductor is connected to the +5V power supply, in series with this inductor are a MOSFET and a capacitor (which are connected in parallel. The gate of the MOSFET is connected to a pin on the microcontroller board, in a similar fashion as the portable driving unit. When a signal from this pin is applied to the gate, the circuit will be connected and current will flow through the inductor, building up a magnetic field. When the signal applied to the gate of the MOSFET is removed, the current will cease, but a magnetic field will persist in the inductor. The inductor must discharge the magnetic field, but the path through the MOSFET is an open circuit when the gate voltage is off. Therefore, the inductor discharges across the capacitor, building up a voltage.

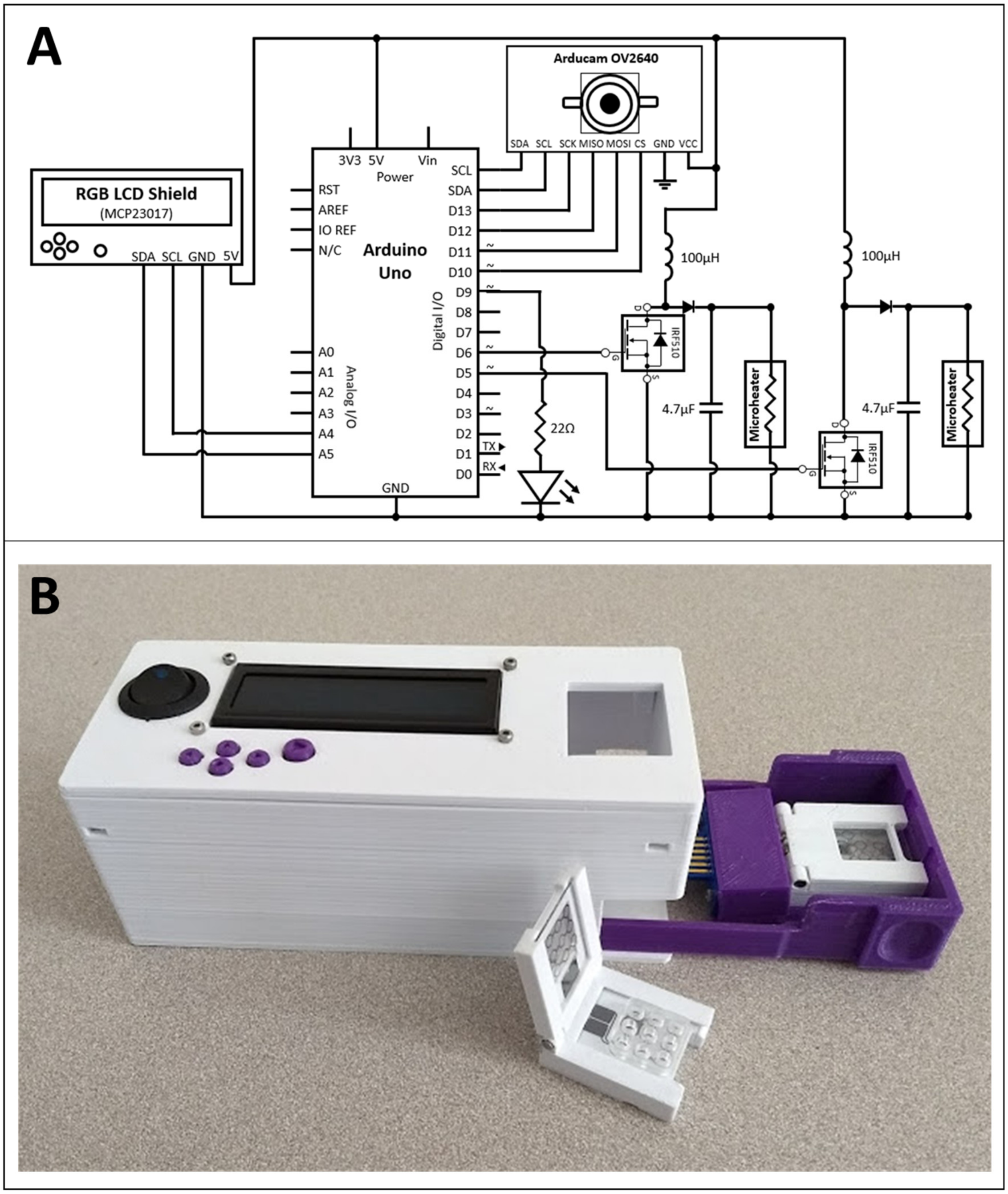

Figure E.5: Realization of the DNA BIT. The portable BIT prototype is controlled by an Arduino Uno (A). An LCD screen provides a user interface and a miniature CMOS camera serves as a detection system. Microheater temperature is controlled by the Arduino through custom circuitry. The physical prototype is produced with 3D printer and traditional fabrication techniques (B). The slider and cartridge set are designed for ease-of-use by a non-technical user.

The voltage on the capacitor will increase every time the switch is cycled on the MOSFET. To prevent the capacitor from discharging back into the inductor, a diode is placed between the two. When a load (i.e. a microheater) is applied across the capacitor it will discharge. As the capacitor discharges, the voltage will be decreased, but at a sort of equilibrium point, the discharge rate of the capacitor will match the charging rate of the inductor due to the switching of the MOSFET. This DNA BIT prototype provides a platform with the modular architecture envisioned in Chapter 6. The on-board control hardware is adaptable to large variety of additional sensors for environmental variables of interest and the user interface is programmable to suit the needs of many different users and use cases. While the DNA-ready shipset is a much simpler diversion from the isothermal ARC chip, it provides a highly customizable system that can provide a level of multiplicity and ease of use that could not be accomplished with traditional tube based field-tests.

The ability to isolate magnetic beads in droplet driven on ARC surfaces was also investigated. It was initially hypothesized that a strong magnet could collect magnetic beads transported in droplets on ARC devices. To accomplish this, a setup was created that separated the ARC substrate from the magnetic field of the electromagnetic motor. A permanent neodymium magnetic was attached to the bottom of the substrate beneath the ARC device (Figure E.6). A solution containing surfactant coated 100 μm magnetic beads with a density of 1.1 g/cm^3 (Cospheric) in diH_2O was created for ARC transport.

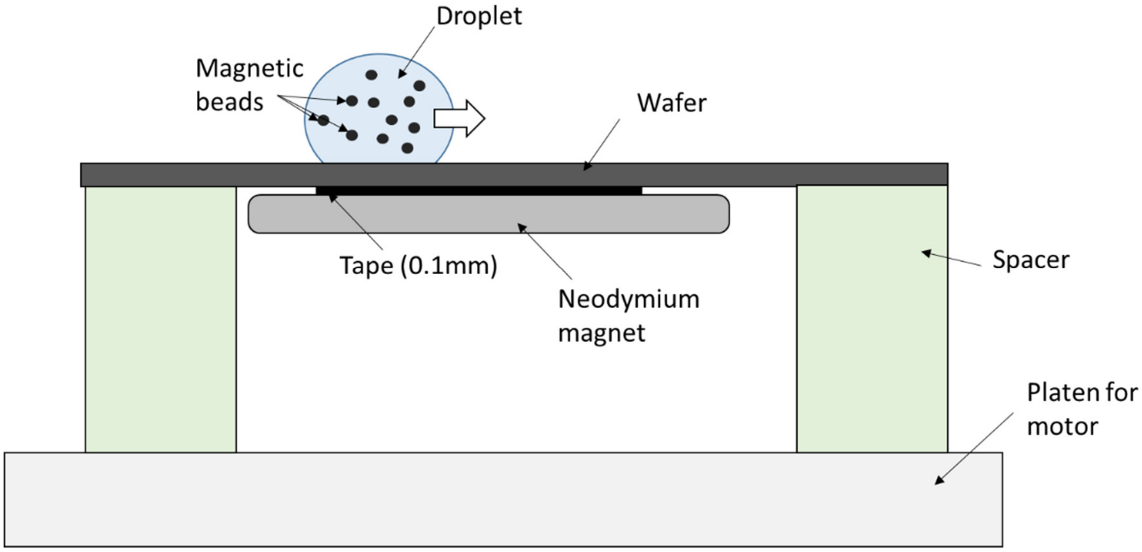

Figure E.6: Magnetic bead separation set-up. In attempt to separate magnetic beads from droplets during transport, a neodymium magnet was placed beneath the ARC substrate. Droplets containing magnetic beads were transport on ARC devices with and without the magnet.

Without the magnet present, beads stayed suspended within the droplet, exhibit small circular motion as expected. However, when these droplets were transported over the magnet, all of the beads aligned within the droplet. This affect did not appear to slow the droplet nor was the magnet able to pull magnetic beads out of the droplet – even if the droplet was allowed to remain at rest on the magnetic prior to transport. While this observation demonstrates the use of magnetic beads is not a promising method for sample preparation on ARC devices, this approach could provide a means of studying droplet transport forces.

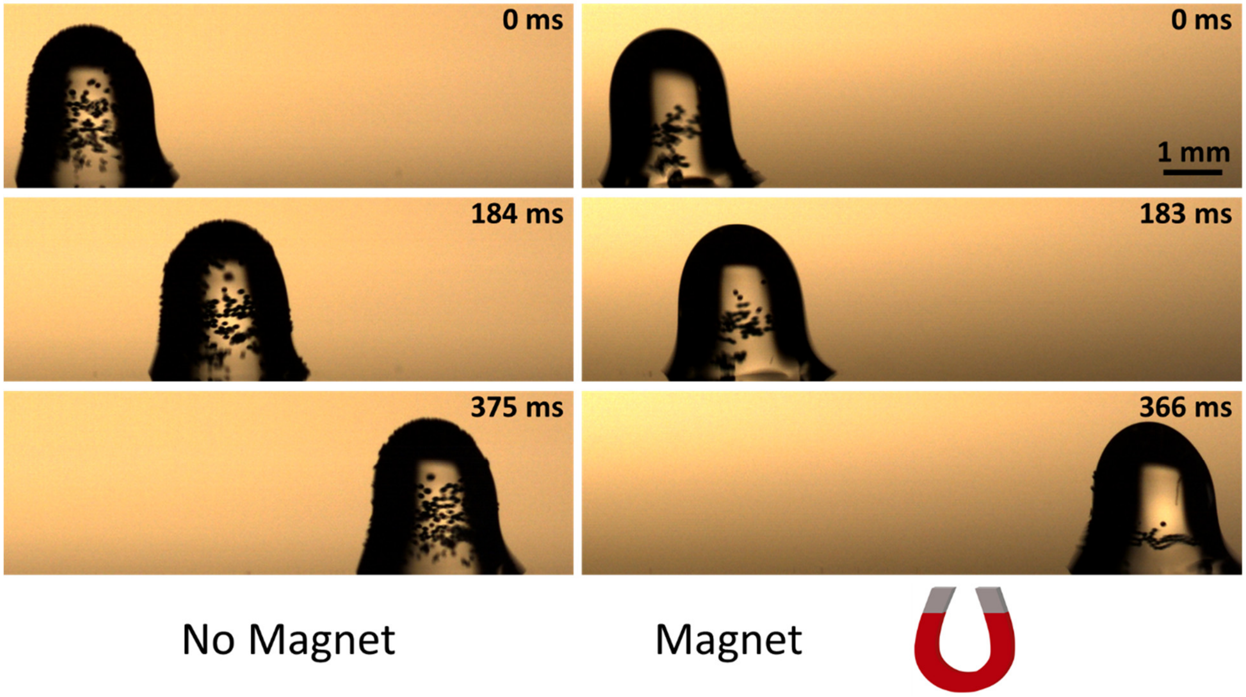

Figure E.7: Magnetic beads align in droplets when a magnetic field is present. Paramagnetic beads (~100 µm diameter – Cospheric) can be transported in droplets on ARCs. Upon passing over a permanent magnet, the beads in the droplet align in the droplet, but are not deposited onto the surface of the substrate.

Initial investigations with timber looked at DNA content in *Pinus strobus* (eastern white pine) and *Swietenia microphylla* (Honduran mahogany). Sections 2 µm in thickness were prepared by a microtome. These sections were then stained with an intercalating dye (ethidium bromide) to spatial identify the location of DNA within these samples (Figure E.8). Fluorescent images of these sections suggest that the DNA is sequestered between cell walls in timber. This finding indicates that while DNA is still present in commercial timber specimens, it is encapsulated by the cell walls, providing a substantial barrier to DNA extraction. This observation implies that simple rupture of the cell wall will not be sufficient to liberate target DNA and that a considerable amount of tissue will have to be dissolved or degraded to access target DNA.

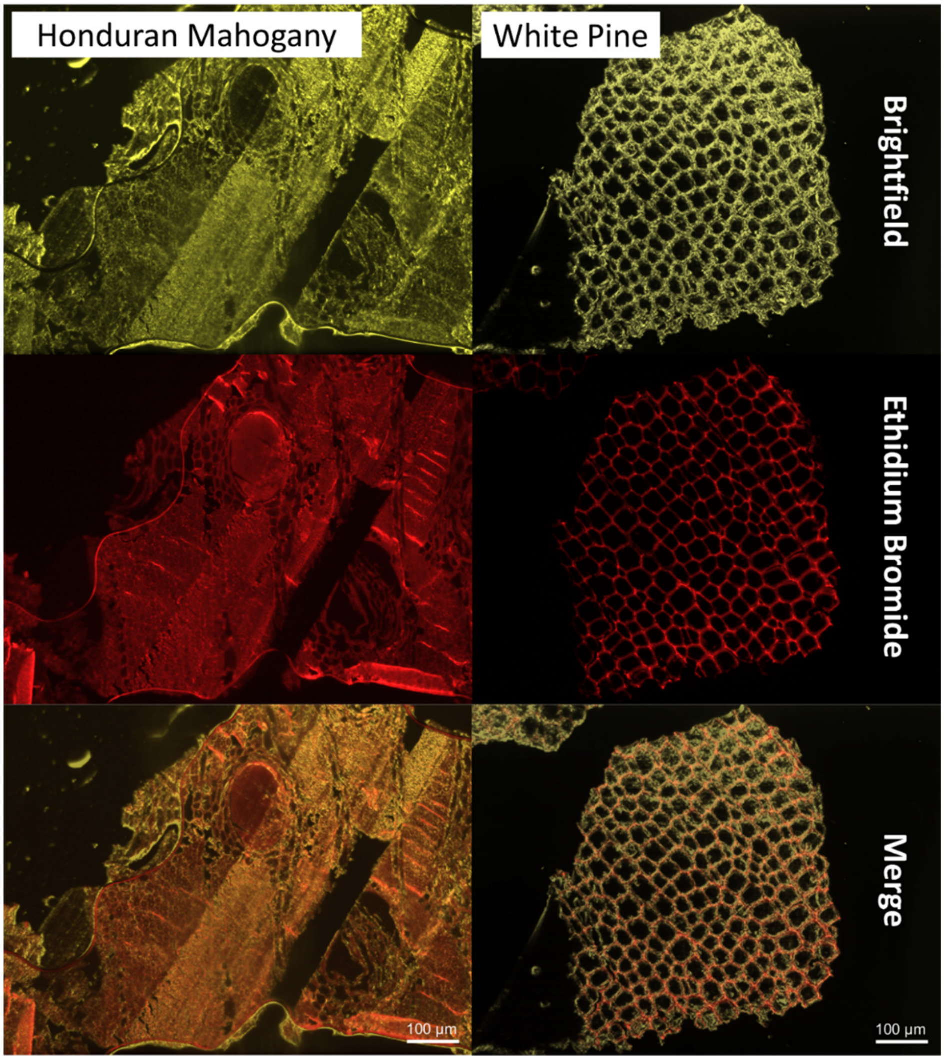

Figure E.8: DNA is sequestered in commercial timber samples. Samples of Honduran mahogany (*Swietenia microphylla*) and eastern white pine (*Pinus strobus*) from commercial woodworking products were sectioned with a microtome (Leica) and stained with ethidium bromide (an intercalating dye for GC rich regions). These sections show that DNA is still present in processed, commercial timber products, but the DNA is sequestered and embedded into the cell walls of the timber tissue.

Particles of *P. strobus* were deposited on a substrate with an ARC track. The transport of a droplet across these particles resulted in capture and transport (Figure E.9). This finding suggests that ARC could be used as a vehicle for timber specimens in on-chip sample preparation regimen for these samples can be developed.

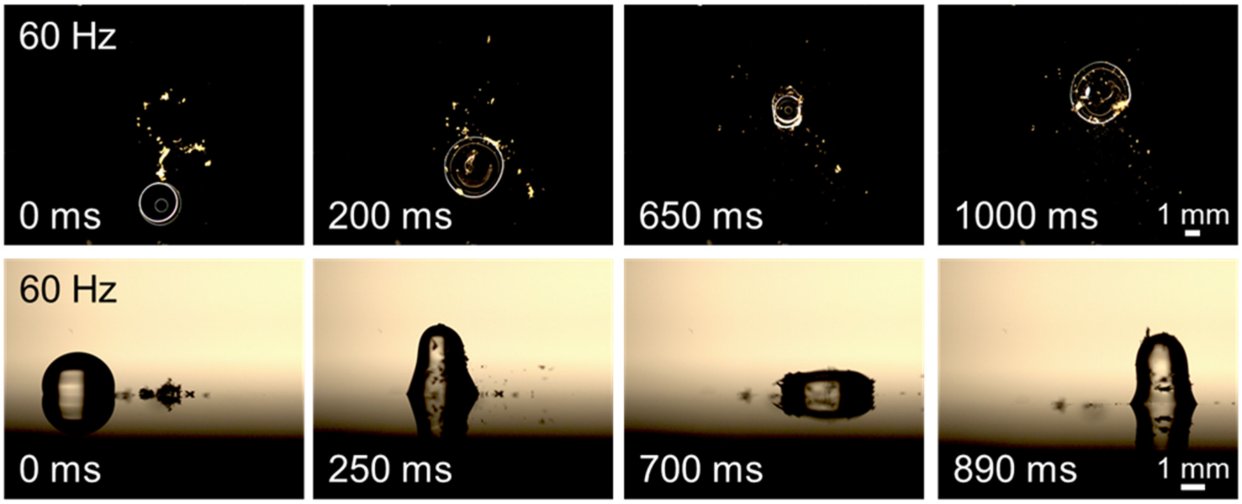

Figure E.9: ARC transport of *Pinus strobus* sawdust particles. Particles from a rotary sander were placed on the surface of an ARC chip. A 10 μL droplet was then placed on an ARC track and transported with 60 Hz vibrations (5.2 g or 360 μm amplitude). Droplet transport was recorded from top (top panel) and side (bottom panel) perspectives. Recordings show droplets capturing and transporting a majority of deposited sawdust particles.

BIBLIOGRAPHY

(1) Bassous, E.; Taub, H. H.; Kuhn, L. Ink Jet Printing Nozzle Arrays Etched in Silicon. *Applied Physics Letters* **1977**, *31* (2), 135–137.

(2) Petersen, K. E. Fabrication of an Integrated, Planar Silicon Ink-Jet Structure. *IEEE Transactions on Electron Devices* **1979**, *26* (12), 1918–1920.

(3) Terry, S. C.; Jerman, J. H.; Angell, J. B. A Gas Chromatographic Air Analyzer Fabricated on a Silicon Wafer. *IEEE Transactions on Electron Devices* **1979**, *26* (12), 1880–1886.

(4) Tuckerman, D. B.; Pease, R. F. W. High-Performance Heat Sinking for VLSI. *IEEE Electron Device Letters* **1981**, *2* (5), 126–129.

(5) Zdeblick, M. J.; Barth, P. P.; Angell, J. B. A Microminiature Fluidic Amplifier. *Sensors and Actuators* **1988**, *15* (4), 427–433.

(6) Gravesen, P.; Branebjerg, J.; Jensen, O. S. Microfluidics - A Review. *Journal of Micromechanics and Microengineering* **1993**, *3* (4), 168.

(7) Petersen, K. E. Silicon as a Mechanical Material. *Proceedings of the IEEE* **1982**, *70* (5), 420–457.

(8) Tiren, J.; Tenerz, L.; Hök, B. A Batch-Fabricated Non-Reverse Valve with Cantilever Beam Manufactured by Micromachining of Silicon. *Sensors and Actuators* **1989**, *18* (3–4), 389–396.

(9) Ohnstein, T.; Fukiura, T.; Ridley, J.; Bonne, U. Micromachined Silicon Microvalve. In *IEEE Proceedings on Micro Electro Mechanical Systems, An Investigation of Micro Structures, Sensors, Actuators, Machines and Robots.*; IEEE: Napa Valley, 1990; pp 95–98.

(10) Jerman, J. H. Electrically-Activated, Micromachined Diaphragm Valves. In *Micro System Technologies 90*; Springer, 1990; pp 806–811.

(11) Smits, J. G. Piezoelectric Micropump with Three Valves Working Peristaltically. *Sensors and Actuators A: Physical* **1990**, *21* (1–3), 203–206.

(12) Gass, V.; Van der Schoot, B. H.; Jeanneret, S.; De Rooij, N. F. Integrated Flow-Regulated Silicon Micropump. *Sensors and Actuators A: Physical* **1994**, *43* (1–3), 335–338.

(13) Judy, J. W.; Tamagawa, T.; Polla, D. L. Surface-Machined Micromechanical Membrane Pump. In *Proceedings. IEEE Micro Electro Mechanical Systems*; IEEE: Nara, 1991; pp 182–186.

(14) Richter, A.; Plettner, A.; Hofmann, K. A.; Sandmaier, H. A Micromachined Electrohydrodynamic (EHD) Pump. *Sensors and Actuators A: Physical* **1991**, *29* (2), 159–168.

(15) Richter, A.; Hofmann, K. A.; Plettner, A.; Sandmaier, H. The Electrohydrodynamic Micro Flow Meter. In *Solid-State Sensors and Actuators, 1991. Digest of Technical Papers,*

TRANSDUCERS ’91., 1991 International Conference on,; IEEE: San Francisco, 1991; pp 935–938.

(16) Branebjerg, J.; Jensen, O. S.; Laursen, N. G.; Leistiko, O.; Soeberg, H. A Micromachined Flow Sensor for Measuring Small Liquid Flows. In *Solid-State Sensors and Actuators, 1991. Digest of Technical Papers, TRANSDUCERS’91., 1991 International Conference on*; IEEE, 1991; pp 41–44.

(17) Yang, C.; Søeberg, H. Monolithic Flow Sensor for Measuring Millilitre per Minute Liquid Flow. *Sensors and Actuators A: Physical* **1992**, *33* (3), 143–153.

(18) Lammerink, T. S.; Tas, N. R.; Elwenspoek, M.; Fluitman, J. H. Micro-Liquid Flow Sensor. *Sensors and actuators A: Physical* **1993**, *37*, 45–50.

(19) Shoji, S.; Esashi, M.; Matsuo, T. Prototype Miniature Blood Gas Analyser Fabricated on a Silicon Wafer. *Sensors and Actuators* **1988**, *14* (2), 101–107.

(20) Nakagawa, S.; Shoji, S.; Esashi, M. A Micro Chemical Analyzing System Integrated on a Silicon Wafer. In *IEEE Proceedings on Micro Electro Mechanical Systems, An Investigation of Micro Structures, Sensors, Actuators, Machines and Robots.*; IEEE: Napa Valley, 1990; pp 89–94.

(21) Zimmerman, W. B. J. *Microfluidics: History, Theory and Applications*; Springer Science & Business Media, 2006.

(22) Zhao, X.-M.; Xia, Y.; Whitesides, G. M. Soft Lithographic Methods for Nano-Fabrication. *Journal of Materials Chemistry* **1997**, *7* (7), 1069–1074.

(23) Whitesides, G. M.; Ostuni, E.; Takayama, S.; Jiang, X.; Ingber, D. E. Soft Lithography in Biology and Biochemistry. *Annual Review of Biomedical Engineering* **2001**, *3* (1), 335–373.

(24) Ziaie, B.; Baldi, A.; Lei, M.; Gu, Y.; Siegel, R. A. Hard and Soft Micromachining for BioMEMS: Review of Techniques and Examples of Applications in Microfluidics and Drug Delivery. *Advanced Drug Delivery Reviews* **2004**, *56* (2), 145–172.

(25) Kim, P.; Kwon, K. W.; Park, M. C.; Lee, S. H.; Kim, S. M.; Suh, K. Y. Soft Lithography for Microfluidics: A Review. *BioChip Journal* **2008**, *2*, 1–11.

(26) Jo, B.-H.; Beebe, D. J. Fabrication of Three-Dimensional Microfluidic Systems by Stacking Molded Polydimethylsiloxane (PDMS) Layers. In *Proc. SPIE 3877, Microfluidic Devices and Systems II*; International Society for Optics and Photonics: Santa Clara, 1999; pp 222–229.

(27) Anderson, J. R.; Chiu, D. T.; Jackman, R. J.; Cherniavskaya, O.; McDonald, J. C.; Wu, H.; Whitesides, S. H.; Whitesides, G. M. Fabrication of Topologically Complex Three-Dimensional Microfluidic Systems in PDMS by Rapid Prototyping. *Analytical chemistry* **2000**, *72* (14), 3158–3164.

(28) Folch, A. *Introduction to BioMEMS*; CRC Press, 2012.

(29) Martinez, A. W.; Phillips, S. T.; Butte, M. J.; Whitesides, G. M. Patterned Paper as a Platform for Inexpensive, Low-Volume, Portable Bioassays. *Angewandte Chemie International Edition* **2007**, *46* (8), 1318–1320.

(30) Martinez, A. W.; Phillips, S. T.; Whitesides, G. M. Three-Dimensional Microfluidic Devices Fabricated in Layered Paper and Tape. *Proceedings of the National Academy of Sciences* **2008**, *105* (50), 19606–19611.

(31) Li, X.; Ballerini, D. R.; Shen, W. A Perspective on Paper-Based Microfluidics: Current Status and Future Trends. *Biomicrofluidics* **2012**, *6* (1), 011301.

(32) Pollock, N. R.; Rolland, J. P.; Kumar, S.; Beattie, P. D.; Jain, S.; Noubary, F.; Wong, V. L.; Pohlmann, R. A.; Ryan, U. S.; Whitesides, G. M. A Paper-Based Multiplexed Transaminase Test for Low-Cost, Point-of-Care Liver Function Testing. *Science Translational Medicine* **2012**, *4* (152), 152ra129-152ra129.

(33) Yetisen, A. K.; Akram, M. S.; Lowe, C. R. Paper-Based Microfluidic Point-of-Care Diagnostic Devices. *Lab on a Chip* **2013**, *13* (12), 2210–2251.

(34) Teh, S.-Y.; Lin, R.; Hung, L.-H.; Lee, A. P. Droplet Microfluidics. *Lab on a Chip* **2008**, *8* (2), 198–220.

(35) Theberge, A. B.; Courtois, F.; Schaerli, Y.; Fischlechner, M.; Abell, C.; Hollfelder, F.; Huck, W. T. Microdroplets in Microfluidics: An Evolving Platform for Discoveries in Chemistry and Biology. *Angewandte Chemie International Edition* **2010**, *49* (34), 5846–5868.

(36) i Solvas, X. C.; deMello, A. Droplet Microfluidics: Recent Developments and Future Applications. *Chemical Communications* **2011**, *47* (7), 1936–1942.

(37) Umbanhowar, P. B.; Prasad, V.; Weitz, D. A. Monodisperse Emulsion Generation via Drop Break off in a Coflowing Stream. *Langmuir* **2000**, *16* (2), 347–351.

(38) Thorsen, T.; Roberts, R. W.; Arnold, F. H.; Quake, S. R. Dynamic Pattern Formation in a Vesicle-Generating Microfluidic Device. *Physical Review Letters* **2001**, *86* (18), 4163.

(39) Anna, S. L.; Bontoux, N.; Stone, H. A. Formation of Dispersions Using “Flow Focusing” in Microchannels. *Applied Physics Letters* **2003**, *82* (3), 364–366.

(40) Huebner, A.; Srisa-Art, M.; Holt, D.; Abell, C.; Hollfelder, F.; deMello, A. J.; Edel, J. B. Quantitative Detection of Protein Expression in Single Cells Using Droplet Microfluidics. *Chemical Communications* **2007**, *0*, 1218–1220.

(41) Huebner, A.; Bratton, D.; Whyte, G.; Yang, M.; deMello, A. J.; Abell, C.; Hollfelder, F. Static Microdroplet Arrays: A Microfluidic Device for Droplet Trapping, Incubation and Release for Enzymatic and Cell-Based Assays. *Lab on a Chip* **2009**, *9* (5), 692–698.

(42) Mazutis, L.; Gilbert, J.; Ung, W. L.; Weitz, D. A.; Griffiths, A. D.; Heyman, J. A. Single-Cell Analysis and Sorting Using Droplet-Based Microfluidics. *Nature Protocols* **2013**, *8* (5), 870–891.

(43) Zheng, B.; Roach, L. S.; Ismagilov, R. F. Screening of Protein Crystallization Conditions on a Microfluidic Chip Using Nanoliter-Size Droplets. *Journal of the American Chemical Society* **2003**, *125* (37), 11170–11171.

(44) Song, H.; Chen, D. L.; Ismagilov, R. F. Reactions in Droplets in Microfluidic Channels. *Angewandte Chemie International Edition* **2006**, *45* (44), 7336–7356.

(45) deMello, A. J. Control and Detection of Chemical Reactions in Microfluidic Systems. *Nature* **2006**, *442* (7101), 394–402.

(46) Abdelgawad, M.; Wheeler, A. R. The Digital Revolution: A New Paradigm for Microfluidics. *Advanced Materials* **2009**, *21* (8), 920–925.

(47) Holmes, H. R.; Böhringer, K. F. Transporting Droplets through Surface Anisotropy. *Microsystems & Nanoengineering* **2015**, *1*.

(48) Mosadegh, B.; Kuo, C.-H.; Tung, Y.-C.; Torisawa, Y.; Bersano-Begey, T.; Tavana, H.; Takayama, S. Integrated Elastomeric Components for Autonomous Regulation of Sequential and Oscillatory Flow Switching in Microfluidic Devices. *Nature Physics* **2010**, *6* (6), 433–437.

(49) Martinez, A. W.; Phillips, S. T.; Whitesides, G. M.; Carrilho, E. Diagnostics for the Developing World: Microfluidic Paper-Based Analytical Devices. *Analytical Chemistry* **2010**, *82* (1), 3–10.

(50) Huebner, A.; Sharma, S.; Srisa-Art, M.; Hollfelder, F.; Edel, J. B.; others. Microdroplets: A Sea of Applications? *Lab on a Chip* **2008**, *8* (8), 1244–1254.

(51) Abdelgawad, M.; Freire, S. L.; Yang, H.; Wheeler, A. R. All-Terrain Droplet Actuation. *Lab on a Chip* **2008**, *8* (5), 672–677.

(52) Lee, J.; Moon, H.; Fowler, J.; Schoellhammer, T.; Kim, C.-J. Electrowetting and Electrowetting-on-Dielectric for Microscale Liquid Handling. *Sensors and Actuators A: Physical* **2002**, *95* (2–3), 259–268.

(53) Mugele, F.; Baret, J.-C. Electrowetting: From Basics to Applications. *Journal of Physics: Condensed Matter* **2005**, *17* (28), R705.

(54) Pollack, M. G.; Fair, R. B.; Shenderov, A. D. Electrowetting-Based Actuation of Liquid Droplets for Microfluidic Applications. *Applied Physics Letters* **2000**, *77* (11), 1725–1726.

(55) Chiou, P.-Y.; Chang, Z.; Wu, M. C. Droplet Manipulation with Light on Optoelectrowetting Device. *Journal of Microelectromechanical Systems* **2008**, *17* (1), 133–138.

(56) Darhuber, A. A.; Valentino, J. P.; Troian, S. M.; Wagner, S. Thermocapillary Actuation of Droplets on Chemically Patterned Surfaces by Programmable Microheater Arrays. *Journal of Microelectromechanical Systems* **2003**, *12* (6), 873–879.

(57) Lim, H. S.; Han, J. T.; Kwak, D.; Jin, M.; Cho, K. Photoreversibly Switchable Superhydrophobic Surface with Erasable and Rewritable Pattern. *J. Am. Chem. Soc.* **2006**, *128* (45), 14458–14459.

(58) Brochard, F. Motions of Droplets on Solid Surfaces Induced by Chemical or Thermal Gradients. *Langmuir* **1989**, *5* (2), 432–438.

(59) Brzoska, J. B.; Brochard-Wyart, F.; Rondelez, F. Motions of Droplets on Hydrophobic Model Surfaces Induced by Thermal Gradients. *Langmuir* **1993**, *9* (8), 2220–2224.

(60) Darhuber, A. A.; Valentino, J. P.; Troian, S. M.; Wagner, S. Thermocapillary Actuation of Droplets on Chemically Patterned Surfaces by Programmable Microheater Arrays. *Journal of Microelectromechanical Systems* **2003**, *12* (6), 873–879.

(61) Hazlett, R. D. Fractal Applications: Wettability and Contact Angle. *Journal of Colloid and Interface Science* **1990**, *137* (2), 527–533.

(62) Chaudhury, M. K.; Whitesides, G. M. How to Make Water Run Uphill. *Science* **1992**, *256* (5063), 1539–1541.

(63) Ichimura, K.; Oh, S.-K.; Nakagawa, M. Light-Driven Motion of Liquids on a Photoresponsive Surface. *Science* **2000**, *288* (5471), 1624–1626.

(64) Kekkonen, V.; Hakola, A.; Kajava, T.; Sahramo, E.; Malm, J.; Karppinen, M.; Ras, R. H. A. Self-Erasing and Rewritable Wettability Patterns on ZnO Thin Films. *Applied Physics Letters* **2010**, *97* (4), 044102.

(65) Noblin, X.; Buguin, A.; Brochard-Wyart, F. Vibrated Sessile Drops: Transition between Pinned and Mobile Contact Line Oscillations. *European Physical Journal E -- Soft Matter* **2004**, *14* (4), 395–404.

(66) Shastry, A.; Taylor, D.; Böhringer, K. F. Micro-Structured Surface Ratchets for Droplet Transport. In *Solid-State Sensors, Actuators and Microsystems Conference, 2007. TRANSDUCERS 2007. International*; IEEE, 2007; pp 1353–1356.

(67) Duncombe, T. A.; Erdem, E. Y.; Shastry, A.; Baskaran, R.; Böhringer, K. F. Controlling Liquid Drops with Texture Ratchets. *Adv. Mater.* **2012**, *24* (12), 1545–1550.

(68) Duncombe, T. A.; Parsons, J. F.; Böhringer, K. F. Directed Drop Transport Rectified from Orthogonal Vibrations via a Flat Wetting Barrier Ratchet. *Langmuir* **2012**, *28* (38), 13765–13770.

(69) Whyman, G.; Bormashenko, E.; Stein, T. The Rigorous Derivation of Young, Cassie–Baxter and Wenzel Equations and the Analysis of the Contact Angle Hysteresis Phenomenon. *Chemical Physics Letters* **2008**, *450* (4–6), 355–359.

(70) Erdem, E. Y.; Baskaran, R.; Bohringer, K. F. Vibration Induced Droplet Generation on Textured Surfaces. In *Micro Electro Mechanical Systems, 2008. MEMS 2008. IEEE 21st International Conference on*; IEEE, 2008; pp 603–606.

(71) Demirel, M. C. Emergent Properties of Spatially Organized Poly(p-Xylylene) Films Fabricated by Vapor Deposition. *Colloids and Surfaces A: Physicochemical and Engineering Aspects* **2008**, *321* (1–3), 121–124.

(72) Agapov, R. L.; Boreyko, J. B.; Briggs, D. P.; Srijanto, B. R.; Retterer, S. T.; Collier, C. P.; Lavrik, N. V. Length Scale Selects Directionality of Droplets on Vibrating Pillar Ratchet. *Adv. Mater. Interfaces* **2014**, *1* (9), n/a-n/a.

(73) Malvadkar, N. A.; Hancock, M. J.; Sekeroglu, K.; Dressick, W. J.; Demirel, M. C. An Engineered Anisotropic Nanofilm with Unidirectional Wetting Properties. *Nature Materials* **2010**, *9* (12), 1023–1028.

(74) Agapov, R. L.; Srijanto, B.; Fowler, C.; Briggs, D.; Lavrik, N. V.; Sepaniak, M. J. Lithography-Free Approach to Highly Efficient, Scalable SERS Substrates Based on Disordered Clusters of Disc-on-Pillar Structures. *Nanotechnology* **2013**, *24* (50), 505302.

(75) Cho, S. K.; Moon, H.; Kim, C.-J. Creating, Transporting, Cutting, and Merging Liquid Droplets by Electrowetting-Based Actuation for Digital Microfluidic Circuits. *Microelectromechanical Systems, Journal of* **2003**, *12* (1), 70–80.

(76) Darhuber, A. A.; Valentino, J. P.; Davis, J. M.; Troian, S. M.; Wagner, S. Microfluidic Actuation by Modulation of Surface Stresses. *Applied Physics Letters* **2003**, *82* (4), 657–659.

(77) Duncombe, T. A.; Kumemura, M.; Fujita, H.; Böhringer, K. F. Integrating EWOD with Surface Ratchets for Active Droplet Transport and Sorting. In *2009 IEEE 22nd International Conference on Micro Electro Mechanical Systems*; IEEE: Sorrento, 2009; pp 531–534.

(78) Varel, C.; Bohringer, K. F. Liquid Droplet Micro-Bearings on Directional Circular Surface Ratchets. In *2014 IEEE 27th International Conference on Micro Electro Mechanical Systems (MEMS)*; 2014; pp 983–986.

(79) Bauer, H. F.; Chiba, M. Oscillations of Captured Spherical Drop of Viscous Liquid. *Journal of Sound and Vibration* **2005**, *285* (1–2), 51–71.

(80) Lu, H.-W.; Bottausci, F.; Fowler, J. D.; Bertozzi, A. L.; Meinhart, C.; Kim, C.-J. “CJ.” A Study of EWOD-Driven Droplets by PIV Investigation. *Lab Chip* **2008**, *8* (3), 456–461.

(81) Burton, J. C.; Rutledge, J. E.; Taborek, P. Fluid Pinch-off Dynamics at Nanometer Length Scales. *Physical review letters* **2004**, *92* (24), 244505.

(82) Cheng, J.-T.; Chen, C.-L. Active Thermal Management of On-Chip Hot Spots Using EWOD-Driven Droplet Microfluidics. *Exp Fluids* **2010**, *49* (6), 1349–1357.

(83) Gong, J.; Cha, G.; Ju, Y. S.; Kim, C.-J. Thermal Switches Based on Coplanar EWOD for Satellite Thermal Control. In *IEEE 21st International Conference on Micro Electro Mechanical Systems, 2008. MEMS 2008*; 2008; pp 848–851.

(84) Jönsson-Niedzió\lka, M.; Lapierre, F.; Coffinier, Y.; Parry, S. J.; Zoueshtiagh, F.; Foat, T.; Thomy, V.; Boukherroub, R. EWOD Driven Cleaning of Bioparticles on Hydrophobic and Superhydrophobic Surfaces. *Lab on a Chip* **2011**, *11* (3), 490–496.

(85) Sekeroglu, K.; Gurkan, U. A.; Demirci, U.; Demirel, M. C. Transport of a Soft Cargo on a Nanoscale Ratchet. *Applied Physics Letters* **2011**, *99* (6), 063703.

(86) Shah, G. J.; Ohta, A. T.; Chiou, E. P.-Y.; Wu, M. C.; Kim, C.-J. "CJ." EWOD-Driven Droplet Microfluidic Device Integrated with Optoelectronic Tweezers as an Automated Platform for Cellular Isolation and Analysis. *Lab on a Chip* **2009**, *9* (12), 1732.

(87) Vergauwe, N.; Witters, D.; Ceyssens, F.; Vermeir, S.; Verbruggen, B.; Puers, R.; Lammertyn, J. A Versatile Electrowetting-Based Digital Microfluidic Platform for Quantitative Homogeneous and Heterogeneous Bio-Assays. *J. Micromech. Microeng.* **2011**, *21* (5), 054026.

(88) Lin, T.-H.; Yao, D.-J. Applications of EWOD Systems for DNA Reaction and Analysis. *Journal of Adhesion Science & Technology* **2012**, *26* (12–17), 1789–1804.

(89) Jary, D.; Chollat-Namy, A.; Fouillet, Y.; Boutet, J.; Chabrol, C.; Castellan, G.; Gasparutto, D.; Pepponet, C. DNA Repair Enzyme Analysis on EWOD Fluidic Microprocessor. *NSTI Nanotech 2006 Technical Proceedings* **2006**, *2*, 554–557.

(90) Park, S.-Y.; Teitell, M. A.; Chiou, E. P. Y. Single-Sided Continuous Optoelectrowetting (SCOEW) for Droplet Manipulation with Light Patterns. *Lab on a Chip* **2010**, *10* (13), 1655–1661.

(91) Duncombe, T. A.; Kumemura, M.; Fujita, H.; Böhringer, K. F. Integrating EWOD with Surface Ratchets for Active Droplet Transport and Sorting. In *Micro Electro Mechanical Systems, 2009. MEMS 2009. IEEE 22nd International Conference on*; IEEE, 2009; pp 531–534.

(92) Mao, X.; Huang, T. J. Microfluidic Diagnostics for the Developing World. *Lab on a chip* **2012**, *12* (8), 1412–1416.

(93) Bohringer, K. F.; Duncombe, T.; Parsons, J. Vibration-Driven Droplet Transport Devices. US9279435B2, March 2016.

(94) Shastry, A.; Case, M. J.; Böhringer, K. F. Directing Droplets Using Microstructured Surfaces. *Langmuir* **2006**, *22* (14), 6161–6167.

(95) Shastry, A.; Taylor, D.; Böhringer, K. F. Micro-Structured Surface Ratchets for Droplet Transport; IEEE, 2007; pp 1353–1356.

(96) Duncombe, T. A.; Erdem, E. Y.; Shastry, A.; Baskaran, R.; Böhringer, K. F. Controlling Liquid Drops with Texture Ratchets. *Advanced Materials* **2012**, *24* (12), 1545–1550.

(97) Duncombe, T. A.; Parsons, J. F.; Böhringer, K. F. Directed Drop Transport Rectified from Orthogonal Vibrations via a Flat Wetting Barrier Ratchet. *Langmuir* **2012**, *28* (38), 13765–13770.

(98) Dong, Y.; Holmes, H. R.; Böhringer, K. F. Converting Vertical Vibration of Anisotropic Ratchet Conveyors into Horizontal Droplet Motion. *Langmuir* **2017**, *33* (40), 10745–10752.

(99) Burns, M. A.; Mastrangelo, C. H.; Sammarco, T. S.; Man, F. P.; Webster, J. R.; Johnsons, B. N.; Foerster, B.; Jones, D.; Fields, Y.; Kaiser, A. R.; et al. Microfabricated Structures for

Integrated DNA Analysis. *Proceedings of the National Academy of Sciences* **1996**, *93* (11), 5556–5561.

(100) Stone, H. A.; Stroock, A. D.; Ajdari, A. Engineering Flows in Small Devices: Microfluidics toward a Lab-on-a-Chip. *Annual Review of Fluid Mechanics* **2004**, *36*, 381–411.

(101) Squires, T. M.; Quake, S. R. Microfluidics: Fluid Physics at the Nanoliter Scale. *Reviews of Modern Physics* **2005**, *77* (3), 977.

(102) Ca, U. Controlled Microfluidic Interfaces. *Nature* **2005**, *437*, 29.

(103) Brochard, F. Motions of Droplets on Solid Surfaces Induced by Chemical or Thermal Gradients. *Langmuir* **1989**, *5* (2), 432–438.

(104) Chaudhury, M. K.; Whitesides, G. M. How to Make Water Run Uphill. *Science* **1992**, *256* (5063), 1539–1541.

(105) Pollack, M. G.; Fair, R. B.; Shenderov, A. D. Electrowetting-Based Actuation of Liquid Droplets for Microfluidic Applications. *Applied Physics Letters* **2000**, *77* (11), 1725–1726.

(106) Pollack, M. G.; Shenderov, A. D.; Fair, R. B. Electrowetting-Based Actuation of Droplets for Integrated Microfluidics. *Lab on a Chip* **2002**, *2* (2), 96–101.

(107) Cho, S. K.; Moon, H.; Kim, C.-J. Creating, Transporting, Cutting, and Merging Liquid Droplets by Electrowetting-Based Actuation for Digital Microfluidic Circuits. *Microelectromechanical Systems, Journal of* **2003**, *12* (1), 70–80.

(108) Zhang, J.; Cheng, Z.; Zheng, Y.; Jiang, L. Ratchet-Induced Anisotropic Behavior of Superparamagnetic Microdroplet. *Applied Physics Letters* **2009**, *94* (14), 144104.

(109) Linke, H.; Alemán, B. J.; Melling, L. D.; Taormina, M. J.; Francis, M. J.; Dow-Hygelund, C. C.; Narayanan, V.; Taylor, R. P.; Stout, A. Self-Propelled Leidenfrost Droplets. *Physical Review Letters* **2006**, *96* (15), 154502.

(110) Lagubeau, G.; Le Merrer, M.; Clanet, C.; Quéré, D. Leidenfrost on a Ratchet. *Nature Physics* **2011**, *7* (5), 395–398.

(111) Buguin, A.; Talini, L.; Silberzan, P. Ratchet-like Topological Structures for the Control of Microdrops. *Applied Physics A* **2002**, *75* (2), 207–212.

(112) Daniel, S.; Sircar, S.; Gliem, J.; Chaudhury, M. K. Ratcheting Motion of Liquid Drops on Gradient Surfaces. *Langmuir* **2004**, *20* (10), 4085–4092.

(113) Buguin, A.; Brochard, F.; De Gennes, P.-G. Motions Induced by Asymmetric Vibrations. *The European Physical Journal E* **2006**, *19* (1), 31–36.

(114) Daniel, S.; Chaudhury, M. K. Rectified Motion of Liquid Drops on Gradient Surfaces Induced by Vibration. *Langmuir* **2002**, *18* (9), 3404–3407.

(115) Noblin, X.; Kofman, R.; Celestini, F. Ratchetlike Motion of a Shaken Drop. *Physical Review Letters* **2009**, *102* (19), 194504.

(116) Malvadkar, N. A.; Hancock, M. J.; Sekeroglu, K.; Dressick, W. J.; Demirel, M. C. An Engineered Anisotropic Nanofilm with Unidirectional Wetting Properties. *Nature Materials* **2010**, *9* (12), 1023–1028.

(117) Daniel, S.; Chaudhury, M. K.; De Gennes, P.-G. Vibration-Actuated Drop Motion on Surfaces for Batch Microfluidic Processes. *Langmuir* **2005**, *21* (9), 4240–4248.

(118) Mettu, S.; Chaudhury, M. K. Motion of Drops on a Surface Induced by Thermal Gradient and Vibration. *Langmuir* **2008**, *24* (19), 10833–10837.

(119) Mettu, S.; Chaudhury, M. K. Motion of Liquid Drops on Surfaces Induced by Asymmetric Vibration: Role of Contact Angle Hysteresis. *Langmuir* **2011**, *27* (16), 10327–10333.

(120) Goohpattader, P. S.; Mettu, S.; Chaudhury, M. K. Stochastic Rolling of a Rigid Sphere in Weak Adhesive Contact with a Soft Substrate. *The European Physical Journal E* **2011**, *34* (11), 1–11.

(121) Goohpattader, P. S.; Chaudhury, M. K. Random Motion with Interfacial Contact: Driven Diffusion Vis-à-Vis Mechanical Activation. *The European Physical Journal E* **2012**, *35* (8), 1–16.

(122) Vukasinovic, B.; Smith, M. K.; Glezer, A. Dynamics of a Sessile Drop in Forced Vibration. *Journal of Fluid Mechanics* **2007**, *587*, 395–423.

(123) Wilkes, E. D.; Basaran, O. A. Forced Oscillations of Pendant (Sessile) Drops. *Physics of Fluids* **1997**, *9* (6), 1512–1528.

(124) Noblin, X.; Buguin, A.; Brochard-Wyart, F. Vibrations of Sessile Drops. *The European Physical Journal Special Topics* **2009**, *166* (1), 7–10.

(125) Lamb, H. *Hydrodynamics*; Cambridge university press, 1932.

(126) McHale, G.; Elliott, S. J.; Newton, M. I.; Herbertson, D. L.; Esmer, K. Levitation-Free Vibrated Droplets: Resonant Oscillations of Liquid Marbles. *Langmuir* **2008**, *25* (1), 529–533.

(127) Sharp, J. S.; Farmer, D. J.; Kelly, J. Contact Angle Dependence of the Resonant Frequency of Sessile Water Droplets. *Langmuir* **2011**, *27* (15), 9367–9371.

(128) Chaudhury, M. K.; Chakrabarti, A.; Daniel, S. Generation of Motion of Drops with Interfacial Contact. *Langmuir* **2015**, *31* (34), 9266–9281.

(129) Mettu, S.; Chaudhury, M. K. Vibration Spectroscopy of a Sessile Drop and Its Contact Line. *Langmuir* **2012**, *28* (39), 14100–14106.

(130) Holmes, H. R.; Böhringer, K. F. Transport Velocity of Droplets on Ratchet Conveyors. *Advances in Colloid and Interface Science* **2017**.

(131) Holmes, H. R.; Gomez, A. E.; Böhringer, K. F. Timing and Synchronization of Droplets on Ratchet Conveyors. In *2016 IEEE 29th International Conference on Micro Electro Mechanical Systems (MEMS)*; IEEE, 2016; pp 796–799.

(132) Duncombe, T. A.; Erdem, E. Y.; Shastry, A.; Baskaran, R.; Böhringer, K. F. Controlling Liquid Drops with Texture Ratchets. *Advanced Materials* **2012**, *24* (12), 1545–1550.

(133) McHale, G.; Elliott, S. J.; Newton, M. I.; Herbertson, D. L.; Esmer, K. Levitation-Free Vibrated Droplets: Resonant Oscillations of Liquid Marbles. *Langmuir* **2009**, *25* (1), 529–533.

(134) Noblin, X.; Buguin, A.; Brochard-Wyart, F. Vibrated Sessile Drops: Transition between Pinned and Mobile Contact Line Oscillations. *European Physical Journal E -- Soft Matter* **2004**, *14* (4), 395–404.

(135) Perez, M.; Brechet, Y.; Salvo, L.; Papoular, M.; Suery, M. Oscillation of Liquid Drops under Gravity: Influence of Shape on the Resonance Frequency. *Europhysics Letters* **1999**, *47* (2), 189.

(136) Jang, L.-S.; Hsu, C.-Y.; Chen, C.-H. Effect of Electrode Geometry on Performance of EWOD Device Driven by Battery-Based System. *Biomedical Microdevices* **2009**, *11* (5), 1029.

(137) Zhu, L.; Feng, Y.; Ye, X.; Feng, J.; Wu, Y.; Zhou, Z. An ELISA Chip Based on an EWOD Microfluidic Platform. *Journal of Adhesion Science and Technology* **2012**, *26* (12–17), 2113–2124.

(138) Holmes, H. R.; Gomez, A. E.; Böhringer, K. F. Enabling Droplet Functionality on Anisotropic Ratchet Conveyors. *Micromachines* **2017**, *8* (12), 363.

(139) Abdelgawad, M.; Wheeler, A. R. The Digital Revolution: A New Paradigm for Microfluidics. *Advanced Materials* **2009**, *21* (8), 920–925.

(140) Park, S.-Y.; Kalim, S.; Callahan, C.; Teitell, M. A.; Chiou, E. P. A Light-Induced Dielectrophoretic Droplet Manipulation Platform. *Lab on a Chip* **2009**, *9* (22), 3228–3235.

(141) Geng, H.; Feng, J.; Marie Stabryla, L.; Kwon Cho, S. Dielectrowetting Manipulation for Digital Microfluidics: Creating, Transporting, Splitting, and Merging of Droplets. *Lab on a Chip* **2017**, *17* (6), 1060–1068.

(142) Fu, E.; Liang, T.; Spicar-Mihalic, P.; Houghtaling, J.; Ramachandran, S.; Yager, P. Two-Dimensional Paper Network Format That Enables Simple Multistep Assays for Use in Low-Resource Settings in the Context of Malaria Antigen Detection. *Analytical Chemistry* **2012**, *84* (10), 4574–4579.

(143) Fu, E.; Liang, T.; Houghtaling, J.; Ramachandran, S.; Ramsey, S. A.; Lutz, B.; Yager, P. Enhanced Sensitivity of Lateral Flow Tests Using a Two-Dimensional Paper Network Format. *Analytical Chemistry* **2011**, *83* (20), 7941–7946.

(144) Fu, E.; Lutz, B.; Kauffman, P.; Yager, P. Controlled Reagent Transport in Disposable 2D Paper Networks. *Lab on a Chip* **2010**, *10* (7), 918–920.

(145) Gervais, L.; Delamarche, E. Toward One-Step Point-of-Care Immunodiagnostics Using Capillary-Driven Microfluidics and PDMS Substrates. *Lab on a Chip* **2009**, *9* (23), 3330–3337.

(146) Holland, C. A.; Kiechle, F. L. Point-of-Care Molecular Diagnostic Systems — Past, Present and Future. *Current Opinion in Microbiology* **2005**, *8* (5), 504–509.

(147) Niemz, A.; Ferguson, T. M.; Boyle, D. S. Point-of-Care Nucleic Acid Testing for Infectious Diseases. *Trends in Biotechnology* **2011**, *29* (5), 240–250.

(148) Britton, S.; Cheng, Q.; McCarthy, J. S. Novel Molecular Diagnostic Tools for Malaria Elimination: A Review of Options from the Point of View of High-Throughput and Applicability in Resource Limited Settings. *Malaria Journal* **2016**, *15*, 88.

(149) Camper, D. V.; Viola, R. E. Fully Automated Protein Purification. *Analytical Biochemistry* **2009**, *393* (2), 176–181.

(150) Berensmeier, S. Magnetic Particles for the Separation and Purification of Nucleic Acids. *Applied Microbiology and Biotechnology* **2006**, *73* (3), 495–504.

(151) Lee, J.; Moon, H.; Fowler, J.; Schoellhammer, T.; Kim, C.-J. Electrowetting and Electrowetting-on-Dielectric for Microscale Liquid Handling. *Sensors and Actuators A: Physical* **2002**, *95* (2–3), 259–268.

(152) Mugele, F.; Baret, J.-C. Electrowetting: From Basics to Applications. *Journal of Physics: Condensed Matter* **2005**, *17* (28), R705.

(153) World Economic Forum. *State of the Illicit Economy*; 2015.

(154) Dormontt, E. E.; Boner, M.; Braun, B.; Breulmann, G.; Degen, B.; Espinoza, E.; Gardner, S.; Guillery, P.; Hermanson, J. C.; Koch, G.; et al. Forensic Timber Identification: It's Time to Integrate Disciplines to Combat Illegal Logging. *Biological Conservation* **2015**, *191*, 790–798.

(155) Golden, R. E.; Warner, K. The global reach of seafood fraud: a current review of the literature http://usa.oceana.org/publications/reports/global-reach-seafood-fraud-current-review-literature (accessed Mar 25, 2018).

(156) Warner, K.; Timme, W.; Lowell, B.; Hirschfield, M. National Seafood Fraud Testing Results. *Oceana Report* **2013**.

(157) Pramod, G.; Nakamura, K.; Pitcher, T. J.; Delagran, L. Estimates of Illegal and Unreported Fish in Seafood Imports to the USA. *Marine Policy* **2014**, *48*, 102–113.

(158) Marko, P. B.; Nance, H. A.; Guynn, K. D. Genetic Detection of Mislabeled Fish from a Certified Sustainable Fishery. *Current Biology* **2011**, *21* (16), R621–R622.

(159) Colautti Robert I.; MacIsaac Hugh J. A Neutral Terminology to Define 'Invasive' Species. *Diversity and Distributions* **2004**, *10* (2), 135–141.

(160) Clavero, M.; García-Berthou, E. Invasive Species Are a Leading Cause of Animal Extinctions. *Trends in Ecology & Evolution* **2005**, *20* (3), 110.

(161) Pimentel, D.; Zuniga, R.; Morrison, D. Update on the Environmental and Economic Costs Associated with Alien-Invasive Species in the United States. *Ecological Economics* **2005**, *52* (3), 273–288.

(162) Myers, J. H.; Simberloff, D.; Kuris, A. M.; Carey, J. R. Eradication Revisited: Dealing with Exotic Species. *Trends in ecology & evolution* **2000**, *15* (8), 316–320.

(163) Bogich, T. L.; Liebhold, A. M.; Shea, K. To Sample or Eradicate? A Cost Minimization Model for Monitoring and Managing an Invasive Species. *Journal of Applied Ecology* **2008**, *45* (4), 1134–1142.

(164) Vander Zanden, M. J.; Hansen, G. J.; Higgins, S. N.; Kornis, M. S. A Pound of Prevention, plus a Pound of Cure: Early Detection and Eradication of Invasive Species in the Laurentian Great Lakes. *Journal of Great Lakes Research* **2010**, *36* (1), 199–205.

(165) Martinez, B.; Dehgan, A.; Zamft, B.; Baisch, D.; McCormick, C.; Giordano, A. J.; Aicher, R.; Shelbe, S.; Hoffman, C. Advancing Federal Capacaties for the Early Detection of and Rapid Response to Invasive Species through Technology Innovation. *National Invasive Species Council Secretariat: Washington D.C.* **2018**.

(166) Gasson, P. How Precise Can Wood Identification Be? Wood Anatomy’s Role in Support of the Legal Timber Trade, Especially CITES. *IAWA Journal* **2011**, *32* (2), 137–154.

(167) Cabral, E. C.; Simas, R. C.; Santos, V. G.; Queiroga, C. L.; Cunha, V. S.; Sá, G. F.; Daroda, R. J.; Eberlin, M. N. Wood Typification by Venturi Easy Ambient Sonic Spray Ionization Mass Spectrometry: The Case of the Endangered Mahogany Tree. *Journal of Mass Spectrometry* **2012**, *47* (1), 1–6.

(168) Cody, R. B.; Dane, A. J.; Dawson-Andoh, B.; Adedipe, E. O.; Nkansah, K. Rapid Classification of White Oak (Quercus Alba) and Northern Red Oak (Quercus Rubra) by Using Pyrolysis Direct Analysis in Real Time (DART^{TM}) and Time-of-Flight Mass Spectrometry. *Journal of Analytical and Applied Pyrolysis* **2012**, *95*, 134–137.

(169) Lancaster, C.; Espinoza, E. Analysis of Select Dalbergia and Trade Timber Using Direct Analysis in Real Time and Time-of-Flight Mass Spectrometry for CITES Enforcement. *Rapid Communications in Mass Spectrometry* **2012**, *26* (9), 1147–1156.

(170) Lancaster, C.; Espinoza, E. Evaluating Agarwood Products for 2-(2-Phenylethyl) Chromones Using Direct Analysis in Real Time Time-of-Flight Mass Spectrometry. *Rapid Communications in Mass Spectrometry* **2012**, *26* (23), 2649–2656.

(171) Espinoza, E. O.; Lancaster, C. A.; Kreitals, N. M.; Hata, M.; Cody, R. B.; Blanchette, R. A. Distinguishing Wild from Cultivated Agarwood (Aquilaria Spp.) Using Direct Analysis in Real Time and Time of-Flight Mass Spectrometry. *Rapid Communications in Mass Spectrometry* **2014**, *28* (3), 281–289.

(172) Espinoza, E. O.; Wiemann, M. C.; Barajas-Morales, J.; Chavarria, G. D.; McClure, P. J. Forensic Analysis of Cites-Protected Dalbergia Timber from the Americas. *IAWA Journal* **2015**, *36* (3), 311–325.

(173) McClure, P. J.; Chavarria, G. D.; Espinoza, E. Metabolic Chemotypes of CITES Protected Dalbergia Timbers from Africa, Madagascar, and Asia. *Rapid Communications in Mass Spectrometry* **2015**, *29* (9), 783–788.

(174) Tsuchikawa, S. A Review of Recent near Infrared Research for Wood and Paper. *Applied Spectroscopy Reviews* **2007**, *42* (1), 43–71.

(175) Russ, A.; Firesova, M.; Gigac, J. Preliminary Study of Wood Species Identification by NIR Spectroscopy. *Wood Research* **2009**, *54* (4), 23–32.

(176) Braga, J. W. B.; Pastore, T. C. M.; Coradin, V. T. R.; Camargos, J. A. A.; da Silva, A. R. The Use of near Infrared Spectroscopy to Identify Solid Wood Specimens of Swietenia Macrophylla (Cites Appendix II). *IAWA Journal* **2011**, *32* (2), 285–296.

(177) Pastore, T. C. M.; Braga, J. W. B.; Coradin, V. T. R.; Magalhães, W. L. E.; Okino, E. Y. A.; Camargos, J. A. A.; de Muñiz, G. I. B.; Bressan, O. A.; Davrieux, F. Near Infrared Spectroscopy (NIRS) as a Potential Tool for Monitoring Trade of Similar Woods: Discrimination of True Mahogany, Cedar, Andiroba, and Curupixa. *International Journal of the Biology, Chemistry, Physics, and Technology of Wood* **2011**, *65* (1).

(178) Sandak, A.; Sandak, J.; Negri, M. Relationship between Near-Infrared (NIR) Spectra and the Geographical Provenance of Timber. *Wood Science and Technology* **2011**, *45* (1), 35–48.

(179) Tsuchikawa, S.; Schwanninger, M. A Review of Recent Near-Infrared Research for Wood and Paper (Part 2). *Applied Spectroscopy Reviews* **2013**, *48* (7), 560–587.

(180) Braun, B.; Germany, W. W. F. Wildlife Detector Dogs–a Guideline on the Training of Dogs to Detect Wildlife in Trade. *WWF Germany, Berlin (DE)* **2013**.

(181) Marco, J.; Artajona, J.; Larrechi, M. S.; Rius, F. Relationship between Geographical Origin and Chemical-Composition of Wood for Oak Barrels. *American Journal of Enology and Viticulture* **1994**, *45* (2), 192–200.

(182) Dejean, T.; Valentini, A.; Miquel, C.; Taberlet, P.; Bellemain, E.; Miaud, C. Improved Detection of an Alien Invasive Species through Environmental DNA Barcoding: The Example of the American Bullfrog Lithobates Catesbeianus. *Journal of applied ecology* **2012**, *49* (4), 953–959.

(183) Crall Alycia W.; Newman Gregory J.; Stohlgren Thomas J.; Holfelder Kirstin A.; Graham Jim; Waller Donald M. Assessing Citizen Science Data Quality: An Invasive Species Case Study. *Conservation Letters* **2011**, *4* (6), 433–442.

(184) Wade, M. J. Evolution: Infectious Speciation. *Nature* **2001**, *409* (6821), 675–677.

(185) Frézal, L.; Leblois, R. Four Years of DNA Barcoding: Current Advances and Prospects. *Infection, Genetics and Evolution* **2008**, *8* (5), 727–736.

(186) Hebert, P. D.; Cywinska, A.; Ball, S. L. Biological Identifications through DNA Barcodes. *Proceedings of the Royal Society of London B: Biological Sciences* **2003**, *270* (1512), 313–321.

(187) Huang, D.; Meier, R.; Todd, P. A.; Chou, L. M. Slow Mitochondrial COI Sequence Evolution at the Base of the Metazoan Tree and Its Implications for DNA Barcoding. *Journal of Molecular Evolution* **2008**, *66* (2), 167–174.

(188) Mishmar, D.; Ruiz-Pesini, E.; Mondragon-Palomino, M.; Procaccio, V.; Gaut, B.; Wallace, D. C. Adaptive Selection of Mitochondrial Complex I Subunits during Primate Radiation. *Gene* **2006**, *378*, 11–18.

(189) Pegg, G. G.; Sinclair, B.; Briskey, L.; Aspden, W. J. MtDNA Barcode Identification of Fish Larvae in the Southern Great Barrier Reef–Australia. *Scientia Marina* **2006**, *70* (S2), 7–12.

(190) Piaggio, A. J.; Engeman, R. M.; Hopken, M. W.; Humphrey, J. S.; Keacher, K. L.; Bruce, W. E.; Avery, M. L. Detecting an Elusive Invasive Species: A Diagnostic PCR to Detect Burmese Python in Florida Waters and an Assessment of Persistence of Environmental DNA. *Molecular Ecology Resources* **2014**, *14* (2), 374–380.

(191) Kress, W. J.; Wurdack, K. J.; Zimmer, E. A.; Weigt, L. A.; Janzen, D. H. Use of DNA Barcodes to Identify Flowering Plants. *Proceedings of the National Academy of Sciences of the United States of America* **2005**, *102* (23), 8369–8374.

(192) Kress, W. J.; Erickson, D. L. A Two-Locus Global DNA Barcode for Land Plants: The Coding RbcL Gene Complements the Non-Coding TrnH-PsbA Spacer Region. *PLoS One* **2007**, *2* (6), e508.

(193) Hollingsworth, P. M.; Forrest, L. L.; Spouge, J. L.; Hajibabaei, M.; Ratnasingham, S.; Bank, M. van der; Chase, M. W.; Cowan, R. S.; Erickson, D. L.; Fazekas, A. J.; et al. A DNA Barcode for Land Plants. *PNAS* **2009**, *106* (31), 12794–12797.

(194) Hollingsworth, M. L.; Andra Clarck, A.; Forrest, L. L.; Richardson, J.; Pennington, R.; Long, D. G.; Cowan, R.; Chase, M. W.; Gaudeul, M.; Hollingsworth, P. M. Selecting Barcoding Loci for Plants: Evaluation of Seven Candidate Loci with Species-Level Sampling in Three Divergent Groups of Land Plants. *Molecular Ecology Resources* **2009**, *9* (2), 439–457.

(195) Ratnasingham, S.; Hebert, P. D. BOLD: The Barcode of Life Data System. *Molecular Ecology Resources* **2007**, *7* (3), 355–364.

(196) Stockle, M. Y.; Hebert, P. D. Barcode of Life. *Scientific American* **2008**, *299* (4), 82–88.

(197) Ward, R. D.; Hanner, R.; Hebert, P. D. The Campaign to DNA Barcode All Fishes, FISH-BOL. *Journal of Fish Biology* **2009**, *74* (2), 329–356.

(198) Finkeldey, R.; Leinemann, L.; Gailing, O. Molecular Genetic Tools to Infer the Origin of Forest Plants and Wood. *Applied Microbiology and Biotechnology* **2010**, *85* (5), 1251–1258.

(199) Lowe, A. J.; Wong, K. N.; Tiong, Y. S.; Iyerh, S.; Chew, F. T. A DNA Method to Verify the Integrity of Timber Supply Chains; Confirming the Legal Sourcing of Merbau Timber from Logging Concession to Sawmill. *Silvae Genetica* **2010**, *59* (6), 263.

(200) Lowe, A. J.; Cross, H. B. The Application of DNA Methods to Timber Tracking and Origin Verification. *IAWA Journal* **2011**, *32* (2), 251–262.

(201) Hellberg, R. S. R.; Morrissey, M. T. Advances in DNA-Based Techniques for the Detection of Seafood Species Substitution on the Commercial Market. *JALA: Journal of the Association for Laboratory Automation* **2011**, *16* (4), 308–321.

(202) Galimberti, A.; De Mattia, F.; Losa, A.; Bruni, I.; Federici, S.; Casiraghi, M.; Martellos, S.; Labra, M. DNA Barcoding as a New Tool for Food Traceability. *Food Research International* **2013**, *50* (1), 55–63.

(203) Nithaniyal, S.; Newmaster, S. G.; Ragupathy, S.; Krishnamoorthy, D.; Vassou, S. L.; Parani, M. DNA Barcode Authentication of Wood Samples of Threatened and Commercial Timber Trees within the Tropical Dry Evergreen Forest of India. *PLoS One* **2014**, *9* (9), e107669.

(204) Ivanova, N. V.; Borisenko, A. V.; Hebert, P. D. Express Barcodes: Racing from Specimen to Identification. *Molecular Ecology Resources* **2009**, *9* (s1), 35–41.

(205) Marx, V. PCR Heads into the Field. *Nature Methods* **2015**, *12*, 393–397.

(206) Meyer, R.; Höfelein, C.; Lüthy, J.; Candrian, U. Polymerase Chain Reaction-Restriction Fragment Length Polymorphism Analysis: A Simple Method for Species Identification in Food. *Journal of AOAC International* **1995**, *78* (6), 1542–1551.

(207) Girish, P. S.; Anjaneyulu, A. S. R.; Viswas, K. N.; Shivakumar, B. M.; Anand, M.; Patel, M.; Sharma, B. Meat Species Identification by Polymerase Chain Reaction-Restriction Fragment Length Polymorphism (PCR-RFLP) of Mitochondrial 12S RRNA Gene. *Meat Science* **2005**, *70* (1), 107–112.

(208) Kim, J.; Easley, C. J. Isothermal DNA Amplification in Bioanalysis: Strategies and Applications. *Bioanalysis* **2011**, *3* (2), 227–239.

(209) Heid, C. A.; Stevens, J.; Livak, K. J.; Williams, P. M. Real Time Quantitative PCR. *Genome Research* **1996**, *6* (10), 986–994.

(210) Zanoli, L. M.; Spoto, G. Isothermal Amplification Methods for the Detection of Nucleic Acids in Microfluidic Devices. *Biosensors* **2012**, *3* (1), 18–43.

(211) Tanner, N. A.; Zhang, Y.; Evans Jr, T. C. Visual Detection of Isothermal Nucleic Acid Amplification Using PH-Sensitive Dyes. *Biotechniques* **2015**, *58* (2), 59–68.

(212) Tomita, N.; Mori, Y.; Kanda, H.; Notomi, T. Loop-Mediated Isothermal Amplification (LAMP) of Gene Sequences and Simple Visual Detection of Products. *Nature Protocols* **2008**, *3* (5), 877–882.

(213) Hataoka, Y.; Zhang, L.; Mori, Y.; Tomita, N.; Notomi, T.; Baba, Y. Analysis of Specific Gene by Integration of Isothermal Amplification and Electrophoresis on Poly(Methyl Methacrylate) Microchips. *Analytical Chemistry* **2004**, *76* (13), 3689–3693.

(214) Notomi, T.; Okayama, H.; Masubuchi, H.; Yonekawa, T.; Watanabe, K.; Amino, N.; Hase, T. Loop-Mediated Isothermal Amplification of DNA. *Nucleic Acids Research* **2000**, *28* (12), e63–e63.

(215) Nagamine, K.; Hase, T.; Notomi, T. Accelerated Reaction by Loop-Mediated Isothermal Amplification Using Loop Primers. *Molecular and Cellular Probes* **2002**, *16* (3), 223–229.

(216) Kaneko, H.; Kawana, T.; Fukushima, E.; Suzutani, T. Tolerance of Loop-Mediated Isothermal Amplification to a Culture Medium and Biological Substances. *Journal of Biochemical and Biophysical Methods* **2007**, *70* (3), 499–501.

(217) Mori, Y.; Notomi, T. Loop-Mediated Isothermal Amplification (LAMP): A Rapid, Accurate, and Cost-Effective Diagnostic Method for Infectious Diseases. *Journal of Infection and Chemotherapy* **2009**, *15* (2), 62–69.

(218) Fang, X.; Chen, H.; Yu, S.; Jiang, X.; Kong, J. Predicting Viruses Accurately by a Multiplex Microfluidic Loop-Mediated Isothermal Amplification Chip. *Analytical Chemistry* **2011**, *83* (3), 690–695.

(219) Hsieh, K.; Patterson, A. S.; Ferguson, B. S.; Plaxco, K. W.; Soh, H. T. Rapid, Sensitive, and Quantitative Detection of Pathogenic DNA at the Point of Care through Microfluidic Electrochemical Quantitative Loop-Mediated Isothermal Amplification. *Angewandte Chemie* **2012**, *124* (20), 4980–4984.

(220) Ayoib, A.; Hashim, U.; Gopinath, S. C. B.; Arshad, M. K. M. DNA Extraction on Bio-Chip: History and Preeminence over Conventional and Solid-Phase Extraction Methods. *Applied Microbiology and Biotechnology* **2017**, *101* (22), 8077–8088.

(221) Asif, M. J.; Cannon, C. H. DNA Extraction from Processed Wood: A Case Study for the Identification of an Endangered Timber Species (Gonystylus Bancanus). *Plant Molecular Biology Reporter* **2005**, *23* (2), 185–192.

(222) Rachmayanti, Y.; Leinemann, L.; Gailing, O.; Finkeldey, R. Extraction, Amplification and Characterization of Wood DNA from Dipterocarpaceae. *Plant Molecular Biology Reporter* **2006**, *24* (1), 45–55.

(223) Rachmayanti, Y.; Leinemann, L.; Gailing, O.; Finkeldey, R. DNA from Processed and Unprocessed Wood: Factors Influencing the Isolation Success. *Forensic Science International: Genetics* **2009**, *3* (3), 185–192.

(224) Finkeldey, R.; Rachmayanti, Y.; Gailing, O. Molecular Genetic Tools for the Identification of the Origin of Wood. *Wood Production, Wood Technology and Biotechnological Impacts.* **2007**, 143–158.

(225) Hedman, J.; Radström, P. Overcoming Inhibition in Real-Time Diagnostic PCR. In *PCR detection of microbial pathogens*; Springer, 2013; pp 17–48.

(226) Kreader, C. A. Relief of Amplification Inhibition in PCR with Bovine Serum Albumin or T4 Gene 32 Protein. *Applied and Environmental Microbiology* **1996**, *62* (3), 1102–1106.

(227) Rossen, L.; Nørskov, P.; Holmstrøm, K.; Rasmussen, O. F. Inhibition of PCR by Components of Food Samples, Microbial Diagnostic Assays and DNA-Extraction Solutions. *International Journal of Food Microbiology* **1992**, *17* (1), 37–45.

(228) Schrader, C.; Schielke, A.; Ellerbroek, L.; Johne, R. PCR Inhibitors–Occurrence, Properties and Removal. *Journal of Applied Microbiology* **2012**, *113* (5), 1014–1026.

(229) Kontanis, E. J.; Reed, F. A. Evaluation of Real-Time PCR Amplification Efficiencies to Detect PCR Inhibitors. *Journal of Forensic Sciences* **2006**, *51* (4), 795–804.

(230) Opel, K. L.; Chung, D.; McCord, B. R. A Study of PCR Inhibition Mechanisms Using Real Time PCR. *Journal of Forensic Sciences* **2010**, *55* (1), 25–33.

(231) Thomsen, P.; Kielgast, J. O. S.; Iversen, L. L.; Wiuf, C.; Rasmussen, M.; Gilbert, M. T. P.; Orlando, L.; Willerslev, E. Monitoring Endangered Freshwater Biodiversity Using Environmental DNA. *Molecular Ecology* **2012**, *21* (11), 2565–2573.

(232) Rees, H. C.; Maddison, B. C.; Middleditch, D. J.; Patmore, J. R.; Gough, K. C. The Detection of Aquatic Animal Species Using Environmental DNA–a Review of EDNA as a Survey Tool in Ecology. *Journal of Applied Ecology* **2014**, *51* (5), 1450–1459.

(233) Ardura, A.; Zaiko, A.; Martinez, J. L.; Samuiloviene, A.; Borrell, Y.; Garcia-Vazquez, E. Environmental DNA Evidence of Transfer of North Sea Molluscs across Tropical Waters through Ballast Water. *Journal of Molluscan Studies* **2015**, *81* (4), 495–501.

(234) Hosono, S.; Faruqi, A. F.; Dean, F. B.; Du, Y.; Sun, Z.; Wu, X.; Du, J.; Kingsmore, S. F.; Egholm, M.; Lasken, R. S. Unbiased Whole-Genome Amplification Directly from Clinical Samples. *Genome Research* **2003**, *13* (5), 954–964.

(235) Wasser, S. K.; Mailand, C.; Booth, R.; Mutayoba, B.; Kisamo, E.; Clark, B.; Stephens, M. Using DNA to Track the Origin of the Largest Ivory Seizure since the 1989 Trade Ban. *Proceedings of the National Academy of Sciences* **2007**, *104* (10), 4228–4233.

(236) Kincaid, D. C.; Longley, T. S. A Water Droplet Evaporation and Temperature Model. *Transactions of the ASAE* **1989**, *32* (2), 457–0462.

(237) Ranz, W. E.; Marshall, W. R. Evaporation from Drops. *Chem. Eng. Prog* **1952**, *48* (3), 141–146.

(238) Sobac, B.; Brutin, D. Thermal Effects of the Substrate on Water Droplet Evaporation. *Physical Review E* **2012**, *86* (2), 021602.

(239) Xu, X.; Luo, J. Marangoni Flow in an Evaporating Water Droplet. *Applied Physics Letters* **2007**, *91* (12), 124102.

(240) Kulinich, S. A.; Farzaneh, M. Effect of Contact Angle Hysteresis on Water Droplet Evaporation from Super-Hydrophobic Surfaces. *Applied Surface Science* **2009**, *255* (7), 4056–4060.